ISBN 0-315-38333-X

PREDICTION OF HIGH TEMPERATURE DEFORMATION TEXTURES IN FCC METALS

by

Brigitte Bacroix

A Thesis Submitted to the Faculty of Graduate Studies and Research in Partial Fulfilment of the Requirements for the Degree of Doctor of Philosophy

Department of Mining and Metallurgical Engineering
McGill University
Montreal, Canada

December 1986

ABSTRACT

A literature review is presented of deformation and annealing textures; it is clearly shown that, when the deformation temperature is increased, the percentage of the so-called "brass" component increases in torsion, rolling and tension. The latter is confirmed by a small-scale experimental investigation of the textures produced by the hot and cold swaging (extension) of aluminum.

The possible mechanisms responsible for the differences observed in the deformation textures produced at low and at high temperatures are listed and modelled. The RW theory of the minimization of the work hardening rate is extended to the deformation of polycrystals. In this treatment, the extent of the ambiguities in the choice of active slip systems present in the FC and RC models is specified. It is also shown that the RW predictions are in good agreement with intermediate temperature results for torsion and rolling but not for tension.

Differences in the ease of cross-slip are simulated in three different ways: i) by employing the colinear slip selection criterion originally introduced by Chin; ii) by the introduction of suitable hardening laws; and iii) by introducing the activation of {110} <110> and {112} <110> cross-slip systems. All three models predict an increase in the brass component when compared to the classical models of texture prediction; this increase is, however, small when the first two methods are applied to torsion and rolling.

The activation of {100} <110> systems is also explored. The composite single crystal yield surface for dual slip on {111} and {100} planes is described. It is shown that the operation of these systems leads to texture components which are never observed at high temperatures. A new model is presented, developed to account for the occurrence of a high degree of recovery concurrently with deformation. It simulates the formation of the polygonized substructure which results from the minimization of the sub-boundary energy. The results obtained for torsion and rolling reproduce qualitatively the experimental deformation textures pertaining to these strain paths. Finally the different models proposed are compared and their validity and limitations are analyzed briefly.

RÉSUMÉ

Lors de l'étude bibliographique concernant les textures formées au cours d'une déformation ou d'un recuit dans les métaux cfc, il est clairement démontré que lorsque la température de déformation augmente, le pourcentage de la composante dite "laiton" augmente en torsion, laminage et traction axisymétrique. Ce dernier point est confirmé par une étude expérimentale succinte des textures produites dans des barres d'aluminium par martelage rotatif à froid et à chaud.

Les mécanismes pouvant être responsables des différences observées entre les textures de déformation à froid et à chaud sont énumérés et modélisés. La théorie de Renouard et Wintemberger, fondée sur la minimisation du taux d'écrouissage, est étendue à la déformation des polycristaux. Lors de ce traitement, le degré de l'indétermination dans le choix des systèmes de glissement actifs est précisé pour les modèles FC (déformation complèment imposée) et RC (déformation partiellement imposée). Il apparait que les prévisions RW sont en bon accord avec les résultats expérimentaux obtenus aux températures intermédiaires en laminage et torsion mais pas en traction.

La possibilité d'un glissement dévié a été simulé de trois manières différentes: i) en utilisant le critère de sélection de systèmes colinéaires, proposé à l'origine par Chin; ii) en introduisant des lois d'écrouissage simplifiées et iii) en permettant l'activation des systèmes de glissement dévié $\{100\}\langle 110\rangle$ et $\{112\}\langle 110\rangle$. Les trois modèles prévoient une augmentation du pourcentage de la composante laiton par rapport aux modèles classiques; Toutefois, cet accroissement est relativement faible dans le cas des deux premiers modèles appliqués à la torsion et au laminage.

L'activation éventuelle des systèmes $\{100\}\langle 110\rangle$ est également envisagée. Le polyèdre mixte associé aux deux familles de systèmes $\{100\}\langle 110\rangle$ et $\{111\}\langle 110\rangle$ est tout d'abord décrit. Il est ensuite démontré que la possibilité de glissement sur ces deux types de plans aboutit à la prévision de composantes de textures qui ne sont pas observées à haute température.

Nous proposons également un nouveau modèle permettant de prendre en compte certains aspects de la restauration dynamique. La formation d'une sous-structure équiaxe résultant de la minimisation de l'énergie des sous-joints est ainsi décrite. Les résultats obtenus en laminage et torsion sont en bon accord avec l'expérience. Finalement, les différents modèles proposés dans cette étude sont comparés entre eux et leur validité et leurs limitations analysées brièvement.

ACKNOWLEDGMENTS

I would like to express my sincere gratitude to Professor J.J. Jonas, director of this research, who communicated to me his enthusiasm for the wide field of physical and mechanical metallurgy, helped me in developing contacts and friendships in this domain and encouraged me with his numerous suggestions. I am also indebted to Dr. F. Montheillet for his constant interest in my work and for his judicious advice.

I am grateful to Dr. U.F. Kocks, who invited me to a Los Alamos workshop in 1984, where I was introduced to the exciting field of textures.

I benefited greatly from fruitful discussions I had with Drs. B.L. Adams, G.R. Canova, J.H. Driver, C. Esling, R. Fortunier, P. Gilormini, K.S. Havner, J. Hirsch, Ph. Lequeu, T.C. Lowe, P.R.Morris, C.N. Tomé and P. van Houtte. I wish to thank them all for having lent me an attentive ear and shown a sincere interest in my research.

Special thanks go to M.J. Bull of the Alcan Laboratories, Kingston and to W.G. Fricke of the Alcoa Research Center, both of whom permitted me to use some of their unpublished results. I also want to express my particular appreciation to T. Ibrahim and P. Vaillant from the Chalk River Nuclear Laboratories and to G. Monge of the CEMEF, Ecole des Mines de Paris, for their help in the experimental part of this work.

The sympathy and useful encouragement I received from my fellow graduate students, as well as from Professor M.G. Akben, Lorraine Mello and Carole Rousseau, will contribute greatly to the excellent memories I will always retain from my years spent at McGill.

Last, but not least, my parents, my brothers, and all my friends in France and Québec never doubted that I would succeed in this project and always supported me during the busy years that it consumed. I am deeply grateful to them for their valuable friendship, without which the achievement of this work would not have been possible.

Il faut n'appeler *Science* que *l'ensemble des recettes qui réussissent toujours*. Tout le reste est littérature.

Paul Valéry.

Tenter, sans force et sans armure,
D'atteindre l'inaccessible étoile
Telle est ma quête.

Jacques Brel.

A mes amis, de partout et de toujours.

TABLE OF CONTENTS

Page

CHAPTER

LIST OF FIGURES

LIST OF TABLES

LIST OF ABBREVIATIONS AND THEIR DEFINITIONS

		see page
AV	Averaging (technique)	130
BH	Bishop and Hill (theory)	73
BHYS	Bishop and Hill yield surface	75
CC	Continuous constraint (model)	92
CODF	Crystallite orientation distribution function	28
CRSS	Critical resolved shear stress	67
CS	Cross slip (model) = Chin model	154
CSL	Coincidence site lattice	58, 206
FC	Full constraint (model)	90
FC-RC	Full constraint-Relaxed constraint (model)	92
GBE	Grain boundary energy	58
HL	Hardening law	164
RC	Relaxed constraint (model)	81
RS	Rate sensitivity	98, 134
RW	Renouard and Wintenberger (criterion)	117
SC	Stress continuity (model)	217
SC+GBE	Stress continuity + grain boundary energy (model)	217
SCYS	Single crystal yield surface	75
SFE	Stacking fault energy	9
YS	Yield surface	75

CHAPTER I

INTRODUCTION

The common metals of industrial practice are polycrystalline aggregates in which each of the individual grains has an orientation that differs from those of its neighbors. However, it is quite unusual for the grains in such metals to have completely random orientations, and the non-random distributions that occur are called *preferred orientations* or *textures*. These purely crystallographic characteristics should not be confused with the alignment of the grain boundaries or structure, or the oriented distribution of second phases, features which can be revealed by optical metallography. Equiaxed grain structures frequently exhibit texture and conversely it is possible, at least in principle, for an elongated grain structure to be randomly oriented [1].

Textures are developed at all stages of the manufacturing processes of metals, but the precise nature of the texture is a complex function of the preceding mechanical and thermal treatments, as well as of the material itself. The important processing factors which can contribute to the development of textures are: solidification, deformation, annealing, and phase transformations. In what follows, we are mainly concerned with deformation textures, but some experimental results concerning annealing textures and their interpretation will also be reviewed to help with the comprehension of mechanisms such as recovery and subgrain coarsening. The effects of solidification and phase transformation on texture development will be completely ignored.

Deformation textures have their origin in the crystallographic nature of the two principal deformation processes of slip and twinning. Where large strains are involved, slip is usually the major factor, but twinning can also be highly significant in texture development because of the massive reorientations that result. These are not necessarily the only possible active mechanisms, especially at high temperatures; the latter range is the main concern of this study, as will be seen below. During crystallographic glide, the restricted

number of slip systems available (the 24 {111}<110> in the case of fcc metals) produces rotations towards a limited number of end-points and so a *deformation texture* is produced. It is clear that the resulting texture will depend on the imposed stress state or strain path, the extent of the deformation, and the operative deformation modes. The latter are themselves defined by the crystal structure and atomic bonding, and also reflect the symmetry of the forming operation.

The annealing of cold or hot worked metals is usually discussed in terms of three generally consecutive, but sometimes overlapping processes: recovery, recrystallization and grain growth. In the first of these, most of the excess point defect are removed and the dislocations rearranged somewhat, but this process only leads to a small change of texture. During recrystallization, new grains are nucleated and grow at the expense of the deformed matrix by the migration of high angle grain boundaries. Locally, there are large changes in orientation and the texture as a whole is modified to become a *primary recrystallization texture*. Frequently but not always, some components of the texture are common to both the deformed and the recrystallized states. After recrystallization is complete, grain growth occurs, involving further grain boundary movement. If this process is normal and continuous, there is a gradual change in texture; if grain growth is abnormal or discontinuous, on the other hand, only a few grains grow and the change in texture can be very large. This latter process is referred to as *secondary recrystallization* and usually results from the presence (and later solution) of a dispersion of second phase particles in the structure [1].

In the past, the processes of deformation and annealing (especially recovery) have generally been treated separately. By constrast, in the present study, the possible effects of an interaction between straining and dynamic recovery, with particular application to the case of hot deformation, are investigated in some detail.

Whatever their origin or type, preferred orientations have profound effects on the mechanical, thermal and electrical properties of materials. In this respect, a textured metal merely reflects the well known *anisotropy* of single crystals. In a strongly textured metal sheet, the yield stress varies with

direction in the plane of the sheet; as a result, non-uniform flow occurs in forming operations such as deep-drawing. Nevertheless preferred orientations are not always undesirable. The use of strongly textured steel sheet in the cores of power transformers is well known, and there are many other examples where textured products have been especially developed for particular applications. For this reason, the control and comprehension of texture evolution has become a subject of increasing importance and a real necessity in certain cases.

In 1966, the understanding of these questions could be summarized by the following quotation:

> "Polycrystalline textures are a matter of extreme complexity. Many details of the mechanism of deformation and the texture development in polycrystalline aggregates are still largely unknown. It is felt that at the present time new ideas and new facts will be most valuable for approaching one of the most complicated things of nature, the deformation textures of metals." [2].

For those working in this subject area today, the above citation is no longer valid. Much progress has been made in the determination of experimental textures, in their interpretation and control, and also in their theoretical prediction. Experimentally, the use of the crystallite orientation distribution function (CODF) has become more and more common; it provides a more complete description of the texture than the traditional pole figure. These improved descriptions have proved very useful in two other ways. They have permitted detailed theories of texture development to be tested in a highly rigorous and critical way. Furthermore, they have contributed greatly to increases in the understanding of the quantitative relationships between texture and the properties of materials.

The present work is concerned with a single aspect of the above problem, namely the prediction of *high temperature* deformation textures in fcc materials. It is divided into the following chapters:

In Chapter II, some of the experimental deformation and annealing textures found in fcc materials are reviewed. Four deformation modes have been selected : tension, compression, rolling, and torsion and the effect of temperature on the deformation textures will be emphasized as much as possible. The various mechanisms involved (twinning, cross-slip, deformation faulting, latent hardening, recovery, recrystallization) will be defined and their possible influences discussed.

In Chapter III, some of the theoretical models employed in the past to predict the evolution of deformation textures will be summarized. The oldest of these are the models developed by Sachs in 1928 [3] and Taylor in 1938 [4]. These two models, as well as some more recent ones, are described here, and the basic mathematical concepts necessary for the comprehension of the theories are defined. The domains of validity of the different models are discussed, as well as their respective advantages and drawbacks.

In Chapter IV, an account is given of the experimental determination of the texture of aluminum rods swaged at different temperatures. As neither the mechanical tests nor the texture measurements were carried out at McGill, this part of the work is not covered in detail.

In Chapter V, the theory of Renouard and Wintenberger [5] related to the minimization of the rate of work hardening is reviewed. This theory is reformulated in a more convenient way and is extended to the deformation of polycrystals. Although it appears to predict low temperature behavior as well, its application to high temperature deformation may be justified by the ease of thermal activation, which can permit dislocations to go back and forth and perhaps choose the "easiest path" in this way.

In Chapter VI, the influence of cross-slip is investigated by first modifying the theory initially developed by Chin [6] for single crystals deformed in tension and also by incorporating a suitable hardening law into the classical models described in Chapter III. Here the present treatments concern other deformation modes and are applied to polycrystals.

In Chapter VII, a further aspect of high temperature deformation is explored, i.e. the activation of slip systems other than the usual {111}<110>. The most probable are the {100}<110>, the {100} planes being the most close-packed after the {111}, followed by the {110}<110> and {112}<110>, the latter two being usually defined as cross-slip systems. The construction of a new single crystal yield surface for slip on the {111} and {100} planes is described in this chapter.

A new model, developed to account for the occurrence of recovery concurrently with deformation is presented in Chapter VIII. This implies the splitting of grains into subgrains, and also involves the minimization of the sub-boundary energy. This energy depends on the misorientation between subgrains [7], and also takes low values at specific orientation relationships (for high angle boundaries).

In each of the above four chapters, the theoretical predictions are compared with selected experimental results. All four of the deformation paths are not always included so as to keep the length of the text within reasonable limits. Finally, in Chapter IX, the general conclusions of the study are drawn and the validity of each model is also discussed.

CHAPTER II

REVIEW OF EXPERIMENTAL TEXTURE OBSERVATIONS

II.1. DEFORMATION TEXTURES

II.1.1. TENSION

The investigation of deformation textures was first carried out for uniaxial geometries (such as wire drawing, extrusion, tension and compression), probably because the representation of the texture is relatively simple in this case. Since the material flow possesses axial symmetry, the orientation of each grain of the polycrystal is adequately described by the crystallographic direction <uvw> that is parallel to the strain axis [8], the other directions being distributed with equal probability around the wire axis. Such a texture is termed a <uvw> fibre texture.

The early results of Hibbard [9,10] described the drawing texture of Cu, Ag, Au, Ni, Pb and Al as a <111> fibre texture and that of certain Cu alloys as a mixture of <111> and <100>. Calnan and co-workers [11,12] at the same time described the pure tensile texture of Al as a mixture of <112> and <111> fibres. These initial studies led the authors to conclude that, for most fcc metals, the end texture is always the <111>, except in some rare cases which were left unexplained. Such results are not in complete agreement with what is known today and this may be due to one or more of the following reasons:

–It is frequently difficult, as mentioned by Dillamore and Roberts [13], to obtain deformations high enough for pronounced preferred orientations to develop in tension because of the lack of mechanical constraints imposed on the specimen.

–The starting orientations were never taken into account. It has been shown more recently by Grewen and Wassermann [14] that the former is of

overriding importance in the development of fibre textures and can lead to misinterpretations. In a more recent study, for example, Bunge [15] determined the texture of drawn Al wires having an initial texture defined by the <111> and <100> fibres. After 84% of deformation, the texture was still a mixture of the two components, but after 99%, the <100> component had disappeared completely. He could only conclude that in pure Al, this last component is not stable, unlike the <111>.

–The influence of the actual deformation mode was generally not considered in these investigations. Although Barrett and Levenson [16] had shown in 1939 that the textures produced in iron by drawing, swaging and elongating tension were similar, there are differences between forming operations because of the inhomogeneities that develop differently along the diameter of a specimen cross-section. Such inhomogeneities result from friction effects, and small values of the ratio of the dimensions of the tool and of the material give rise to a gradient of deformation in the radial direction. In extrusion, the layers at different depths from the surface deform by a strong shearing strain, the shear direction being parallel to the tensile axis. This shear strain, which is superimposed on the tensile strain, changes in magnitude continuously from the surface to the center of the rod, and so do the textures. Normally only the central regions display the texture that is typical for uniaxial tension, since here the superimposed shear must be zero by reason of symmetry [8].

The first systematic study of this problem was that of McHargue et al. [17], which established the temperature and strain rate dependence of the extrusion texture in 99.99% pure aluminum. Two extrusion speeds were used at each of 24, 232, 343 and 454°C, the higher speed being 490 ft/min at 24°C and 738 ft/min at 454°C and the lower speed 0.7 ft/min at 24°C and 0.3 ft/min at 454°C. A duplex <111> + <100> texture was observed at all temperatures for the slow speed and up to 232°C at the fast speed. But at the fast speed at 343°C, a <115> texture was found, and at 454°C the texture was <118>. Some of their results are presented in Figure 2.1 as inverse pole figures. The contour lines show the frequency with which the various directions in the crystal coincide with the tensile axis of the specimen. Evidence was presented by the authors to show that the <100> texture component was largely due to recrystallization

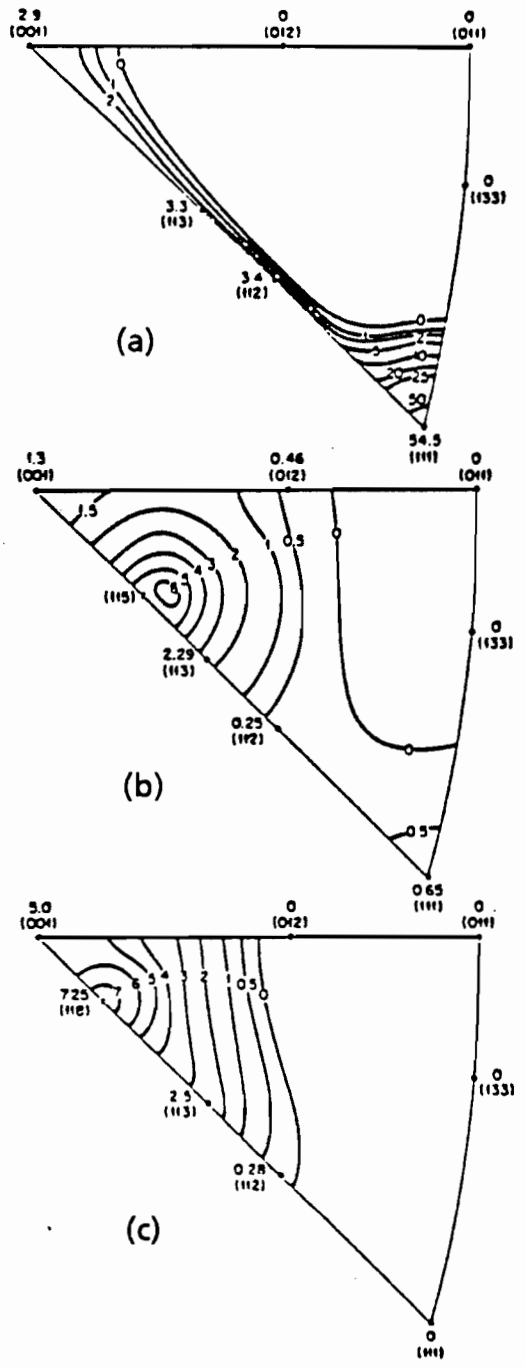

Figure 2.1. Fibre-axis distribution charts for specimens taken from the middle sections of 99.994% aluminum after 91.8% R.A by extrusion at: a) 615 ft/min at 232°C; b) 659 ft/min at 343°C; c) 738 ft/min at 454°C [17].

(though this may not be the only explanation) and an additional sample extruded slowly at sub-zero temperature had a texture consisting of 92% <111> compared with 76% <111> at room temperature. It was concluded

that the main effect of strain rate was in the attendant temperature rise at high strain rates which led to the <115> or <118> "recrystallization" texture. (This subject will be treated further in Section II.2.)

Butt [18] working with commercial or superpure aluminum obtained results essentially similar to those of McHargue et al. [17] for the variation with temperature, and Roberts and Butt [19] have suggested that the <100> texture component arises from the <115> component by deformation subsequent to recrystallization. This differs from the interpretation of McHargue et al. [17], who invoked the possibility that the elastic stresses during deformation favour the formation of <100> recrystallization nuclei. Both sets of workers demonstrated that the <100> component has a lower dislocation density than the <111>. Support for this view is obtained from the observation of Grewen and Wassermann [20] that the proportion of the <111> component in aluminum extrusions is greater the lower the purity and that chill-cast billets give less <100> than continuously cast billets. They explained this as being due to the effect of the dissolved impurities in retarding recrystallization.

Finally, around 1965, clear evidence was presented that the deformation texture of fcc metals is a mixture of these two fibres (and not necessarily due to the occurrence of recrystallization). This evolved from the systematic study of English and Chin [21] as well as from the bibliographical work of Barrett and Massalski [22] and Chin [6]. English and Chin [21] studied several fcc materials covering a wide range of stacking fault energy (SFE) with particular attention to some very low SFE alloys. They determined the percentage of each of the 2 fibres after a reduction by drawing of 99% and plotted the percentage of the <100> component as a function of the SFE. Their results are presented in Figure 2.2.

The most important conclusion from this figure is that the general trend toward larger proportions of <100> with reduced SFE is reversed for the lowest values of γ/Gb. This reversal is not easy to explain on the basis of any single mechanism, such as the influence of cross-slip proposed by Brown [23]. The figure suggests, instead, the presence of two or more superimposed factors, as will be explained below.

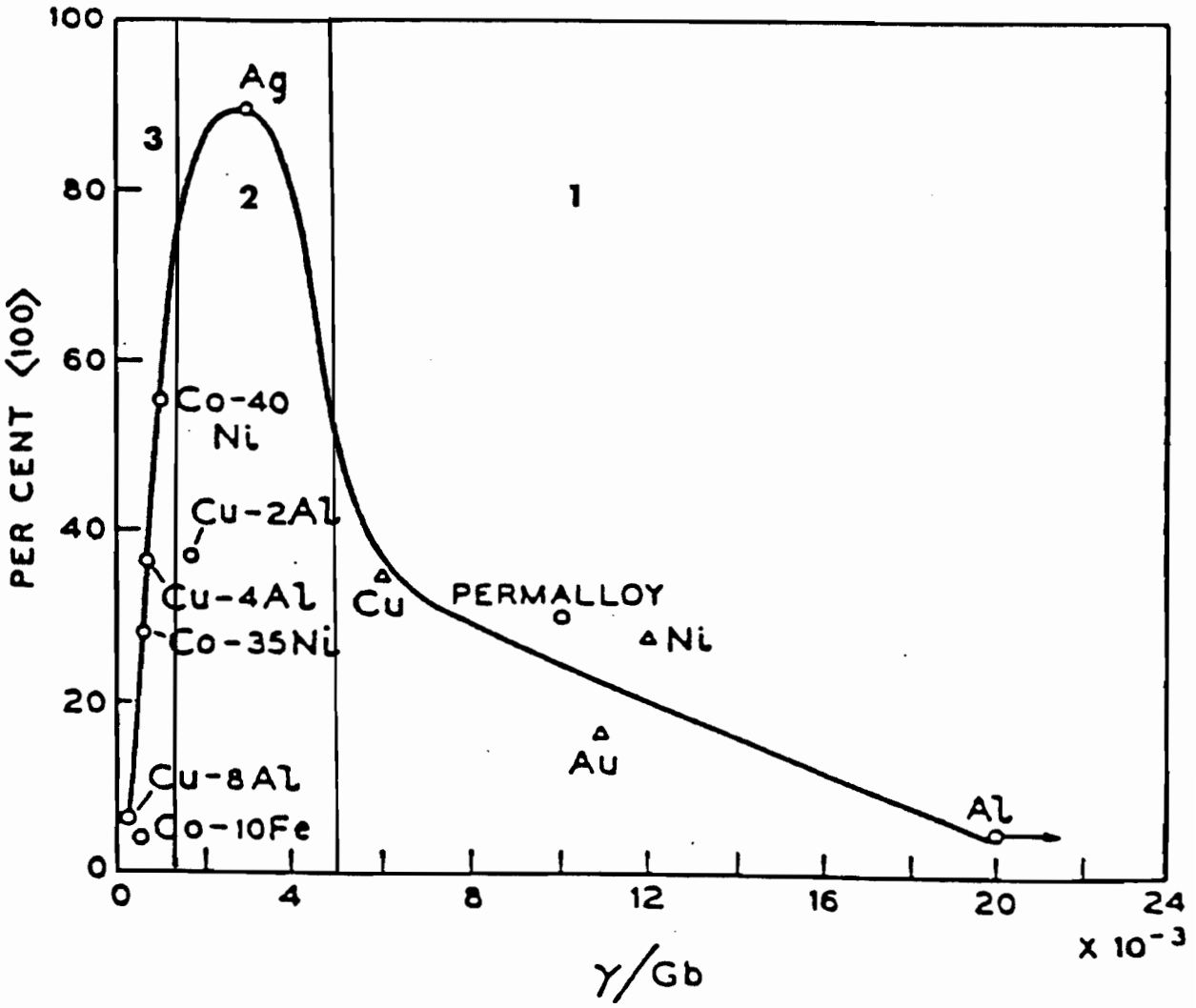

Figure 2.2. Wire textures of various fcc metals and alloys as a function of the parameter γ/Gb at room temperature. Stacking fault energy increases towards the right side of the figure. Both high and low SFE lead to sharp <111> textures [21].

All the more recent results found in the literature as well as those presented in the reviews quoted earlier [6,8,13,21,22] confirm the trend suggested by Figure 2.2. For example, Aernoudt et al. [24] found a strong <100> fibre in drawn silver, Ahlborn [25] determined that the orientation of single crystals of Cu was either <100> or <111>, depending on the initial orientation, in proportions which are in good agreement with Figure 2.2.

Chin [6], Gil Sevillano et al. [26] and Mecking [8] considered all these observations and interpreted them in terms of several mechanisms, such as cross-slip, latent hardening, deformation faulting and twinning. The occurrence of one of these mechanisms was then justified either by experimental observation on a suitable material [8,26] or by comparison with some theoretical model which takes into account the proposed phenomenon [6]. Apparently, the last type of justification is not completely convincing since there is still considerable debate about what really happens in the material. These theoretical assessments will be treated in the next chapter. To summarize the above interpretations, Figure 2.2 has been divided into three parts, each corresponding to a different hypothetical mechanism:

Part 1 corresponds to the high SFE materials such as aluminum or to high temperature deformation behavior; it is usually associated with the ease of cross-slip. There is ample evidence from single slip experiments that cross-slip occurs more easily in high stacking fault energy metals and at high temperature, as described by Nabarro et al. [27] and illustrated in Figure 2.3. One is thus tempted to generalize this to the multiple slip situation in constrained deformation. In the case where all the slip systems harden equally, the <111> component involves the activation of 6 slip systems having 3 different slip directions and 3 different slip planes, i.e. 3 pairs of colinear systems. By contrast, the <100> orientation involves the activation of 4 pairs of colinear systems. One may conclude that, as cross-slip is likely to favor the activity of colinear slip systems, its occurrence will favor in turn the presence of the<111> component and the absence of the <100> one. Such cross-slip has been observed in aluminum [23,28,29] and the interpretation has been supported theoretically by Chin [6].

Part 2 of Figure 2.2, corresponds to intermediate SFE's and is usually associated with the occurrence of mechanical twinning. According to the definition by the mineralogist Dana [30], a lattice is twinned when "one or more parts, regularly arranged, are in reverse position with the other part or parts". This definition means that the twinned and untwinned parts of a crystal are mirror reflections of each other in a certain plane of the crystal. This mirror plane is called the "composition plane" (see Figure 2.4) [31]. The composition or twinning plane is usually given the symbol k_1, the shear direction η_1 and the

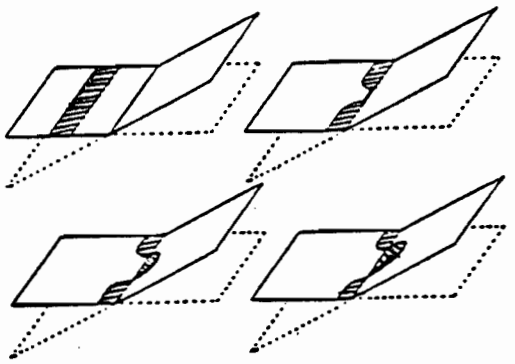

Figure 2.3. Model of the cross-slip process after Nabarro et al. [27]. The dissociated dislocation must combine prior to movement into the cross-slip plane. Hence, cross-slip is easier for high SFE metals.

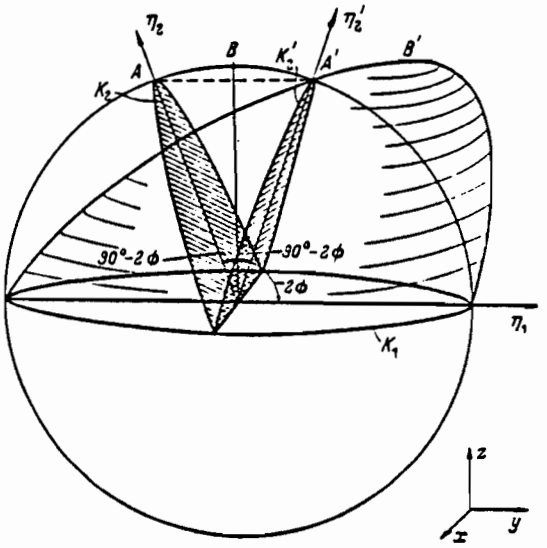

Figure 2.4. Relation of sphere and twinned ellipsoid [31].

plane perpendicular to k_1 and containing η_1 is the "plane of shear". For fcc materials, the twin systems are (111) for k_1 and $[11\bar{2}]$ for η_1, the theoretical shear on such systems being equal to $1/\sqrt{2}$. Twinning is observed when the critical resolved shear stress (CRSS) for this process is almost equal to the one associated with slip. This will happen in fcc materials when the SFE is low or if

the deformation temperature is very low. In such a case, after sufficient deformation, the flow stress will be high enough to produce mechanical twins, and orientations near <111> will twin first because the resolved shear stress for twinning is the highest for these. By twinning, the <111> orientation is transposed into a <115> orientation, which will rotate by slip towards <100>. This can explain why the relative strength of the <100> component increases with decreasing stacking fault energy, when twinning is made easier.

A number of studies, including that of Aernoudt and co-workers [24], have established that fcc metals of low stacking fault energy do twin, especially when deformed at low temperatures and high strain rates. However, it is hard to explain why the <100> component gradually disappears when the stacking fault energy falls below that of silver, conditions under which twinning is still very easy. This leads us to the interpretation of the third part of the diagram.

Part 3 is the most difficult one to explain and several different interpretations have been proposed:

–The <100> fibre orientation loses its preferential role if twinning becomes so easy that all orientations form twins [8].

–Venables [32,33] has indicated that, as the SFE is reduced, twin propagation may become increasingly difficult although nucleation is made easier. One may therefore expect that the amount of twinning (and hence, the percentage of <100>) will reach a maximum for some intermediate SFE, just as observed.

–The increase in the <111> component in this range can also be attributed to latent hardening. Experiments have been performed in which pairs of slip systems have been tested [34-36]. These reveal that prior slip on one system hardens all other systems more than itself, except a coplanar system, where the hardening ratio is equal to one. Under these conditions, there is a tendency for the hardening on non-coplanar systems to increase with decreasing SFE. For Al, the increase is about 20% [35], for Cu [36] and Ag [34], about 40%. These data were obtained by first activating one system, and then the other, and it is not obvious that they are applicable to the simultaneous

activation of both systems. It also remains to be seen why such hardening on non-coplanar systems should imply the increase of the <111> component. This has been investigated theoretically by Chin [6], who selected those combinations among the equivalent slip systems which maximize coplanar slip. "Somewhat surprisingly", in his own words, he found an increase in the <111> component and concluded that latent hardening (coplanar slip) also favors this component, in agreement with the results of Figure 2.2.

–A further interpretation of part 3 of the diagram is again given by Chin [6] and implies the occurrence of deformation faulting. For energetic reasons, a $(111)[01\bar{1}]$ dislocation is normally split into two Shockley partials of the {111}<112> type connected by a strip of stacking fault whose width is inversely proportional to the SFE of the material. Thus widely-spaced faults are common in cold-worked low SFE metals. Usually, the separated partials "zig-zag" in correlated sequential movement - first along $[\bar{1}2\bar{1}]$ and then along $[11\bar{2}]$. The result is then the same as for normal $(111)[01\bar{1}]$ slip and there need be no alteration of the pattern of texture development except through the extra latent hardening on the non-coplanar systems, as described above. However, if the partials become widely separated, texture development may be altered because the effective slip direction now switches from <110> to <112>. This is the mechanism proposed by Hu et al. [2] to account for the dominance of the <111> wire texture in low SFE metals. In their analysis, they considered the independent motion of the two partials equally likely. In effect, however, probably only the leading partial can do so. Chin [6] tested the validity of this model and of this last assumption and found that only the <111> component was stable. Thus he concluded that intrinsic faulting favors a strong <111> wire texture, reinforcing the effect of coplanar slip for very low SFE alloys.

These results can be summarized as follows: the predominance of the <111> component at very high values of SFE is due primarily to the ease of cross-slip (or of colinear slip). The same predominance at very low values of SFE is probably due to twinning in all the grains of the material or coplanar slip and intrinsic faulting. It has to be added at this point that, while Chin [6] proposed the last two interpretations, he also suggested that the decrease in the <100> component in this range was perhaps not as large as shown in Figure 2.2. The appreciable <100> peak near Ag can be accounted for by twinning,

chiefly after the orientations of the crystals have reached the <111> position via a slip process. It is also worth noting that there are two transitions as the SFE is increased. This differs from the situation in rolling, as will be seen later, where copper and brass have distinct rolling textures. The latter remark suggests that the results concerning part 3 of Figure 2.2 are partly wrong or at least inaccurate. This is a question to which we will return below, after presentation of the pertinent results obtained in this investigation.

II.1.2. COMPRESSION

There are few results reported in the literature concerning compression. This may be due in part to the difficulty of achieving large strains in pure axisymmetric compression without shearing or barrelling of the samples; a further contribution arises from the fact that the most important conclusions about compression can be deduced from the tension ones. The forces imposed on a polycrystal being opposite in tension and compression, the rotations of the crystallographic planes can be expected to occur in opposite directions. This was verified experimentally by Barrett and Levenson [37], who reported that the compression texture of Al consists of a strong <110> component with considerable spread to <311>, plus weak intensities scattered to <100> and with <111> relatively empty (Figure 2.5a). This is also the type of texture expected from the Taylor model on the basis of {111}<110> slip (see Chapter III). Moreover, when the concept of colinear (cross) slip (presumably favored in Al) is introduced in this model as was done by Chin [6], it has the effect of sharpening this component.

Very recently, H. Naaman and co-workers [38] determined the compression texture of copper (99.999%) and also found a high intensity near the <110> component and in a band between the <110> and <115> positions. Some of their results are presented in Figures 2.5c to 2.5e. Unfortunately, quantitative experimental data for other materials are not available for comparison. Barrett and Levenson [37] also examined the compression texture of 70-30 brass (Figure 2.5b). Here the texture still consists of a strong <110> component with some spread to <311>, but now the <100> orientation is vacant and some intensity appears near <111>. The emptying of the <100> region in

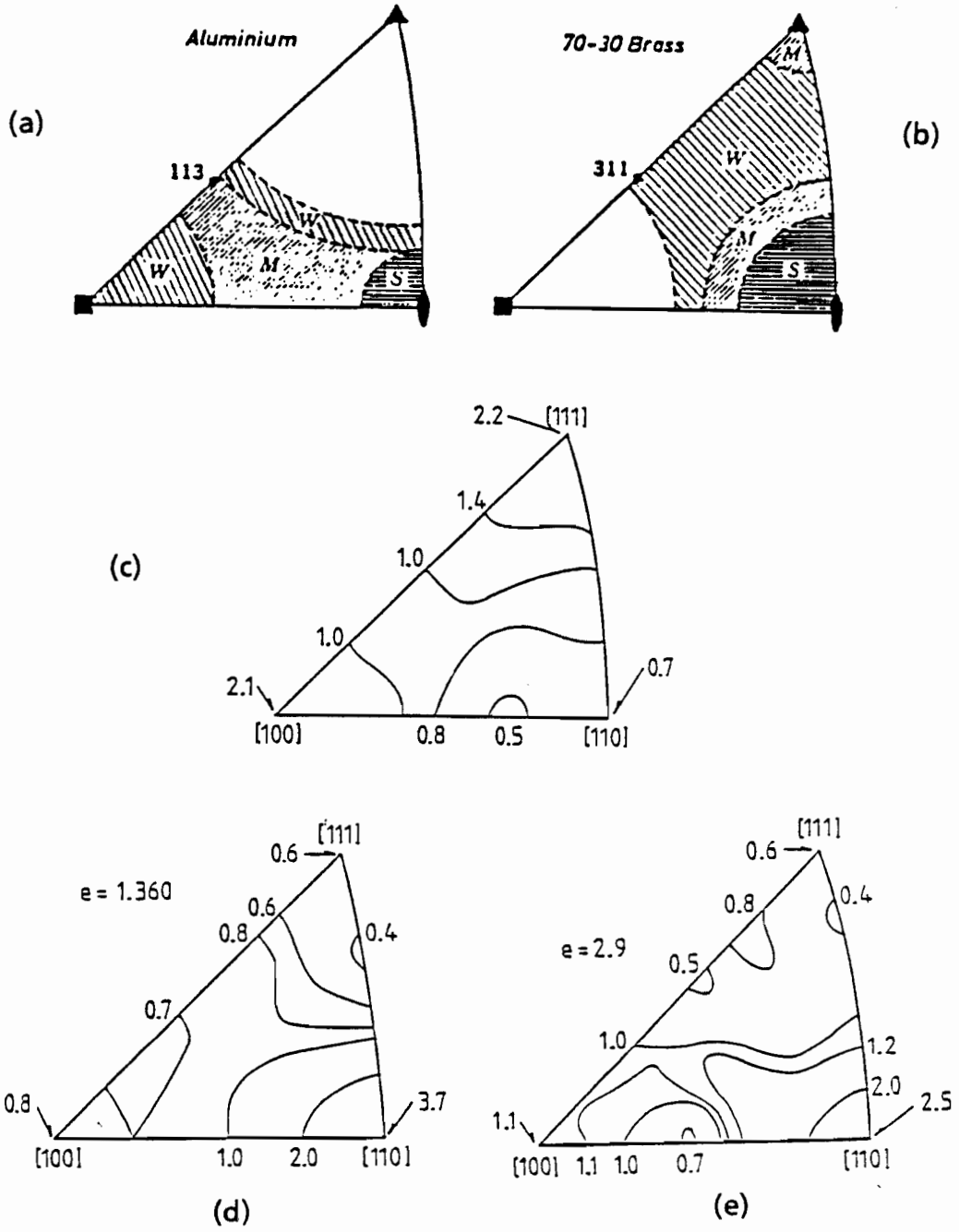

Figure 2.5. Compression textures of Al, brass and Cu: a) Al and b) brass after 97% R.A. [37]. W = weak, M = medium, S = strong. Texture of high purity Cu: c) before compression, d) after a strain of 1.36 and e) after a strain of 2.9 [38].

favor of the <111> is most likely to result from mechanical twinning. In compression, the <100> (and near <100>) vicinity twins most easily while the <111> is most reluctant to twin. At <100>, all four twin planes can operate, converting the compression axis to <221>, which is only 15° from <111> on the <111>–<100> line. (Incidentally, while the <110> is also favored to twin, it transforms into itself (its negative, to be exact)). If slip becomes favored after twinning, the occurrence of coplanar slip suggests that the <111> intensity of brass should decrease at still higher reductions. Similar conclusions can be reached if intrinsic faulting is important [6]. So, despite the lack of experimental results concerning different materials, the mechanisms described for tension are also assumed to be responsible for the variations observed in compression.

Now that we have seen the axisymmetric textures of fcc materials, we can turn to the case of another mode of deformation, i.e. rolling or plane strain compression.

II.1.3. ROLLING

Investigations of texture evolution during rolling are very numerous in the literature and have been performed most extensively on Cu, α-brass (Cu-Zn alloys) and Al. This is because many forming operations are carried out on rolled materials and the forming capability of different metals depends strongly on their texture after rolling. Furthermore the use of crystallite orientation distribution functions (CODF) has been developed mostly for rolled materials where the symmetry of the process makes them relatively simple to derive. For this reason, this section will be divided into two parts:

1) The first summarizes the "earlier work" in the area, in which only pole figures were determined and where the textures were interpreted only in terms of ideal orientations.

2) The second consists of a synthesis of the more recent work, in which the use of CODF's leads to a more quantitative interpretation of the observed textures. In these two sections, some research carried out on rolled single

crystals will also be mentioned [2,8,39] because these studies have helped to clarify the basic deformation processes.

1) Early work

It has been long recognized that the rolling texture of α-brass is not the same as that of copper (or of many other fcc metals). In these two materials, two distinct types of texture develop, and the differences between them were first established by Hu, Sperry and Beck [40]. These are represented in Figure 2.6 in the form of <111> pole figures [41] generally referred to as the "Cu-type texture" and the "brass-type texture". This distinction is somewhat arbitrary and, as will be seen below, the brass-type texture can be produced in Cu and vice versa, depending on the deformation temperature. It has also been found that the two types are characteristic of the rolling textures of most fcc metals [2,8,13,22,40,42,43]; for example, most fcc metals (except silver) are of the copper type, whereas silver and most fcc alloys are of the brass type. Aluminum alloys display a Cu texture and, depending on their composition, have a greater or lesser percentage of the brass component.

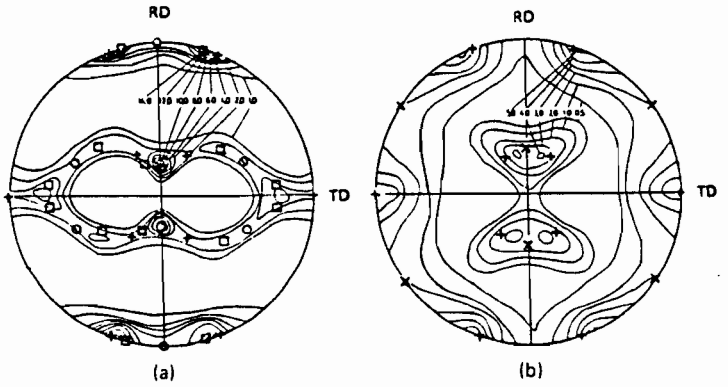

Figure 2.6. <111> pole figures for a) Cu and b) α-brass after rolling at room temperature. The symbols give the positions of the (111) poles of the main components ; o: {112}<111>, □: {123}<634>, +:{110}<112>, ×:{110}<100> [41].

The copper texture can be interpreted as the superposition of 3 components: {112}<111> (Cu-component), {123}<634> (S-component) and {110}<112>

(brass-component); by contrast, the brass texture involves the superposition of only two: the brass-component {110}<112> and the Goss-component {110}<100>. These are displayed in Figure 2.7 in the form of <111>, <110> and <100> pole figures. Additionally, the locations of the <111> poles of the ideal components are plotted on the experimental pole figures of Figure 2.6. In what follows, the term Cu-texture will be used for the complete set of ideal orientations, whereas the term Cu-component will refer only to the single ideal orientation. It should also be noted that only single orientations are represented in Figure 2.7; nevertheless, because of the symmetry of the process, the components which are symmetrical with respect to the rolling direction and to the rolling plane normal must also be included.

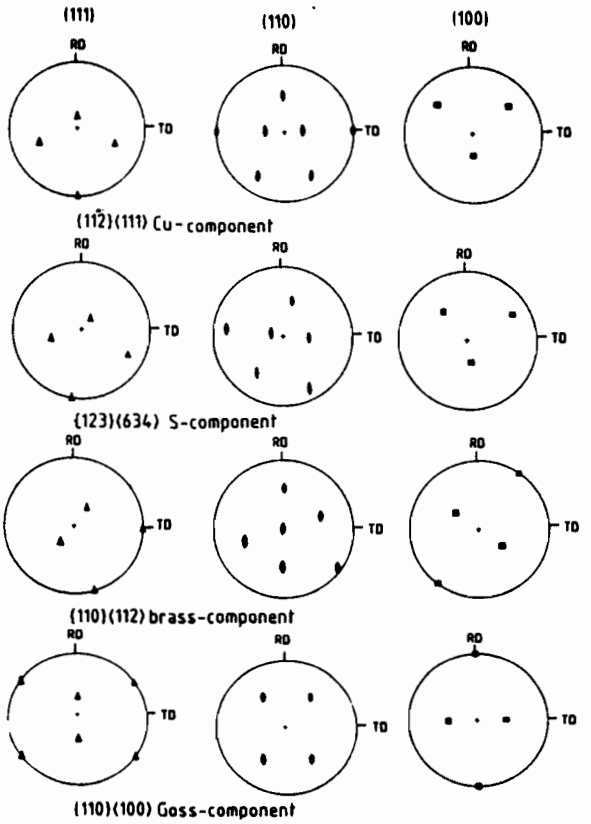

Figure 2.7. Positions of the <111>, <110> and <100> poles of the main components of the rolling texture [8].

The early studies also showed that a transition from the brass to the copper texture can be affected by changing the alloy composition or the deformation

temperature. This transition was associated with changes in the SFE, as in the cases of tension and compression.

Texture transition by alloy additions. The effect of solute addition on the deformation texture of a number of fcc metals was investigated extensively by Smallman [43,44]. Liu and Richman [45,46] also made a systematic study of the textural changes in copper as a function of alloy concentration for several solute elements. These authors showed that, for a given solute, a minimum amount is required to initiate the transition, and the degree of the transition increases with increasing solute concentration. For complete transition, a certain amount of the solute is required, which varies from solute to solute. These results were confirmed by other workers and a typical example is given in Figure 2.8, which shows the textural changes in a series of α-brasses as the concentration of zinc is increased [47].

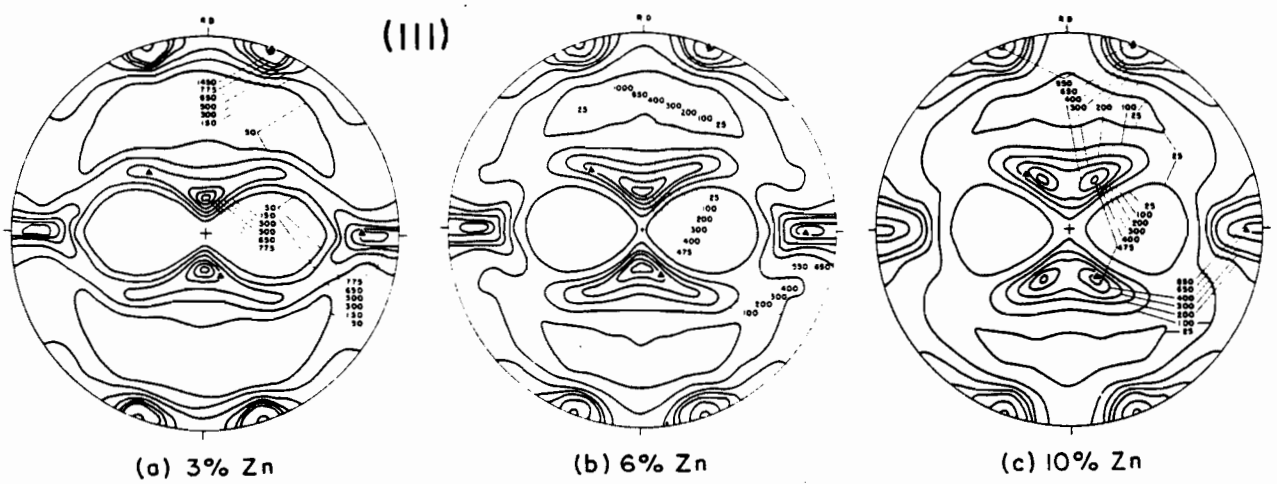

Figure 2.8. Texture transition in brass as a function of zinc content; a)3%, b) 6 %, and c) 10% Zn. Rolling reduction 96% [47].

Texture transition by changing the deformation temperature. The effects of deformation temperature and of heat treatment prior to cold rolling were also investigated by Smallman [44]. The original idea was that, since the deformation characteristics of solid solutions could be affected by temperature and heat treatment, the resulting texture should also vary with temperature. Smallman showed that the rolling textures of aluminum alloys that were

slowly cooled and then rolled were somewhat different from those that were quenched, then rolled. More interesting is the effect of the deformation temperature. For brass containing 5% Zn, rolling at –183°C produced a brass texture (mainly a {110}<112> component), whereas rolling at 200°C produced a copper texture. To test the idea proposed by Brown [23] that the wire texture may depend on the SFE and ease of cross-slip, Hu and co-workers [41,48-50] conducted a series of investigations regarding the temperature dependence of the rolling texture transition in high-purity silver, electrolytic copper, and austenitic 18-8 stainless steel. It was shown that in all these metals, the copper-type / brass-type transition can be affected by changing the temperature of deformation. With increasing temperature, the texture changes gradually from the brass-type to the copper-type; with decreasing temperature, a transition in the opposite direction occurs. Copper rolled at room temperature exhibits a Cu texture, whereas rolling below room temperature leads to the brass-type. Similarly, silver rolled at room temperature exhibits the brass-type, but when rolled at higher temperatures changes to the Cu-type [22].

In these early studies, no experiment was carried out on a high SFE material rolled at high temperatures. As will be seen below, this has been done more recently to test whether there is a second transition from the one type to the other. However, no useful quantitative measure of the amount of the transition associated with a particular temperature could be deduced from these investigations and only the use of CODF's (as described in part 2) below) will be able to provide such an analysis. Figure 2.9 shows the texture of electrolytic copper rolled at −80, −140 and −196°C [41]. The striking resemblance between the textures produced by increasing the alloy content or by lowering the rolling temperature is evident when Figures 2.8 and 2.9 are compared. The temperature dependence of the texture transition was also found to depend on the impurity level [40,41].

The results just described indicated that there is a general correlation between the texture transition and the SFE of the material. This is partly in agreement with the results obtained in tension, where *two* transitions were observed when the SFE was increased, instead of only one as in the case of rolling. Generally speaking, it was concluded at this time that the development of the copper texture in high SFE materials can be attributed to the ease of

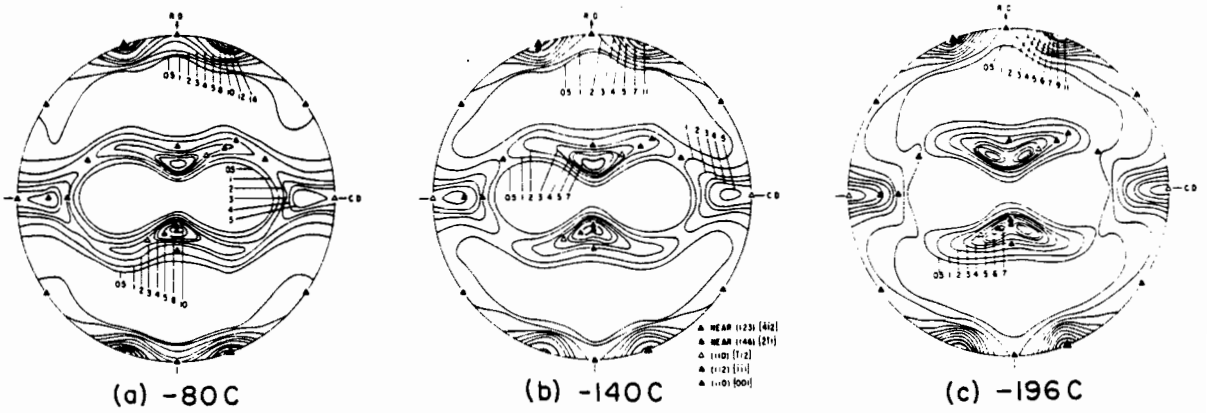

Figure 2.9. Texture transition in copper as a function of deformation temperature; a) −80°C, b) −140°C, c) −196°C. Rolling reduction 96.6% [41].

cross-slip, as in the case of tension; the development of the brass texture in low SFE materials can be attributed as before to the occurrence of twinning or deformation faulting. In addition, some new explanations appeared in which the possibility of nonoctahedral slip was discussed. The different points of view that prevailed can be summarized under the headings that follow.

1) Transition caused by cross-slip. The suggestion that extensive cross-slip is responsible for the formation of the copper rolling texture was made by Dillamore and Roberts [29] as well as by Smallman and Green [28]. The ideas of these authors are similar to those of Brown [23] for wire textures. The rate of cross-slip depends on the SFE of the metal and the temperature of deformation. Dillamore and Roberts [29] claimed that all fcc metals first develop the brass texture by normal slip. Then, for low SFE materials, where cross-slip is very difficult, plastic deformation occurs largely by normal slip and the final texture remains of the brass type. For high SFE metals, cross-slip occurs with ease. The normal slip texture, the brass component, undergoes further reorientation by cross-slip to transform into the copper texture. Since the SFE of materials decreases with increasing alloy addition, and since cross-slip can be activated by thermal fluctuations, the cross-slip hypothesis appears to be consistent with both the composition and temperature dependence of the texture transition. There exist, however, some weak points in this proposition.

One of them is that abundant cross-slip is observed in brass [51], even at low deformations. Similarly, at high deformations in rolling, differences in the ease of cross-slip do not seem to be responsible for the texture differences.

2) Transition caused by nonoctahedral slip. An alternative view was advanced by Haessner [52], who considered that normal octahedral slip leads to the brass texture whereas, when slip occurs on {100} planes along <110> directions, the copper texture is produced. In connection with the effect of SFE on texture, Haessner assumed that, for low SFE metals, cubic slip becomes more difficult as the separation of the partials in the {111} plane becomes greater. Some evidence that slip takes place on the {100} planes in aluminum has been reported [53]; its occurrence seems to depend strongly on the initial orientation of the crystal and on the temperature of deformation. Moreover, it appears to be difficult to differentiate this type of slip from cross-slip. Nevertheless, as the hypothesis was advanced for the case of rolling, and as this type of slip occurs more easily, if at all, at high temperatures, it is of interest to investigate the effect of {100} slip on texture formation. This was done in the present study, and the results obtained will constitute the subject of one of the chapters that follow.

3) Transition due to mechanical twinning. If mechanical twinning of the {111}<112> type is considered as a mechanism of plastic deformation additional to normal slip, then the copper-component $(112)[11\bar{1}]$ can be converted by twinning into the $(552)[\bar{1}\bar{1}5]$, which is rotated into the (110)[001] (Goss-component) orientation by further slip. The $(011)[21\bar{1}]$ texture (brass-component), on the other hand, retains its orientation during deformation, because twinning would lead to shape changes that do not meet the strain requirements of the rolling process. The proposed mechanism is supported by evidence of the rolling textures developed in silver single crystals as well as by the observations of the temperature dependence of twinning in these crystals [54]. However, this interpretation requires the brass texture to be developed after the copper texture is formed. Evidence for this view has not been observed. Furthermore, as mentioned by Haessner [55], there are alloys in which there was no mechanical twinning at the rolling temperature employed, yet the brass texture was still produced.

4) Transition due to deformation faulting. The initial work done in order to assess the effect of deformation faulting on the textures developed in fcc metals was carried out on single crystals having specific orientations. Hu, Cline and Goodman [2] studied the stability of (110)[1$\bar{1}$2] and (112)[11$\bar{1}$] single crystals of high-purity copper and of an alloy containing 4%wt Al. Their results and interpretation can be summarized as follows:

(110)[1$\bar{1}$2] crystals (brass-component). The orientation of the Cu crystals remains stable, whereas the intensity of the brass orientation in the Cu-4%Al crystals decreases up to the point where the crystal splits into two symmetrical brass-oriented crystals. The explanation given was the following: for normal slip on the {111}<110> systems, the primary and conjugate slip systems, (111)[01$\bar{1}$] and (11$\bar{1}$)[101], are symmetrically oriented to receive a large shear stress. If slip occurs accidentally to a larger extent on one of these two systems, such as (11$\bar{1}$)[101], slip direction [101] rotates towards the rolling direction, and the [11$\bar{1}$] slip plane normal rotates in a similar manner towards the normal to the rolling plane. Such rotations result in a continuously decreasing resolved shear stress on the active slip system and a continuously increasing shear stress on the conjugate (111)[01$\bar{1}$]. Hence, at a certain point, the (111)[01$\bar{1}$] system is activated, and the crystal begins to rotate in the opposite direction. Thus, the change in orientation of the crystal during deformation by slip only on these two systems is self-correcting. That is what is considered to happen in the pure copper crystals where the brass texture remains extremely sharp and this has been confirmed by slip-line examination.

However, if deformation faulting or *slip by partials* can make a significant contribution to the deformation in addition to normal slip, the stability of the (110)[1$\bar{1}$2] orientation will be impaired. Faulting will result in slip on the {111}<112> systems and for this special orientation, the (111)[2$\bar{1}$1] and (111)[$\bar{1}$2$\bar{1}$] systems can operate alternately without net orientational changes. The other two systems, (11$\bar{1}$)[112] and (111)[11$\bar{2}$], however, do not possess a self-correcting feature for maintaining the crystal orientation. Hence, for a single crystal of silver, brass, or other fcc alloy of low SFE, the (110)[1$\bar{1}$2] orientation is expected to be unstable, particularly at high deformations at which slip by partials makes a significant contribution to the plastic deformation. Hu and co-workers [2] observed that the texture of Cu-4%Al

crystals shows a rather large orientation spread, probably due to the addition of the complementary orientation.

(112)[11$\bar{1}$] crystals (Cu-component). The behaviors of crystals of copper and Cu-4%Al having this orientation differ markedly, even at low deformations. While the copper crystal retains its initial orientation and shows a very sharp texture, the Cu-4%Al crystal develops a large orientation spread and a strong component of the (552)[$\bar{1}\bar{1}$5] twin orientation. In fact, both the matrix and twin orientations are displaced from their ideal positions by rotation around the transverse direction. In this case as well, the explanation given by the authors is similar to the one given previously. Slip on the ($\bar{1}$11)[110] and (1$\bar{1}$1)[110] systems induces rotation of the crystal towards the rolling direction. While the resolved shear stress on these systems decreases continuously with crystal rotation, the other systems, (111)[$\bar{1}$01] and (111)[0$\bar{1}$1], are subjected to increasingly higher resolved shear stresses. When a certain critical point is reached, the latter two slip systems begin to operate and cause the crystal to rotate in the opposite direction. Thus, these two pairs of systems are able to correct the orientation changes accidentally produced by one or the other and this results in the stability of the orientation if only normal slip occurs, as in pure copper.

For the Cu-4%Al crystal, on the other hand, extensive faulting occurs on the (111)[$\bar{1}\bar{1}$2] system. As a consequence, a (552)[$\bar{1}\bar{1}$5] twin component develops, and with further deformation, the matrix rotates to the (111)[11$\bar{2}$] orientation, whereas the twin rotates towards (110)[001]. So again in this case, the copper crystals remain stable and only normal slip occurs, whereas the orientation of the Cu-4%Al crystals splits into 2 different orientations because of the *deformation faulting*. The assumption of deformation faulting (i.e. slip by partials) has been extensively checked by the authors by means of electron microscopy. In two sets of Cu-4%Al single crystals, they observed the presence of stacking faults and microtwins, but *no* massive twinning. However, similar studies of single crystals of Cu and brass (and not Cu-4%Al) having these specific orientations were also carried out by Mecking [39] and Bauer [56]. These authors have given a different interpretation of their results, attributing the observed differences to *mechanical twinning* (the presence of which was confirmed by electron microscopy). They also found that a Cu single crystal of

the (112)[111] orientation rolled at room temperature was stable whereas, when it was rolled at a lower temperature, it split into 2 symmetrical brass-oriented crystals.

Similarly, in a brass single crystal of (112)[11$\bar{1}$] initial orientation, half the crystal had twinned towards (552)[11$\bar{5}$] after 50% of deformation. As in the Cu crystals rolled below room temperature, the matrix and twin later behaved differently than if they were each present alone. This is because the (112)[11$\bar{1}$] and (552)[11$\bar{5}$] orientations have a special relationship between them; having a common (111) plane, dislocations prefer to slip on this plane to avoid compatibility stresses. As a result, the two orientations rotate towards two symmetrical Cu components. Before these are reached, the scatter around them increases, and the final texture is composed of two brass components.

Mecking [39] also studied the behavior of Cu and brass single crystals of initial orientation ($1\bar{1}0$)[112] (brass component). He found that the Cu crystals were stable but that the brass crystals were stable only if the deformation was really unconstrained (i.e. if the crystal is allowed to shear on the tranverse plane in a sense parallel to the rolling direction, which would be the case for perfectly lubricated rolling). However, if this shear is forbidden or restricted (because of friction produced by the rolls), twinning occurs, and the final texture is again composed of two brass orientations.

From these studies on single crystals, two important remarks can be made:

a) The results depend strongly on the experimental conditions such as lubrication. It is very hard to obtain really unconstrained deformation in rolling, but the degree of friction differs markedly from one experiment to another and it is rare to find this contribution quantified in the literature. The less friction there is, the less stable will the brass orientation be in a brass single crystal for example. These experimental conditions will affect the polycrystal texture in a different way by producing variations in the texture from the center to the outer surface of the material [8]. At the surface, a shear-type of texture will develop, as has been shown very clearly by the experiments of Regenet and Stüwe [57].

b) The orientation instability of the brass and Cu-4%Al single crystals can be attributed to twinning and to microtwinning (due to deformation faulting). It is difficult at this point to decide which of these two mechanisms is the most active, but the choice does not make a great difference with respect to texture prediction. Since the crystallographic effects of the two are the same, i.e. they both imply the activation of the {111}<112> twinning or slip systems, the results obtained will be similar. Furthermore, both types of twins have been observed recently by Hatherly et al. in pure copper as well as in brass deformed by rolling at different temperatures [58].

Following this study of single crystals, extensive research was carried out on texture development in electrolytic copper and 70-30 brass to test the idea that deformation faulting is the primary factor in determining whether the texture is of the copper type (if deformation faulting or twinning is absent or limited) or of the brass type (if faulting or twinning contributes strongly to the deformation) [2]. Extreme care was taken in the preparation of the samples in order to start with a fine grained structure and a nearly random texture. It was found that, at up to 40% reduction, the two materials exhibit almost the same texture (see Figure 2.10); but, after 50% reduction, each of them has already developed its own characteristics. At about 90% reduction, the two types of texture are fully developed and there was no evidence that the copper developed the brass texture first which transformed later into the copper type, or that the brass developed a copper texture first, which transformed later into the brass type. There was ample evidence in this study of the development of a twin orientation of the copper component in the brass, and of further rotation of both the matrix and the twin. The results obtained after 90% reduction are similar to the ones shown in Figure 2.6 and can be taken as confirmation of the presence of deformation faulting *or* twinning in the brass.

To conclude this review of the early studies of rolling textures, it can be said that there is evidence at this point of a transition from the brass to the copper type of texture with increasing SFE (for materials deformed at room temperature or below). This can be interpreted in terms of the following mechanisms: twinning and faulting on the brass side, new active slip systems and ease of cross-slip on the copper side. Again here, no single mechanism can be seen to be responsible for the transition and no experimental observation

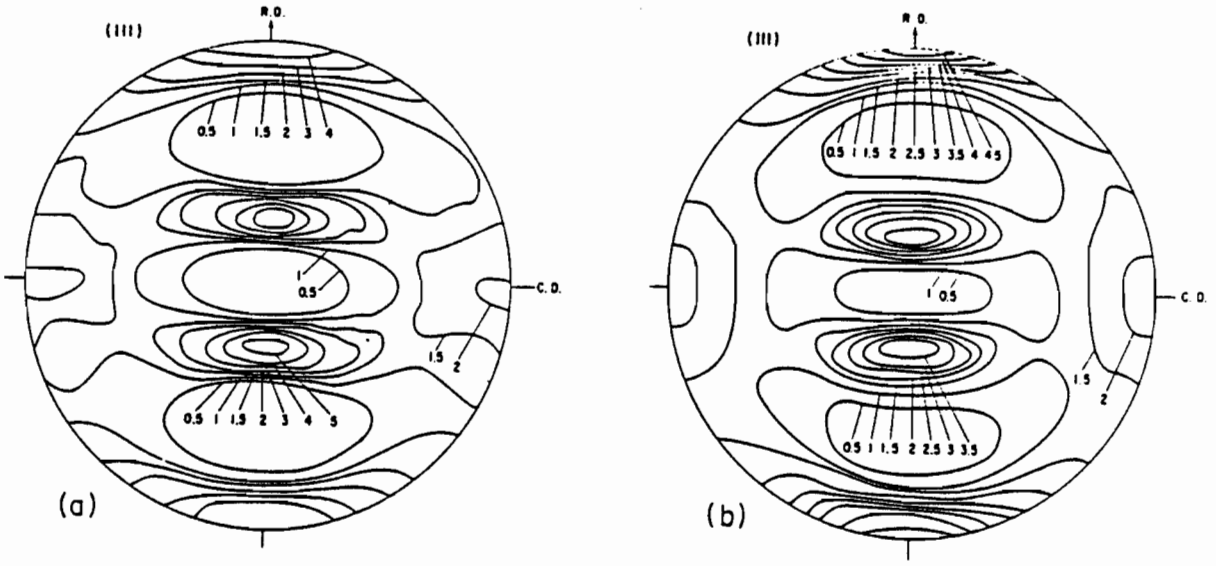

Figure 2.10. Texture of a) copper and b) brass, rolled 40% at 25°C. Note that there is no appreciable difference in texture between copper and brass at relatively low deformations [2].

definitely proves that one or the other happens. Only with the introduction of CODF's does the picture became clearer and it is time now to review the more recent studies of rolling texture development.

2) Recent studies

The recent investigations all make use of the orientation distribution function to represent the texture of a material. If we designate the crystallographic orientation of individual crystallites within a sample by g (which will be specified more precisely later), then the orientation distribution function (ODF) of the crystallites is defined by the volume fraction of crystallites that have the orientation g within a certain infinitesimal orientation element dg. The ODF is thus defined by

$$dV/V = f(g).dg \tag{2.1}$$

The function $f(g)$ is normalized in such a way that in the case of a random distribution, it is equal to 1 for every g. This normalization can be expressed by the relation

$$\int_{\Omega} f(g).dg = 1 \tag{2.2}$$

The orientation of a crystallite g in a sample is usually defined by the orientation of the crystal coordinate system (defined by the 3 <100> axes of the crystal) with respect to the sample coordinate system (in the case of rolled sheet, it is natural to choose the rolling RD, transverse TD, and normal ND directions for the coordinate axes). This is usually represented by three Euler angles in the following way: the crystal system is first assumed to coincide with the sample coordinate system. It is then rotated successively:

1. about the crystal z' axis through ϕ_1
2. about the crystal x' axis through Φ
3. about the crystal z' axis through ϕ_2 (see Figure 2.11)

Thus, the angles ϕ_1, Φ and ϕ_2 are the three Euler angles which describe the orientation of the crystal in the sample

$$g = \{\phi_1, \Phi, \phi_2\} \tag{2.3}$$

This terminology corresponds to the one defined by Bunge [59]. A slightly different one also exists, due to Roe [60], but the latter will not be used here. All possible orientations can be obtained within the range

$$0 \leqq \phi_1 \leqq 2\pi \qquad 0 \leqq \Phi \leqq \pi \qquad 0 \leqq \phi_2 \leqq 2\pi \tag{2.4}$$

It is convenient to plot these parameters as cartesian coordinates in three-dimensional space (Figure 2.12), which is called orientation space or, in the case of the Euler angles as orientation parameters, Euler space. Each crystal is then represented by several points in this space because of the symmetry of the crystal and the symmetry of the process. For fcc materials, a given orientation can be defined by 24 different sets of Euler angles (cubic symmetry) [61]. Furthermore, the orthorhombic symmetry of rolling implies that each point of Euler space is associated with 3 equally probable further ones. A given orientation can thus be described by as many as 96 different points in Euler space (for the case of cubic materials deformed in rolling); this allows us to represent the associated ODF in a reduced space. Usually, the ODF of rolled materials is plotted in a "cube" (i.e. each angle varies from 0 to $\pi/2$, which is still more than the minimum necessary, but gives a clear picture).

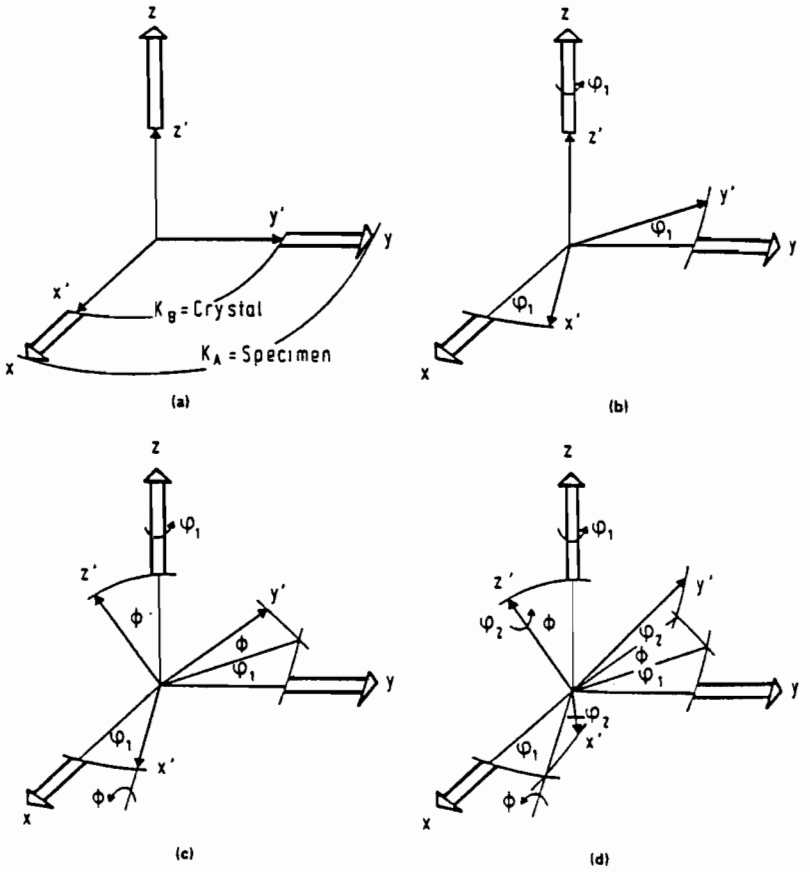

Figure 2.11. Definition of the Euler angles [59].

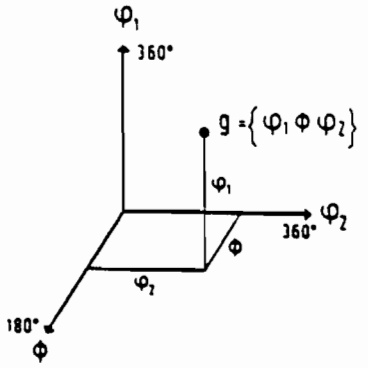

Figure 2.12. Definition of the Euler space [59].

In such a space, the ODF is generally characterized by contour lines, in sections of constant ϕ_2. The ODF's of Cu and brass obtained in this way after 95% reduction, are shown in Figure 2.13 [62]. Similar results have been reported by Kallend and Davies [63] but are not reproduced here to avoid confusion as their results are plotted using the Roe definition of the Euler angles [60]. Bunge and Haessner [64] also determined the ODF of rolled pure copper and found essentially the same results as Hirsch. The appearance of these texture functions in Euler space is illustrated in Figure 2.14. All the texture components of the fcc metals lie on two "fibres" or "tubes", the β fibre extending from the Cu through the S to the brass component (this corresponds to the Cu texture). The α fibre in turn extends from the brass to the Goss position (and corresponds to the brass texture). In these two figures, all the texture components typical of the copper and brass textures can once again be found. The question therefore arises whether the introduction of ODF's brings something new to the analysis of texture development. But the advantages of this type of representation compared to pole figures are numerous:

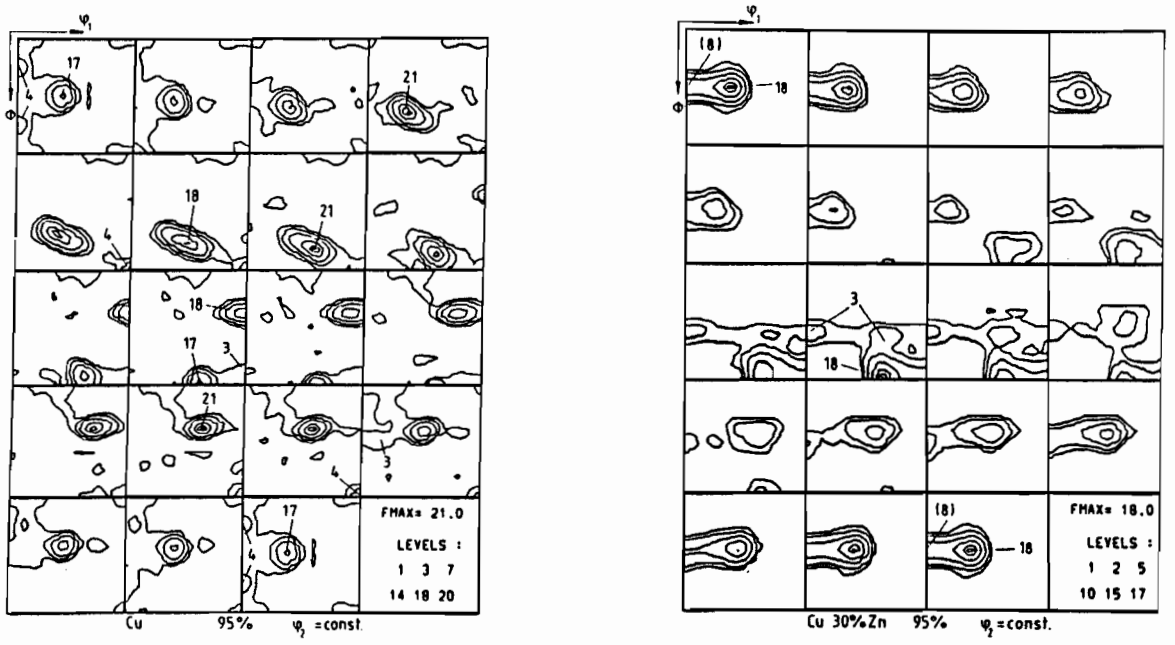

Figure 2.13. ODF of rolling textures of fcc metals after 95% rolling reduction: a) pure copper, b) brass (Cu-30% Zn) (after Hirsch [62]).

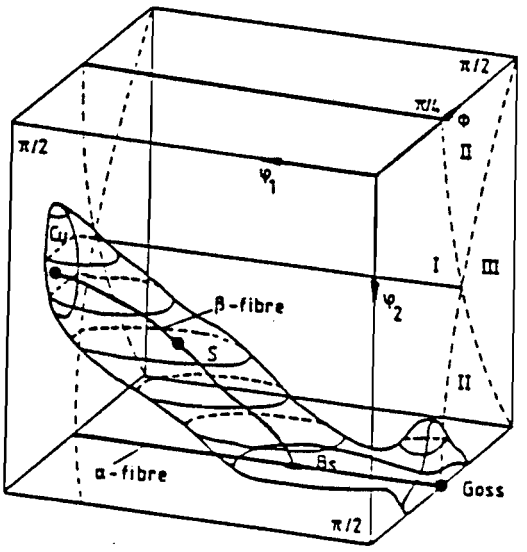

Figure 2.14.
Three-dimensional representation of the main components of an fcc rolling texture in Euler space [62].

1) A pole figure is only a two dimensional plot of preferred orientations which are three dimensional. In this sense, the ODF, which is also 3 dimensional, is more complete and more appropriate.

2) If the value of the function *f(g)* is known exactly at every point in Euler space, we can know all the texture components which are present in the material, even very minor ones, with their exact intensities as well as the scatter around each orientation.

3) From these data it is then possible to : (i) determine the elastic, magnetic and plastic properties of the material; (ii) study quantitatively the influence on texture of the composition, starting texture, temperature, grain size and shape, misorientation between neighboring grains, etc.

4) The ODF permits us to follow precisely the evolution of texture with deformation.

5) It also enables the validity of texture development models to be tested more carefully (see Chapter III).

Hirsch and co-workers [62,65-67], who have worked extensively in this area, have determined the texture of Cu-Zn and Cu-Ge alloys rolled at room temperature. They studied the evolution of texture with deformation, composition and temperature and found a transition from the Cu to the brass texture with decreasing SFE (see Figure 2.13). To follow this transition quantitatively, they made special cuts of the ODF in Euler space, one of which is the $\phi_1 = 90°$ and $\phi_2 = 45°$ subspace, in which the Cu, Goss and twin Cu orientations are found. By plotting the variation of $f(g)$ as a function of the third angle for different alloys and rolling reductions, it is possible to follow the development of twinning for example. This is done in Figure 2.15 for the Cu-Zn alloys [65]. Along this Φ-line, the orientation change due to twinning of the Cu-position and further slip can be readily demonstrated. In the low deformation range for the low Zn alloy, the Cu position intensity increases constantly with strain. In the 70/30 brass, by constrast, after a first increase up to around 50% rolling reduction, the Cu intensity starts to decrease and is replaced by intensities in the twin position. It is clearly visible that with further deformation the twin orientations shift from {552}<115> towards the {332}<113> position, whereas the Goss intensity remains almost constant. In the same deformation range, an increase in intensity along the whole <111> fibre can be detected in the low SFE alloys, with some concentration at {332}<113> and {111}<110>. It is interesting to also plot the variation of $f(g)$ along the two fibres of interest. This is done in Figure 2.16 for the pure copper and the 70/30 brass [62] and again the difference between the two materials is quite clear.

Hirsch and co-workers [68] also investigated the influence of the starting texture. In aluminum rolled at room temperature, they found that they could get a brass texture if the starting texture was mainly composed of the Goss component. Conversely, they obtained a strong S-component if the starting material had a strong cube texture. If the initial Goss or cube texture was rotated around the compression axis by 45°, a strong copper texture was produced. What seems to happen in these materials is that the grains rotate

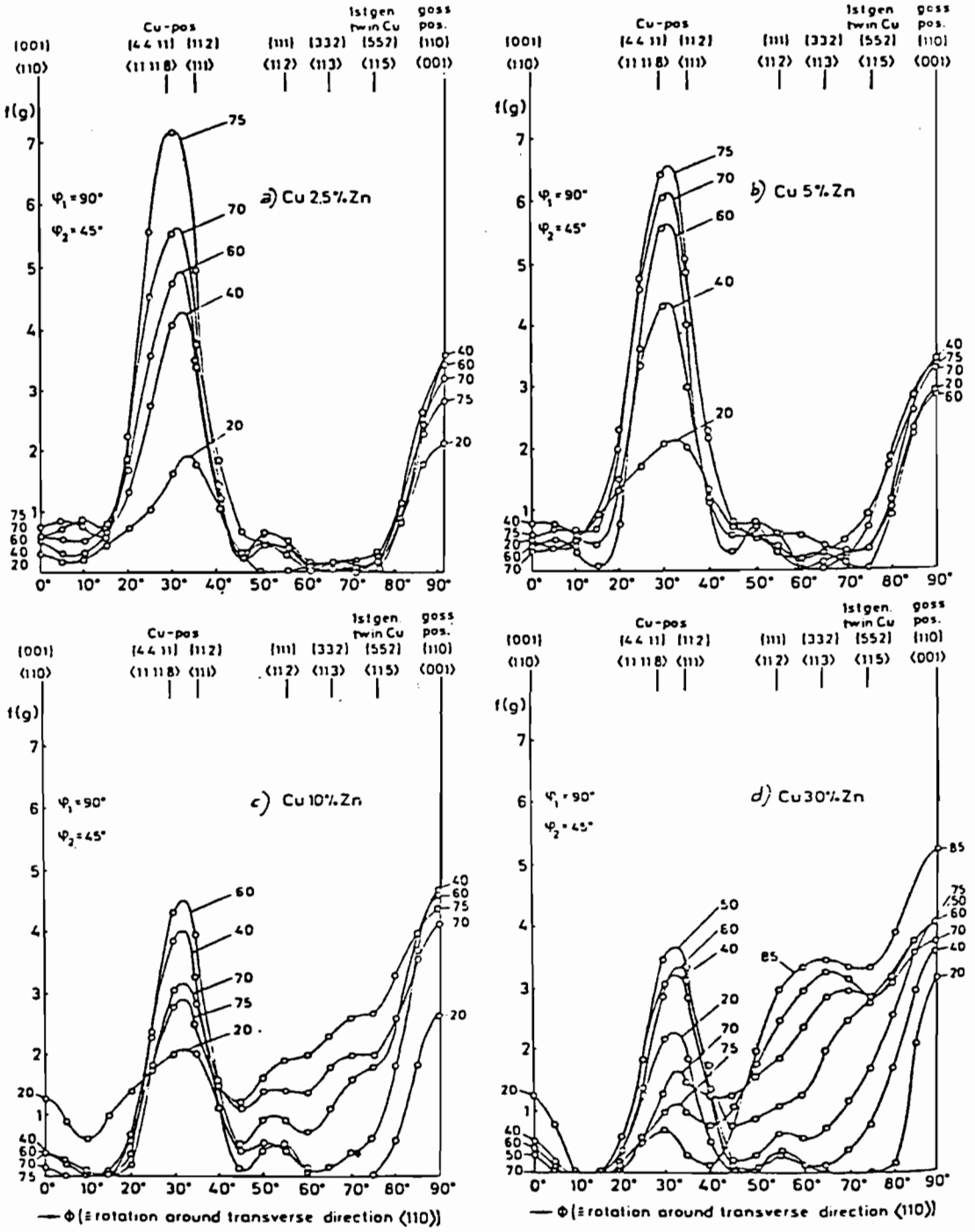

Figure 2.15. Plot of the experimental intensities f(g) versus Φ ($\phi_1 = 90°$ and $\phi_2 = 45°$) of Cu-Zn alloys at different rolling reductions (numbers indicate the degree of rolling) [65].

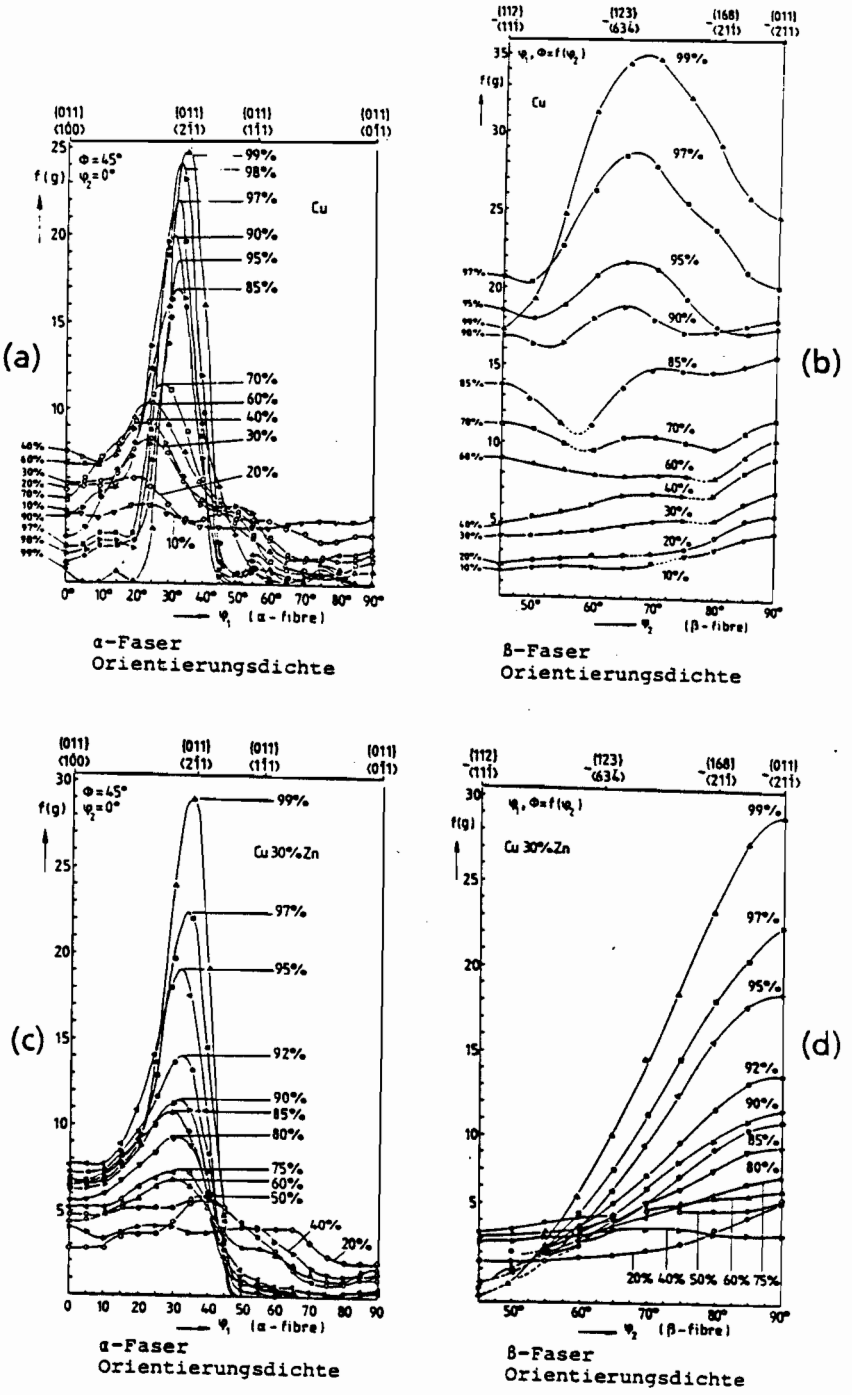

Figure 2.16. Variations in the orientation distribution function along the α and β fibres in a) and b) pure copper, c) and d) 70/30 brass [62].

rather quickly at first towards the two fibres and then eventually rearrange themselves much more slowly within the fibres.

With the aid of these experimental results, it can be seen that there is apparently only one transition as the temperature or SFE is increased, and that is from the brass to the copper type of texture. But the effect of increasing temperature was only investigated below room temperature. Some more recent studies have demonstrated that when aluminum or copper is rolled at an intermediate temperature (before recrystallization takes place), the intensity of the brass-component once again increases at the expense of the copper one. Hatherly and co-workers [58], for example, determined the ODF's of pure copper rolled at increasing temperatures between room temperature and 550°C. The increase in the brass component from 20 to 275°C can be readily visualized by looking at the intensity along the β fibre in Figure 2.17.

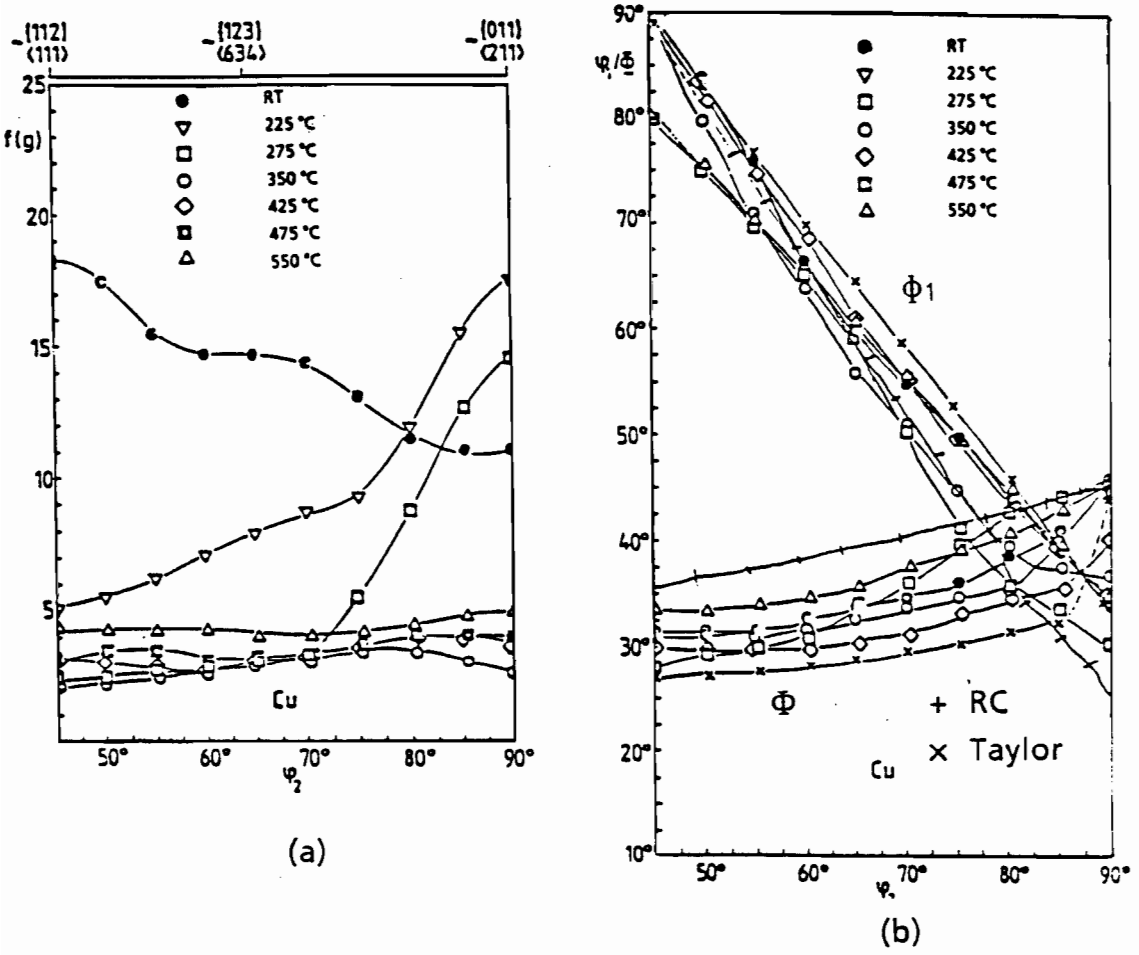

Figure 2.17. a) Intensity variation along the β fibre in pure copper
b) Position of the β fibre in Euler space [58].

These changes were attributed by Hatherly et al. to the occurrence of recrystallization between 225 and 275°C followed by superplastic deformation so that the intensity along the fibre decreases. The increase in the brass component was accompanied by the appearance of other components which are typical of recrystallization textures, such as the cube texture (as will be seen later). However, a similar increase in the brass component was also found in aluminum [69,70], in which only recovery takes place (which has been assumed up to now to cause *no* textural change) and in which no other recrystallization component was found. This leads us to conclude that the increase in the brass component reported by Hatherly et al. [58] below 300°C may be due, not to recrystallization, but to recovery.

In Figure 2.18, some further results concerning aluminum are presented in the form of pole figures, the ODF plots not being available [69]. These results are in good agreement with earlier texture measurements performed on aluminum deformed at different temperatures [71], and lead us to conclude that there really are *two* transitions in rolling as the temperature is increased: the first is from the brass to the copper type, and the second involves a return to the brass type. The second transition is harder to detect because of the small changes involved. It must also be noted that no explanation is given in the literature for the increase in the brass component during warm deformation. It is the purpose of this work to propose one.

II.1.4. TORSION

This is the last deformation path that we are going to consider in this study. Dillamore and Roberts [13] and Cohen [72] have given excellent reviews of the deformation textures of fcc metals deformed in torsion or simple shear. The textures were determined either after torsion (measured at the outer surface of the sample) or simple shear experiments. Some textures were also determined at the surface of rolled specimens subjected to high degrees of friction. The results obtained by Backofen [73], Backofen and Mundy [74], Regenet and Stüwe [57] and Williams [75] are summarized in Table 2.1, which is reproduced from reference [13]. In this table, the ideal orientations are listed in order of increasing intensity and are identified as A, $\bar{A}$, B, $\bar{B}$, A_1^*, A_2^* and C, labels

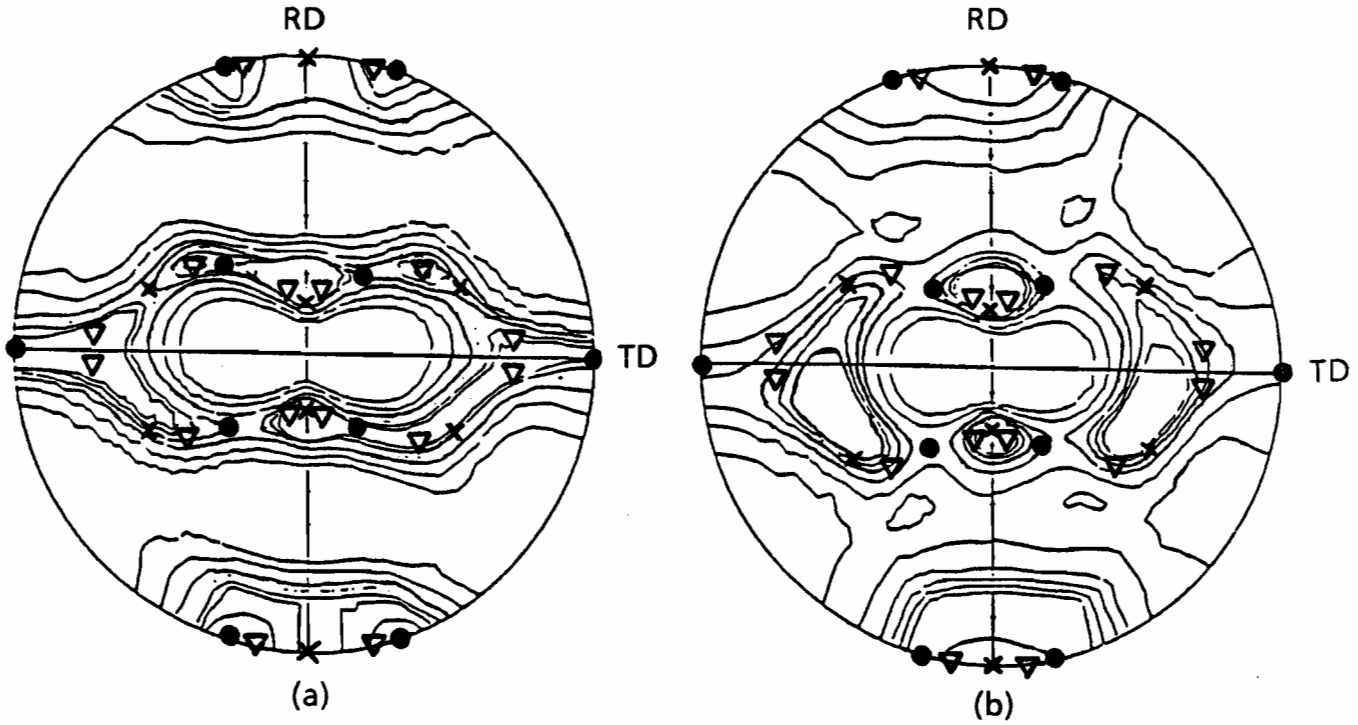

Figure 2.18. {111} pole figures for pure Al rolled to a reduction of 80% at a) T = 150°C and b) T = 20°C. ∇ = S, ● = brass and × = Cu [69].

Metal	Texture Component	Type of Test	Ref.
Aluminum	(100)[011] C (111) fibre (111)[$\bar{1}\bar{1}$2] A_1* (111)[1$\bar{1}$0] A	Torsion or Rolling	57
Copper	(100)[011] C (111) fibre (111)[$\bar{1}\bar{1}$2] A1* (111)[1$\bar{1}$0] A (112)[1$\bar{1}$0] B	Torsion Torsion Torsion or Simple shear Simple shear	73,57,75 57 57,75 57,75 75
Lead	(100)[011] C (111) fibre (111)[$\bar{1}\bar{1}$2] A_1*	Torsion or Rolling	57
Silver	(112)[1$\bar{1}$0] B	Torsion or Rolling	57
70/30 brass	(111)[$\bar{1}\bar{1}$2] A_1* (100)[011] C (111)[1$\bar{1}$0] A (112)[1$\bar{1}$0] B	Simple Shear Torsion,Shear Torsion Tubes id.	75 74,75 74 74

Table 2.1. Shear textures observed in some fcc metals [13].

which will be used in what follows. The indices (hkl)[uvw] correspond to the shear plane normal and the shear direction, respectively. It is also specified whether these data were obtained from torsion, simple shear or rolling experiments.

The locations of the {111} poles pertaining to each of these ideal orientations are shown in Figure 2.19. Due to the geometry of the torsion test [76,77], these orientations are either centro-symmetric or "self-symmetric" (such as A_1^*,A_2^* and C). This means that they obey the symmetry of the torsion test which requires the pole figures of Figure 2.19 to be symmetrical with respect to the center of the figure. The orientations that are not "self-symmetric" are present in the form of "twin-symmetric" sets of two orientations in centro-symmetry, such as A/$\bar{A}$ and B/$\bar{B}$.

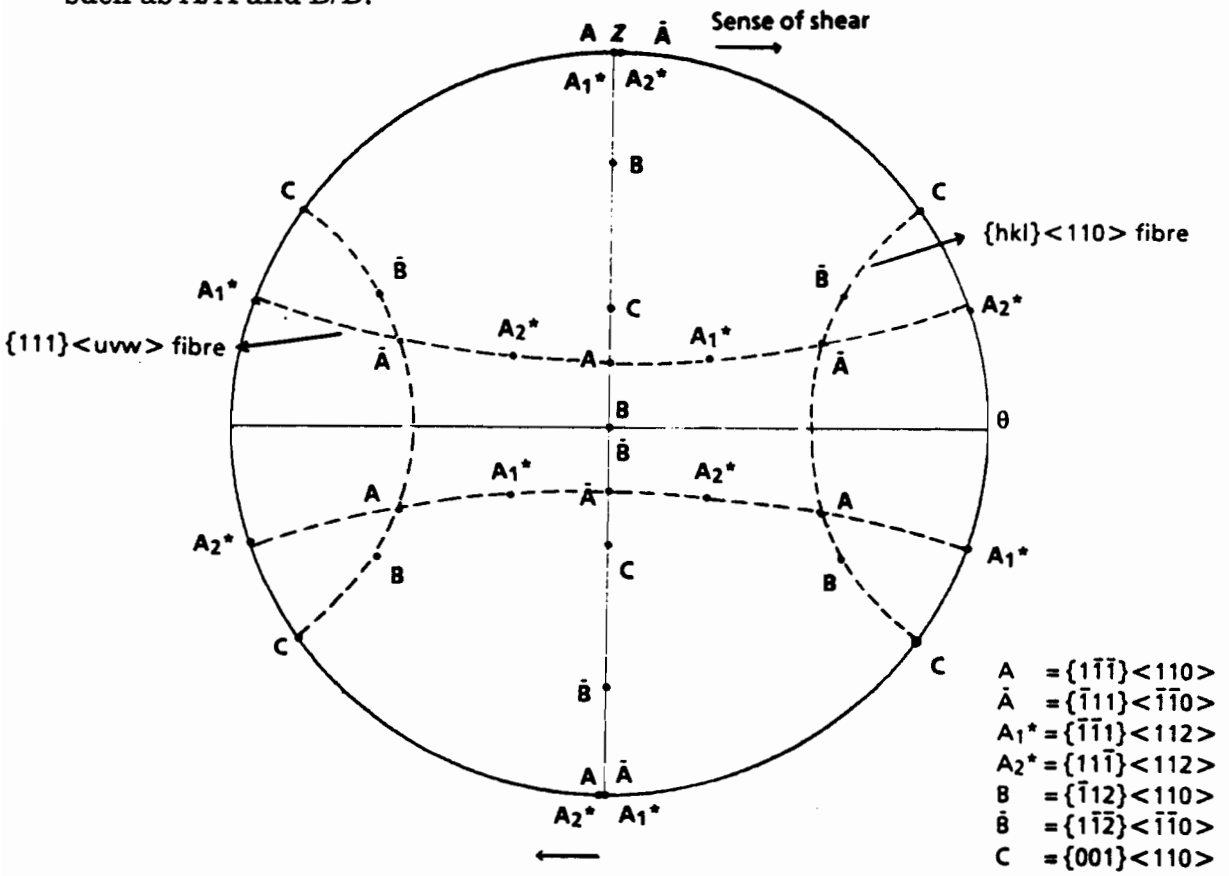

Figure 2.19. Position of the {111} poles associated with each of the ideal orientations found in the torsion of fcc materials.

In the more qualitative early studies, there was no obvious difference between the behaviour of the brass and the copper. Backofen and Mundy [74] even concluded that there was absolutely *no* difference between the two materials: all the textures were composed of the ideal orientations A/$\bar{A}$, B/$\bar{B}$, A_1^* and C, with a partial fibre around a {111} axis parallel to the longitudinal axis of the specimen. (see Figure 2.19.)

More recently, Van Houtte and co-workers [26,78-81] performed torsion experiments at room temperature on pure copper, Cu-Zn alloys containing 3%, 6% and 30% Zn, and on Cu-Al alloys with 1%, 2%, 3% and 4% Al. The textures of the outer layers of the specimens were then determined by the X-ray back reflection method. From these measurements, they were able to show clear evidence for *two* types of texture, depending again on the SFE and on the total strain; one was called the brass and the other the copper texture, in analogy with rolling. These two types are presented as {111} and {200} pole figures in Figure 2.20. The authors then selected one specimen of each type for ODF analysis. The selected copper-type specimen was pure copper, deformed at room temperature up to a shear strain of 5. The brass-type specimen was a Cu-3%Zn alloy which was deformed to fracture ($\gamma > 8$). The pole figures corresponding to these specimens are shown in Figure 2.20. The ODF's for the two samples are presented in Figures 2.21 and 2.22. Note that the domain of variation of the 3 Euler angles is larger in torsion than in rolling due to the reduced symmetry of the process. The ODF's can be interpreted in terms of the 5 ideal orientations specified above whose measured intensities are listed in Table 2.2 (The original notation A-F used by the authors has been replaced by the notation used here in order to remain coherent with the rest of the text).

From Figures 2.21 and 2.22, we can see that each of the ODF's is composed of two partial fibres. One is of the type {hkl}<110>; it begins at $(11\bar{1})[1\bar{1}0]$ (A), goes to $(11\bar{2})[1\bar{1}0]$ (B), passes through $(0\bar{1}0)[\bar{1}01]$ (C), continues to $(2\bar{1}\bar{1})[01\bar{1}]$ (B) and ends at $(\bar{1}\bar{1}1)[\bar{1}10]$ (A). The other partial fibre is of the type {111}<uvw>; it begins at $(11\bar{1})[2\bar{1}1]$ (A_1^*), moves to $(11\bar{1})[1\bar{1}0]$ (A), jumps over to the orientation $(\bar{1}\bar{1}1)[\bar{1}10]$ (A) and from there moves on to $(\bar{1}\bar{1}1)[\bar{1}21]$ (A_2^*). Table 2.2 shows that the most striking difference between the experimental copper and brass type textures is the sharp peak reached by the copper type at the C orientation. The density is much more evenly distributed for the brass type of

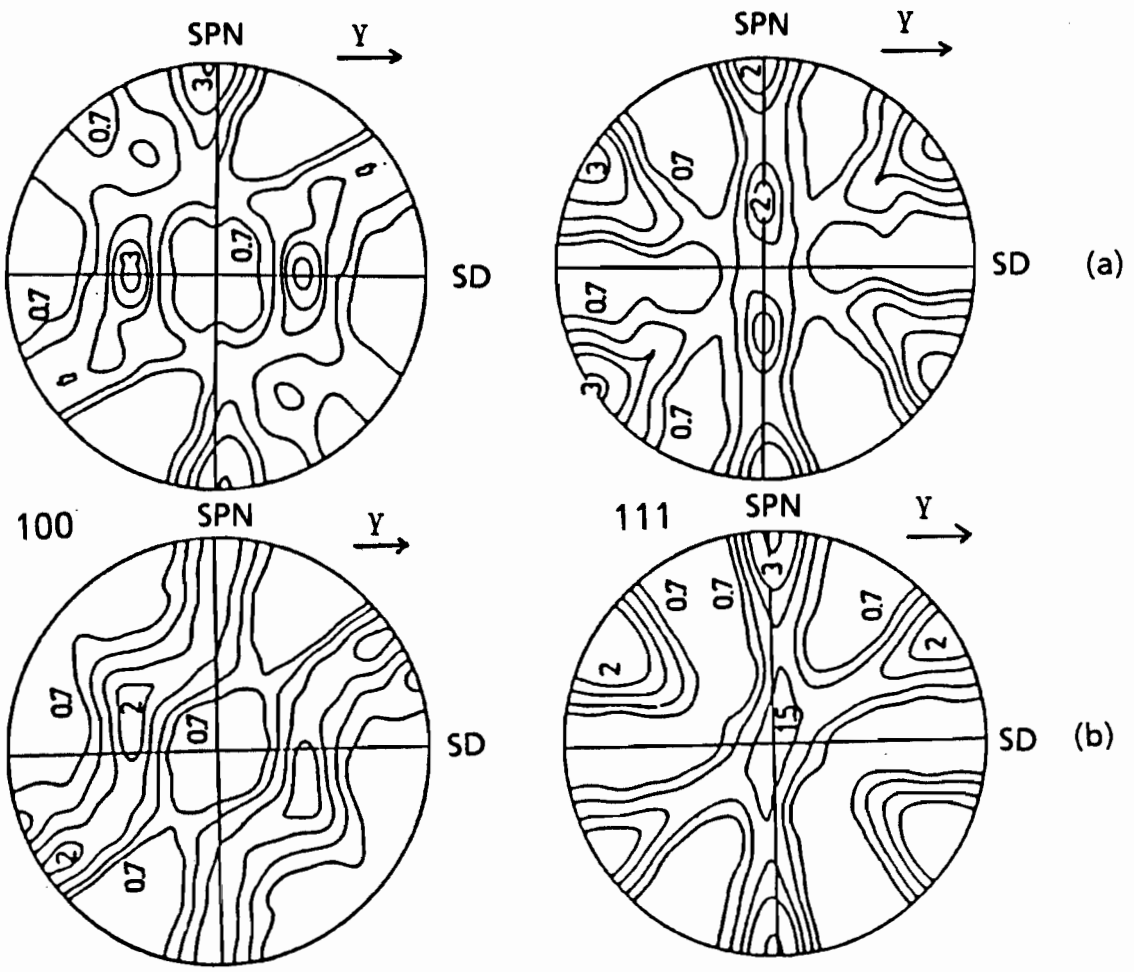

Figure 2.20. Recalculated pole figures of a) the copper-type texture and b) the brass-type texture [78].

texture. The B orientation has often been called the typical orientation of the brass torsion texture [79]. It can be seen from Table 2.2 that its relative importance is indeed greater in the brass texture, but it is nevertheless also present in the copper texture. It has to be noted that this is in agreement with what is found in rolling. Looking again at Figure 2.16, it can be seen that, whereas the copper component of rolling is nearly absent in brass, the brass component is present in both copper and brass rolled at room temperature (though stronger in the brass). Thus, Table 2.2 displays the components of the two extreme textures, the brass and copper types, the intermediate concentrations of Zn giving intermediate textures, just as in rolling.

Cohen and co-workers [72,82] also determined torsion textures; they studied aluminum, copper, and α-iron deformed to different strains at various strain rates and temperatures. The results found at room temperature for aluminum

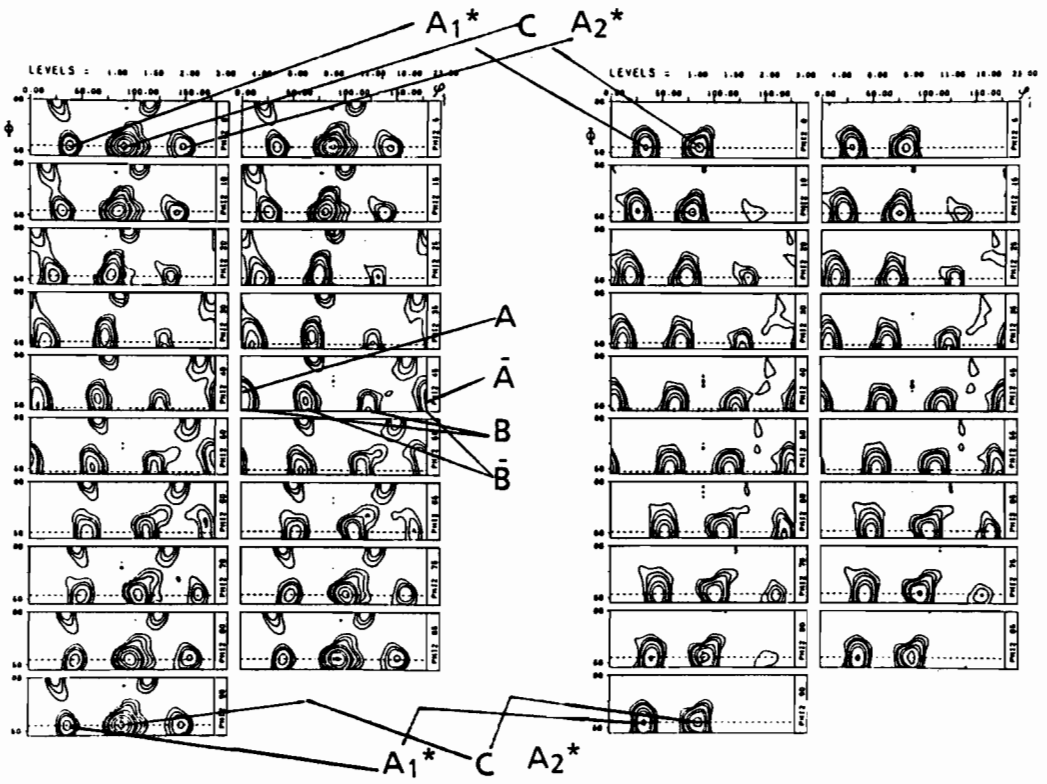

Figure 2.21. ODF of the measured copper-type texture [78].

Figure 2.22. ODF of the measured brass-type texture [78].

Code	Type	Measured Intensity	
		Cu-type	Brass-type
A/Ā	$(11\bar{1})[1\bar{1}0]$	3.4	3.4
B/B̄	$(11\bar{2})[1\bar{1}0]$	3	5.3
C	$(100)[0\bar{1}1]$	14.1	6.7
A_1*	$(11\bar{1})[2\bar{1}1]$	3.4	5.4
A_2*	$(\bar{1}\bar{1}1)[\bar{1}21]$	2.9	-

Table 2.2. Value of the ODF at various points of the skeleton line for the two types of torsion texture [78].

and copper are in full agreement with the previous ones and the evolution of the texture with deformation is presented in Figure 2.23 for the copper and in Figure 2.24 for the aluminum. In the case of the copper, the initial texture was nearly random as a result of the annealing treatment and again, the

orientations A/$\bar{A}$, A_1^*, A_2^*, B/$\bar{B}$ and C are present. The A component decreases in intensity with increasing strain, while the C component increases. The authors also noted that these ideal orientations were slightly rotated about the R-axis of the specimens. They furthermore concluded that these slight departures from completely symmetric positions are connected to the senses of the axial forces present during fixed end torsion tests. This last point will not be developed any further in this paragraph, whose purpose is principally to review the observed textures, but this matter will be exploited further in the chapters dealing with theory that follow. The evolution of these axial forces in fact constitutes a good test of the validity of a new texture theory since it is very sensitive to the texture of the material.

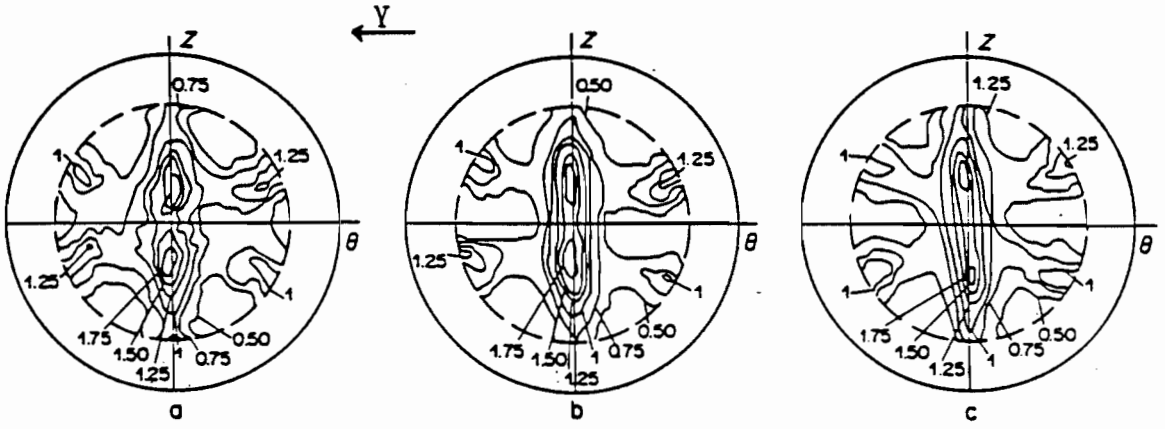

Figure 2.23. Development of the copper torsion texture at 20°C and 5.10^{-3} s^{-1}; {111} pole figures; at a) $\bar{\varepsilon}=0.84$, b) $\bar{\varepsilon}=2.8$, c) $\bar{\varepsilon}=4.7$ [82].

It was observed moreover, that in the copper the A and C components were initially rotated in the sense opposite to that of the imposed shear. At larger strains, whereas the A component tended to disappear, the C component increased in intensity but was rotated in the *same* sense as the shear. With respect to the A^* components, the A_1^* variety was stronger at low strains, whereas the A_2^* variant was more intense at large strains. (The components A_1^* and A_2^* do not both need to be present at the same time since each of them respects the symmetry of the process.) Finally, the B component gradually becomes more intense at large strains and appears to be rotated in the sense opposite to the shear. The case of the aluminum (Figure 2.24) is less clear

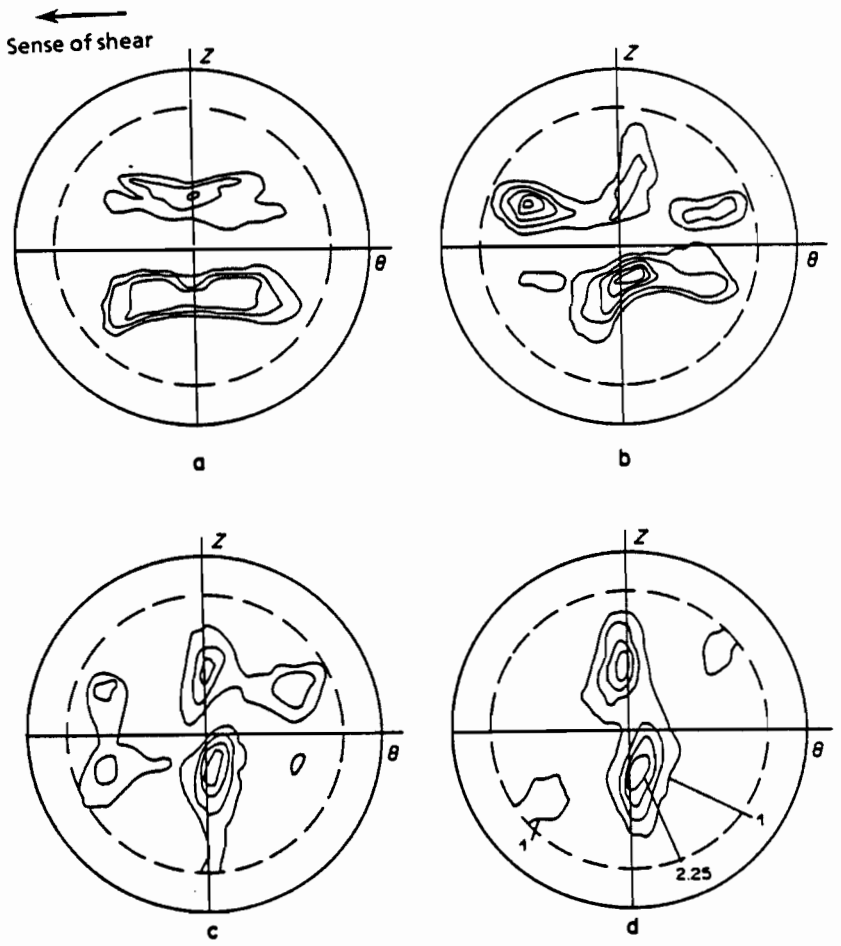

Figure 2.24. Development of the aluminum torsion texture at 20°C and 7.10^{-3} s^{-1}; {111} pole figures; at a) initial state, b) $\bar{\varepsilon}=0.62$, c) $\bar{\varepsilon}=2.18$, d) $\bar{\varepsilon}=4.98$ [82].

because of the presence of an initial texture. Despite this perturbing factor, the Al textures are very similar to those of the copper. The A component present at small strains vanishes at larger strains, whereas the C component becomes stronger. Only the A_2^* component can also be detected.

More interesting to us is the evolution of the "final" textures with temperature (i.e. the textures observed just before fracture of the specimen or within the steady state region when the latter is reached). It constitutes in fact, the only study of this kind found in the literature and, because of the large strains involved, establishes clearly the differences between cold and warm deformation textures in fcc materials. Figure 2.25 shows the evolution of the final texture with temperature for aluminum. The A_2^* and C components

present at low temperatures are gradually replaced by the B/$\bar{B}$ component as the strain and temperature are increased. At 400°C, for a strain of 31, this component is the only one remaining and it is very sharp. Figure 2.26 illustrates the case of copper. As in the aluminum, the A_2^* and C components disappear progressively with increasing temperature, and the B/$\bar{B}$ component becomes sharper, as in the case of Al. Concurrently, the A/$\bar{A}$ orientation develops, which is clearly present at 200°C (see Figure 2.26e). At higher temperatures (between 300 and 500°C), the A/$\bar{A}$ and B/$\bar{B}$ orientations are still present, but they appear to be more and more scattered. This is because the textures are increasingly affected by dynamic recrystallization, which tends to randomize the orientations. It should be noted, however, that the two parts of the B orientation are more resistant to recrystallization than is the A component. Furthermore, this orientation is very strong in Al at high temperatures and cannot be attributed to recrystallization in this case.

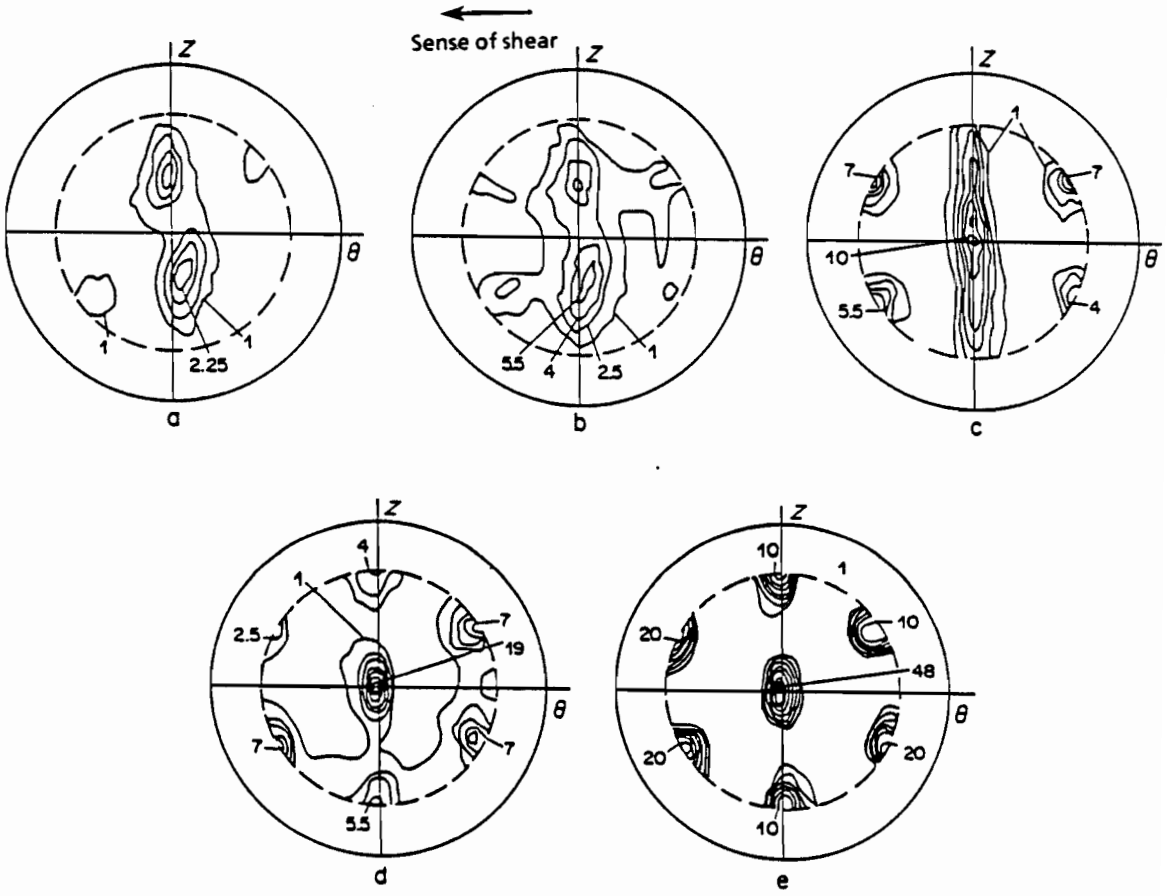

Figure 2.25. Dependence of the "final" aluminum textures on temperature; a) 20°C, $\bar{\varepsilon}=4.97$, b) 200°C, $\bar{\varepsilon}=5.58$, c) 300°C, $\bar{\varepsilon}=10.54$, d) 350°C, $\bar{\varepsilon}=31$, e) 400°C, $\bar{\varepsilon}=31$ [82].

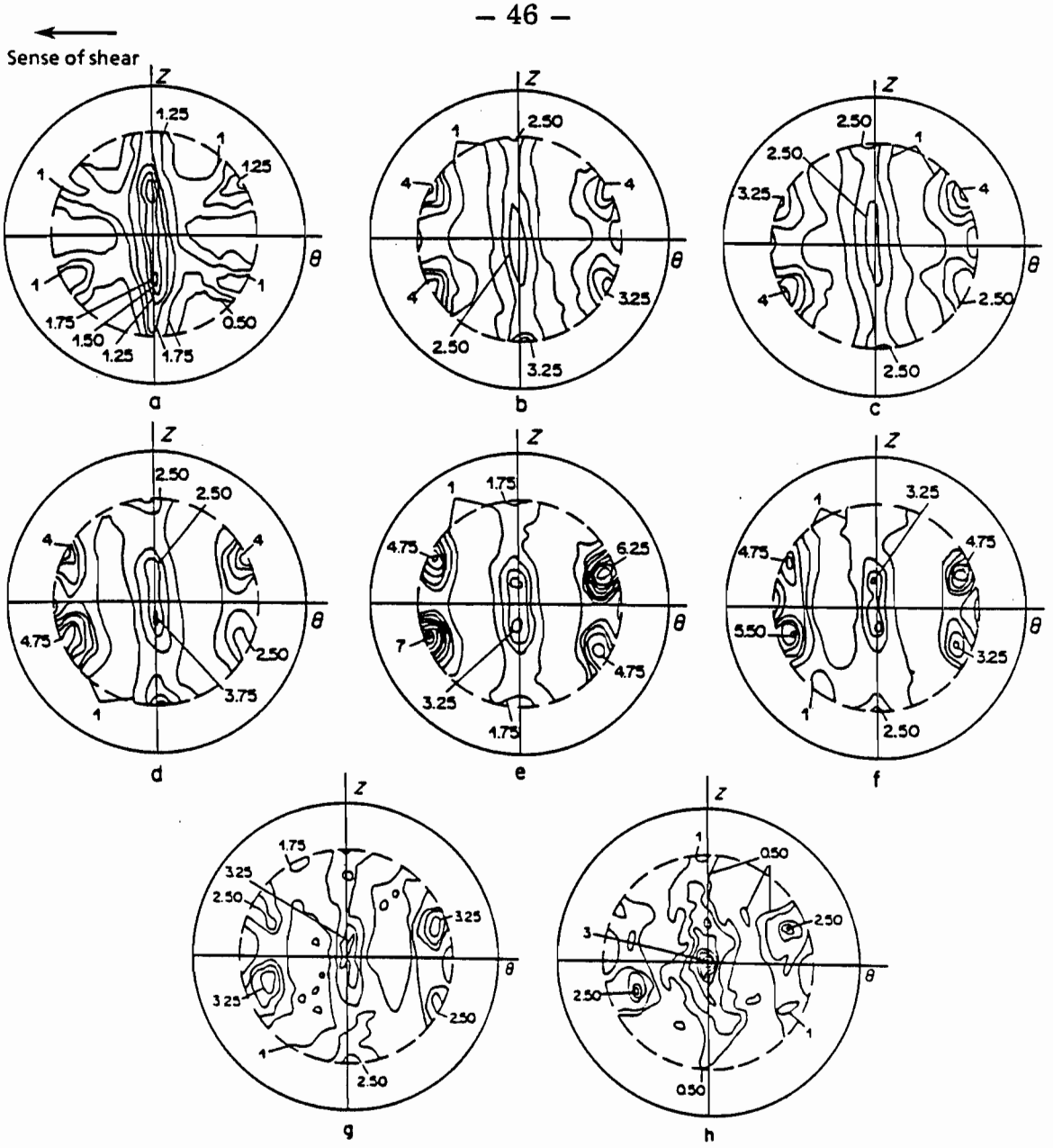

Figure 2.26. Dependence of the "final" copper textures on temperature; a) 20°C, $\bar{\varepsilon}=4.7$, b) 100°C, $\bar{\varepsilon}=4.65$, c) 125°C, $\bar{\varepsilon}=5.89$, d) 150°C, $\bar{\varepsilon}=10.85$, e) 200°C, $\bar{\varepsilon}=31$, f) 300°C, $\bar{\varepsilon}=31$, g) 400°C, $\bar{\varepsilon}=31$, h) 500°C, $\bar{\varepsilon}=31$ [82].

These hot torsion results are in good agreement with the only other reference found in the literature [83] which concerns copper deformed at 200°C. The latter results can be summarized as follows:

i) At small strains and at room temperature, the A orientation is the first to appear in the case of Al (in the presence of an initial texture) and both A and B appear in copper.

ii) At intermediate strains (i.e. prior to fracture), the C self-symmetric orientation is the principal component at room temperature.

iii) As the temperature and the fracture strain increase, the C component is replaced by the B/$\bar{B}$ orientation, sometimes accompanied by the A/$\bar{A}$ component.

It thus appears that there exists a smooth transition when the temperature is increased: A/$\bar{A}$ – C – B+C – B. It must be noted that the pole figure corresponding to the copper deformed at 150°C to a strain of 10 (Figure 2.26d) is similar to the *brass type* texture of Figure 2.20, whereas the pole figure corresponding to copper deformed at 20°C to a strain of 4.7 (Figure 2.26a) is similar to the *copper type* texture of Figure 2.20. Thus the brass-to-copper type of transition observed at room temperature by increasing the SFE is apparently inverted by an increase in temperature (or equivalently of SFE). This is in agreement with the situation found in rolling where the proportion of the brass component increases in aluminum with increasing temperature. Thus, in torsion, as in rolling, there is clear evidence for a "double" transition: brass-to-copper-to-brass with increasing temperature.

II.1.5. CONCLUSIONS REGARDING DEFORMATION TEXTURES

We can thus define a brass type of texture and a copper type of texture for all the deformation modes investigated here. The conditions of SFE and temperature associated with each of these are represented schematically on a diagram analogous to Figure 2.2 in Figure 2.27. The brass texture corresponds to the <100> fibre in tension, the α fibre in rolling and the B (+ some A and C) in torsion. The copper texture, on the other hand, corresponds to the <111> fibre in tension, the β fibre in rolling and the C component in torsion. This describes all the texture components which are expected to develop at high temperatures (in the range where no recrystallization takes place). It does not, however, provide any physical explanation for what really happens in the material.

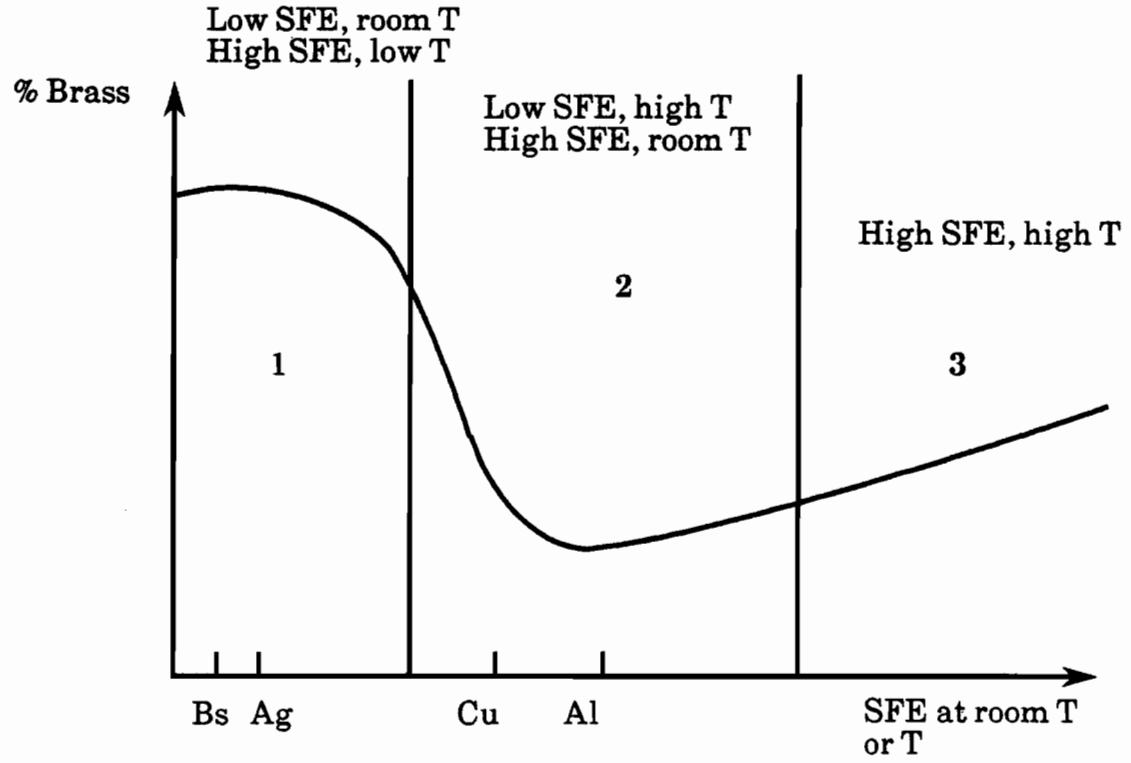

Figure 2.27. Schematic representation of the variation in the deformation texture of fcc materials as a function of SFE and temperature. The brass type is described in the table below.

	Brass-Type	Copper-Type
Tension	<100> fibre	<111> fibre
Rolling	α fibre	β fibre
Torsion	mostly B	mostly C

As in the case of Figure 2.2, we can define three different regions in Figure 2.27. Region 1 is usually explained in terms of twinning , latent hardening and faulting. As the last 3 mechanisms are particularly associated with low temperatures or low SFE, they will not be considered further in the rest of this work. Region 2 is generally interpreted in terms of the relative ease of cross-slip. Region 3, which is the domain of interest in this study, can be interpreted in terms of the ease of cross-slip, the activation of new systems, and recovery.

In the review of the papers dealing with deformation textures, it was seen that none of the authors cited interpreted the warm deformation textures in terms of recovery. Only one such example was found, which was not cited here because it dealt with the cold, warm and hot rolling of bcc metals [84]. The author observed a modification of the cold rolling texture at intermediate temperatures (due to recovery) and a drastic change at high temperatures (due to recrystallization). He explained the development of high temperature deformation textures with the aid of the theories classically ascribed to annealing textures. These are generally interpreted in terms of recrystallization and grain growth. Although recrystallization is beyond the scope of the experimental part of this study, it will be useful at this point to describe briefly the annealing textures observed in fcc metals, as well as the theories developed to explain them. In this way, it will be possible to determine whether some of the mechanisms responsible for texture change during annealing can be responsible for some of the texture changes taking place during deformation. In the section that follows, emphasis will especially be put on recovery.

II.2. ANNEALING TEXTURES

This term is quite general and designates the texture produced in a material on annealing after deformation, whatever the softening processes involved. In general, an annealing texture is the result of a competition between recovery, recrystallization and grain growth (normal or abnormal), and sometimes the final result is influenced by more than one of these processes. On going through the literature, it becomes rapidly obvious that different terms are used for the same mechanism and sometimes the same term designates different processes. So before going further, it will be important to define the terms which are going to be used throughout this discussion. The definitions given below are the ones which have been found to be the most common.

During annealing, *recovery* generally designates the softening process which precedes recrystallization, during which there are local annihilations of dislocations, accompanied by the formation of sub-boundaries (polygonization). There is usually no migration of grain boundaries, but the continuous growth of

subgrains takes place, leading to an increase in misorientation which can even produce high angle sub-boundaries [84]. *Primary recrystallization* is composed of the two processes : *nucleation* and *normal growth* of the nuclei (sometimes also called *continuous* grain growth or recrystallization) by the migration of high angle boundaries. Both nucleation and grain growth can be orientation dependent. *Secondary recrystallization* generally designates the *discontinuous*, *abnormal* or *exaggerated* grain growth which can follow the normal growth. It is only possible in a matrix stabilized against normal grain growth. Certain orientations cause matrix stabilization and thus actually initiate secondary recrystallization (or "discontinuous" grain growth). In this process, both the orientation dependence of the grain boundary mobility and of the surface energy must be taken into account [22]. Finally, *tertiary recrystallization* arises from orientation-dependent differences in the surface energy [80]. Whenever one of the basic processes is orientation dependent, the recrystallized grains of a deformed and annealed single crystal can possess only certain quite definite orientations. This is also true in the case of a deformed and textured polycrystal for which a rise in temperature leading to softening will cause a definite annealing texture to develop from the deformation one.

During deformation, these terms can designate somewhat different mechanisms. *Recovery* can signify either the process defined above or, more exceptionally, *continuous subgrain and grain growth*, i.e. a type of primary recrystallization without nucleation. In the latter case, the migration of high angle boundaries is made possible because of the high level of strain achieved during deformation; this can occur at intermediate and elevated temperatures. Under certain conditions [84], this process is followed by *recrystallization*, which in fact is what we have referred to above as *secondary recrystallization*, since it follows *normal grain growth* [84]. We will use here the term *recovery* to signify the absence of nucleation (whether there is high angle boundary migration or just subgrain growth) and the terms *primary* or *secondary* recrystallization to signify *continuous* or *discontinuous* growth following nucleation.

As these mechanisms and their influence on the texture have been investigated almost solely during annealing and not deformation, whereas it is the latter which is of interest in this investigation, it will be useful at this point to review the theories associated with the formation of annealing textures in

order to determine the extent to which these theories can be transposed to the case of dynamic recovery. In studies of annealing textures, much attention has been directed towards finding the nature, location, and orientation of the nuclei of the recrystallizing grains, and to the factors that govern their growth into the cold worked or recovered surrounding material and also their growth into other recrystallized grains if this occurs. With so many factors and their interactions being involved to different extents in different experiments, it is not surprising that alternative interpretations have been proposed throughout the history of research in this field, and that theories frequently rest on unproven or controversial assumptions, or seem to apply only under strictly limited conditions.

Annealing textures have been most extensively studied after rolling because of the importance of this deformation mode in forming operations and the influence of texture on the directionality of properties in the finished products. In this section, only the annealing textures developed after rolling will be reviewed and the existing theories of the formation of recrystallization textures will be described. The annealing textures developed after axisymmetric deformation such as compression, extrusion or drawing will be ignored because few papers dealing with this subject were found and the results are rather dated and show little agreement.

II.2.1. EXPERIMENTAL OBSERVATIONS

Because of the importance of rolling both industrially and in the development of CODF's, many results concerning the recrystallization texture of aluminum, copper and nickel alloys can be found in the literature. The influence of annealing temperature and time, composition, and the presence of precipitates was studied but the interpretation of the results is rather complex and even contradictory. In particular, it is still impossible to predict with any degree of reliability the annealing texture that will result from a new deformation texture. The reason for this uncertainty lies in the lack of knowledge about important details of the deformed state and about recrystallization processes in general. Minor details of the deformed state – irrelevant for understanding the deformation behavior – can become important factors during recrystallization.

Inhomogeneities of deformation in small volume fractions, practically invisible in the deformation texture, can serve as nucleation sites for recrystallization.

Accordingly, the choice of the experimental results reviewed here was based on the following two considerations:

i) They should serve as examples to illustrate the different theories.
ii) They should cover more or less the whole range of annealing textures found in fcc materials.

The work covered can be grouped in three different categories:

- The 2 extreme cases of the annealing textures formed in brass and copper (which correspond to the extreme cases described above for the rolling textures).
- One example of the transition between the two, in Cu alloys.
- One example of the partial retention of a deformation texture in Al alloys.

In Figure 2.28 [85], some typical textures measured after rolling and subsequent primary recrystallization are displayed for Cu and a Cu-5%Zn alloy: on annealing, the copper-type rolling texture is transformed into a strong cube texture, while the brass-type rolling texture transforms into one having {326}<835> as the main component. Intermediate rolling textures give intermediate recrystallization textures which do not necessarily lie between the two extreme cases. In other words, unlike the transition in the rolling textures, the transition here is not continuous. Similar results were reported by Eichelkraut and co-workers [67] for a series of Cu-Ge alloys. Their results are presented in Figure 2.29 in the form of ODF's and the volume fractions of the principal components as a function of the Ge content in Figure 2.30. The two extreme components, {100}<010> and {236}<385>, are associated with the lowest and highest concentrations of Ge, but the transition between the two appears to occur in several stages with different intermediate components so that a rather complex transition range is observed. The authors divided the concentration range of Ge investigated, 0 to 9%, into 4 subranges, in which the observed texture components are the following:

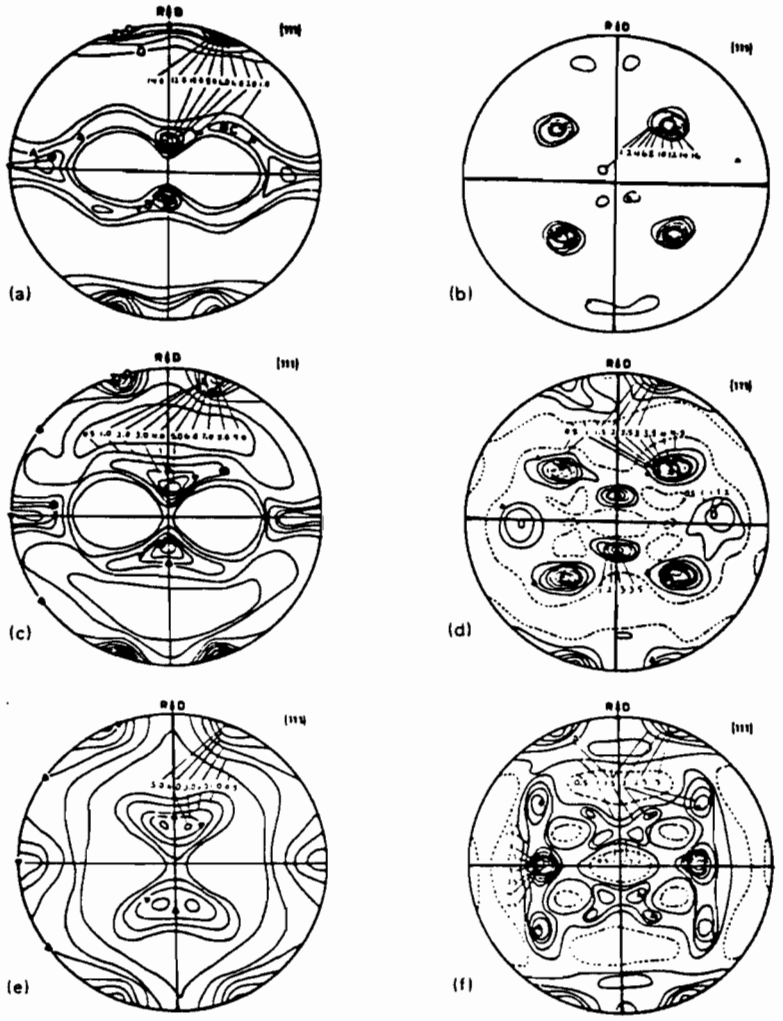

Figure 2.28. {111} pole figures of rolling textures of Cu and Cu-Zn alloys before and after recrystallization. a), c) and e) subsequent to rolling with 95% thickness reduction of a) Cu and c) Cu-5%Zn at room temperature and e) Cu-5%Zn at 77 K. b), d) and f) show the corresponding textures after primary recrystallization [85].

1) Range 1 (pure copper): the recrystallization texture is characterized by the dominance of the cube texture.

2) Range 2 (0.4 to 2% Ge): here there is a sharp reduction in the strength of the cube component and its first and second generation twins appear. They

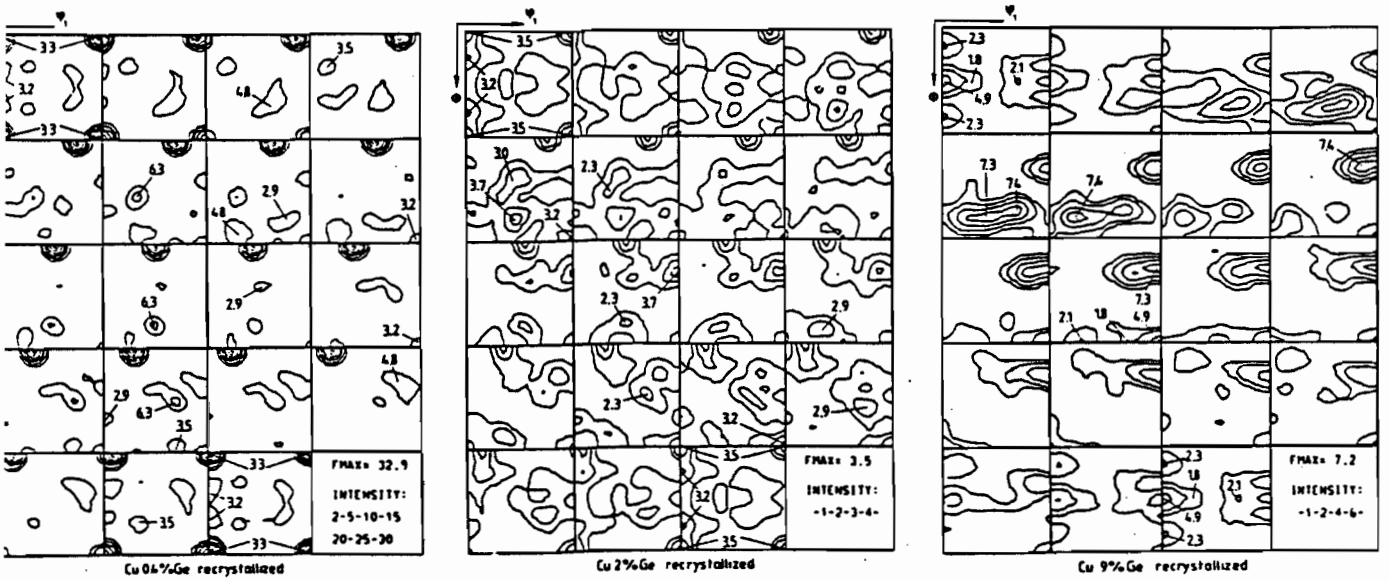

Figure 2.29. Some typical recrystallization textures of Cu-Ge alloys (0.4, 2, 9 wt%). ODF sections ϕ_2 = constant through Euler space [67].

have the orientations {122}<212> and {148}<841>, and {148}<474> and {447}<184>, respectively.

3) Range 3 (2 to 4% Ge): in this range, the rolling texture changes drastically, leading to a marked change in the recrystallization texture. The cube component and its twins disappear, and 3 new components are formed: {114}<221> as the principal component, {258}<121> and {236}<385> (the brass-type recrystallization texture).

4) Range 4 (6 to 9% Ge): all the components except {236}<385> disappear and this one becomes very sharp.

These results for the Cu-Ge alloys are similar to the ones quoted previously for the Cu-Zn alloys. The situation, however, is different in the Al alloys, where two main components were found, i.e. the cube texture and a strong {123}<634> orientation, which has often been called the R (for recrystallization) component [86,87]. The latter is only found in aluminum

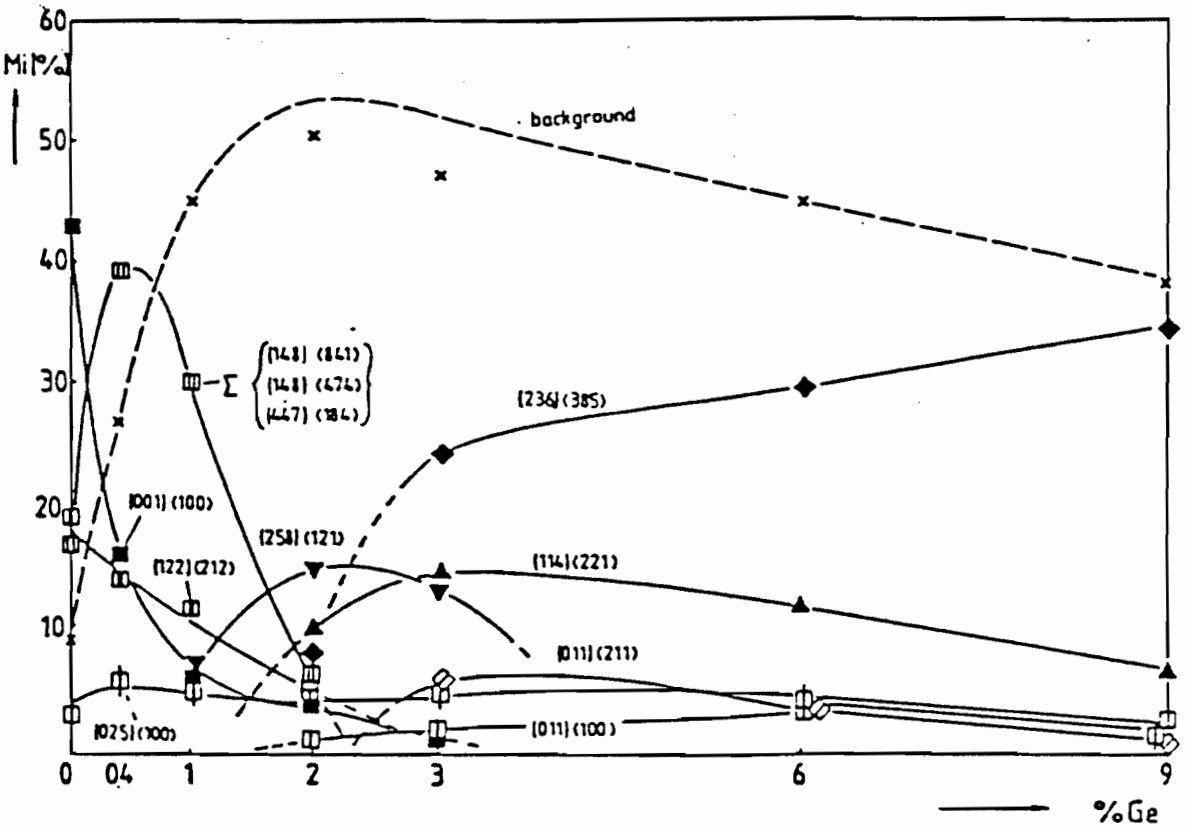

(a)

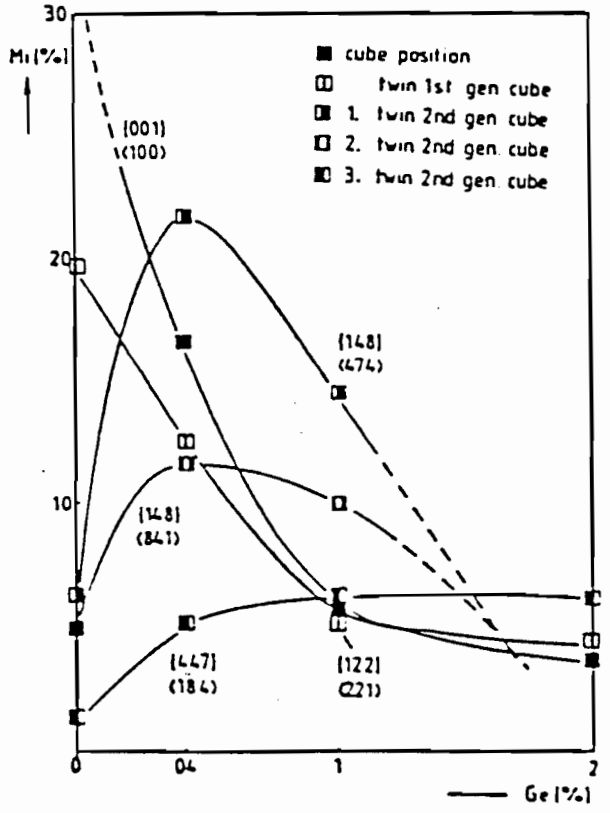

(b)

Figure 2.30.
Dependence on Ge concentration of the volume fraction of:
a) the recrystallization texture components and
b) the cube orientation and its second and third order twins [67].

alloys and is close to the S rolling component which is very strong in Al alloys. This particular annealing texture is thus viewed as corresponding to the partial retention of the rolling texture. Note that here S designates the main rolling component found in Al alloys which is close to {123}<211>. This definition differs from the one given for copper where the S component is {123}<634> (and which is called R here).

These different components have been interpreted in the literature in terms of the two main theories of recrystallization: the oriented nucleation and oriented growth mechanisms, which are now going to be reviewed in turn.

II.2.2. THEORIES OF THE FORMATION OF ANNEALING TEXTURES

The *oriented nucleation* theory, first proposed by Burgers and Louwerse[88], rested on the hypothesis that the orientation of the recrystallized grains is determined entirely by the orientation of the recrystallization nuclei. However, a general principle for predicting which orientations of the many that are present will act as nuclei has not been obvious either from theory or from experiment. The *oriented growth* theory, first proposed by Barrett [89], is based on the principle that certain orientations grow into the deformation-texture containing material more rapidly than others. This means that the shifting of atoms from the strained matrix to a recrystallized grain proceeds only slowly when the new grain has nearly the same orientation as the cold worked matrix, and much faster when its orientation differs in certain particular ways from the orientation of the matrix [22].

The oriented nucleation theory

A great variety of mechanisms have been proposed for the oriented nucleation theory; these include the following [8]:

a) Nucleation in the average structure of the matrix by growth of the subgrains with a statistical size advantage attained during recovery (e.g. by dissolution of certain sub-boundaries). The recrystallization texture and

deformation texture possess common components when this process plays an essential role.

b) Preferred nucleation by subgrain relaxation in regions of strong orientation gradient, e.g. where subgrains are elongated and can pick up large orientation differences rapidly with respect to the environment. In this case, components of the recrystallization texture are expected to lie somewhere between the various components of the deformation texture.

c) Creation of nuclei with new orientations by the inverse Rowland transformation. Rowland [90] proposed a twinning mechanism which leads from a single original fcc lattice to two new fcc lattices having a twin orientation relationship with respect to one another. The homogeneous shear necessary to accomplish this decreases the length of the [100] vector of the original lattice by a factor $1/\sqrt{2}$, so that it becomes the 1/2[110] vector in both lattices. Similarly, the [001] vector of the original lattice, extended by the factor $\sqrt{3/2}$, becomes $[1\bar{1}2]$. Accordingly, the (010) plane of the original lattice becomes $(\bar{1}11)$, which is parallel to the composition plane that the two twin-related lattices have in common. According to Burgers and Verbraak [91], the mechanism whereby cube-oriented nuclei are formed in heavily deformed copper on annealing is the inverse of the above shear mechanism; it leads from two adjacent twin-related lattices having a common (111)-type composition plane to a single fcc crystal lattice of a different orientation. For example, adjacent twin-related lattice regions of two $\{112\}<111>$ type crystals present in highly rolled polycrystalline copper undergo jointly the required inverse Rowland shear on annealing, forming a cube-oriented nucleus. This mechanism is assumed to be thermally-activated and does not require the presence of *any* cube-oriented regions in the cold rolled material prior to annealing. According to this mechanism, the deformation texture is transformed into the recrystallization texture by very particular orientation relations. Although the geometry of this model seems correct, it has not met general acceptance since it is difficult to determine what the driving force is for such a shear.

d) Formation of annealing twins possibly as a result of growth accidents during the growth of normal nuclei. This process can accompany any of the above nucleation mechanisms and should occur predominantly in materials

with low SFE. It can provide practically any orientation and in this way promotes a randomization of the orientation distribution even if the deformation texture is very sharp.

The oriented growth theory

Nucleation is definitely an important factor in recrystallization, but it does not inevitably dominate the evolution of microstructure and texture. In fact, even orientations with very high nucleation rates can remain completely invisible in the final recrystallization texture if their growth rates are too small. Beck and Hu [92], who were strong supporters of the oriented growth theory, even claimed that *none* of the oriented-nucleation mechanisms satisfactorily explains the formation of the particular texture for which it was initially proposed. They argued that the oriented growth theory, on the other hand, was quite general and could explain most of the results obtained in all kinds of materials, except perhaps the single crystals in which there is a scarcity of nuclei in the orientations favorable for growth.

It has long been recognized that grain boundary mobility is strongly orientation dependent. It was found, for example, that in both the primary and secondary recrystallization of aluminum, the fastest growing grains are those having a nearly 40° <111> rotational orientation relationship with the matrix. Boundary migration rates for recrystallized grains in deformed aluminum crystals as a function of the orientation difference across the boundary were measured by Liebmann and co-workers [93] and some of their results are presented in Figure 2.31. 0° and 60° correspond to positions of minimum grain boundary energy (60° being the twin position) and a strong maximum is observed around 40°.

These observations can be interpreted using the concept of the coincidence site lattice first introduced by Kronberg and Wilson [94], which recognizes that at particular rotations a network of a specific fraction of lattice sites (Σ) is continuous across the grain boundary. It will be seen in Chapter VIII in more detail that the energy of such special boundaries is lower than for random boundaries and that the actual value of the GBE depends on the fraction of lattice sites which is continuous through the boundary. The migration rate

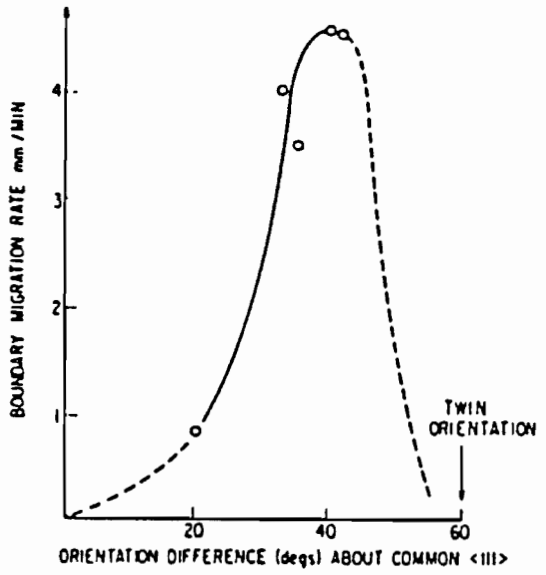

Figure 2.31.
Boundary migration rate versus orientation difference across boundary (rotation around common <111>) in recrystallization of extended aluminum crystals of commercial purity [93].

through the boundaries, however, not only depends on the orientation of the two adjacent crystals but also on the orientation of the GB itself. It is a maximum when:

a) atom movements are possible through the boundary; and

b) the movements required by an atom to diffuse from one crystal to the other are small.

The first condition only concerns perfect coincidence sites. For these positions, if the grain boundary lies in the most densely packed planes of the coincidence lattice, diffusion will be impossible through the boundary and the migration rate will be zero (see Chapter VIII). This is probably the case of the twin boundary represented in Figure 2.31. The second condition is met for boundaries which:

i) correspond exactly to a coincidence relationship, but where the GB does *not* lie in the most densely packed planes of the CSL or

ii) approximate, but deviate somewhat from an ideal coincidence relationship (in general less than 3°) [95,96].

In both these cases, boundary migration is easier because of reduced atom movements, since certain atoms remain nearly in position while the remainder are only required to shuffle by small amounts (on the order of one-third of an interatomic movement). The second type is the most commonly observed; the reported high mobilities correspond to the following relationships: 40° <111> (coincidence site 38.3°, $\Sigma=7$), 20° <111> (coincidence site 27.8°, $\Sigma=13$), 35° <100> (coincidence site 36.9°, $\Sigma=5$), 40° <110> (coincidence site 38.9°, $\Sigma=9$) and 25° <100> (coincidence site 22.6°, $\Sigma=13$).

Many experimental observations seem to be in agreement with this theory [92]. Schnell and Grewe [97] determined the misorientations found in deformed and annealed copper samples. They found a large concentration of twin boundaries in highly deformed copper (i.e. positions of minimum boundary energy) and a large concentration of high mobility boundaries in annealed copper (in particular the 40° <111> and 40° <110> orientation relationships). The above observation suggests that the CSL theory can also be used for the prediction of high temperature textures, but for a different reason than in the case of annealing textures. In the latter instance, the controlling factor is the migration rate, whereas in the former, the GBE seems to be more important. (Because of concurrent deformation, the migration of boundaries has no time to occur.) This will be explored in Chapter VIII of this thesis, in which a new model is developed to account for the effect of dynamic recovery on texture evolution at high temperature. It will be argued that polygonization leads to the development of an equiaxed substructure through the glide and climb of dislocations, and that the subgrains within a particular grain do not deform independently. As a result, whenever there is an ambiguity in the choice of active slip systems in a given subgrain, the ambiguity is suppressed by choosing the sets of slip systems which minimize the GBE.

There is in the literature much evidence for the theory of oriented growth. One of its advantages compared to the nucleation theory is that it is much easier to use. However, it is also easy to find arguments against this or the first theory. Most of these have been published by Beck and Hu [92] and some are listed below:

– The oriented nucleation theory assumes that specific orientations have a higher nucleation rate than others. These orientations can be present in the deformed state or be created by an inverse Rowland transformation, for example. However, few of the available rapidly nucleating orientations are found in recrystallized materials, and it is hard to know a priori which ones.

– Similarly, the oriented growth theory assumes a high migration rate for some specific orientations. However, it predicts the formation of a texture consisting of all the crystallographically equivalent orientations corresponding to maximum boundary mobility. But, in general, the complete set of equivalent orientations is not observed. The oriented growth theory is therefore obliged to rely on ad hoc assumptions regarding the orientations which will occur and for what reasons.

– It has often been observed that similar rolling textures can lead to different recrystallization ones and that different rolling textures can lead to similar recrystallization ones. No simple explanation can be given for this generalization, especially on the basis of only one of the above theories.

For these reasons, the actual explanation probably relies on a combination of the two theories, which means that the nucleation processes govern the range of orientations available, and that there is further selection from among these through the orientation dependence of the growth rate. With the aid of such an *oriented nucleation/selective growth* theory, it is then possible to provide an interpretation of the results reported above.

II.2.3. INTERPRETATION OF THE EXPERIMENTAL RESULTS

Brass and copper annealing textures

The brass type of recrystallization texture, which issues from the brass type of rolling texture, Figure 2.28, is generally interpreted in terms of 40° <111> rotations. The two recrystallization components, {326}<835> and {013}<100>, are fast-growing orientations which can be deduced from two twin components of the {110}<112> part of the rolling texture. However, if

only oriented growth were important, we should find the {211}<011> component as well, which can also be deduced from the {110}<112> orientations by a 40° <111> rotation, but which is never observed. This is evidence for the view that nucleation also plays a role in the development of this texture. It should be noted that the {013}<100> orientation is already present at the deformed stage and that suitable nuclei may be formed by ordinary subgrain growth (mechanism "a" of the nucleation theory). The same mechanism cannot, on the other hand, produce the {326}<835> orientation, which lies far outside the spread of the rolling texture. However, second generation twins of these orientations fall just midway between the two main rolling components {110}<112> and {110}<001>. So this orientation can be provided with suitable nuclei by subgrain rotation and relaxation in transient regions together with the formation of annealing twins (mechanisms "b" and "d" of the nucleation theory). By contrast, the {211}<011> orientation, which is also a fast growing one, cannot be created by any of the above mechanisms. So, the brass recrystallization texture can be understood as evolving from the rolling texture by selected growth, but one in which not all fast-growing orientations are supplied with suitable nuclei.

The cube texture is possibly one of the most important and certainly the most investigated texture in fcc metals. It has sometimes been accounted for on the basis of the concept of oriented growth [8]. However, since the main components of the rolling texture and the cube component are not related by known relationships for maximum growth rate, it has to be explained as a compromise texture with a fairly good growth rate being applied to several components of the rolling texture. It is assumed that this orientation is a good example of a case where oriented nucleation is the controlling mechanism. Whether the nuclei are present in the deformed state or are created by an inverse Rowland transformation (mechanism "c"), cube nuclei have been observed to appear, polygonize and grow faster than any other orientation, so that they eventually consume the rest of the material. The principal controlling factor in this case is the nucleation rate.

Brass - to - copper texture transition

The texture transition depicted in Figures 2.29 and 2.30 can be interpreted in terms of the superposition of four different influences:

i) Rolling texture changes due to the decrease in SFE brought about by increasing the Ge content.

ii) Changes in the microstructure of the deformed state, particularly the development of inhomogeneities such as mechanical twins and shear bands, which become more dominant with increasing Ge concentration.

iii) The increase in the frequency of recrystallization twins with decreasing SFE (nucleation theory).

iv) The change in mobility of the grain boundaries as boundary segregation increases with the Ge content (growth theory).

The four ranges of recrystallization behaviour of the Cu-Ge alloys described in Section II.2.1 have been interpreted in the literature [67] as follows:

1) The case of the pure copper, which exhibits the strong cube texture, is given the same interpretation as the one outlined above (compromise between oriented nucleation and oriented growth).

2) Two points of view have been expressed regarding the preference of the twin to the cube position as the Ge concentration is increased. The first considers that the addition of Ge decreases the mobility of the cube boundaries. The second point of view is that the strong decrease in SFE increases the frequency of recrystallization twinning and thus favors the formation of *higher generation twins* (nucleation theory). It should be added that the second generation twins are *favorably oriented for growth* (growth theory) and that increasing the twinning frequency by increasing the Ge content has the effect of increasing their volume fraction, a trend which is observed experimentally.

3) In this range, the three recrystallization components are twin related to the three major components of rolling. These orientations are apparently present in small quantities in the rolling texture and are the first to form nuclei. However, they have a low migration rate and the grains remain small unless recrystallization twinning occurs, which is assumed to be the controlling mechanism in this range.

4) The fourth range corresponds to the development of the brass recrystallization texture; it has already been interpreted on the basis of a mixed oriented nucleation / selective growth theory.

Al alloys

The last component that will be interpreted here is the R ideal orientation, found only in Al alloys, at a level that depends on the purity of the alloy. As this component is very close to one of the main rolling textures, namely the S component, this has often been interpreted as a partial retention of the rolling texture (R texture as retained rolling texture). Ito et al. [86] concluded that this is the case only if continuous grain growth (i.e. what we have called *recovery*) occurs in the material. Due to the presence of impurities in the material, however, this component can also be formed by discontinuous recrystallization or grain growth, i.e. by an oriented growth mechanism (since each of the 4 symmetrically equivalent components of the S texture is oriented to the other three components by an approximate 40° <111> rotation). Recently, Hirsch and Lücke [87] have shown that both mechanisms, i.e continuous and discontinuous grain growth, can occur in these alloys. The retention of the rolling texture in aluminum alloys has also been observed by others researchers [98]; these workers have established clearly that polygonization and subgrain coalescence occur, together with grain boundary migration, without the nucleation of newly oriented grains.

II.2.4. CONCLUSIONS REGARDING ANNEALING TEXTURES

We conclude this brief review of recrystallization textures with the following three comments:

a) It is very difficult to predict and even to explain annealing textures on the basis of only one mechanism or theory. Both nucleation and growth are orientation dependent and the two must play significant roles.

b) The importance of *oriented growth* has been clearly demonstrated in both the recovery and recrystallization processes. It makes use of the coincidence site model which relies in turn on two recognized facts:

i) For specific misorientations, the grain boundary energy is a minimum. This leads to very stable boundaries which also have a minimum migration rate. These boundaries are often observed in cold worked materials.

ii) The migration rate of these boundaries depends strongly on the relative orientation of the adjacent grains. A grain boundary that is close to, but deviates slightly from the ideal position has the highest mobility. These fast migrating orientations are observed to be active during the operation of softening processes.

c) The above principles apply to deformation as well as annealing, and to recovery (during which fast migrating boundaries can develop by subgrain formation) as well as recrystallization (during which the nucleation of new grains provides the special boundaries). It thus appears that the coincidence-site theory might be useful in accounting for the influence of increasing temperature during metal processing. An attempt to do so has been made in the present investigation; the results of this endeavour are described in Chapter VIII below.

II.3. OVERALL CONCLUSIONS

At the end of Section II.1, we advanced the hypothesis that, in high SFE materials, an increase in the temperature produces an *increase* in what we call the brass component for any mode of deformation. We have seen that this generalization is well supported by experimental observations in the cases of rolling and torsion, but remains to be proved in detail for tension and compression.

The accurate prediction of compression textures could constitute the subject of a thesis in itself since an unusual phenomenon is frequently observed in this deformation mode, i.e. curling of the grains [8]. Thus, it was felt that this deformation mode is not suitable for a first study of the influence of

temperature since mechanisms such as grain curling could prevent the sole effect of temperature from being isolated.

It was therefore decided to check the above hypothesis only in tension, or more precisely, in axisymmetric extension. Swaging was selected for this purpose, which allows high levels of deformation to be reached with the aim of comparing some cold and warm textures in aluminum. The description of this study constitutes the subject of Chapter IV.

Another reason for reducing the extent of the experimental part of this work was that no detailed texture measurements could be performed at McGill during the course of this investigation.

It has also been established in this chapter that the following mechanisms may be responsible for the aspects of high temperature behaviors described:

- cross-slip,
- increases in rate sensitivity,
- activation of systems other than the $\{111\}<110>$ which operate at room temperature,
- development of a substructure through glide and climb and minimization of the sub-boundary energy.

These mechanisms have been introduced in the past to interpret the deformation textures of high SFE metals deformed at room temperature. It was felt in the present study that they could be adequately modelled to account for the high temperature deformation behavior of the high SFE metals as well. This is done in Chapters V to VIII.

CHAPTER III

THEORIES OF THE DEVELOPMENT OF DEFORMATION TEXTURES

III.1. GENERAL REQUIREMENTS

Before reviewing the classical theories of texture development, it is useful to define the different steps that must be followed in order to calculate the reorientation of the grains of a polycrystal following a particular deformation path.

1) The basic assumption in all the models described below is that the only mechanism involved in plastic deformation is slip, supplemented in certain cases by twinning. This starting point has two consequences:

i) The Schmid law [99] must be respected in each grain of the polycrystal. This law, first expressed in 1924 for the case of uniaxial tension, may be stated in a form that is applicable to any stress state [100]: "a single crystal yields on any particular slip system if the shear stress resolved on that slip plane and slip direction reaches a critical value which is "the yield strength" or "critical resolved shear stress" (CRSS) on that slip system". If we designate by $\underset{\sim}{\sigma}$ the stress state inside the crystal and by τ_c^s the CRSS on a given system s, this can be expressed as:

$$\tau^s = m_{ij}^s \sigma_{ij} \leq \tau_c^s \tag{3.1}$$

where m_{ij}^s is a geometric factor characteristic of slip system s, and defined by:

$$m_{ij}^s = \frac{1}{2}(n_i^s b_j^s + n_j^s b_i^s) \tag{3.2}$$

with n and b being respectively the slip plane normal and the slip direction. The Schmid law does not necessarily assume that τ_c is the same for all slip systems and can even be generalized to the case of twinning. τ can never exceed the critical value τ_c and the systems s for which equality holds in equation 3.1 are

the ones which are potentially active. The mathematical expression of the Schmid law also implies that purely hydrostatic stresses are incapable of causing plastic deformation. In such a case, τ will be zero for all slip systems. This reduces to 5 the number of independent components of the stress tensor. Similarly, the assumption that there is no change in volume during plastic deformation reduces to 5 the number of independent components of the strain rate tensor.

ii) The assumption that the deformation is accommodated solely by slip according to the Schmid law (supplemented perhaps by twinning) has the further consequence that the components of the strain rate tensor $\underset{\sim}{\dot{\varepsilon}}$ imposed on the grain (the microscopic strain rate tensor) can be expressed as:

$$\dot{\varepsilon}_{ij} = \sum_s m_{ij}^s \dot{\gamma}^s \tag{3.3}$$

where the sum is carried out on all the active slip systems s (i.e. those for which $\tau = \tau_c$).

We can see that equation 3.1 is a special form of the general yield criterion

$$f(\sigma_{ij}) \leq c \tag{3.4}$$

commonly used in the mathematical theory of plasticity. Similarly, equation 3.3 follows from equation 3.1 by use of the associated flow rule

$$\dot{\varepsilon}_{ij} = \frac{\partial f}{\partial \sigma_{ij}} \dot{\lambda} \tag{3.5}$$

which is another basic hypothesis of this theory. Equation 3.5 is equivalent to the statement that the function f in the yield criterion is also the plastic potential [100,101]. The available slip systems are of the type $\{111\}<110>$ (12 of them) and the possible twinning systems are of the type $\{112\}<110>$ for fcc metals.

2) Once the basic equations describing the mechanism of slip in a single crystal have been set up, the next step is to define the boundary conditions applied to the polycrystal, i.e. the macroscopic states of stress and strain rate described by two tensors called $\underset{\sim}{S}$ and $\underset{\sim}{\dot{E}}$. Again here, because of the existence of a plastic potential and of an associated flow rule describing the plastic behavior

of a polycrystal, these two tensors are related, and only half of the ten independent components of the two tensors need to be prescribed. The different components of these tensors are usually known or assumed to be known.

3) Some further assumptions have to be made in order to derive the states of stress and strain rate $\underset{\sim}{\sigma}$ and $\underset{\sim}{\dot{\varepsilon}}$ in each grain of the polycrystal from the macroscopic tensors. This is where the different theories diverge in the sense that each of them involves a different assumption leading from the macroscopic to the microscopic quantities. Here again, only half of the stress and strain rate components need to be defined, the rest can be derived with the aid of equations 3.1 and 3.3, as explained below.

4) Once the microscopic strain rate tensor is known, it is possible to calculate the shear rate $\dot{\gamma}^s$ on each slip system in each grain with the aid of equation (3.3) and from there to calculate the rotation of the crystallographic axes of a given grain with respect to some external axes linked to the specimen. It is not obvious at first sight how given shears on specific systems produce a rotation of the crystallographic axes. This can be visualized with the aid of Figure 3.1 [102], which illustrates the case of a single crystal deformed in tension. The deformation is imagined to take place by single slip. During deformation, the blocks of crystal between the active slip planes, and thereby the crystal lattice, rotate in such a way as to align the slip direction with the tensile direction. Similarly, the lattice rotation in a compression experiment tends to align the slip-plane normal with the direction of compression. These rotations are produced by the boundary conditions imposed on the single crystal in the sense that the tension axis and compression plane are forced to remain fixed with respect to the laboratory reference system.

In the case of a polycrystal, the situation is somewhat more complex and, apart from the stress and strain rate states in each grain, some further assumptions have to be made in order to assess the crystallographic rotation. For example, in tension, we will assume that the tensile axis remains fixed in all the grains of the polycrystal. Similarly, in rolling, we will assume that the rolling plane and rolling direction are fixed in each grain. These statements are equivalent to assuming that certain components of the displacement rate gradient tensor are zero while others are not. However, these assumptions have

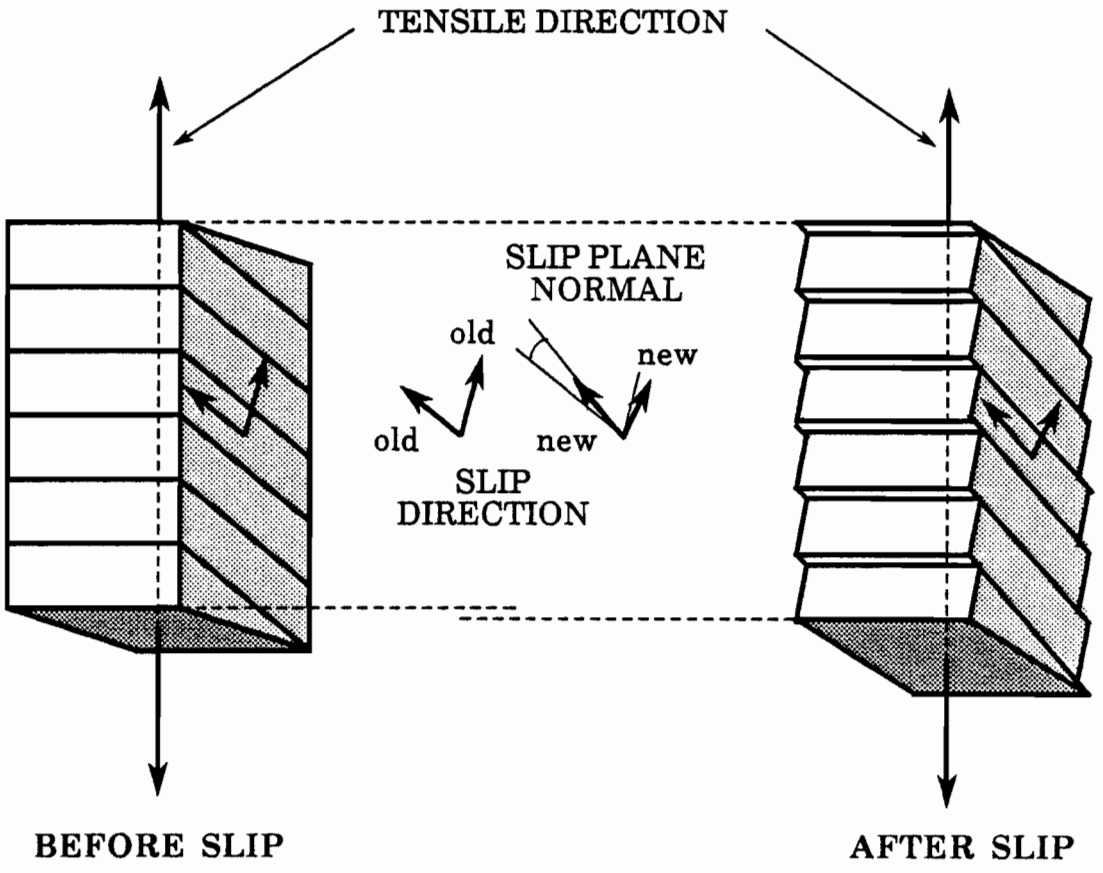

Figure 3.1. The lattice rotation produced by tensile deformation [102].

to be made explicitly when using complex theories, and this is rarely done in the papers dealing with this subject. We have chosen here to use the method originally developed by Kocks and Chandra [103] and also used by Canova [104] and Leffers [102] which is explained in detail in Appendix 1.

These general requirements being valid for all the models of deformation texture development, we can now review individual theories and point out the differences between them.

III.2. THE TAYLOR THEORY (1938)

Taylor [4] was interested in two different problems: i) first, the selection of the active slip systems in a deformed single crystal for which the 5 components of strain rate are known and the calculation of the subsequent shear rates and rotation of the crystallographic axes; and ii) the calculation of the shear rates and rotations in all the grains of a polycrystal for which only the macroscopic quantities are known. In the first part, he made use of what is often called the Taylor criterion and in the second part, he made use of what is known as the Taylor hypothesis.

III.2.1. THE TAYLOR CRITERION

When all five components of the strain rate tensor $\dot{\underset{\sim}{\varepsilon}}$ are imposed on a crystal, equation 3.3 constitutes a set of five equations in which the unknowns are the quantities $\dot{\gamma}^s$. It seems convenient at this point to adopt a matrix and vector instead of a tensor notation. The one adopted in this thesis is described in Appendix 2 [108]. With this notation, equation 3.3 can be rewritten as

$$\dot{\varepsilon} = M\dot{\gamma} \tag{3.6}$$

where $\dot{\varepsilon}$ has five rows and one column. Equation 3.6 can now be solved uniquely for the shears provided that it can be rearranged as

$$\dot{\gamma} = M^{-1}\dot{\varepsilon} \tag{3.7}$$

which means mathematically that the matrix M must have five rows and five columns and has an inverse matrix. This implies that we must only consider five slip systems at a time and that these systems must be independent (for the determinant of the matrix M to be different from zero), i.e. the individual shears on each of these systems cannot be decomposed into shears on the remaining systems [5].

Noting that for fcc metals there exist many ways of choosing 5 independent systems among the possible 12, Taylor considered which particular combinations will actually operate under a given state of strain rate and postulated that the preferred sets of slip systems will be the ones for which the

sum of the shears on all systems is a minimum. In his work, he took the CRSS to be the same for all slip systems, and consequently, the internal work rate can be written as

$$\dot{W}_i = \tau_c \sum_s |\dot{\gamma}|^s \tag{3.8}$$

Taylor in fact postulated that the *internal work rate* (and not the sum of the shears) had to be a minimum. This criterion is now known as the *minimum internal work rate criterion* and can be generalized to the situation where the CRSS has different values on different slip systems:

$$\dot{W}_i = \sum_s \tau_c^s \dot{\gamma}^s = Min \tag{3.9}$$

In equation 3.9, the convention that τ_c and $\dot{\gamma}^s$ have the same sign has been used so that $\tau_c.\dot{\gamma}^s$ is always positive. It is well known that there are 384 combinations of 5 independent systems [5,110] so that Taylor had to invert equation 3.6 for each combination in order to find the solution. Nowadays, however, this can be solved very easily with the aid of linear programming techniques [111]. The most interesting result of Taylor's work is his discovery that, given a unique value of the CRSS, the solution is never unique and that the total number of possible slip systems is always 6 or 8. For this reason, he was obliged to calculate all the possible solutions and rotations for each grain and then take the average solution. Having thus more or less solved the problem of the single crystal, he then approached the problem of the polycrystal.

III.2.2. THE TAYLOR ASSUMPTION

By looking at a micrograph of the cross-section of a drawn wire, Taylor noticed that all the grains were elongated in the direction of extension, and contracted in the two perpendicular directions. He concluded that each grain of a polycrystal suffers exactly the same strain as the surrounding bulk material. It is known nowadays that this is not exactly true, but the assumption has the advantage of assuring continuity of the strain rate through the grain boundaries so that no holes are created. This assumption can be written

$$\dot{\varepsilon} = \dot{E} \tag{3.10}$$

Taylor [4] investigated the axisymmetric extension of an aggregate constituted of 50 differently oriented grains and selected the active slip systems for each with the minimum internal work rate criterion. He then calculated the possible rotations of the grains after a given increment of strain. Obviously, different stresses are induced in differently oriented grains, so that equilibrium at the grain boundaries cannot be fulfilled. Taylor claimed that the stress differences across the boundaries can be accommodated by elastic strains. His results are well known and will not be presented here.

It is of more interest to compare some predictions based on the Taylor theory for large deformations with experimental results. This is done for the case of rolling in Figure 3.2a which is taken from the work of Mecking [39]. It can be seen that the agreement between theory and experiment is reasonable for the *copper-type* rolling texture. The main component predicted by the Taylor theory is very near the Cu component but the S and brass components are absent. The Taylor predictions are better for tension and lead to a very strong A component for torsion, as will be seen later. All the results given by the Taylor theory are in good agreement with observations for intermediate strains. However, at large strains, the stress differences between grains are unlikely to still be accommodated by elastic stresses and the agreement deteriorates with increasing deformation. It will be seen later that the Taylor theory can be modified to produce a considerable improvement. Finally, some comments will be made about the stress state. Taylor was not especially interested in stresses in his early work and did not even assume that the shear stress on all the active slip systems was the same. He never referred to the Schmid law and did not even mention the dislocation! With the aid of equation 3.1, however, it is possible to calculate the stress components once the active slip systems are known. A still more direct method is to use the yield criterion developed by Bishop and Hill [101,112] which will now be described.

III.3. THE BISHOP AND HILL THEORY (1951)

Just as in Taylor, Bishop and Hill first considered the case of a single crystal and then applied their theory to the polycrystal, again using the Taylor assumption of uniform strain. They first demonstrated that the Taylor criterion

Figure 3.2. Theoretical {111} pole figures obtained for 80% rolling reduction predicted by:

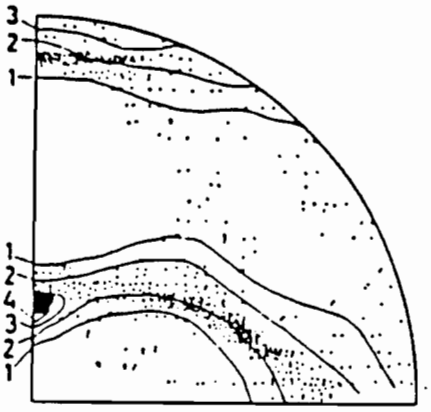

a) the Taylor model compared with an experimental copper texture [39].

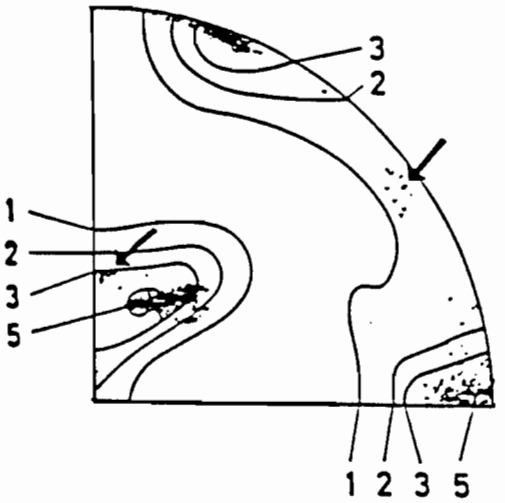

b) the Sachs model compared with an experimental brass texture (94% reduction) [102].

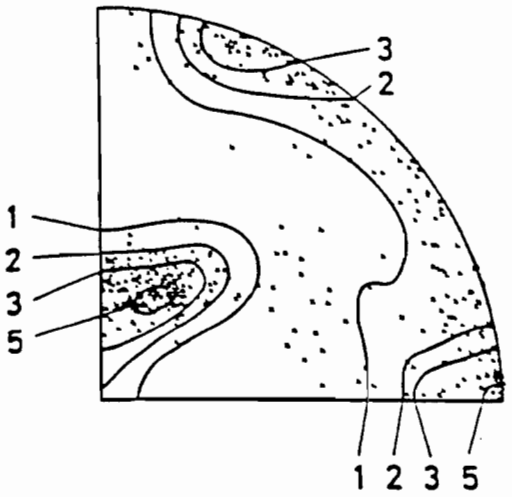

c) the modified Sachs model of Leffers. The state of stress is a combination of the Sachs stress state plus a random distribution. This is compared to a brass-type texture [102].

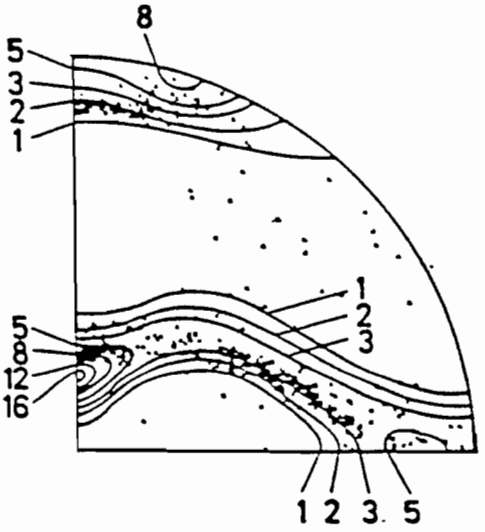

d) the Leffers model which accounts for the effect of cross-slip. A combination of the Taylor strain rate and some random components was used. This is compared to a copper-type texture [102].

was equivalent to the stress criterion for yielding expressed by the Schmid law. In other words, they proved that if the stress state in a given crystal σ is such that $\tau = \tau_c$ on each active slip system and $\tau < \tau_c$ on the others, then the internal work rate expended on the active slip systems is a minimum. They postulated the single crystal yield surface (SCYS), which is the geometric representation of the yield criterion. Equation 3.1 can be rewritten with the vector notation of Appendix 2 as follows

$$\sigma_i N_i^s - \tau_c^s \leq 0 \tag{3.11}$$

Clearly, equation 3.11 defines a set of hyperplanes in a 5 dimensional space, the normal to each hyperplane being the vector N^s. All the hyperplanes associated with the 24 possible slip systems (the 12 mentioned above plus their opposites) define a 5 dimensional polyhedron which has flat faces and sharp corners. When the CRSS has the same value for all systems, this polyhedron has 56 vertices, at each of which 6 or 8 hyperplanes intersect; this is called the single crystal yield surface (SCYS) and all the possible stress states for plastic deformation lie on this surface. Bishop and Hill observed that when 5 independent slip systems are required, only the 56 vertices (28 plus their opposites) correspond to possible stress states; they postulated further that the state of stress associated with a given strain rate tensor is the one which maximizes the external work rate. This is known as the *maximum external work rate principle* and is expressed by

$$\dot{W}_e = \sigma_{ij} \dot{\varepsilon}_{ij} = \sigma_i \dot{\varepsilon}_i = Max \tag{3.12}$$

A great advantage of this method is that, once the strain rate vector is specified, $\dot{W}_e$ can readily be calculated for the 28 vertices and the maximum value found in this way. This procedure is very rapid and the active slip systems are quickly found. In 1969, Chin and Mammel [113] proved that the principles of maximum external and minimum internal work rate are completely equivalent. Kocks [100], Van Houtte [114] and Renouard and Wintenberger [115] also came to the same conclusion. It should be added at this point that the two principles are convenient ways of finding the active slip systems and stress state and are *both* consequences of the Schmid law.

Once equations 3.1 and 3.3 are accepted, the following consequences are implied:

i) If we rewrite the Schmid law

$$\tau_c^s = \sigma_i N_i^s \tag{3.13}$$

and equation (3.3) in vector form

$$\dot{\varepsilon}_i = N_i^s \dot{\gamma}^s \tag{3.14}$$

the external work rate can be written as:

$$\dot{W}_e = \sigma_i \dot{\varepsilon}_i = \sigma_i (N_i^s \dot{\gamma}^s) = (\sigma_i N_i^s) \dot{\gamma}^s = \tau_c^s \dot{\gamma}^s = \dot{W}_i \tag{3.15}$$

This means that the internal and external work rates are equal.

ii) Suppose that we consider another stress state σ^* together with the actual slip systems which are the solution to the problem. These slip systems cannot be activated under such a stress state because, for at least one system s of the group, we have:

$$\sigma_i^* N_i^s < \tau_c^s \tag{3.16}$$

which implies that

$$\sigma_i^* \dot{\varepsilon}_i = \sigma_i^* (N_i^s \dot{\gamma}^s) = (\sigma_i^* N_i^s) \dot{\gamma}^s < \tau_c^s \dot{\gamma}^s = \sigma_i \dot{\varepsilon}_i = \dot{W}_e \tag{3.17}$$

so that the external work rate $\dot{W}_e$ is a maximum for the solution.

iii) Similarly, let us consider another set of slip systems characterized by the vectors $N^{s'}$ and compatible with the strain rate vector. These systems not corresponding to a solution, they are not at a critical state, so that

$$\sigma_i N_i^{s'} < \tau_c^{s'} \quad \textit{for at least one } s' \tag{3.18}$$

With the aid of

$$\dot{\varepsilon}_i = N_i^{s'} \dot{\gamma}^{s'} \tag{3.19}$$

we can write that

$$\tau_c^{s'} \dot{\gamma}^{s'} > (\sigma_i N_i^{s'}) \dot{\gamma}^{s'} = \sigma_i (N_i^{s'} \dot{\gamma}^{s'}) = \sigma_i \dot{\varepsilon}_i = \tau_c^s \dot{\gamma}^s = \dot{W}_i \tag{3.20}$$

which means that the internal work rate $\dot{W}_i$ is minimum for the solution of the problem.

iv) It then follows that the principle of the maximum work rate is equivalent to saying that the SCYS is convex and that the strain rate vector $\dot{\varepsilon}$ must be perpendicular to the yield surface or must lie inside the cone of normals of the vertex corresponding to the actual stress state. As $\dot{W}$ (3.12) represents the projection of $\dot{\varepsilon}$ on σ, this product is necessarily a maximum for this condition (see Figure 3.3).

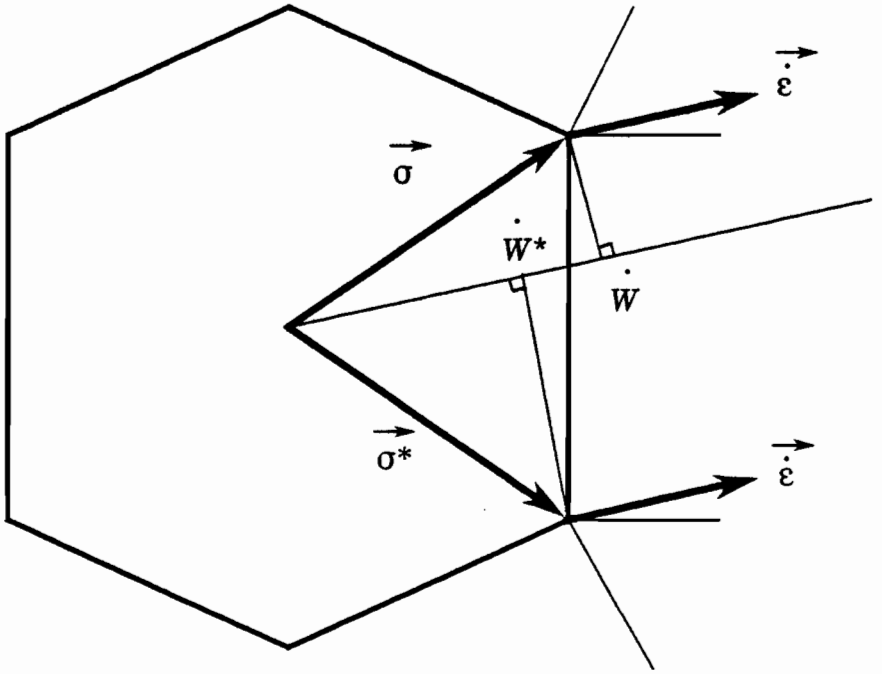

Figure 3.3. Illustration of the normality rule on the SCYS. If the principle of maximum work is verified, then $\dot{W} > \dot{W}^*$ implies that $\dot{\varepsilon}$ must lie in the cone of normals of the vertex σ.

The Taylor and Bishop and Hill theories being equivalent, they obviously produce the same answer. There are, however, two weaknesses associated with these theories:

1) When the critical resolved shear stress is the same for all the systems, there are ambiguities in the choice of the active slip systems. This problem can, for example, be solved by taking the average value of all the possible rotations. Such an average has no physical meaning, except that it can represent the behavior of a grain divided into several regions which do not deform along exactly the same path, each of them selecting a different equivalent solution.

Other criteria can also be used : e.g., the use of the Renouard and Wintenberger criterion (Chapter V) or that of a rate-sensitive technique, and the selection of specific combinations in the case of cross-slip (Chapter VI). The extent of the ambiguity problem will be considered further in Chapter V. If, however, different values of the CRSS are introduced, when the twinning systems are added, for example, or to account for latent hardening, the ambiguities are reduced considerably and can even be completely suppressed (Chapter VI).

2) The equilibrium of stresses is not satisfied and this has led investigators to develop other theories, such as ones that follow.

III.4. THE SACHS MODEL

III.4.1. THE ORIGINAL SACHS MODEL (1928)

Soon after Schmid [99] discovered that crystals deform when a critical shear stress τ_c is reached on a crystallographic slip system (1924), this criterion was applied to polycrystals by Sachs [3]. He assumed that the state of stress in each grain is proportional to the macroscopic stress in such a way that the CRSS τ_c is achieved in all the grains for at least one slip system. If S designates the macroscopic stress vector, the microscopic stress vector σ in grain g is simply:

$$\sigma = \lambda_g S \tag{3.21}$$

where λ_g is a parameter which depends on orientation such that, for at least one system s in this particular grain, we have, according to the Schmid law:

$$\tau_c^s = \sigma N_g^s \tag{3.22}$$

Here $\tau_c{}^s$ is the resolved shear stress on system s and $N_g{}^s$ is the 5 dimensional normal associated with system s.

In his model, Sachs was not interested in texture development and there was no mention of strain rate vectors. He only wanted to calculate the stress state in the polycrystal and only the stress direction was imposed. In order to predict texture development with such a model, at least one component of

strain rate has to be imposed on the polycrystal and on the grains, using the Kochendörfer assumption, for example [116]. Kochendörfer wanted to calculate the strain rate in each grain in a uniaxial tensile test using the Sachs model. He assumed that each grain undergoes the same tensile strain as the polycrystal. In this way, both the stress and the strain rate components can be determined in each grain, and the rotation of the grains can also be calculated. The same can be done in rolling where, in addition to the conditions on the stresses, we can for example require all the grains to deform by the same amount in the compression direction.

These assumptions imply that all the grains deform plastically simultaneously, usually by single slip, except in the case of very symmetrical orientations. Sachs tried to justify his assumptions by metallographic evidence of only one set of slip lines in some samples (which does not necessarily imply one kind of slip system). However, the Sachs approach violates the equilibrium condition for the stresses, which can be different from grain to grain. Sachs further suggested that this could be solved by inducing elastic stresses. More probably, this model should lead to material separation at the grain boundaries, which has never been observed [39]. Some results of a Sachs calculation were presented in Figure 3.2b for the case of rolling [102]. It can be seen that the texture obtained in this way is very sharp and mainly composed of the *brass component*. A few points can also be seen near the Goss position.

III.4.2. THE LOWER BOUND THEORY

In order to assure equilibrium of the stresses, an alternative is often proposed [104] which is also referred to as a Sachs theory. The assumption made is that the stress in each grain is the same and equal to the macroscopic one, in such a way that only one grain of the polycrystal is plastified (the "weakest point of the aggregate"). Usually only single slip takes place in the grain which is critically stressed. This theory is known as the *lower bound theory* in plasticity because it gives a lower limit to the "length" of the macroscopic stress vector. Similarly, the Taylor assumption of uniform strain rate produces an upper limit to the same quantity and by extension to the macroscopic work rate and in this way is referred to as the *upper limit theory*.

The validity of these limits is demonstrated in Appendix 3. Used together, they provide good estimates of the plastic properties of a polycrystal. While the Taylor and Sachs (with the addition of the assumption about one strain rate component) theories are widely used in texture calculations, the lower bound theory is not, since it deals only with the initiation of plastic deformation.

It was stated at the beginning of this chapter that half the 10 components of the stress and strain rate vectors have to be imposed on a grain in order for the others to be assessed. One extreme is the Taylor model where the 5 components of the strain rate are imposed, and the other is the Kochendörfer model where 4 stress directions are imposed together with one component of strain rate. In between these limits, there remains room for "intermediate" situations which will now be examined. These include the "modified Sachs model" employed by Leffers [102] as well as the *relaxed constraint theory* originally proposed by Honneff and Mecking [117].

III.5. INTERMEDIATE MODELS

III.5.1. THE MODIFIED SACHS MODEL (1975)

Leffers [102] recently made the observation that the Taylor assumption was too strict and was only applicable to materials having high SFE's where, because of extensive cross slip, the deformation can be reasonably homogeneous. So he proposed a new model which he called a modified Sachs theory because, like Sachs, he first applied a stress state to the material and then considered that the active system in each grain is the one which is the most highly stressed. To calculate the rotation of the crystallographic axes, he simply allowed a shear increment of fixed length to take place in the grain. To account for differing microscopic mechanisms in different materials, he adjusted the stress state imposed on the grain. For example in rolling, the basic stress state imposed is composed of only 2 normal stress components (one in the compression direction and one in the transverse one). In this case, the grains are allowed to shear, which is very close to the Kochendörfer type of slip. Leffers claimed that this model should account for the texture development of low SFE materials in which single slip is observed in the interior of the grains

and pile ups of dislocations at the grain boundaries. Of course, neither the continuity of strain rate nor the equilibrium of stress is respected. Leffers suggested that these conditions can be satisfied by "alien slip" near the grain boundaries. In such a case, the central part of the grains is allowed to deform freely and also to constitute the major component of the texture. The deformation mode in the alien slip zones is not specified and their effect on the texture is considered to be part of the background or texture scatter rather than of the main texture. This is simulated by simply adding some random stresses to those that are imposed.

For high SFE materials on the other hand, because of extensive cross-slip at the grain boundaries, the deformation is nearly homogeneous in the whole grain, as in the Taylor model. The variation in internal stress from grain to grain is simulated in this model by the addition of random stresses. Some of his results were presented in Figures 3.2c and d above, for the case of the basic stress system compared to a brass texture and for the case of the "statistical Taylor" model compared to a copper texture. His results are very close to the ones obtained with the strict Sachs and Taylor models, except that they are less sharp, which is in better agreement with experiment; nevertheless, no new texture component was found. The only objection to his model is that the stresses are simply added by a process of trial and error, the level adopted being the one that is consistent with the experimental results. His theory has the advantage of improving the Sachs model considerably by reducing the stress incompatibilities, a modification which also improves the calculated macroscopic mechanical properties.

III.5.2. THE RELAXED CONSTRAINT THEORY

Several of the observations reviewed above have led a number of researchers to propose a modified version of the Taylor model in which certain components of the strain rate tensor are not imposed on the grain. These are that:

1) Slip on less than 5 systems is often observed in polycrystals as well as single crystals when the boundary conditions are "mixed" (i.e. half expressed in terms of the stresses and half in terms of the strain rate components [103,118]).

2) It appears that the grain shape in a polycrystal must be taken into account for accurate modelling. This is especially true at high deformations where the grains become heavily elongated or flattened. In such cases, it is evident that material continuity at the "short" grain boundaries can be maintained by *local* polyslip and does not require overall polyslip [119].

The RC model was first developed by Honneff and Mecking [117] for single crystals deformed under mixed boundary conditions and polycrystals deformed in rolling. It was then reformulated differently by Kocks and Chandra [103] for the case of single crystals. Later, the Kocks and Chandra model was adapted to the deformation of polycrystals using grain shape considerations, independently by Canova and co-workers [104,105,119] and by Van Houtte [114,120] using two different methods. Let us first review the theory developed for single crystals.

THE HONNEFF AND MECKING MODEL (1978)

This model was proposed initially for the plane strain compression of single crystals when the strain rate tensor is not entirely known. The boundary conditions associated with such a test are presented in Figure 3.4a together with the allowed shear rates. It can be seen that only 3 out of the 5 components of the strain rate vector are known. To simulate such a test, the basic idea of Honneff and Mecking was the following: when the piston exerts an increasing compression stress, the flow stress will be reached first in that system which is the most favorably oriented with respect to the compression direction and slip will be activated. Generally, the corresponding strain rate tensor will have components in the transverse direction which are forbidden by the die. Reaction stresses will therefore build up, which suppress the activation of the initial system. In order to enforce further plastic deformation, the compression stress of the piston has to be increased, which in turn leads to an increase in the reaction stress. Due to the interrelation between the external force and the reaction stress, the net stress tensor changes until a second system is activated.

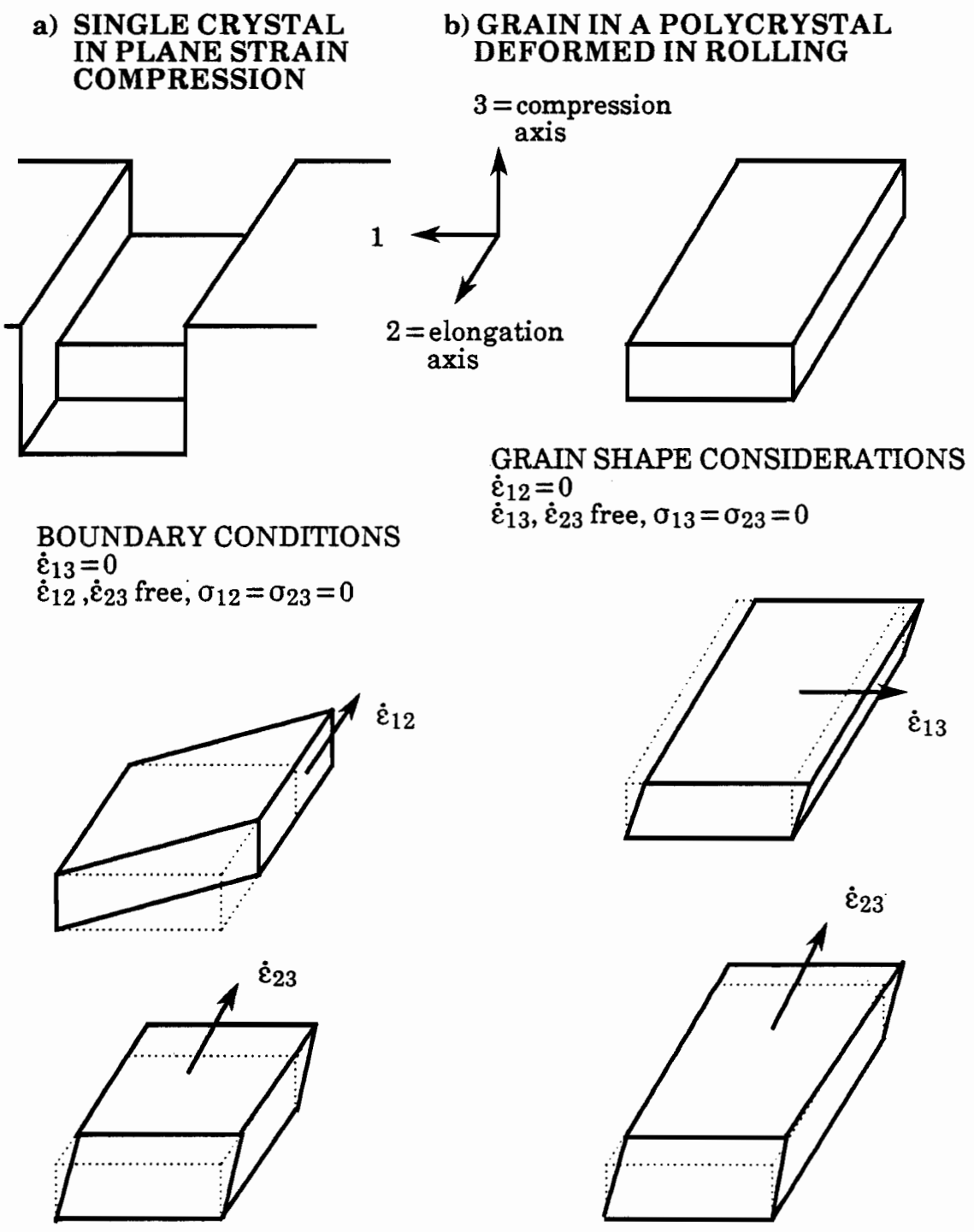

Figure 3.4. Allowed shear rates according to the RC model
a) for a single crystal deformed in a channel die
b) for a grain in a polycrystal deformed in rolling.

If the second system is oriented so that it can compensate for the lateral strains of the first, the crystal can deform by means of these two systems alone. However, this is not usually the case, and a third or even fourth system has to be found in order to satisfy the external strain rate.

Honneff and Mecking noted that their model was equivalent to the usual Taylor-Bishop and Hill model if they went up to five systems. They also stated that it was unlikely that the reaction stresses required for the activation of the fourth or fifth systems can be built up in the central part of the crystal when it becomes flat. They therefore found it reasonable to forbid the activation of these systems. They then applied the same model to a polycrystal deformed in rolling. In this case, the non-imposed strain rate components are described in Figure 3.4b.

THE KOCKS AND CHANDRA FORMULATION

These authors [103] solved the same problem but used a different approach. They started from the boundary conditions described in Figure 3.4a and noted that in the case where 2 components of the stress are set equal to zero, the actual stress vector in the grain can be found on a three dimensional section of the SCYS, i.e. one obtained by cutting the SCYS by the two hyperplanes $\sigma_{12}=\sigma_{23}=0$. They then determined the actual stress vector in that subspace by using the "generalized maximum work rate principle" introduced initially by Renouard and Wintenberger [121]. The demonstration of this principle as well as of the corresponding "generalized minimum work rate principle" and the calculation of the actual number of slip systems needed to accommodate such mixed boundary conditions were derived by Renouard and Wintenberger well before the existence of any RC model. Their treatment was reformulated in a more convenient notation by the present author [5] and the part concerning the validity of these principles is presented in Appendix 4.

For the moment, it is sufficient to know that it is possible to derive a 3 dimensional cross-section of the SCYS on which the stress state in a particular crystal can be found by application of the maximum work rate principle (i.e. the work rate associated with the non-imposed stress components). This stress state corresponds to the activation of 3 or 4 slip systems and, as only 3 components of

the strain rate tensor are known, 3 systems are sufficient to accommodate the deformation. Kocks and Chandra also demonstrated that their method is equivalent to the one developed by Honneff and Mecking. Driver and co-workers [122-124] used the same approach as Kocks and Chandra to calculate the reorientation of single crystals deformed in plane strain compression. They, however, additionally employed the Renouard and Wintenberger criterion to solve for the rotation in the presence of the ambiguities. It will be seen in Chapter V that this does not change the results appreciably since the extent of the ambiguities is sharply reduced under relaxed constraints. In summary, the fact that only 3 systems are needed in channel die compression is imposed by the boundary conditions. For a polycrystal, the reasons are different and they will now be described.

THE RC MODEL APPLIED TO POLYCRYSTALS

Kocks and Canova [119] were the first to establish the number of slip systems needed to accommodate the deformation in a heavily deformed polycrystal in which the grains are flat or elongated during tension, compression and torsion. For the case of rolling, their basic arguments are similar to those of Honneff and Mecking [117]. When the grains become very flat, 2 shear rates are permitted to be "free" in the interior of the grain and the continuity of strain across the smaller grain boundaries is fulfilled within the limited volume fraction contiguous with these boundaries. The argument here is that the two "free" shear rates lead to very small displacements, which is why they can be accommodated in the grain boundary regions (see Figure 3.4b). The third shear rate (i.e. $\dot{\varepsilon}_{12}$) leads to a large displacement and is thus set equal to zero in each grain of the polycrystal. In this way the grain is divided into 3 different zones, as illustrated in Figure 3.5a, but it is first assumed that the central part contributes the most to the texture and therefore that all the polycrystal deforms according to the RC mode. In order to select the 3 slip systems and the stress state in all the grains, two methods are available: (i) the use of sub-yield surfaces and the principle of maximum external work rate of the non-imposed stress components; or (ii) the use of the minimum internal work rate (see Appendix 4) together with the linear programming technique. The first was used by Canova et al. [104,105,119] and the second one was used by Van Houtte [114,120].

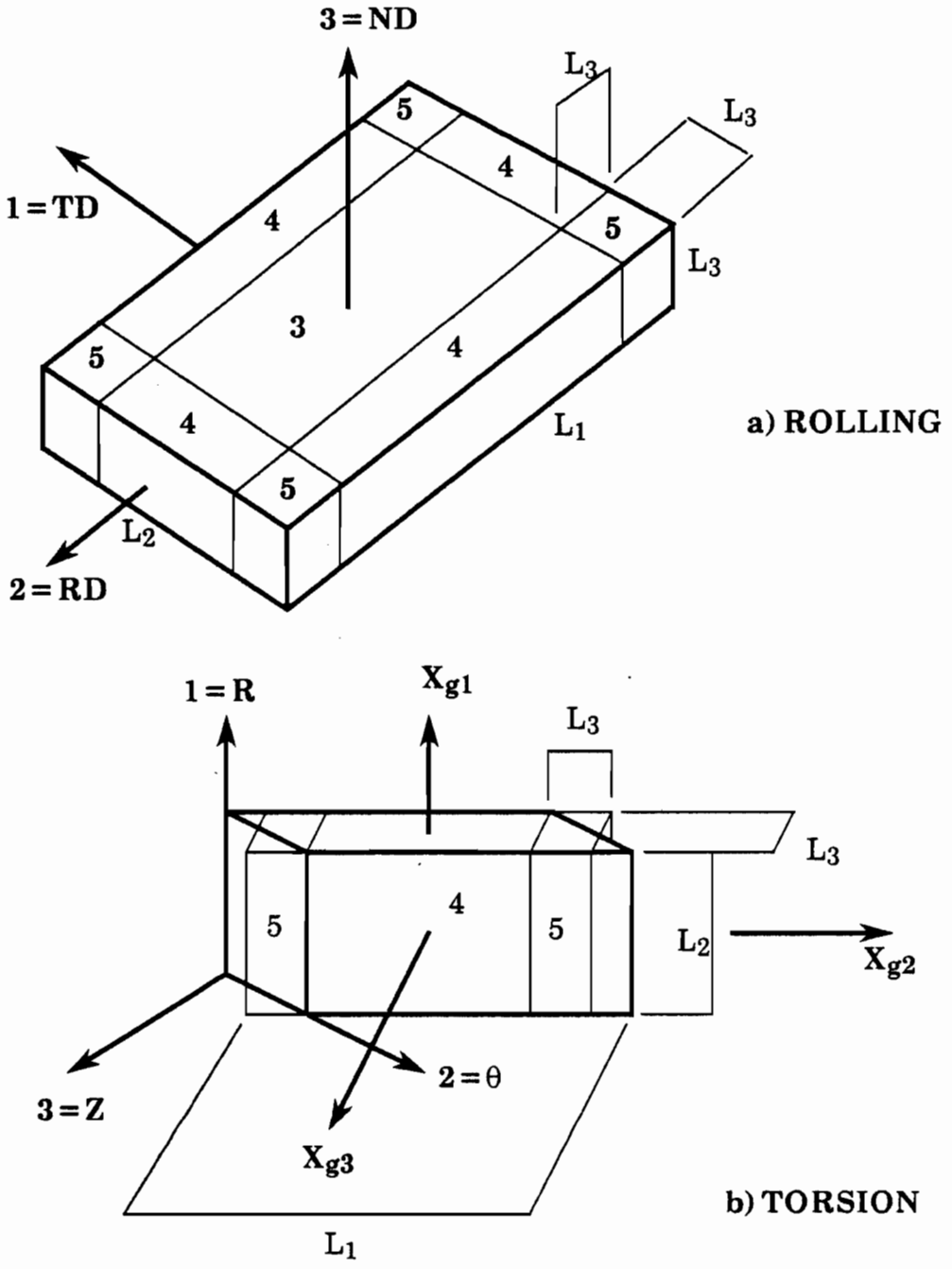

Figure 3.5. Number of active slip systems according to the RC theory in different parts of a grain deformed in a) rolling and b) torsion [125].

The use of "sub-surfaces" implies the calculation of the full yield surface in the reference system in which the zero stress components are imposed. In the case of rolling, for example, the conditions $\sigma_{13}=\sigma_{23}=0$ are imposed in a reference system linked to the sample axes, whereas the SCYS is known in the

crystal axes. The matrix used to go from one system to the other is usually expressed in terms of the Euler angles characterizing the orientation of the grain under consideration. It is thus evident that we first have to express the coordinates of all the vertices of the SCYS in the sample reference system for each grain and each increment in order to calculate the cross-section of interest. This was the method used by Kocks and Chandra [103] as well as by Driver and co-workers [122-124] and Morris [126] in the case of fcc and bcc metals.

This approach obviously involves long calculations and Canova [104] developed a method which reduces the computation time considerably. The full yield surface is characterized by 56 vertices, whose coordinates were calculated by Bishop and Hill and 24 facets, each associated with one of the 24 slip systems. However, the description is more complete if the edges of the surface are also taken into consideration. These edges are subspaces of dimension 1, 2 or 3 [127] in which 4, 3 or 2 independent systems, respectively, are activated. A fourth order edge is a one-dimensional subspace falling between 2 vertices in which at most 4 independent systems can be activated. A third order edge is a two-dimensional subspace extending between 3 or 4 vertices in which at most 3 independent systems can be activated. A second order edge is a three-dimensional subspace extending between 5, 6 or 8 vertices in which 2 independent systems can be activated. Finally a vertex is a zero-dimensional space in which 5 independent systems can be activated and a facet is a four dimensional space delimited by 16 vertices in which only one system can be activated.

Canova and co-workers [104,105] listed all the edges together with the connecting vertices and associated slip systems and found 108 fourth order (plus opposites) and 135 third order (plus opposites) edges. In order to calculate the stress state in the case where only 3 or 4 components of strain rate are imposed on a given grain, the procedure is the following. In the case of rolling for example, two components of the stress are set equal to zero, which implies that only 3 independent systems are required. The actual stress state then lies on a third order edge. It is enough to consider each of the 135 edges, one by one, to determine if there is a point on this edge satisfying $\sigma_{13}=\sigma_{23}=0$. If not, the edge is excluded. If such a point is found, it constitutes one of the vertices of the 3D yield surface; the operating one is then selected using the principle of

maximum external work. As the edges only need to be listed once, this calculation does not explicitly involve the calculation of the entire 3D surface.

The above procedure is completely equivalent to the one used by Van Houtte (i.e. using the principle of *minimum* work) and some results for rolling are presented in Figure 3.6 in terms of {111} pole figures. One obtained with the classical Taylor ("full constraint") calculation is shown as well. These results are taken from the work of Van Houtte [128], and illustrate two different RC models. The first is called the "lath" model in which only one shear is allowed to be free in the grains ($\dot{\varepsilon}_{23}$ relaxed); this seems appropriate for materials which have needlelike microstructures in which the thin cells or crystallites are much longer than they are wide. The lath model calls for the activation of 4 slip systems. The other is the "pancake" model, in which 2 shears are allowed to be free in the grains ($\dot{\varepsilon}_{13}$ and $\dot{\varepsilon}_{23}$ relaxed), which is appropriate when flat grains which are approximately as wide as they are long are produced. This calls for the activation of 3 systems.

When these results are compared with the experimental ones of Chapter II for the case of the copper texture, it is evident that the agreement is better for the two RC than for the FC model. The best agreement is found with the "pancake" model, according to which both the Cu and S components are found. The brass component, however, is still absent. Detailed study of all these results reveals that, by relaxing one or two of the strain rate components, the agreement between the theoretical predictions and experimental observations of the copper type rolling texture improves from a qualitative to a quantitative level. In fact, almost all of the experimental ODF's of these textures can be described by suitably weighted mixtures of the three theoretical textures. A Taylor type texture can even be found experimentally in aluminum, which is very sensitive to the starting texture [128]. Exactly how the mixture is to be chosen is yet unclear; this seems to be related to the microstructure or the substructure of the metal.

In this connection, Driver and co-workers [123] have suggested that, apart from grain shape considerations, an energetic criterion must also be included, i.e. even a flat grain could choose to deform by the FC model if this is energetically more favorable. For the sake of completeness, we have included in

Figure 3.6. Theoretical {111} pole figures of rolling textures for 56% reduction by rolling [128] predicted by:

a) the Taylor model

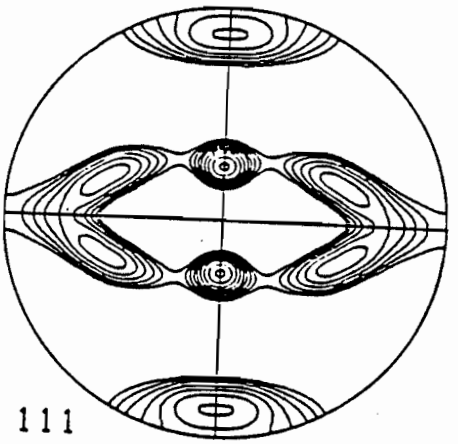

b) the RC lath model

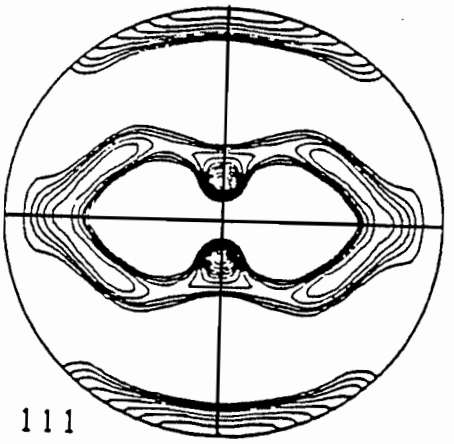

c) the RC pancake model.

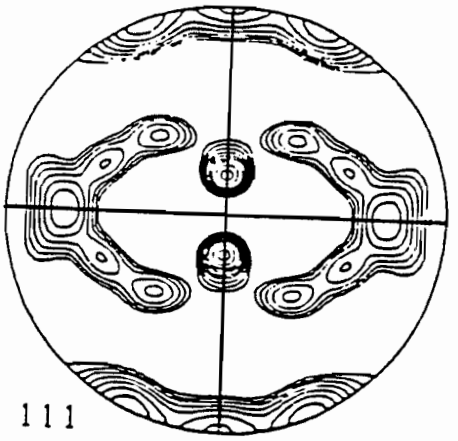

Figures 3.7 to 3.9 the CODF's calculated by Van Houtte [128] corresponding to the three pole figures of Figure 3.6. Since the result of a calculation is given in terms of the complete list of all the orientations present in the material, this representation is useful because it permits the textures to be compared in terms of the theoretical and experimental CODF's.

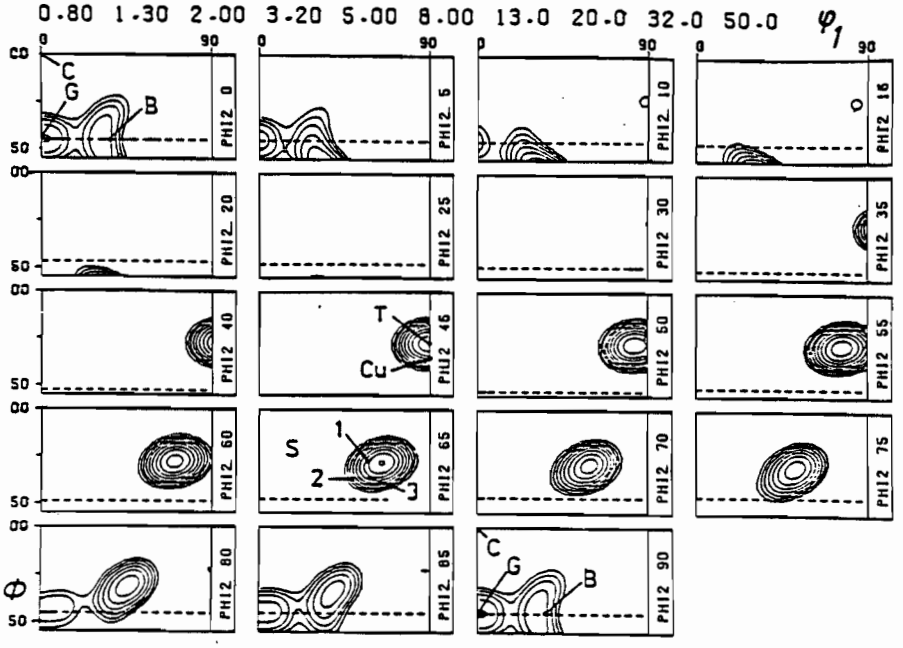

Figure 3.7. ODF of a rolling texture predicted for an 86% reduction using the Taylor model; C = cube, B = brass, G = Goss, T = Taylor component (7° from Cu) [128].

It appears that up to now the Taylor (or FC) model better predicts texture development in equiaxed grains i.e. at the beginning of deformation, whereas the RC model better predicts texture development in previously deformed materials, i.e. at large deformations. It therefore seems legitimate to set up a transition between the two models as the deformation proceeds. This approach was developed by Tomé and co-workers [125] on the argument that different numbers of slip systems are required in different parts of each grain, and that the volume fraction of each region changes as the strain is increased. This was illustrated in Figure 3.5 above for the cases of rolling and torsion, and similar arguments have been advanced for tension and compression as well. Tomé et al. proposed that the volume fractions within individual grains in which 3, 4 or 5 strain components are imposed be interpreted as fractions of all the grains in

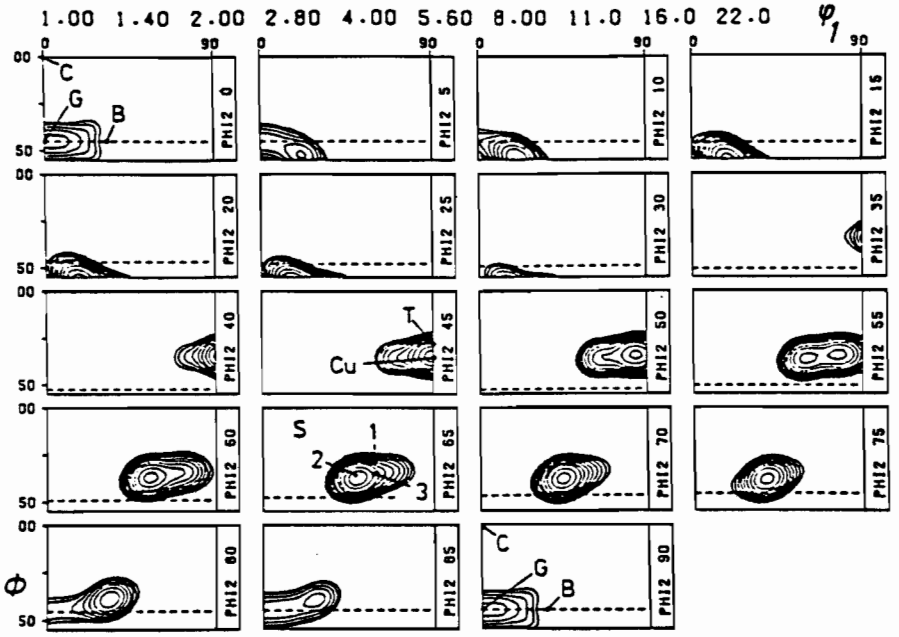

Figure 3.8. ODF of a rolling texture predicted for an 86% reduction using the pancake version of the RC model; C = cube, B = brass, G = Goss, T = Taylor component (7° from Cu) [128].

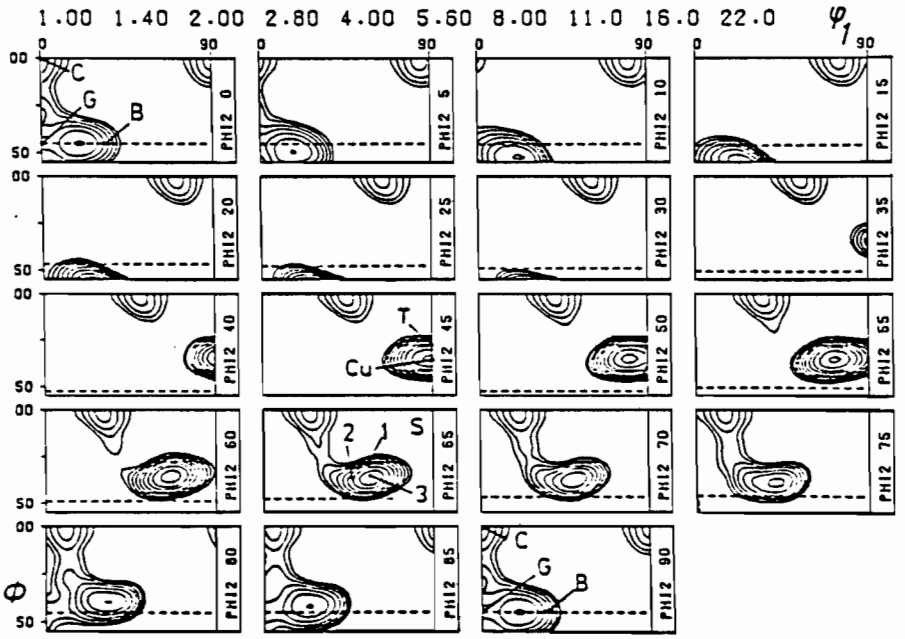

Figure 3.9. ODF of a rolling texture predicted for an 86% reduction using the lath version of the RC model; C = cube, B = brass, G = Goss, T = Taylor component (7° from Cu) [128].

the population. In this way, a statistically smooth transition takes place during deformation: all the grains start to deform according to the FC model and, as the deformation is increased, the number of grains deforming according to the RC model increases.

Some results calculated in this way for torsion are presented in Figure 3.10. They are compared with experimental pole figures determined on copper. It is evident that the agreement between the FC model and experiment is much better at small strains while the RC model agrees better with the results obtained at large strains. A calculation based on the FC-to-RC transition would predict a texture very close to the FC one at small strains and another very close to the RC one at large strains. Using the definitions introduced in Chapter II, it can also be seen that the FC calculation results in a mixture of the three components named A, A_2* and C which are characteristic of low strain textures in aluminum and copper, whereas with the RC model, the components A and A* vanish to be replaced by a strong C component characteristic of large strains. The B component is absent from the results of FC and RC calculations just as the brass component was absent in rolling. Apart from the Sachs model or of an RC calculation performed with 3 shear rates relaxed instead of two (which is forbidden by grain shape considerations), the normal way of obtaining the brass component in rolling or torsion is by the introduction of twinning in the classical FC and RC models. This has been done by Van Houtte [81] and Wierzbanoswki [129] and some of Van Houtte's results are reproduced in Figure 3.11 for the cases of rolling and torsion. In both cases, the presence of the brass component is very clear.

Before leaving the section concerning the RC model, it must be added that a new approach called the CC model (continuous constraints) has been developed by Fortunier and Driver [130]; this also produces a smooth transition from the FC to the RC mode, but it takes place *within each grain* instead of in a statistical way. Up till now, this model has only been applied to the deformation of single grains but it seems to be a very promising one for the deformation of polycrystals.

Up to this point, only models where the grains of the polycrystal are treated separately have been reviewed. A more recent approach consists of analyzing

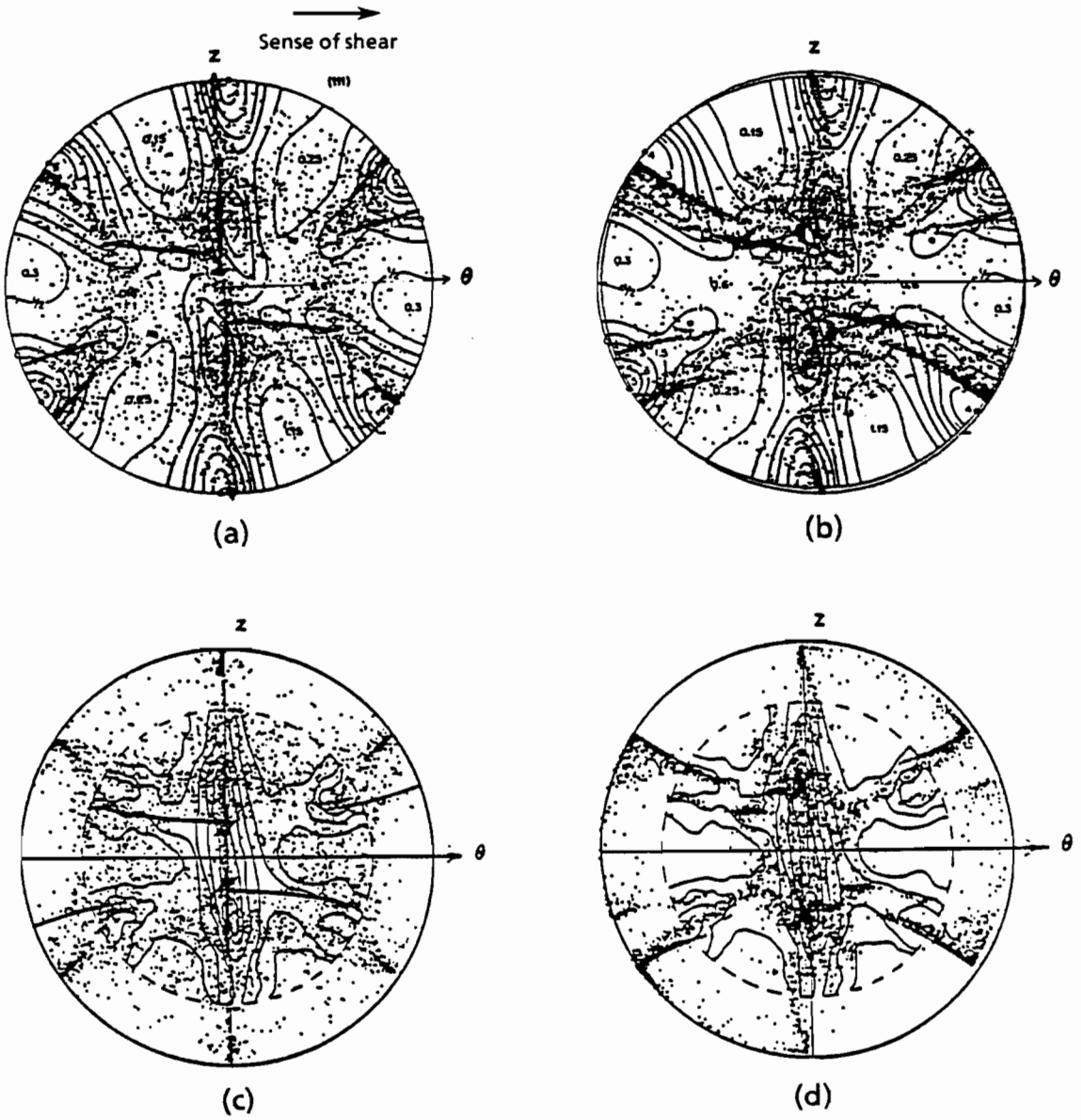

Figure 3.10. Torsion textures predicted by the FC and RC models and compared with experimental ones determined on copper: a) FC, $\gamma = 3.25$, b) RC, $\gamma = 3.25$, c) FC, $\gamma = 8.1$, d) RC, $\gamma = 8.1$. Note that the agreement with the FC model is better at small strains and with the RC model at large strains [77].

the interactions between a given grain and its environment, a homogeneous matrix whose behavior is a priori unknown. This is the basis of the self-consistent schemes which will now be reviewed.

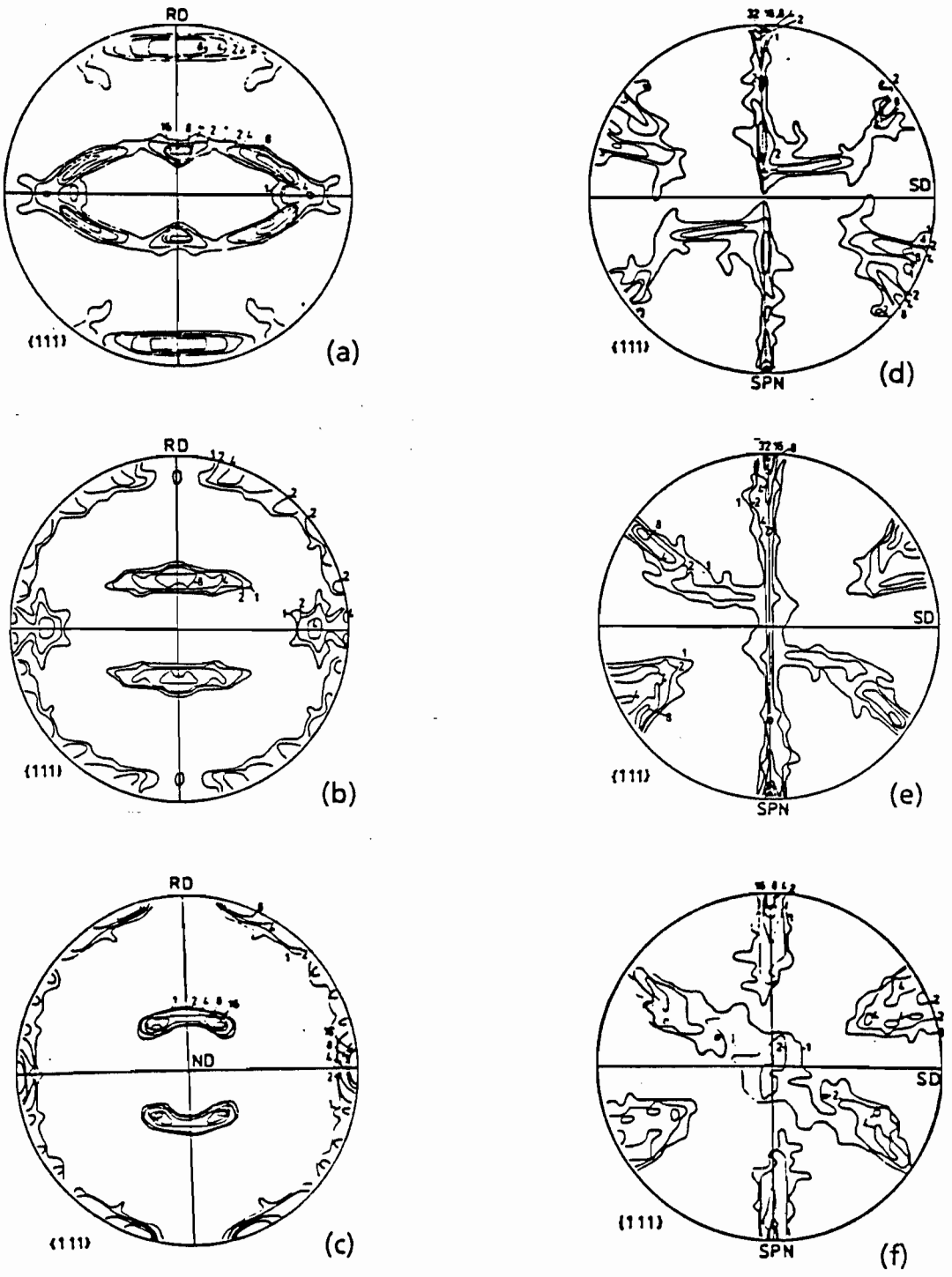

Figure 3.11. Influence of twinning on rolling and torsion. Textures predicted with the Taylor model as a function of the parameter $\alpha = \tau_c(\text{slip}) / \tau_c(\text{twinning})$. 86% reduction by rolling, a) $\alpha = \infty$, b) $\alpha = 1.1$, c) $\alpha = 0.8$. Torsion, $\gamma = 4$, d) $\alpha = \infty$, e) $\alpha = 1.1$, f) $\alpha = 0.8$ [81].

III.6. SELF CONSISTENT MODELS

The first self-consistent model was developed by Kröner [131] in 1958. He assumed that each grain of a polycrystal can be considered to be surrounded by an isotropic continuum. A stress $\underset{\sim}{S}$ is applied to the entire sample, as a consequence of which the material deforms. If a grain (assumed here to be ellipsoidal) is previously cut out of the material, surface tractions must be applied at the hole to produce the same stress in the surrounding matrix as if the hole were still filled with an "isotropic" piece of the material. Removal of the material has caused the hole to deform by an amount $\underset{\sim}{E}$ of plastic strain. $\underset{\sim}{S}$ is now applied to the grain itself, producing a plastic strain $\underset{\sim}{\varepsilon}$. Because of its anisotropy, it will not fit into the hole if a replacement is attempted. To achieve this, a distribution of internal stresses and elastic strains must be applied to the grain. If the grain is ellipsoidal, the internal stress will be uniform (as shown by Eshelby [132]) and in the direction opposite to that of the difference between the plastic strains of the grain and the hole. If we designate by $\underset{\sim}{S}$ and $\underset{\sim}{E}$ the macroscopic quantities and by σ and ε the microscopic ones, Kröner showed that the following relation applies between the two sets of quantities:

$$\underset{\sim}{\sigma} = \underset{\sim}{S} + 2\mu(1-\beta)(\underset{\sim}{E} - \underset{\sim}{\varepsilon}) \tag{3.23}$$

Here μ is the elastic shear modulus and β a parameter which depends upon the grain shape and the elastic properties of the matrix.

This first self-consistent scheme was relatively straightforward due to the simplifying hypotheses involved. The general framework of self-consistent formulations adapted to elasto-plastic deformation was further developed by Hill in 1965 [133]. According to Hill, if L_g and L_m designate the instantaneous moduli for the grain and the matrix, their inverse compliances being M_g and M_m respectively, it is possible to write that:

$$\begin{aligned} \dot{\underset{\sim}{\sigma}} &= L_g \dot{\underset{\sim}{\varepsilon}} \\ \dot{\underset{\sim}{S}} &= L_m \dot{\underset{\sim}{E}} \\ \dot{\underset{\sim}{E}} &= \langle \dot{\underset{\sim}{\varepsilon}} \rangle \\ \dot{\underset{\sim}{S}} &= \langle \dot{\underset{\sim}{\sigma}} \rangle \end{aligned} \tag{3.24}$$

where the brackets designate an average over all the grains. The solution is then given by:

$$\dot{\underset{\sim}{\sigma}} = \dot{\underset{\sim}{S}} + L^*(\dot{\underset{\sim}{E}} - \dot{\underset{\sim}{\varepsilon}}) \tag{3.25}$$

where L^* is a fourth rank tensor called the "overall constraint tensor" by Hill; it again depends on grain shape and on L_m and can only be evaluated after complete resolution of the equations. From equations 3.24 and 3.25, one obtains:

$$(L^* + L_g)\dot{\underset{\sim}{\varepsilon}} = (L^* + L_m)\dot{\underset{\sim}{E}} \tag{3.26}$$

and

$$\dot{\underset{\sim}{\sigma}} = L_g(L_g + L^*)^{-1}(L_m + L^*)\dot{\underset{\sim}{E}} \tag{3.27}$$

It gives us for L_m, using 3.24 and 3.27:

$$L_m = < L_g(L_g + L^*)^{-1}(L_m + L^*) > \tag{3.28}$$

This implicit equation is very hard to solve and its resolution has only been attempted for very small deformations by Hutchinson [134]. A simplified version was also proposed by Hill [133] as well as by Berveiller and Zaoui [135], for the case of an isotropic matrix (L_m). L^* can then be expressed as:

$$L^* = L_m(\underset{\sim}{S}_E^{-1} - I) \tag{3.29}$$

where $\underset{\sim}{S}_E$ is Eshelby's tensor in the case of an ellipsoidal inclusion [132]. Equation 3.25 reduces in that case to

$$\dot{\underset{\sim}{\sigma}} = \dot{\underset{\sim}{S}} + L_m(\underset{\sim}{S}_E^{-1} - I)(\dot{\underset{\sim}{E}} - \dot{\underset{\sim}{\varepsilon}}) \tag{3.30}$$

A further simplification introduced by Berveiller and Zaoui [135] allows us to rewrite this last expression as:

$$\dot{\underset{\sim}{\sigma}} = \dot{\underset{\sim}{S}} + 2\mu\alpha(1-\beta)(\dot{\underset{\sim}{E}} - \dot{\underset{\sim}{\varepsilon}}) \tag{3.31}$$

where α designates the plastic accommodation.

An obvious limitation of this formulation is that, since it assumes the isotropy of the surrounding matrix, it cannot really treat the case of heavily textured materials. Zaoui [136] then showed that, using an expression similar to 3.31, it is possible to regroup all the existing models under the following equation

$$\dot{\underset{\sim}{\sigma}} = \dot{\underset{\sim}{S}} + K\mu(\dot{\underset{\sim}{E}} - \dot{\underset{\sim}{\varepsilon}}) \tag{3.32}$$

where $K=\infty$ corresponds to the Taylor model, $K=2(1-\beta)$ is the value for the Kröner model, $K=2\alpha(1-\beta)$ holds for the Berveiller-Zaoui formulation and $K=0$ is associated with the lower bound (static model).

These self-consistent schemes appear to provide a quite general description of the plastic behavior of materials. Through the use of S_E, the influence of grain shape can be modelled [137] and in this case, the results are close to the RC ones. There are however, two objections to these models:

i) They are solvable only if the matrix is isotropic, and this can be valid only at the beginning of the deformation.
ii) They involve very long and complex calculations.

For these two reasons, they have only been used for the prediction of textures at low and intermediate strains. Examples are given in Figure 3.12 [137] for the case of rolling. At this stage of the deformation, the copper and brass textures are not fully developed and are still similar (see Chapter II, Figure 2.10). The results presented in Figure 3.12 are in good agreement with experimental results both for brass and copper and thus nothing can be concluded about the validity of the self consistent model at this stage of development of the theory.

III.7. OTHER CONSIDERATIONS

Except for the self consistent results presented in the last figure, all the other models reviewed until now have only been used in the case of isotropic hardening. The basic argument for doing so is that the calculations are generally much simpler in such a case and that the variations in τ_c^s in any event are quite small. Nevertheless it is possible to incorporate more realistic hardening laws to account for the latent hardening frequently observed in single crystals [34,138-142] and the effect of rate sensitivity [143,144] can be included as well.

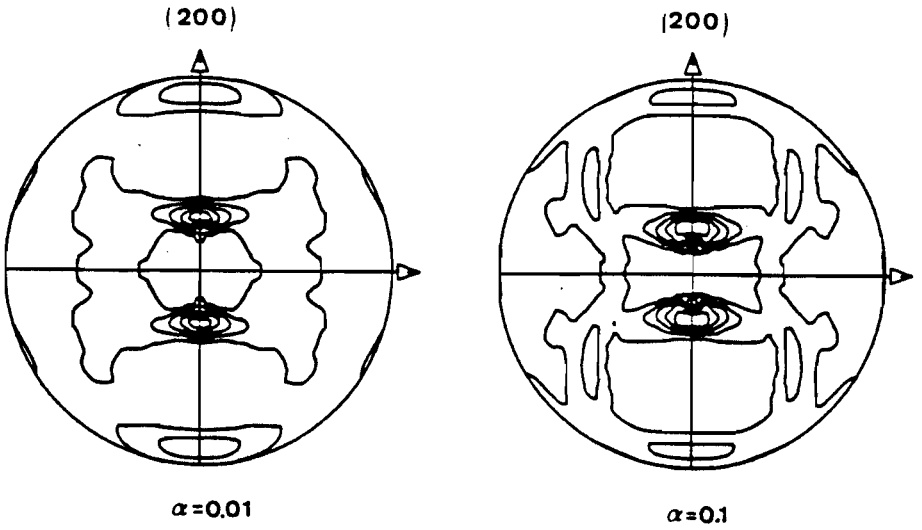

Figure 3.12. {200} pole figures calculated using the Berveiller and Zaoui self-consistent model after 50% rolling reduction. The parameter α is a plastic accommodation parameter which takes into account the partial plastic relaxation of the deformation incompatibility at the grain boundaries. This parameter varies from 0.01 and 0.1 [137].

Two rate sensitive models have been developed and adapted to polycrystal deformation. The first is the one proposed by Asaro and Needleman [143] which utilizes a rate sensitive hardening law in an elasto-plastic Taylor-type model. This leads to very long calculations which are similar in many ways to ordinary Taylor calculations. The improvement due to the addition of rate sensitivity is balanced by the fact that the Taylor assumption is not really valid for large deformations. The other rate sensitive model was developed by Canova and Kocks [144] in a very simple manner: the effect of this model is that it suppresses the ambiguities completely by rounding off the vertices of the SCYS. The results obtained with such a model will be discussed briefly in Chapter V but are close to straight FC or RC predictions. One reason for this is that they include the rate sensitivity in their FC-RC model, in which the number of ambiguities is already small.

Two models have also been advanced to account for latent hardening by incorporating a suitable hardening law for single crystals. One was proposed by Franciosi [138,139], in which the latent hardening parameters are determined experimentally. The other was developed by Havner and Le [141,142], who were interested in rotation predictions for highly symmetrical orientations of

single crystals deformed in plane strain compression. In this case, ambiguities are present in a classical model because of the high symmetry of the orientation and their results are in good agreement with experimental results [122,123]. However, these models have not yet been adapted to polycrystal deformation and it is unlikely that they will lead to results which differ appreciably from the classical ones. Latent hardening appears to have only a minor effect on texture development (except when highly symmetrical orientations are involved). A more serious contender would be a model which describes the state of stress and strain within each grain with accuracy. A new theory which tries to incorporate the influence of neighboring grains (as individual grains and not as a uniform matrix) is the cluster model developed recently by Kocks and co-workers [145]. This model seems promising since it can predict different rolling components going from brass to copper for different types of matrices. It violates, however, the grain shape considerations discussed above.

A last category of model is the one in which emphasis is placed on the problem of the ambiguities. These can include considerations of cross-slip, latent hardening, and rate sensitivity as well as the use of the Renouard and Wintenberger criterion. These different alternatives will be developed below and some of the results obtained in this way will also be presented.

III.8. CONCLUSIONS

The main purpose of this chapter was not to review all the existing models but to describe enough of them so that the rest of this work, as well as the choice of a starting model, would be put into context. The results reported here only concerned plastic deformation at room temperature. Some of the mechanisms present at higher temperatures, such as cross-slip or the activation of $\{100\}\langle 110\rangle$ systems have been incorporated in existing models only to account for the behavior of high SFE materials at room temperature. The behavior of these metals at high temperatures has never been investigated.

All the major results reported to date as well as others of minor importance have been summarized in two tables. Table 3.1 lists all the observations concerning rolling and torsion, and Table 3.2 concerns tension and

compression. The reader will also find in these tables the corresponding references and some general remarks about the validity of the models involved.

It was seen that two different approaches can be used to deduce the microscopic states of stress and strain rate from the macroscopic quantities. The first consists of assuming that some components of the σ and $\dot{\varepsilon}$ are known a priori in all the grains, which can thus be treated individually. The second considers the surrounding matrix in an implicit form and, as all the grains have to be treated simultaneously, implies long and complex calculations.

It was decided to base the present study on the first approach, which permits the high temperature deformation mechanisms listed in Section II.3. to be added without involving calculations which are longer and more complex than can readily be performed at McGill. The FC and RC models were thus selected as a starting point in the present simulations. The RW criterion, the ease of cross-slip (through the selection of colinear systems or the introduction of hardening laws), the activation of new slip or cross-slip systems and the influence of recovery (through modification of the grain shape arguments and the minimization of the GBE) can be added to these models in a relatively simple manner.

MODEL	ROLLING	TORSION	REMARKS
Taylor / BH averaging	near Cu component [128]	A, A*, C [104]	valid for small strains high SFE metals
Sachs	brass component [102]	-	very sharp low SFE metals
Leffers 1 Sachs + random	brass component + spread [102]	-	low SFE metals improved SACHS
Leffers 2 Taylor + random	near Cu component + spread [102]	-	small strains high SFE metals improved TAYLOR
RC p=4	near Cu + near S [128]	C [104]	large strains high SFE metals
RC p=3	Cu+S components [128]	not valid (grain shape)	large strains high SFE metals better than RC p=4 for rolling
FC-RC	Cu+S [144]	C [144]	all strains high SFE
CC	id. [146]	id.[146]	id.
Asaro rate sensitive	-	A, A*, C [143]	very complex like Taylor
RS+FC-RC	id. FC-RC [144]	id. FC-RC [144]	very similar to FC-RC
Latent hard.	more brass comp.[26,139]	-	limited data
Cluster	brass or Cu texture [145]	id. FC-RC C [145]	limited data more spread violation of GS arguments for rolling
Taylor + twinning	brass texture [81]	brass texture [81]	small strains low SFE
Self consistent	intermediate brass-Cu textures[137]	-	complex intermediate strains

Table 3.1. Theoretical results obtained with different models in rolling and torsion.

MODEL	TENSION	COMPRESSION	REMARKS
Taylor + averaging	70%<111> + 30%<100> [6]	spread between <100>-<113> [6]	high SFE metals
Colinear slip (FC)	77%<111> + 23%<100> [6]	-	high SFE metals room temperature cross-slip
Coplanar slip (FC)	id. [6]	-	low SFE metals room T latent hardening
Intrinsic faulting (FC)	100% <111> [6]	-	low SFE metals room T
Twinning (FC)	more <100> [6]	-	low SFE metals
RC + rate sensitive	id. FC + aver. [144]	not good [144]	no improvement on Taylor FC
Latent hardening	more <100> [26]	-	low SFE metals
Twinning {111}<112>	100% <100> [147]	-	low SFE metals
Hosford curling	-	strong <110> [148]	very good agreement high SFE metals
Self consistent	id. Taylor [149]	-	very small strains high SFE metals

Table 3.2. Theoretical results obtained with different models in tension and compression.

CHAPTER IV

EXPERIMENTAL PROCEDURE AND RESULTS

IV.1. EXPERIMENTAL MATERIAL

The material investigated was Alcan 1S aluminum received in the form of extruded rods 3.80 cm in diameter. The chemical analysis performed at McGill revealed that the principal impurities present were iron (0.19%) and silicon (0.06%).

Optical metallography showed that the as-received rods exhibited a fibrous, "cold-worked" microstructure, as shown in Figure 4.1a. The original grains of the samples were elongated in the direction of extrusion. The rods were then annealed at 550°C for one hour, a process which transformed the microstructure into a more or less equiaxed form, as seen in the transverse section shown in Figure 4.1b.

IV.2. EXPERIMENTAL PROCEDURE

The rods were remachined to a diameter of 3.05 cm so as to be able to fit into the swaging machine of the Chalk River Nuclear Laboratories, where the tests were performed. Two deformation temperatures were employed: room temperature and 250°C. The latter temperature was selected according to two criteria: first, it had to be in the temperature range where no recrystallization takes place; second, it should not be too high, since in the swaging process the rods are forced into the dies by hand.

The tests were performed in a series of passes, each corresponding to a different die. The cold rods were only deformed to a total strain of $\varepsilon = 0.8$, which corresponds to 9 passes. After that, it became impossible to push them into the swaging machine because of strain hardening; this was in spite of the use of a lubricant to reduce the friction. The hot rods were given 20 passes of

Extrusion axis

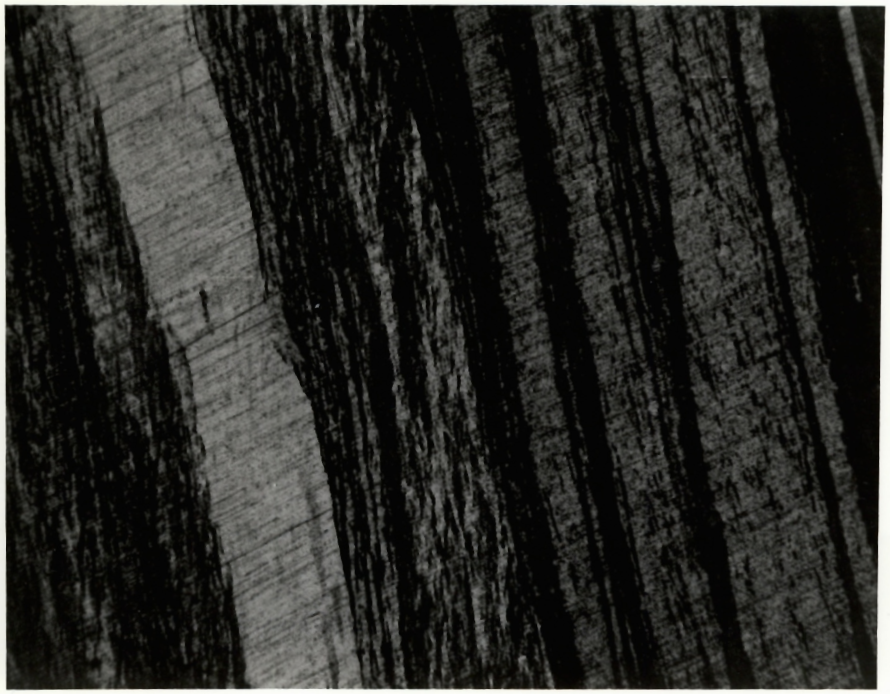

Figure 4.1. Optical micrographs of

a) as received aluminum

Extrusion axis

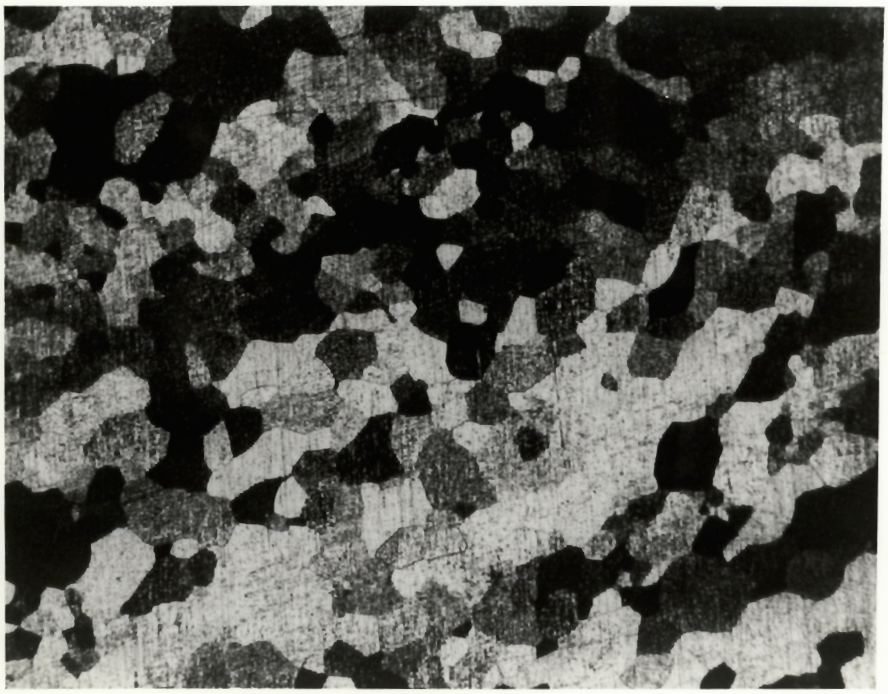

b) Al annealed at 550°C for 1 hour.

Magnification ×70

deformation, the total strain being equal to $\varepsilon = 2.16$. Between two successive passes, the rods were held in an adjoining furnace at the constant test temperature of 250°C; they were remachined whenever they became too long to fit into the furnace. During deformation, the temperature of the rods varied since the reductions were not performed inside a furnace. The balance between cooling in air and heating due to the high degree of deformation and of friction was such that the temperature difference between the beginning and the end of the deformation was not more than 50°C. This temperature variation was considered to be small enough to have little influence on the texture.

The process of swaging results in the axisymmetric elongation of the central part of the rod, on which is superimposed a shear deformation at the surface of the rod because of friction. The samples were therefore remachined before the X ray measurements were made in order to remove the outer layer. The advantage of this process, compared to tension, is that the deformation in the center remains homogeneous up to the final strain of 2.16, which would not have been the case in tension because of the occurrence of necking.

IV.3. EXPERIMENTAL DETERMINATION OF THE TEXTURE

The X ray measurements were performed at the CEMEF (Centre de Mise en Forme) of the Ecole des Mines de Paris at Sophia Antipolis in France.

IV.3.1. PREPARATION OF THE SAMPLES

As the final diameter of the hot swaged rods was 1.03 cm, composite samples were prepared in order to have a sufficient surface area to investigate. The specimens were cut as illustrated in Figure 4.2; both transverse and longitudinal sections were prepared in this way, and mechanically polished.

The diffraction measurements were carried out using the reflection method on a Philips PW 1078 goniometer. This goniometer is connected to a computer which performs the necessary corrections on the diffracted intensities step by step and then executes the pseudo-normalization of the pole figures over the angular domain associated with the reflection method, i.e. between 0 and 70°.

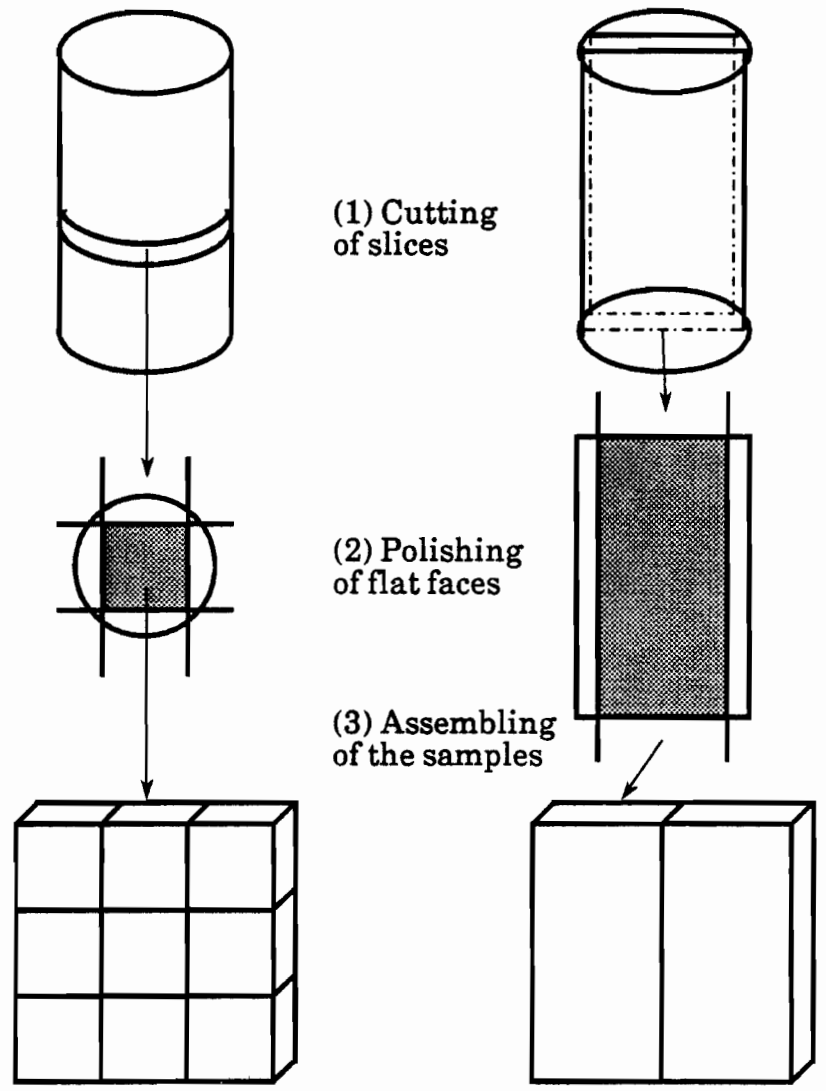

Figure 4.2. Preparation of composite samples for texture measurement.

IV.3.2. EXPERIMENTAL RESULTS

The results are presented below as incomplete {111} pole figures for both the transverse and longitudinal sections. The combination of these two sections provides enough information regarding the texture to overcome the fact that the pole figures are incomplete. Although the texture was determined after each swaging pass, only a few of the results are presented here to illustrate the general trends observed. Figure 4.3 shows the initial texture of the material,

which was far from random even after annealing. On this figure, the positions of the {111} and {100} fibres are also indicated. In Figure 4.4 the textures obtained after a strain of $\varepsilon = 0.8$ are compared for the cold and warm conditions and, in Figure 4.5, the texture obtained after a strain of 2.16 in the warm condition is illustrated.

IV.4. DISCUSSION OF THE RESULTS

The combination of the two incomplete pole figures provides the following information:

i) On the transverse section, the intensity at the center indicates the percentage of the {111} fibre. Each grain of {111} orientation has a pole in the center. The other three poles are distributed along a circle located 70° from the center which cannot be seen here since it lies at the limit of the angular range for reflection. The presence of the {100} fibre is indicated by the circular ring located at around 55°. Each {100} grain has its four poles distributed around this circular region.

ii) On the longitudinal section, both fibres are visible, although they are rather close. Furthermore, only a part is visible, because of the limitations of the reflection method, and the intensity is not constant along the fibre. An indication of the relative percentage of the two fibres can be gained from the position of the maximum intensity as well as from the spread around the two fibres.

An examination of Figures 4.3 to 4.5 leads to the following conclusions. First, the initial texture was composed of a relatively strong mixture of the two fibres of interest; this resulted from extrusion followed by annealing. Moreover, the intensity of the {100} component is much larger than that of the {111}, which is not what is expected if the deformation texture existing prior to the annealing treatment is retained. Usually, the extrusion texture of aluminum consists of a strong {111} and a weak {100} fibre (see Figure 2.2). The initial texture of the present specimens seems to have resulted from annealing; part of the extrusion texture was retained and a strong {100} component was formed

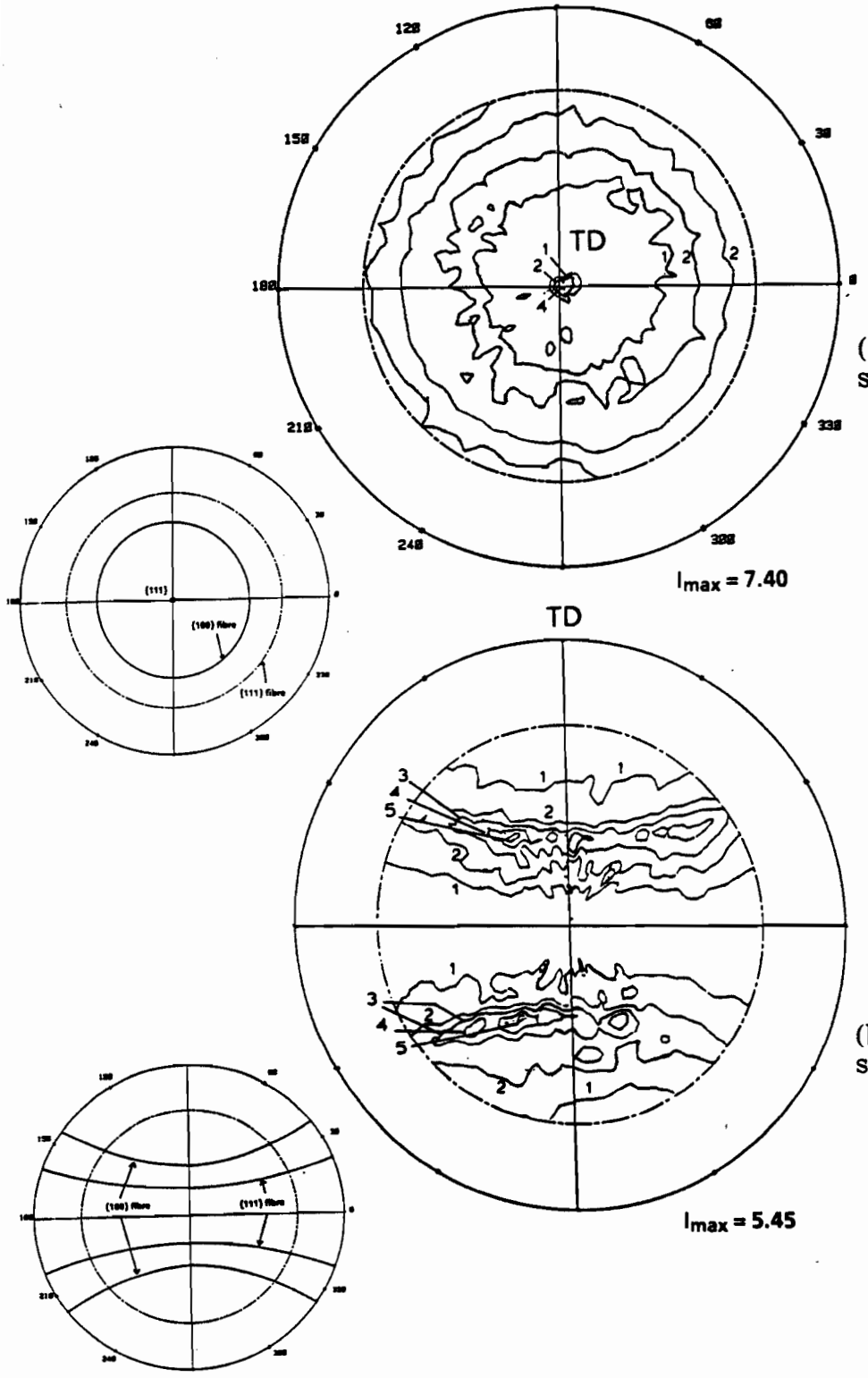

Figure 4.3. {111} pole figures for the annealed material.

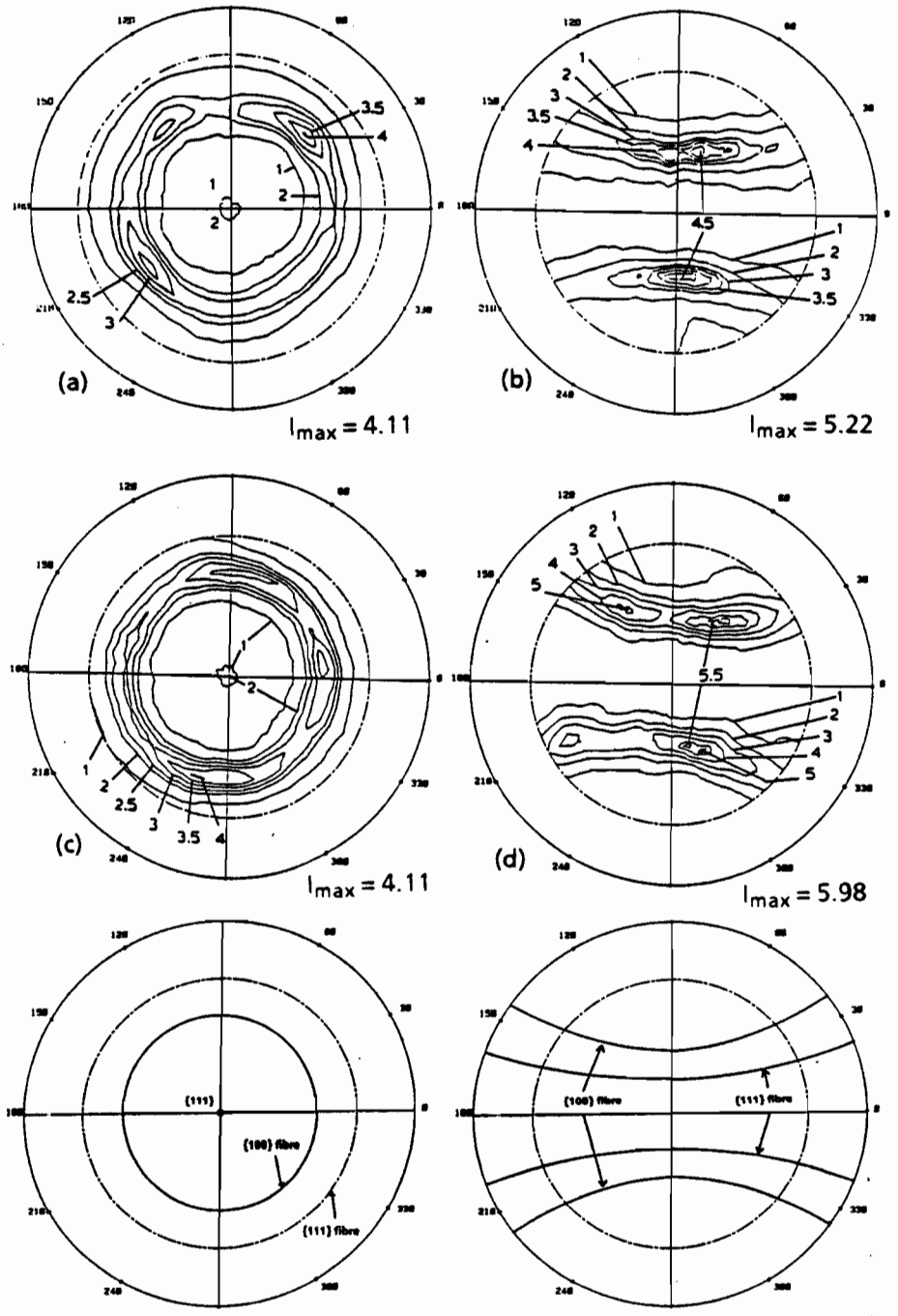

Figure 4.4. {111} pole figures for: the cold deformed rod, a) transverse section and b) longitudinal section; the hot deformed rod, c) transverse section and d) longitudinal section; $\varepsilon = 0.8$.

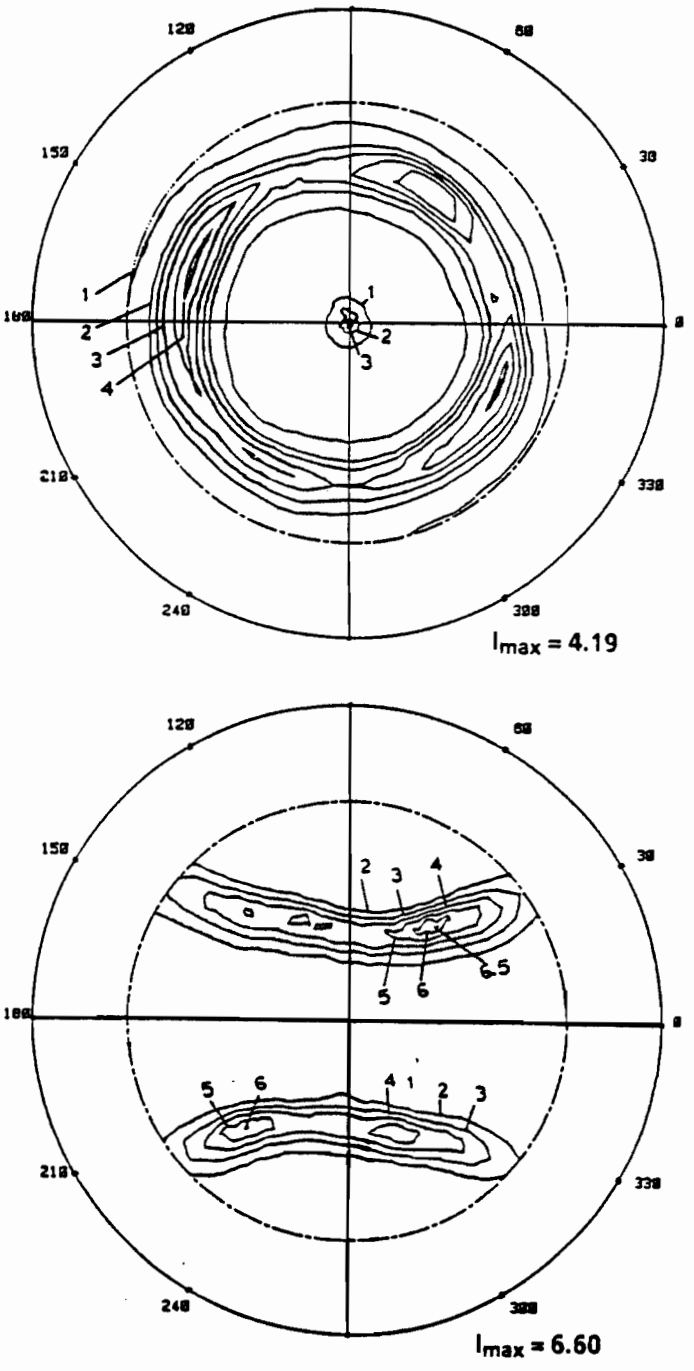

(a)Tranverse section

(b)Longitudinal section

Figure 4.5. {111} pole figures for the hot deformed rod swaged to a total strain of $\varepsilon = 2.16$.

during annealing by a process similar to the formation of the cube texture after rolling. Unfortunately, both components are stable during deformation and, as a result, only small variations can be expected during swaging; this is exactly what was observed. However, as the initial scatter around the {111} and {100} was quite large, the observed variations after deformation can be ascribed to different rearrangements of the orientations situated within the spread, which are not stable. A decrease in the intensity of the {111} can be noted in the first stages of deformation at the two temperatures, followed by a sharpening of the two components. This sharpening is not exactly the same in the two cases (i.e. for cold and warm deformation).

To obtain more quantitative information, three further parameters were investigated: the position of the maximum intensity; the spread around it in the longitudinal sections; and the variation in the average intensity of an annulus in the transverse sections as a function of the angle θ. Comparing the longitudinal sections of Figure 4.4 first for the two temperatures investigated, it can be seen that there is some spread around both the {111} and {100} fibres, with the maximum intensity located on the {100} fibre and a relatively low intensity around the {111} fibre (between 1 and 2 times random). However, the maximum seems to be slightly higher in the hot deformed material, i.e. 5.98 instead of 5.22. This indicates that, for a same amount of deformation, the percentage of the {100} component is higher for the hot deformed material than for the cold deformed one; although the difference is not great, this could confirm the hypothesis advanced in Chapter II regarding the effect of temperature. Such a conclusion can only be tentative for the following reasons.

i) Only parts of the two fibres are visible on these sections. It is clear that the grains are not evenly distributed along the two fibres, as indicated by the intensity peaks, and there appears to be more spread on the outer part of the pole figure.

ii) The plotting routine employed may not have been very accurate. This involves numerous interpolated values between the measured ones, which probably led to some errors. As a consequence, the intensities reported on the transverse and longitudinal sections are sometimes contradictory. That is why the average intensity within an annulus in the transverse section was plotted.

This average is calculated from the measured (and normalized) values only and is not comprised of any interpolated values.

iii) It is also possible that the differences are due to differences in the kinetics of rearrangement of the unstable orientations. These may reach stable positions faster at an elevated than at room temperature.

It was therefore decided to examine the variation in the average intensity at a given radius in the transverse section as a function of the angle θ going from 0° at the center to 70° at the outer limit. These variations are presented in Figure 4.6 for the pole figures shown in Figures 4.3 to 4.5. The average intensity is plotted here as a function of $\cos(\theta)$, which enables the proportions of the {100} and {111} fibres to be calculated in a constant volume in Euler space [17]. This was done as follows: first an area around each of the two fibres equal to 5% of the total area of the stereographic triangle was defined. This is shown in Figure 4.7 together with the corresponding areas in the {111} pole figure. The area was divided into two parts for the {111} component. One lies around the center and the other lies around a circle situated at 70° from the center. This last part is not considered here since it is out of the measured range. In a random texture, 5% of the total number of poles would be distributed in each of these areas, which would correspond in turn to 5% of the number of orientations. In a non random texture, the percentage of orientations located in 5% of the total area around the {100} position will be equal to one quarter of the area below the curve in Figure 4.6 around the {100} (between the two vertical lines defining 5% of the total area). For the {111} fibre, since only the central part of the area under consideration is visible on the pole figures, the percentage of orientations located in 5% of the total area around {111} is exactly equal to the area (marked 5%) below the curve near the center. The calculation of the areas marked on Figure 4.6 thus indicates the variation in the percentage of orientations around the two fibres with respect to the random case (for which the percentages are equal to 5%). The choice of 5% was made so that the two areas considered do not overlap in the {111} pole figure. The way in which these percentages evolve with deformation and temperature will now be described.

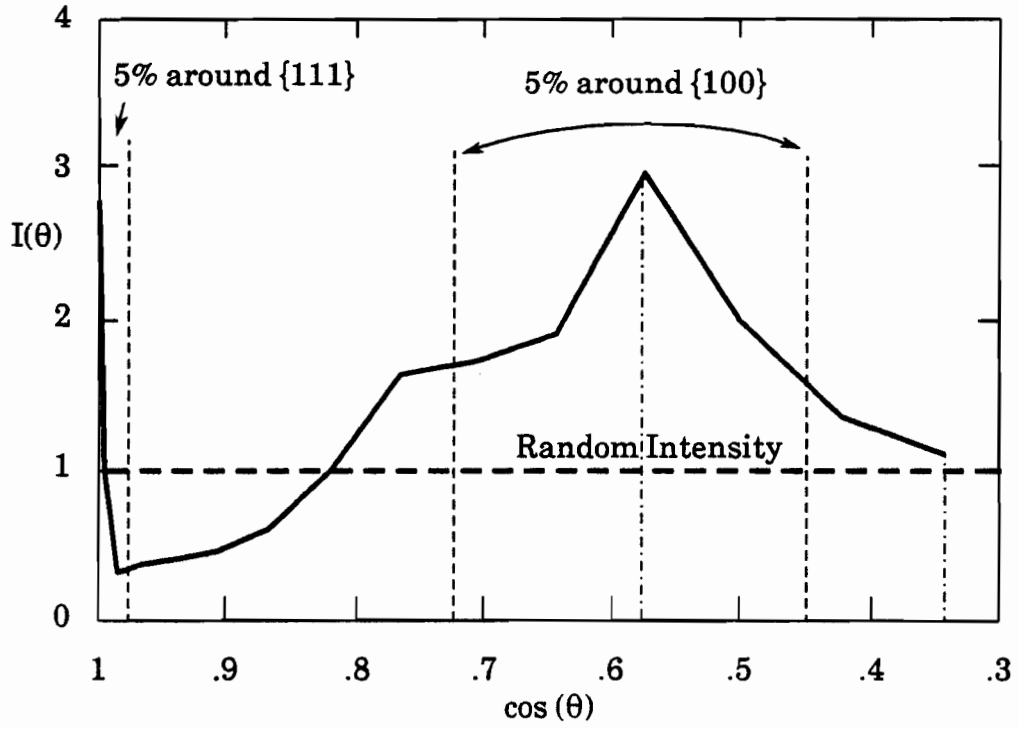

Figure4.6a. Intensity as a function of cos(θ) for the annealed state.

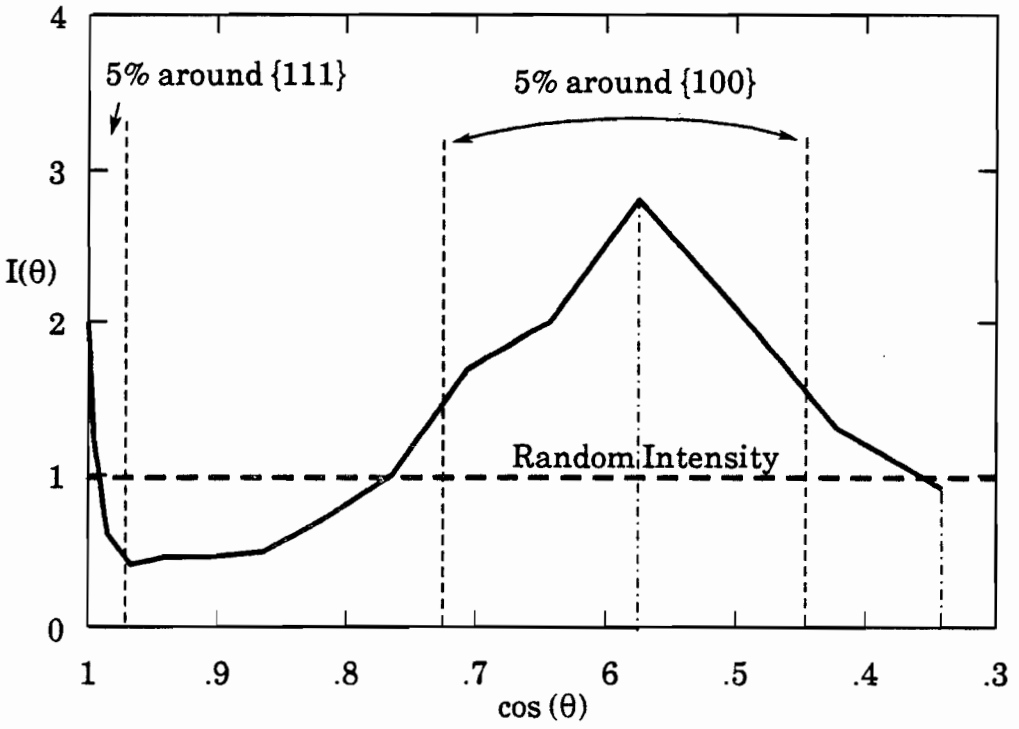

Figure 4.6b. Intensity as a function of cos(θ) for the cold deformed material; $\varepsilon = 0.8$.

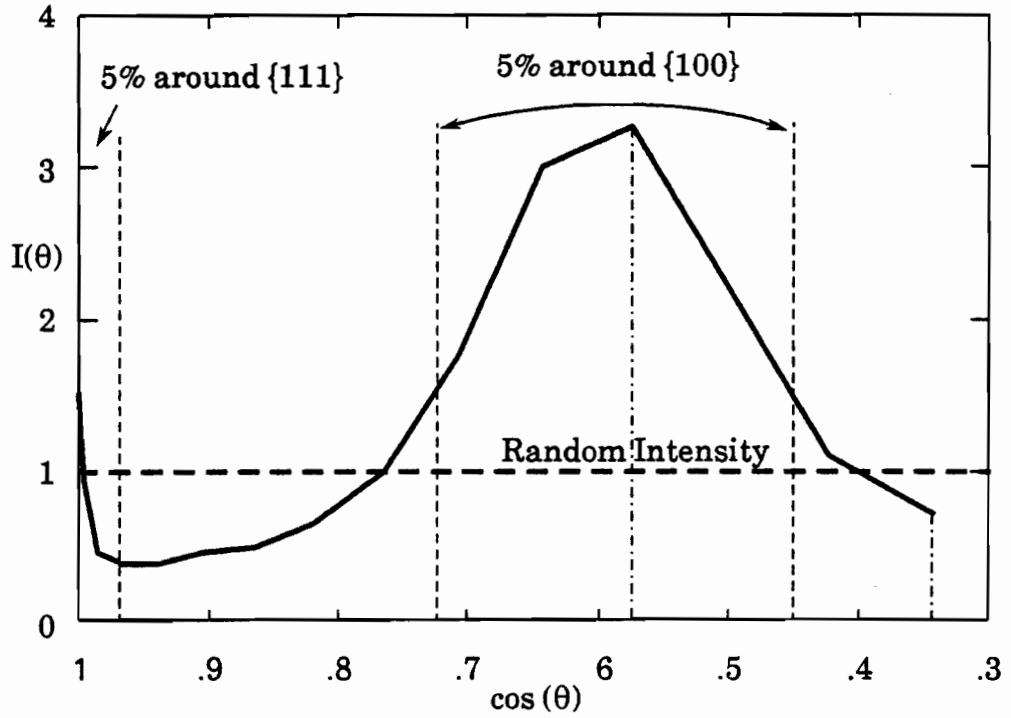

Figure 4.6c. Intensity as a function of cos(θ) for the warm deformed material; $\varepsilon = 0.8$.

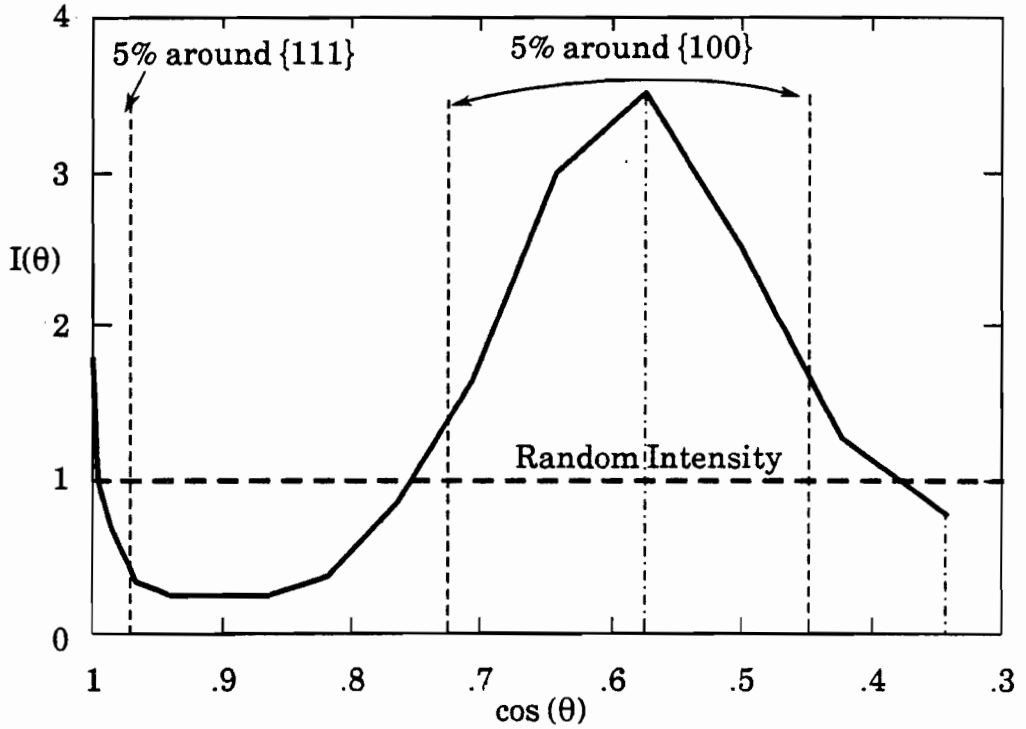

Figure 4.6d. Intensity as a function of cos(θ) for the warm deformed material; $\varepsilon = 2.16$.

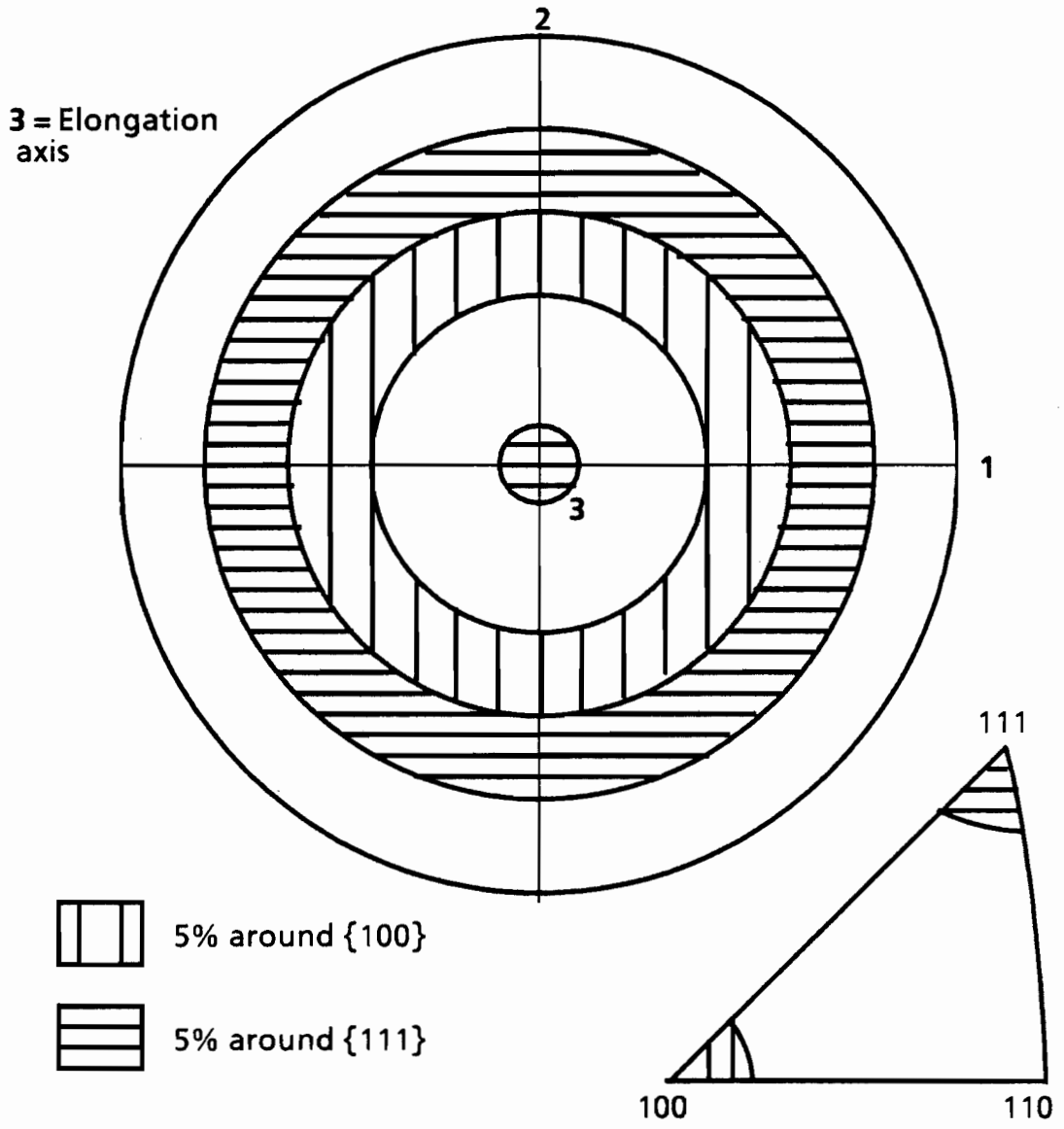

Figure 4.7. Definition of constant area around the {111} and {100} fibres.

Figure 4.6a corresponds to the initial texture. The calculated percentages near {111} and {100} are 2.9 and 11.3% (instead of 5% in the random case). There is a very narrow peak right in the center, as seen on the tranverse section, but this corresponds to a small percentage of poles in the volume considered. A large spread around {100} is also clearly visible on this figure.

Turning now to the the cold deformed material (Figure 4.5b), the calculated percentages are 3.5 and 11.3%, respectively. The {100} intensity has not changed but the {111} intensity has increased slightly with strain. The spread

around {100} is still large. This indicates that some of the orientations near {100} rotate slowly towards {111} instead of going to the {100} position, a development which would have resulted in the sharpening of the latter component.

In the hot deformed samples, by contrast (Figures 4.6c and 4.6d), a sharpening of the {100} is visible. The calculated percentages are 2.7% for the {111} fibre and 13.7% for the {100} fibre at $\varepsilon = 0.8$ and 2.8 and 14.6% at $\varepsilon = 2.16$. Most of the unstable orientations have rotated towards {100} in this case and the {111} intensity has remained almost constant.

IV.5. CONCLUSIONS

Three conclusions can be drawn from this brief description of the experimental work.

i) Because of the presence of a relatively strong initial texture, due to the previous deformation (and despite recrystallization), only small variations of texture could be detected. These resulted from the reorientation of the initially unstable orientations, i.e the ones located in the spread around the stable positions.

ii) The results indicate clearly that the hypothesis advanced in Chapter II of a stronger {100} fibre at elevated temperatures is correct. This component was referred to as the "brass" component for tension, since it is also the one found in the low SFE metals deformed at room temperature, frequently attributed in the latter case to twinning. During cold deformation, the observed trend is a sharpening of the {111} component, while during warm deformation, there is an evident sharpening of the {100} fibre.

iii) The results also suggest that the rotation of the grains towards stable positions takes place more quickly at higher temperatures. As a result, the amount of spread around the two fibres is greater at room temperature than at the higher temperature (compare Figures 4.6b and 4.6c).

CHAPTER V

THE THEORY OF RENOUARD AND WINTENBERGER

After having generalized the principles of the maximum (external) and minimum (internal) work rates, Renouard and Wintenberger [150] introduced another criterion for the selection of the active slip systems in the presence of ambiguities. This criterion states that the actual set of active slip systems is the one, among the possible ones, which minimizes the work hardening rate. Before reviewing their theory and reformulating it in a more convenient notation, it is first useful to consider the extent of the ambiguities involved.

V.1. EXTENT OF THE AMBIGUITIES PRESENT IN THE FC AND RC THEORIES

It was seen above that when 5, 4, or 3 strain rate components are imposed, the actual stress state in the crystal lies on a vertex or on a fourth or third order edge of the SCYS, respectively. It is also known that 6 or 8 slip systems are activated simultaneously at a vertex (where only 5 are needed). Similarly, the fourth order edges, at which a maximum of four independent slip systems can be found, are formed of 4, 5 or 6 hyperplanes and the third order edges, at which a maximum of three independent systems can be found, are associated with three or four systems [104,105]. Thus, even in the case of the RC theory, when a constant CRSS is taken for all the slip systems, some ambiguities are present in the choice of the latter. It is therefore of interest to consider the vertices and edges of the yield surface and to identify both the total number of systems, as well as the *number of combinations of independent slip systems*, associated with each.

The number of slip systems pertaining to the positive vertices and edges of the yield surface have been listed by Kocks et al. [105] and are reproduced in Tables 5.1 to 5.4 [5], which correspond to the $p = 5, 4, 3$ and 2 cases, respectively.

Type of vertex and no. of slip systems (n)	Number of vertices of given type	Total no. of comb.of 5 systems per vertex, C_n^5	Number of comb. of 5 indep. systems per vertex	Number of indep. 3 plane comb. Type (2,2,1,0) No. of slip directions			Number of indep. 4 plane comb. Type(2,1,1,1) No. of slip directions		
				3	4	5	3	4	5
A(8)	3	56	32[b]	8	8		8	8	
B(6)	4	6	6[b]	6					
C(8)	3	56	32[b]	8	8		8	8	
D(6)	12	6	4[b]		4				
E(8)	6	56	36[b]		12	4		12	8
Total No.	28[a] [105]		480[a][104]	72	168	24	48	120	48
Total No.			384[110,151, 152]	48	144	24	24	96	48

[a]Plus their opposites
[b]Ambiguities present

Table 5.1. Classification of the combinations of five independent slip systems under pentaslip (p = 5) conditions.

Type of edge and no. of associated slip systems (n)	Type of connecting vertices	Number of edges of given type	Total number of comb. of 4 systems per edge	Number of comb. of 4 independent systems	No. of slip directions		
					2	3	4
4A(4)	A-C	6	1	1x6			6
4B(6)	A-E	12	15	12x12[b]		120	24
4C(4)	B-C	12	1	1x12	12		
4D(4)	B-D	12	1	1x12		12	
4E(4)	B-D	12	1	1x12		12	
4F(4)	C-D	24	1	1x24		24	
4G(4)	C-E	6	1	1x6			6
4H(5)	D-E	24	5	4x24[b]			96
Totals		108[a]		312[a]	12	168	132

[a]Plus their opposites.
[b]Ambiguities present.

Table 5.2. Number of combinations of four independent slip systems under tetraslip (p=4) conditions.

(Here p refers to the number of strain rate components imposed or to the number of independent systems which are needed.†) To these, we have added:

† In Table 5.1, the vertices are classified in terms of the types of loading required for their activation. Type A is rendered operational by tension (or compression) along a cube direction (<100> tension), type B by tension (or compression) along a <111> direction, type C involves pure shear in a cube direction along a cube face ({100}<100> shear), type D corresponds to a combined state of stress and involves both shear and tension (or compression) ({100}<011> shear +<100> compression), whereas type E involves shear along a noncrystallographic direction ({100}<100> shear+{110}<110> shear). These five groups include all the 56 vertices of BH, but the latter workers subdivided the vertices into different categories, which depend instead on the number of slip systems associated with each vertex.

Type of edge and no. of associated slip systems (n)	Type and number of connecting vertices	Number of edges of given type	Number of comb. of 4 independent systems	No. of slip directions	
				3	2
3A(3)	A-C-D-E(4)	24	1x24	24	
3B(4)	A-E-A-E(4)	3	4x3[b]		12
3C(4)	A-E-D-E(4)	12	4x12[b]	48	
3D(3)	B-C-D(3)	24	1x24		24
3E(3)	B-C-D(3)	24	1x24		24
3F(3)	B-D-E-D(4)	24	1x24	24	
3G(3)	C-D-E(3)	24	1x24	24	
Totals		135[a]	180[a]	120	60

[a]Plus their opposites.
[b]Ambiguities present.

Table 5.3. Number of combinations of three independent slip systems under trislip (p = 3) conditions.

Type of edge and no. of associated slip systems	Number of connecting vertices	Number of edges of given type	Number of comb. of 2 independent systems	No. of slip directions in one comb.
2A(2)	8	12	1x12	2
2B(2)	6	6	1x6	1
2C(2)	8	12	1x12	2
2D(2)	5	24	1x24	1
2E(2)	8	12	1x12	2
Totals		66[a]	66[a]	

[a]Plus their opposites.

Table5.4. Number of combinations of two independent slip systems under bislip (p = 2) conditions.

i) The number of combinations of p independent systems associated with each yield condition. These combinations were determined by the method of Kocks et al. [105] as follows: for each of the $C^5_8=56$ or $C^5_6=6$ possible combinations associated with Table 5.1, the transformation matrix for passage from the 5 dimensional space in which the stress and strain rate tensors are defined (see Appendix 2) to that associated with the set of 5 slip systems being considered is drawn up; then the 5x5 determinant of this matrix is calculated and only the combinations for which the determinant is different from zero are retained. This transformation matrix is expressed through equation A4.1 in terms of the m_{ij} coefficients.

ii) The number of different slip directions in each set of 5, 4, 3 or 2 independent systems. These numbers will be useful in the treatment of cross-slip.

In Table 5.1 are listed the number of combinations of 5 slip systems (without regard to independence) that can be selected from the 6 or 8 available, as well as the number of combinations of 5 *independent* slip systems [104]. In this table, we distinguish, as did Taylor [4], between: i) those that involve 2, 2, 1 and 0 systems on each of the 4 different slip planes; and ii) those that involve 2, 1, 1 and 1 slip systems on each of the four planes. This distinction gives us the number of slip planes associated with each combination. The actual number of possible combinations is thus 4 or 6 in the case of the D and B vertices, 32 for the A and C types and 36 for the E vertices. Finally, the total number of independent combinations is 480.

This result is at first sight surprising because Taylor [4] in 1938 found only 216; Later, he modified this to 384 [110], a figure subsequently verified by Hershey [151] and others [152]. The reason for the difference is that the earlier workers considered only 12 systems instead of 24, allowing the appropriate $\dot{\gamma}^s$ shear rates to be negative when necessary. They then determined the total number of combinations of 5 systems $C^5_{12}=792$, from which they subtracted the combinations which are not independent, leaving 384. By contrast, by following the Bishop and Hill approach here, we only permit positive shearing on each slip system ($\dot{\gamma}^s$ positive), and compensate by considering both the "positive" and "negative" systems (i.e. those which have the same n but opposite b vectors, or the same b and opposite n vectors, which is equivalent),

since a particular system and its opposite do not belong to the same vertex. The exact source of discrepancy lies in the way in which the vertices of class A (1,2 and 3) and class C (8, 9 and 10) are related. Vertices 1 and 8 are composed of different facets in the Kocks et al. [105] notation, and therefore have different sets of slip systems associated with them. Similar remarks apply to vertices 2 and 9, and 3 and 10. By contrast, when no account is taken of the direction of the vectors n and b (definitions of Taylor [4] and Hirth and Lothe [152]), the same sets of slip systems are associated with vertices 1 and 8 (and in turn with vertices 2 and 9, and 3 and 10). Thus there are 96 different combinations of independent slip systems associated with the A set of vertices and a further 96 with the C set. When no distinction is made between positive and negative shearing on a given slip plane [110,151,152], the A and C sets can no longer be distinguished, and the 96 combinations lost in this way reduce the total number apparently available from 480 to 384.

The number of combinations of five independent systems listed in Table 5.1 is actually an upper limit to the true number of possible combinations because of the need to respect the normality rule. The latter consideration requires the five dimensional strain rate vector $\dot{\varepsilon}$ to lie inside the cone of normals corresponding to the five slip systems of the combination being evaluated (i.e. within the reduced cone of normals associated with the smaller number of slip systems). Otherwise, negative values of the shear rates $\dot{\gamma}^s$ are involved, which are not admissible. In the case of a vertex associated with 6 slip systems (B or D types), although there are 6 or 4 possible combinations of 5 independent systems, for a given $\dot{\varepsilon}_{ij}$, there are in fact only 2 possible combinations [153]. These two combinations will give in turn two "extreme" rotations, all the intermediate rotations being equally valid. For the A, C and E type vertices, the actual number of possible combinations cannot be given here since it depends on the specific orientation of the grain and varies from case to case. A possible maximum obtained from a statistical evaluation of all the cases treated would be approximately equal to half the total number of possible solutions. (Analogous considerations apply to the combinations of four and three independent systems described below).

With regard to the $p=4$ case, it can be seen from Table 5.2 that ambiguities are present for 2 types (out of 8) of the fourth order edges. Again here, the

independence of the four slip systems was tested by calculating all the determinants of the 4x4 submatrices of the 4x5 matrix (defined by equation A4.1) until one was found to be non-zero [104]. There are 312 different combinations of 4 independent slip systems under p=4 conditions (and their opposites); 240 of these are associated with edges where ambiguities are present.

Turning now to the p=3 case, it can be seen from Table 5.3 that for 2 types of third order edges, among the 7 available, ambiguities are still present. 3 combinations are associated with each 3B edge and 12 with each 3C edge. These ambiguities thus concern 60 out of 135 combinations of 3 independent systems.

The case p=2 (Table 5.4) does not involve any ambiguities and is included for completeness only. It involves a total of 66 edges and thus of 66 combinations.

In summary then it can be said that the selection of independent systems involves ambiguities at: i) *all* the vertices associated with the p=5 case; ii) 36 of the 108 edges associated with the p=4 case; iii) 15 of the 135 edges associated with the p=3 case; and iv) *none* of the p=2 edges.

These results indicate that the ambiguities present in the RC theory are far less numerous than in the FC theory. The problem of selection can thus be considered to be of minor importance since it was seen above that the RC theory applies especially well to the case of large deformations. Moreover, it can be argued that the ambiguities have little physical meaning for a real material since they can be removed with the aid of one of the following assumptions:

i) the introduction of rate sensitivity,
ii) the use of a realistic hardening law.

The rate sensitivity of the material can be thought of as a useful parameter to represent high temperature deformation. However, the introduction of this coefficient in a model does not generally produce new texture components; it only changes the rate of formation of these components [154]. Thus, it cannot by itself account for the differences observed between materials deformed at low

and at high temperatures. Furthermore, it will be seen below that the introduction of the RW criterion also influences the rate of formation of textures and can thus be seen as a kind of rate sensitive criterion, but one which is based on energetic considerations in this case.

Using a realistic hardening law is certainly one of the physically most appropriate ways of improving existing models; unfortunately, this is a very complex alternative, and is sometimes almost impossible to carry out. Some very simple hardening laws, apart from the Taylor hardening law, will be examined in the chapters that follow, especially in the treatment of cross-slip. The use of a complex and more realistic law involves measurements of hardening parameters which must be very precise, and are always subject to reservation. Moreover, the values of these parameters change from sample to sample, depending on the previous deformation history of the material, and are thus very hard to determine with accuracy. Once the parameters have been determined, the introduction of the hardening law in a model can lead to computations so complex that simplifications are essential before any calculations can be performed at all and it then becomes difficult to determine if the model is still realistic.

Thus, the introduction of a further criterion for the removal of ambiguities in a non rate sensitive model (in which the hardening of the systems is assumed to be isotropic) can be seen as a way of introducing a kind of complex hardening law in a simplified way. Minimizing the work hardening rate of the material can also be seen as a qualitative way of representing the rate sensitive response of a material.

V.2. THE SECOND ORDER PLASTIC WORK CRITERION

V.2.1. THE THEORY OF RENOUARD AND WINTENBERGER

The removal of the ambiguities concerning slip system selection inherent in the power minimization and maximization methods described in Appendix 4 involves a further optimization, which is summarized below in terms of the generalized Taylor and Bishop and Hill theories [118,150]. The second

operation consists of selecting one slip system combination from all those available to accommodate the prescribed strain rate as follows. Let the prescribed strain rate tensor operate during a time dt; for each set of slip systems, this leads to an infinitesimal crystal rotation. Denoting as $\dot{W}_1$ and $\dot{W}_2$ the work rates associated with the prescribed components of strain rate $\dot{\varepsilon}_{ij}$ before (state 1) and after (state 2) the rotation, respectively, the method consists of finding the slip system combination which minimizes $\dot{W}_2$, and therefore also minimizes $\dot{W}_2 - \dot{W}_1 = d\dot{W}$.

In terms of the present notation, the RW analysis can be described as follows. Assuming that the critical slip systems (i.e. those for which $\tau^s = \tau_c{}^s$) remain the same in state 1 and 2 (whether they are active, $\dot{\gamma}^s \neq 0$, in both states, or not), the difference $\dot{W}_2 - \dot{W}_1$ can be written as

$$\dot{W}_2 - \dot{W}_1 = d\dot{W} \tag{5.1}$$

with

$$\dot{W}_1 = \sum_s (\tau_c^s - \tau_0^s) . \dot{\gamma}^s \tag{5.2}$$

and

$$\dot{W}_2 = \sum_s (\tau_c^s + d\tau_c - \tau_0^s - d\tau_0^s) . (\dot{\gamma}^s + d\dot{\gamma}^s) \tag{5.3}$$

Here the summation is carried out over the critical systems, and thus involves the above assumption regarding the "continuity of criticality". In equation 5.3, $\tau_0{}^s = \sigma''_{ij} m^s{}_{ij}$ (equation A4.4) is the *prescribed* component of the shear stress. In terms of the BH analysis for the $p=5$ (FC) case, this means that no change of vertex is permitted, which is always possible by choosing a small enough strain increment. (Similarly, in the case of the RC theory, this means that no change of the stress state expressed in the crystal system is allowed.)

An exception to the above generalization occurs when the strain rate vector is exactly at the edge of the cone of normals of the active vertex, i.e. it has moved to a fourth ($p=4$) or lower ($p \leqq 3$) order edge. Under these conditions, two (or more) vertices are active simultaneously (see Tables 5.2-5.4). This exception does not need to be addressed here because, in such a case, only the slip systems common to the two or more vertices are active (i.e. the systems associated with the edge of the yield surface). There are always less than five independent slip

systems forming such edges, thus there is almost no ambiguity involved in this case. In equation 5.3, $d\tau_c^s$ represents the change in the critical resolved shear stress τ_c^s due to work hardening on the operating systems during deformation from state 1 to 2, $d\tau_0^s$ the change in the resolved shear stress acting on each slip system attributable to the *prescribed* stresses, and $\dot{\gamma}^s + d\dot{\gamma}^s$ the values of the shear rates *on the original set of slip systems* after rotation of the crystal (state 2). The latter change by amounts $d\dot{\gamma}^s$ because of the grain rotation produced by the shear rates $\dot{\gamma}^s$ associated with state 1.

In a similar way, the prescribed strain rate components are given by

$$\dot{\varepsilon}'_{ij}(1) = \sum_s \dot{\gamma}^s m_{ij}^s \quad (p \leq 5 \text{ equations with } \dot{\gamma}^s > 0) \tag{5.4}$$

and

$$\dot{\varepsilon}'_{ij}(2) = \sum_s (\dot{\gamma}^s + d\dot{\gamma}^s).(m_{ij}^s + dm_{ij}^s) \tag{5.5}$$

where $dm^s{}_{ij}$ refers to the changes in the components of the generalized Schmid factor brought about by the grain rotation taking place between states 1 and 2.

We now evaluate $d\dot{W}$ by subtracting equation 5.2 from equation 5.3

$$d\dot{W} = \sum_s (d\tau_c^s - d\tau_0^s)\dot{\gamma}^s + \sum_s (\tau_c^s + d\tau_c^s - \tau_0^s - d\tau_0^s)\, d\dot{\gamma}^s \tag{5.6}$$

Bearing in mind that the $\dot{\varepsilon}'_{ij}$ are the same for both states 1 and 2, equations 5.4 and 5.5 can be combined to give

$$0 = \sum_s \dot{\gamma}^s dm_{ij}^s + \sum_s d\dot{\gamma}^s.(m_{ij}^s + dm_{ij}^s) \tag{5.7}$$

Multiplying equation 5.7 by σ'_{ij} and summing over i and j leads to

$$\sum_s (\tau_c^s - \tau_0^s)\, d\dot{\gamma}^s = -\sum_s \sigma'_{ij}\, dm_{ij}^s (\dot{\gamma}^s + d\dot{\gamma}^s) \tag{5.8}$$

Equations 5.6 and 5.8 can now be combined and simplified, after recognizing that $d\tau_0^s = \sigma''_{ij}\, dm^s{}_{ij}$ (the σ''_{ij}, being prescribed, do not change between states 1 and 2), so that

$$d\dot{W} = \overbrace{\sum_s (d\tau_c^s - \sigma_{ij}\, dm_{ij}^s)\dot{\gamma}^s}^{(I)} + \overbrace{\sum_s (d\tau_c^s - \sigma_{ij}\, dm_{ij}^s)\, d\dot{\gamma}^s}^{(II)} \tag{5.9}$$

In this relation, the first term on the RHS (I) is composed of quantities that depend only on the characteristics of state 1, i.e. on the actual combination of slip systems being considered. The second term (II) depends, through the values of $d\dot{\gamma}^s$, on the characteristics of state 2. However, as it involves the products of increments, it will not be considered further here. The "real" solution can therefore be found by minimizing

$$d\dot{W} = \sum_s (d\tau_c^s - \sigma_{ij}\, dm_{ij}^s)\, \dot{\gamma}^s \tag{5.10}$$

If one assumes isotropic hardening, the only term which needs to be minimized (with respect to the alternative sets of $\dot{\gamma}^s$) is

$$d\dot{W} = \sum_s -\sigma_{ij}\, dm_{ij}^s\, \dot{\gamma}^s \tag{5.11}$$

Renouard and Wintenberger performed this optimization in the following way. They expressed $d\dot{W}$ (equation 5.11) in terms of *all* the possible systems, n $\dot{\gamma}^s$. In a similar manner, they expressed the constraints (equation 5.4) as a set of p equations. They then solved for $d\dot{W}$ and obtained a function of $(n\text{-}p)$ $\dot{\gamma}^s$ terms. Finally, the minimum value of this expression, which is a function of 1, 2, or 3 variables depending on the "order" $(n\text{-}p)$ of the ambiguity, was found using for example the linear programming technique. For this purpose, the σ_{ij} are determined from the coordinates of the edge or vertex activated in state 1, and the $dm^s{}_{ij}$ from the rotations produced by each of the slip system combinations that can operate between states 1 and 2.

V.2.2. RW CRITERION EXPRESSED IN TERMS OF TAYLOR FACTOR MINIMIZATION

In the present investigation, we have used the RW criterion in a somewhat modified form by incorporating the following definition of the Taylor factor

$$M = \frac{\sigma'_{ij}\, \dot{\varepsilon}'_{ij}}{\tau_c\, \dot{\bar{\varepsilon}}} = \frac{\sum_s (\tau_c - \tau_0^s)\, \dot{\gamma}^s}{\tau_c\, \dot{\bar{\varepsilon}}} = \frac{\dot{W}}{\tau_c\, \dot{\bar{\varepsilon}}} \tag{5.12}$$

In this expression, $\dot{\bar{\varepsilon}}$ is the von Mises equivalent strain rate and $\dot{W}$ is the work rate associated with the active vertex (i.e. either the maximum value of

$\dot{W} = \sigma'_{ij}\dot{\varepsilon}'_{ij}$ calculated for all the different vertices or the minimum value of $\Sigma(\tau_c - \tau_0{}^s)\dot{\gamma}^s$ calculated for all the possible combinations of slip systems).

The basic computer programs used to simulate an FC or RC calculation were developed at McGill by Canova [104]. These programs are described briefly in Appendix 5; they dealt with ambiguities by taking the average of all possible combinations. In the present work, they were modified to incorporate the RW criterion as follows: we begin by selecting the active vertex in state 1 and its associated Taylor factor M_1. To this vertex correspond N possible combinations of p independent systems, as described above. The shear rates, $\dot{\gamma}^s$, pertaining to the slip systems of each possible combination are calculated, from which both the grain rotation (according to the method presented in Appendix 1) as well as the new Taylor factor are deduced. This is done by calculating the new value of σ'_{ij}, and therefore of $\sigma'_{ij}\dot{\varepsilon}'_{ij}$, where the yield surface has now been rotated slightly. Each of the N possible combinations is considered in this way and the corresponding new grain orientation and new Taylor factor M_2 are evaluated in turn. The slip system combination which leads to the minimum value of M_2 is then selected as the solution for state 1 of the deformation.

As indicated above, this is equivalent to minimizing $\dot{W}_2 = \dot{W}_1 + d\dot{W}$ for a finite number of alternative solutions, each of which is characterized by the same value of $\dot{W}_1$. The various "solutions" to be tested correspond to different locations of the active vertex in state 2, and $\dot{W}_1$ and $\dot{W}_2$ can be expressed in terms of the respective Taylor factors for this situation. The Taylor factor minimization carried out as described above results in the choice of the lowest possible value for $dM/d\bar{\varepsilon}$, where $d\bar{\varepsilon}$ is the equivalent strain increment. Defining the work hardening rate $d\bar{\sigma}/d\bar{\varepsilon}$ for a given grain as

$$\frac{d\bar{\sigma}}{d\bar{\varepsilon}} = M\frac{d\tau_c}{d\bar{\varepsilon}} + \tau_c\frac{dM}{d\bar{\varepsilon}} \tag{5.13}$$

where $\bar{\sigma}$ is the von Mises equivalent stress, and assuming that $d\bar{\tau}_c / d\bar{\varepsilon}$ is independent of the slip system combination selected, this is equivalent to selecting the combination that leads to the lowest possible rate of macroscopic work hardening. The lowest possible work hardening rate (positive or negative) signifies in turn that $d^2W / d\bar{\varepsilon}^2$ is a minimum, which is why Renouard and

Wintenberger referred to their theory as the minimization of the "second order term for the plastic work".

One advantage of calculating all the possible rotations and selecting the one which gives the lowest value of M_2 is that in the presence of any remaining ambiguities, the average can still be taken, whereas if linear programming is used, any one of the possible solutions will simply be selected by the program. The advantage of the present procedure is that the validity of the RW hypothesis can be tested directly without having to worry about the random choices performed by a particular algorithm.

Some predictions obtained with this method will now be presented for the cases of both fully and partially constrained deformation (of single crystals as well as polycrystals). They are compared to experimental results as well as to the predictions obtained from other models: i) the classical FC or RC model (with averaging on all possible rotations) and ii) the rate sensitive model developed by Canova and Kocks [144].

V.3. COMPARISON WITH EXPERIMENTAL RESULTS OF THE VARIOUS PREDICTIONS FOR THE CASE OF FULLY CONSTRAINED DEFORMATION

Since the number of ambiguities is maximum in the $p=5$ case, it is useful to test the validity of the RW criterion for this condition. Two different cases will be considered here: the fully constrained deformation of single crystals and the fully constrained deformation of polycrystals in the case of tension.

V.3.1. PLANE STRAIN COMPRESSION OF SINGLE CRYSTALS

The experimental work used for comparison was performed by Driver and co-workers [118,122,123,155]. It involved the channel die compression of tricrystals prepared in such a way that the central crystal was prevented from shearing by the two crystals enclosing it. Under these conditions, the central grain deforms in very nearly pure plane strain compression, i.e. the

deformation is completely prescribed, and only the two plane strain components of the strain rate tensor are non-zero. Driver and co-workers measured the orientation changes of the central grain in five such crystals at different stages during the deformation up to $\bar{\varepsilon} = 1$. They also performed calculations using the RW criterion [150], but they were based on the principle of minimum internal work rate, as described in Section V.2.1, and employed the linear programming technique.

In our calculations, the measured initial orientations of the five crystals were employed, and simulations of grain rotation were performed using three different methods for resolving the problem of the ambiguities described above; i.e.:

1) the classical Bishop and Hill theory applied to the calculation of grain rotations by averaging the rotations produced by the alternative sets of slip systems belonging to a particular ambiguity class;
2) the RW criterion in the present modified form in which Taylor factor minimization is carried out;
3) the rate sensitivity method, in the version developed by Canova and Kocks [144].

The results obtained in this way are presented in Figures 5.1 to 5.5 for the five tricrystals in the form of two inverse pole figures, the first showing the path followed by the compression axis X_3, and the second that followed by the elongation axis X_2.

The first two grains (Figures 5.1 and 5.2) represent the case where there is little difference between the predictions of the three methods. This is because they concern the operation of 6-fold vertices of the B type, so that there is little ambiguity during most of the experiment. In such cases, the Bishop and Hill theory would normally call for a 6-fold ambiguity of order n-p = 1 (Table 5.1); however, because of the restrictions imposed by the normality rule [153], this is reduced to a 2-fold ambiguity, to give only two different possible rotations. In the specific examples under consideration here, these two rotations were very close to each other [118]. Thus the averaging calculation led to a result which was near the one obtained by choosing that rotation (out of two) which minimized the Taylor factor after a small rotation (RW method) and by the rate

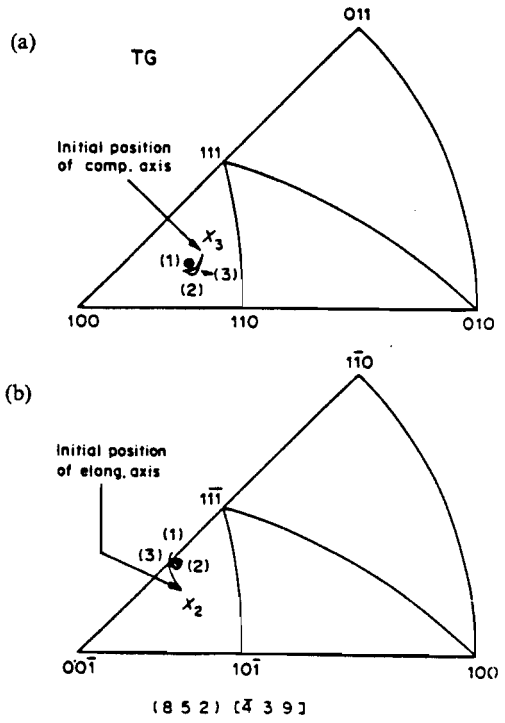

Figure 5.1. Predicted and experimentally observed rotations of crystal TG during plane strain compression ($\bar{\varepsilon}=1$).

The following legend applies to Figures 5.1 to 5.5:

a) motion of the X_3 (compression) axis,
b) motion of the X_2 (elongation) axis.

(1) p=5; averaging
(2) p=5; RW
(3) p=5; rate sensitivity.

In Figures 5.1 to 5.5, the approximate Miller indices corresponding to the orientations of grains studied are also indicated.

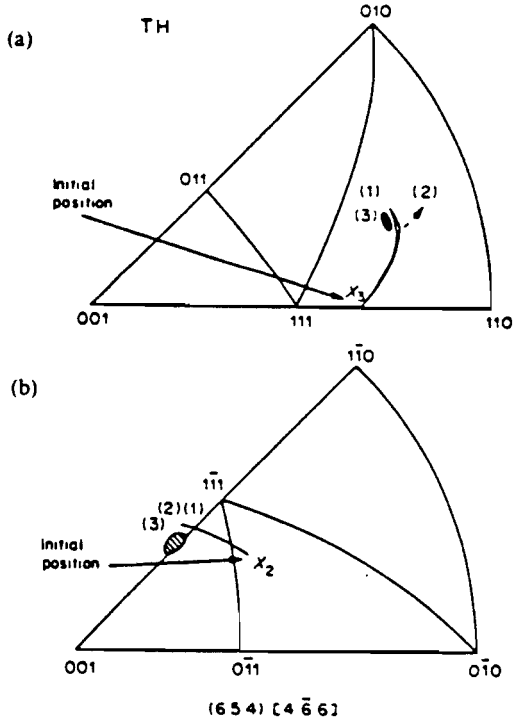

Figure 5.2. Predicted and experimentally observed rotations of crystal TH during plane strain compression ($\bar{\varepsilon}=1$).

sensitive method as well. All three predictions are therefore in good agreement with the experimental results in these two cases.

In Figure 5.3, a slightly larger difference can be seen between the three predictions, which arises because this case involves the activation of 8-fold vertices (types A and E, Table 5.1, in alternation). According to the BH method, there is a maximum 32- or 36-fold ambiguity of order $n-p=3$, so that the various possible rotations differ considerably from each other. The present averaging method, by taking the mean of the alternative rotations, reduces considerably the differences between the BH prediction and those of the other two methods. In this case, there is a detectable difference between the orientation changes called for by the RW method and those of the rate sensitive (RS) approach, indicating that these two techniques do not always select the same combination of slip systems. Nevertheless, as in the previous two examples, all three predictions are in good agreement with the experimental rotations.

In Figures 5.4 and 5.5, two cases are illustrated in which the use of the RW criterion leads to distinctly better predictions than are obtained from either of the other two methods. Figure 5.4 concerns the activation first of 8 slip systems (vertex type C) and then, after $\bar{\varepsilon}=0.3$, of 6 (vertex type B). The activation of 8 slip systems frequently leads to large indeterminacies in the rotation; in the present case, this is considerably reduced because only four slip systems are actually active (i.e. for which $\dot{\gamma}^s \neq 0$). This is why the three predicted paths coincide at the beginning of the deformation. At larger strains, when a 6-fold vertex is activated, although only two different rotations are possible, the differences between the three sets of predictions continue to increase. It is also evident from Figure 5.4 that both the averaging (BH) and rate sensitive (RS) models lead to rotations that are smaller than the experimental ones, the RS rotations diverging substantially from those reported (especially for the X_2 axis). By contrast, the RW predictions are in excellent agreement with the experimental observations.

In Figure 5.5, once again, the averaging (BH) technique and the RS method lead to rotations that are smaller than those of the RW method. In this case, as before, we are first concerned with an 8-fold vertex (type C) and then with a 6-

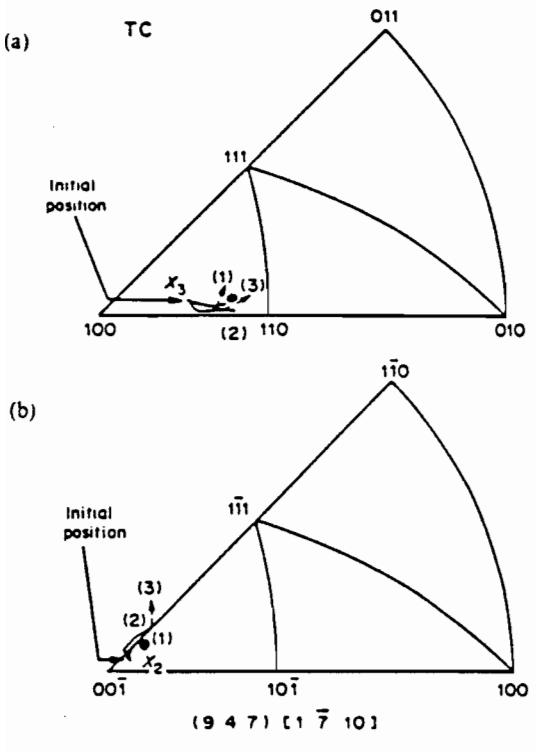

Figure 5.3. Predicted and experimentally observed rotations of crystal TC during plane strain compression ($\bar{\varepsilon}=1$).

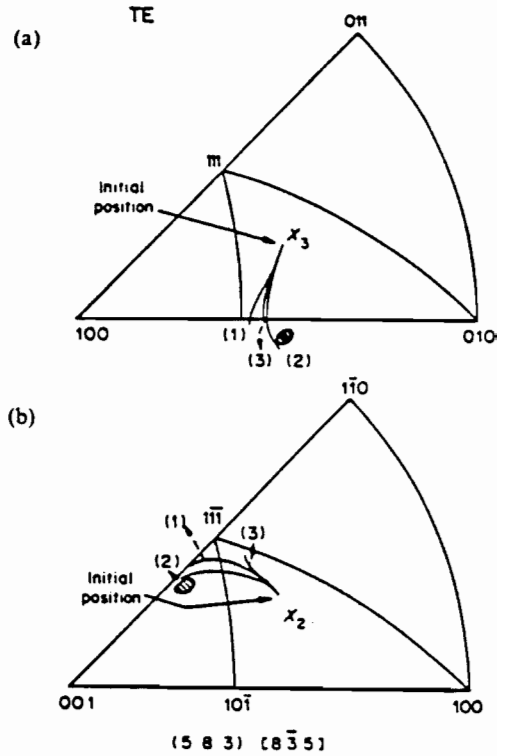

Figure 5.4. Predicted and experimentally observed rotations of crystal TE during plane strain compression ($\bar{\varepsilon}=1$).

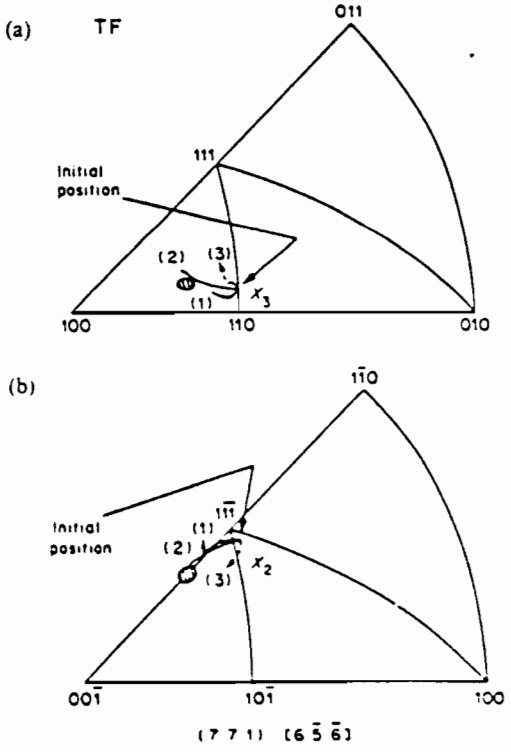

Figure 5.5. Predicted and experimentally observed rotations of crystal TF during plane strain compression ($\bar{\varepsilon}=1$).

fold vertex (type B). Unlike the case of Figure 5.4, the differences between the possible rotations are significant during the entire experiment and simple averaging leads to erroneous results. Moreover, the RS method seems to select active slip systems which differ from the observed ones over an appreciable range of the deformation. By contrast, as in the case of Figure 5.4, the RW simulation leads to orientation changes which are consistent with those observed.

From these five examples, several tentative conclusions can be drawn regarding the effect of the indeterminacy in slip system selection and the validity of the three alternative methods:

i) First, it is apparent that the magnitude of the uncertainty in the rotations does not depend solely on the order $n-p=3$ or 1 of the indeterminacy (e.g. whether there are 32 or 36 possible combinations at an 8-fold vertex or 6 possible combinations at a 6-fold vertex), but also on the detailed orientation of the grain.

ii) Although the averaging method can sometimes compensate for the indeterminacy, particularly when the range of alternative rotations is small (as in Figure 5.3), it can also increase the error by restricting the extent of the orientation change (Figure 5.5).

iii) In the cases where the indeterminacy is large and not substantially reduced by the averaging technique (Figures 5.4 and 5.5), only the RW treatment among those compared leads to results which are in satisfactory agreement with the observations.

It should be added that a new version of the RS model has now been prepared by Canova [156]. He has stated that there was an error in the first version and that the second is improved and more likely to be correct. Unfortunately, the second version has not yet been published and so could not be tested here. Nevertheless, it can be expected to lead to results which differ from those presented in this work; such new predictions may indeed be in better agreement with the experimental results.

This preliminary study allows us to conclude that the RW criterion gives good results in the case of high SFE materials deformed at room temperature.

The method also seems promising for the simulation of high temperature textures. One way of checking this possibility is to predict the fibre texture obtained in axisymmetric tension with a Taylor model and then to compare the theoretical results obtained with (i) the averaging technique and (ii) the RW criterion with experimental textures.

V.3.2. THE FULLY CONSTRAINED DEFORMATION OF POLYCRYSTALS

To test the validity of the RW criterion in a calculation for polycrystals, it was decided to apply some Taylor type calculations to axisymmetric tension. This choice was motivated by two reasons: i) it has recently been shown [157] that the grain shape arguments on which the RC theory is based prevent the relaxation of *any* strain rate components in tension and thus imply that tension should only be treated with the FC model; and ii) it has also been shown [4] that, for a random distribution of grain orientations, the extent of the ambiguities is large in tension (see next chapter).

The inverse pole figures obtained after strains of $\bar{\varepsilon} = 0.5$ and 1 are presented in Figure 5.6. The results for two different models are shown: those pertaining to a classical FC calculation in which the average is taken over all possible rotations (FC + AV), and an FC calculation in which the ambiguities are removed with the RW criterion (FC + RW). The corresponding {111} pole figures are illustrated in Figure 5.7 and the average densities of the {111} poles along a radius of the pole figures in Figure 5.8.

The following remarks can be made regarding these results:

i) It can be seen from Figures 5.6a and 5.6b, that the FC + AV calculation gives results which are in good agreement with experimental observations for intermediate to high SFE materials deformed at room temperature. If the numbers of grains in a constant volume around the {100} and {111} fibres (out of a total of 950) are calculated from Figure 5.8, the percentage of the {100} fibre obtained with the FC + AV calculation is seen to be approximately 22%. This value is intermediate between the ones found experimentally for copper and aluminum (see Figure 2.2).

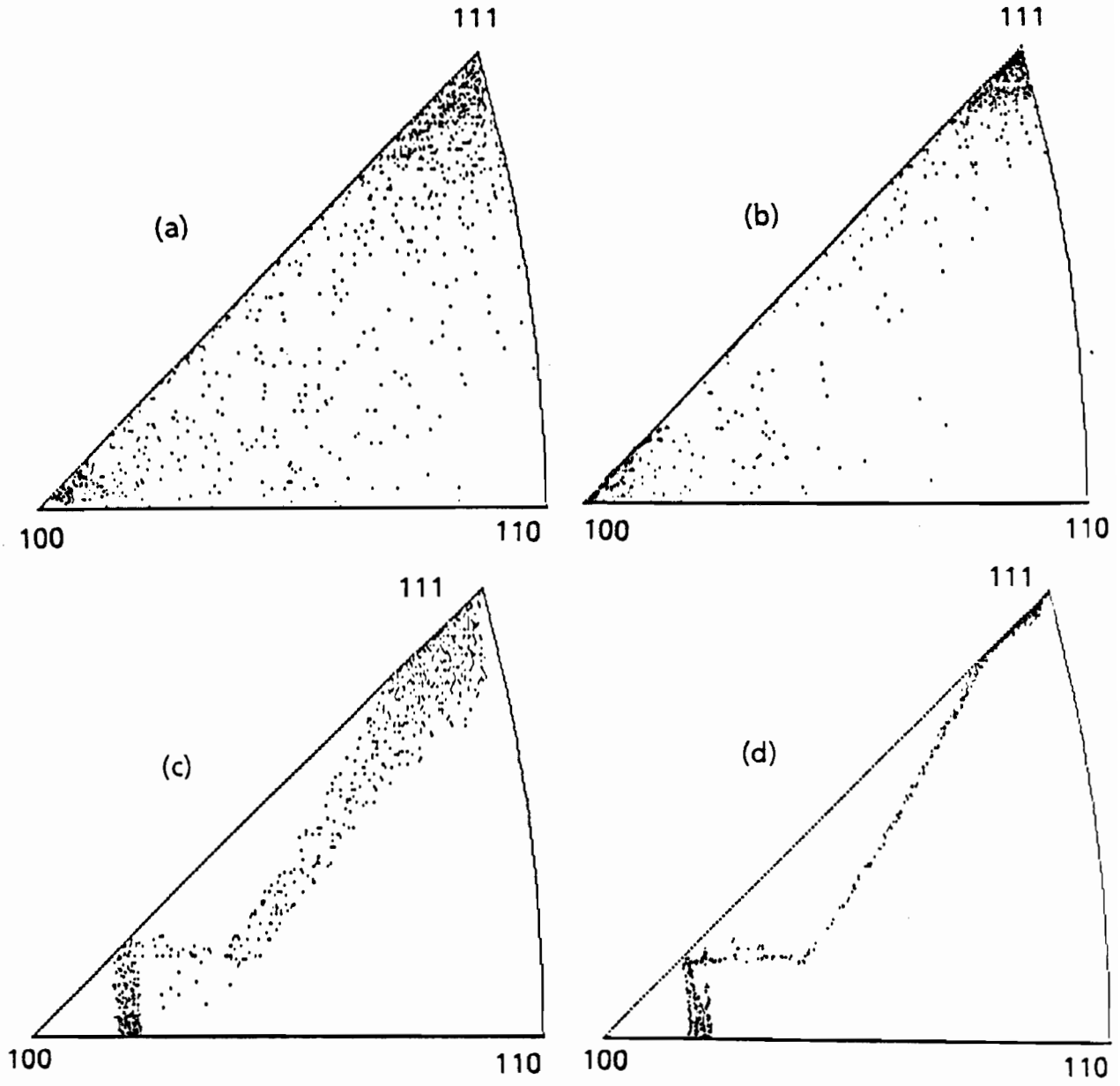

Figure 5.6. Inverse pole figures of the textures predicted for an initially random polycrystal deformed in axisymmetric tension; a) $\bar{\varepsilon}=0.5$, FC+AV, b) $\bar{\varepsilon}=1$, FC+AV, c) $\bar{\varepsilon}=0.5$, FC+RW, and d) $\bar{\varepsilon}=1$, FC+RW.

ii) Also of interest is the spread around these two fibres in the FC+AV calculation (see Figures 5.7a and 5.7b). It is apparent that the averaging procedure tends to reduce the rotation rates.

iii) Turning now to the results obtained with FC+RW (Figures 5.6c and 5.6d), it can be seen that the {100} fibre is completely absent and is replaced by

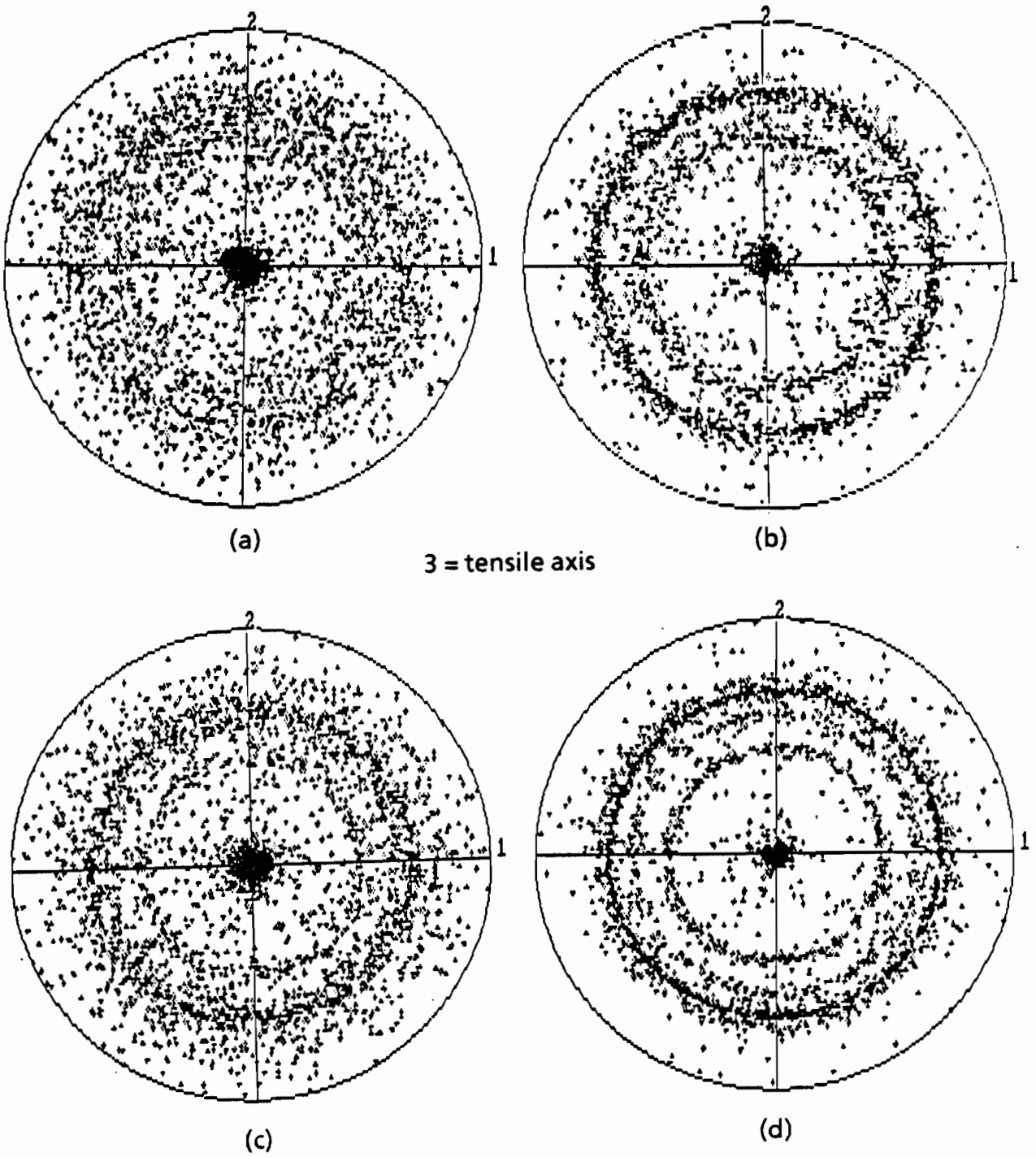

Figure 5.7. {111} pole figures corresponding to the textures represented in Figure 5.6; a) $\bar{\varepsilon}=0.5$, FC+AV, b) $\bar{\varepsilon}=1$, FC+AV, c) $\bar{\varepsilon}=0.5$, FC+RW, and d) $\bar{\varepsilon}=1$, FC+RW.

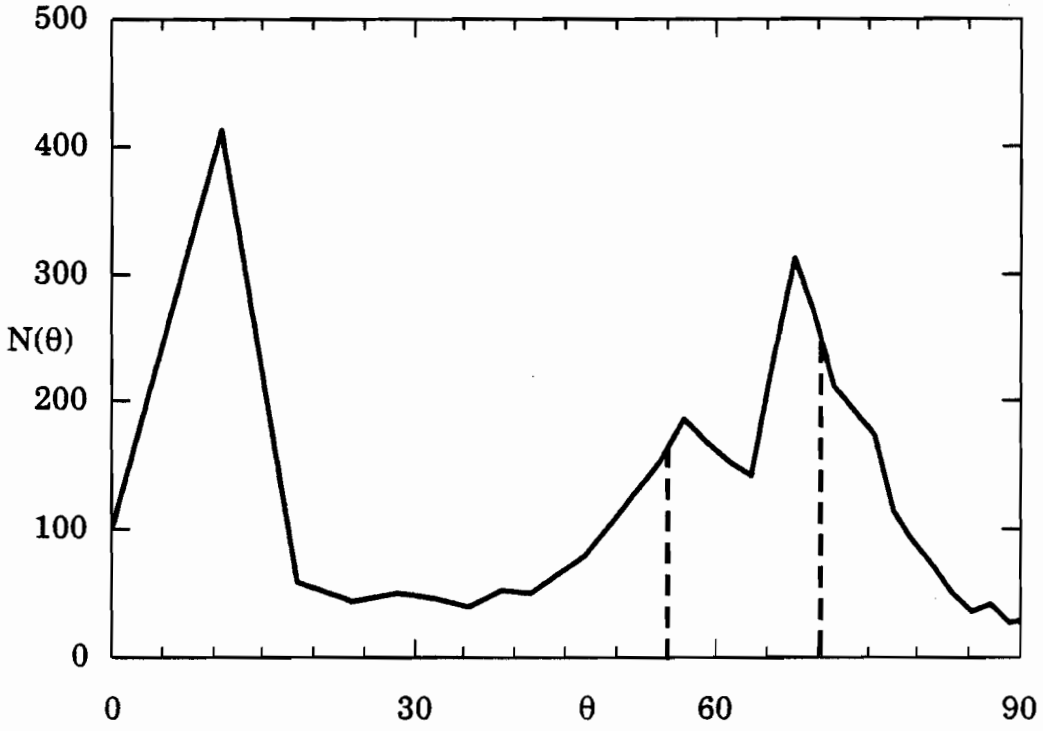

Figure 5.8a. Number of {111} poles as a function of θ at ε=0.5 in an FC+AV calculation.

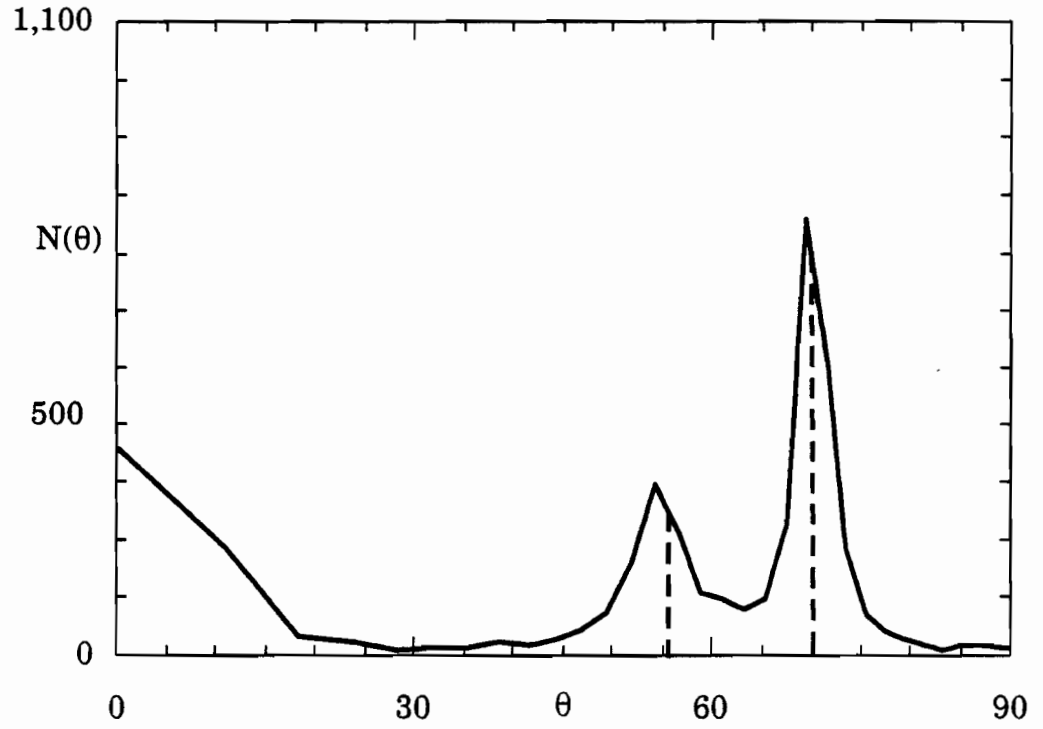

Figure 5.8b. Number of {111} poles as a function of θ at ε=1 in an FC+AV calculation.

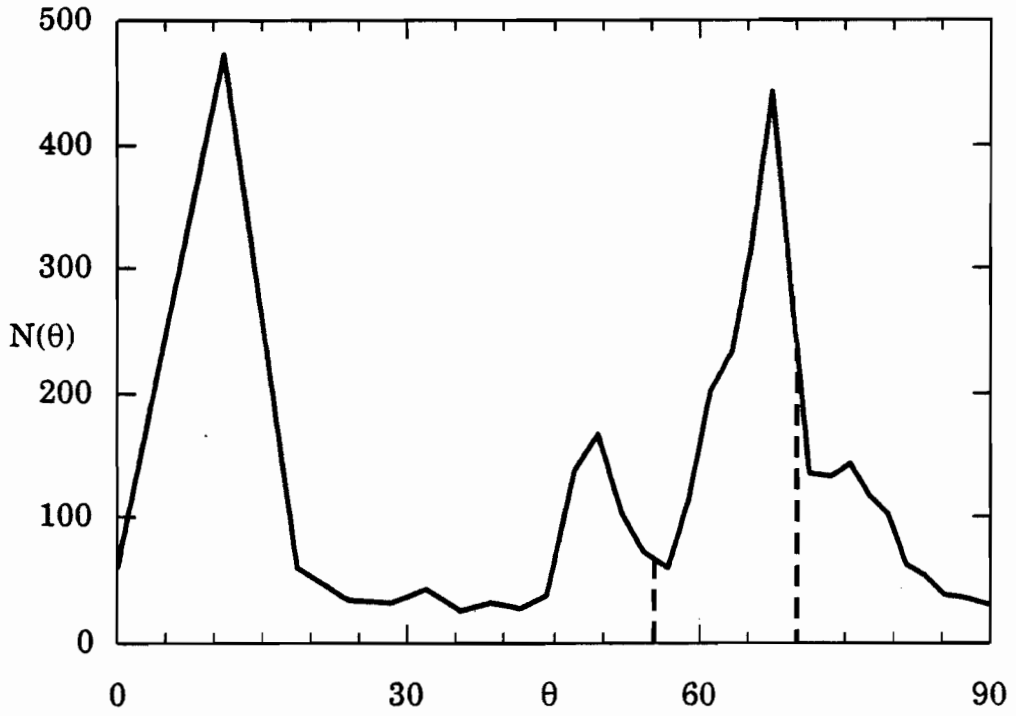

Figure 5.8c. Number of {111} poles as a function of θ at ε=0.5 in an FC+RW calculation.

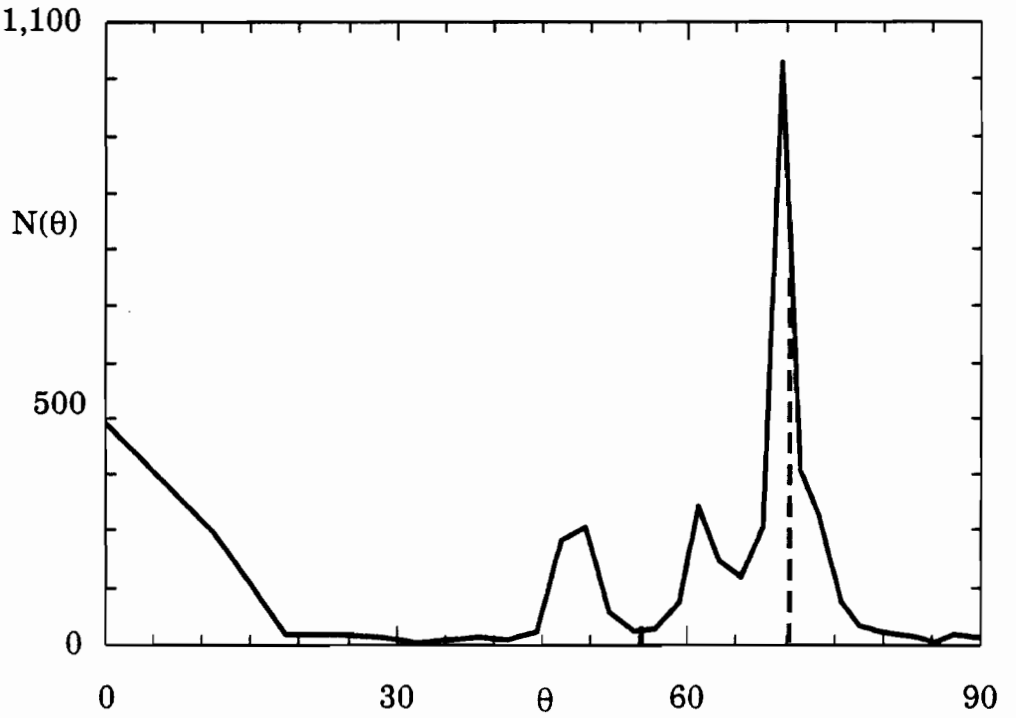

Figure 5.8d. Number of {111} poles as a function of θ at ε=1 in an FC+RW calculation.

another fibre not very far from {100}, but which corresponds to the minimum Taylor factor.The Taylor factor map calculated by Chin and Mammel [158] is reproduced in Figure 5.9 and the correlation between Figure 5.6d and Figure 5.9 becomes quite clear.

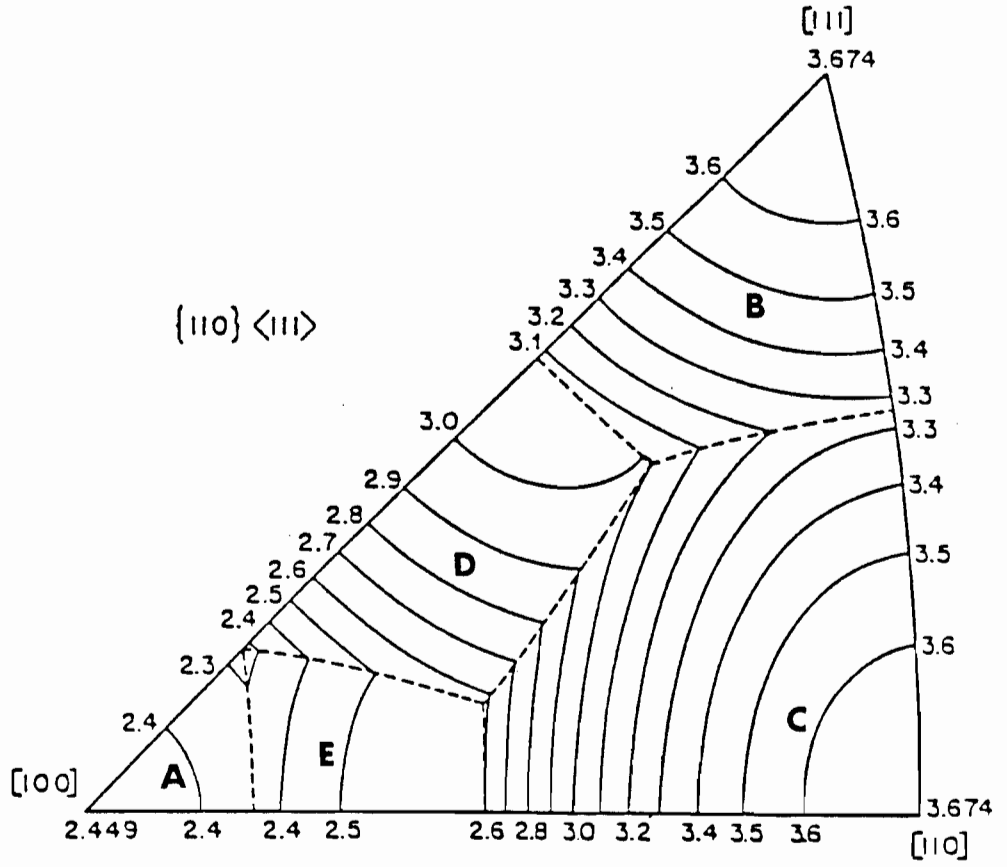

Figure 5.9. M contours obtained from computer solutions of the Taylor analysis for axisymmetric flow. Case of {111}<110> slip. Dashed boundaries delineate regions within which a specific type of vertex is selected [158].

iv) The texture obtained with RW is sharper than the one produced by AV. It can indeed be argued that the RW textures are much too sharp when compared with experimental pole figures. This is at least partly because no "splitting" of the grains (i.e. subdivision into different deformations and rotations in different parts of the grains) was allowed. A good way to improve this situation and to represent realistic textures would be to introduce a scatter around each orientation, as observed in real crystals [108]. This was not done here since the "pure" influence of the RW criterion was sought. The results presented in Figures 5.6 to 5.8 also lead to the conclusion that the rotations of

the grains towards stable positions are faster with RW than with AV. As most of the stable orientations are local minima in terms of the Taylor factor (one exception being the {111} fibre), the use of the RW criterion forces the grains to rotate more quickly towards these stable positions.

v) The calculated percentage around {100} is equal to 10% at a strain of 1 with FC + RW (compared to 22% with FC + AV). This value could correspond to the percentage obtained at room temperature on very high SFE materials.

vi) Because the {100} fibre is replaced by a *near* {100} fibre, it appears that the RW criterion does not lead to any improvement with respect to the classical FC calculation. Furthermore, it does not seem to be suitable for the prediction of high temperature textures since it does not call for an increase in the {100} component.

Nevertheless, in order to confirm conclusions about the validity of the RW criterion, some further simulations were thought to be desirable. For this reason, it was introduced into an RC calculation, the results of which form the subject of the next section.

V.4. COMPARISON OF THE VARIOUS PREDICTIONS WITH EXPERIMENTAL RESULTS IN THE CASE OF DEFORMATION UNDER RELAXED CONSTRAINTS

The validity of the RW criterion is tested below with respect to two different types of calculation: (i) an RC calculation in which some components of the strain rate are relaxed from the beginning to the end of the deformation; and (ii) an FC-RC calculation in which there is a statistical transition from FC to RC conditions, according to the model of Tomé et al. [125]).

V.4.1. THE RW CRITERION IN AN RC MODEL

Simulations were carried out of the grain rotations taking place during the rolling of the coarse grained aluminum sheets described by Driver et al. [123,124]. These sheets were initially 2 mm (sheet A) and 4 mm (sheet B) in thickness and contained grains 20-40 mm in diameter. Such crystals can be expected to deform according to the RC theory with $p=3$ (see Appendix 4), i.e.

with the shear rates $\dot{\varepsilon}_{23}$ and $\dot{\varepsilon}_{13}$ in each grain free to differ from the corresponding macroscopic components (which are zero in the case of rolling).

Driver and co-workers also compared their experimental results to the predictions obtained with the RW+RC and RW+FC models. They found that most of the grain orientations followed the predictions of the conventional RC theory (p=3). However, some of the grains deformed according to the FC theory as supplemented by the RW criterion. The latter were either smaller than the RC grains or the RC theory predicted unreasonably large values of the $\dot{\varepsilon}_{23}$ and $\dot{\varepsilon}_{13}$ shear rates.

We carried out several types of RW calculations (i.e. FC and RC with p=3 and 4) and compared them with the corresponding FC+AV or RC+AV calculations. An example of such a prediction is illustrated in Figure 5.10 in terms of an inverse pole figure showing the path followed by the compression axis X_3 and the elongation axis X_2. For this specific example, the two FC calculations are very close, whereas the RC ones are identical, so that only the RC+RW results are presented. Most of the results obtained for these coarse grains lead to similar conclusions: i.e. that i) the coarse and flat grains deform according to the RC theory; and ii) the introduction of the RW criterion does not significantly influence the results because of the small amount of ambiguity present.

In this study of the behavior of the coarse grains deformed in rolling, some minor results were also found which are worth mentioning:

i) Some small and nearly equiaxed grains were found to deform according to the FC model. Because of their small size, they were essentially fully constrained by their neighbors. For more details, see reference [5].

ii) The position of a grain inside the sheet was also shown to influence the deformation mode. Some grains located at the corners of the sheet were found to deform according to a different RC+RW type of calculation, i.e. a p=3 case, in which the shear rates $\dot{\varepsilon}_{23}$ and $\dot{\varepsilon}_{12}$ were set free (instead of $\dot{\varepsilon}_{23}$ and $\dot{\varepsilon}_{13}$).

iii) For nearly symmetrical orientations, both the RC and FC (+RW and RS) theories predict much larger rotations than the experimental ones. By contrast, the FC theory using averaging, which is equivalent to considering

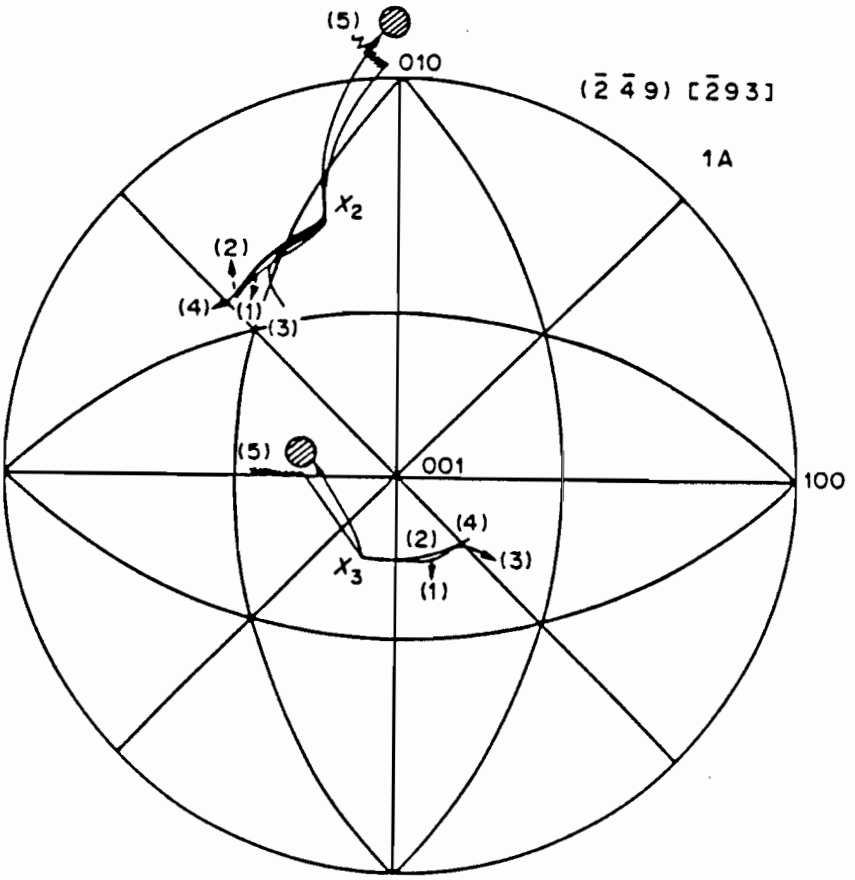

Figure 5.10. Predicted and experimentally observed rotations of grain 1A during rolling ($\bar{\varepsilon}=1.67$). The numbers 1 to 5 correspond to the following deformation modes: (1) AV, p=5; (2) RW, p=5; (3) RW, p=4 ($\dot{\varepsilon}_{23}$ free); (4) RW, p=4 ($\dot{\varepsilon}_{13}$ free); and (5) RW, p=3 ($\dot{\varepsilon}_{23}$ and $\dot{\varepsilon}_{13}$ free).

that 6 or 8 slip systems are active ($\dot{\gamma}^s \neq 0$) concurrently, respects the symmetry of the orientation and is thus successful in predicting the small rotations observed experimentally.

From this study, which is described in more detail in reference [5], it can be concluded that the RC model complemented with the RW criterion leads to results which are similar to those obtained from the RC+AV model. However, since the strict RC model is not the most suitable for predicting the evolution of the texture of a polycrystal (initially composed of equiaxed grains), it was decided to perform some calculations using the FC-RC model [125] as well, in

which the ambiguities present at each step are suppressed by the use of the RW criterion under both FC and RC conditions.

V.4.2. THE RW CRITERION IN AN FC-RC SIMULATION OF A POLYCRYSTALLINE TEXTURE

The path selected here was torsion and the predictions of two models are compared below to experimental results: the FC-RC + AV and the FC-RC + RW models. For relatively small deformations, the results of the FC + AV and FC + RW models will also be presented. The results of the two FC type calculations corresponding to a strain of $\bar{\varepsilon} = 2$ are presented in Figure 5.11. It is clear from this figure that the FC + RW model leads to a sharper texture than the FC + AV calculation; i.e. the different grains of the polycrystal rotate more quickly towards the stable orientations. The B component (i.e. the one present in hot deformed aluminum) is present in greater proportions with the FC + RW than with the FC + AV model.

This can be explained by the fact that the B orientation corresponds to a local minimum in the Taylor factor (for the FC model). To illustrate this fact, the Taylor factor was calculated for the range of values of the Euler angles ϕ, θ and ω and iso-M curves were plotted in Euler space. The angles ϕ and θ were varied from 0 to 90° and the angle ω from 0 to 180°. M was then plotted as a function of ϕ and θ for constant ω. One of these sections (i.e. for $\omega = 90°$) is shown in Figure 5.12. The other sections are presented in Appendix 6. The section presented in Figure 5.12 is interesting since it includes the three orientations usually found in torsion, which are labelled A, B and C. It can be seen that all three orientations lie on the $\phi = 45°$ line, which is an axis of symmetry of the figure. All the points located on this line are local minima in terms of the Taylor factor and the absolute minimum is the A orientation (where there is activation of only one slip system and $M = \sqrt{3}$).

Now in the case of large deformations, the FC theory is no longer adequate and has to be replaced by the FC-RC model. The interesting point here is that the orientation of each grain at the stage where the transition from FC to RC is made will in general be different with RW on the one hand and AV on the other; thus its subsequent evolution is expected to also be different under RC

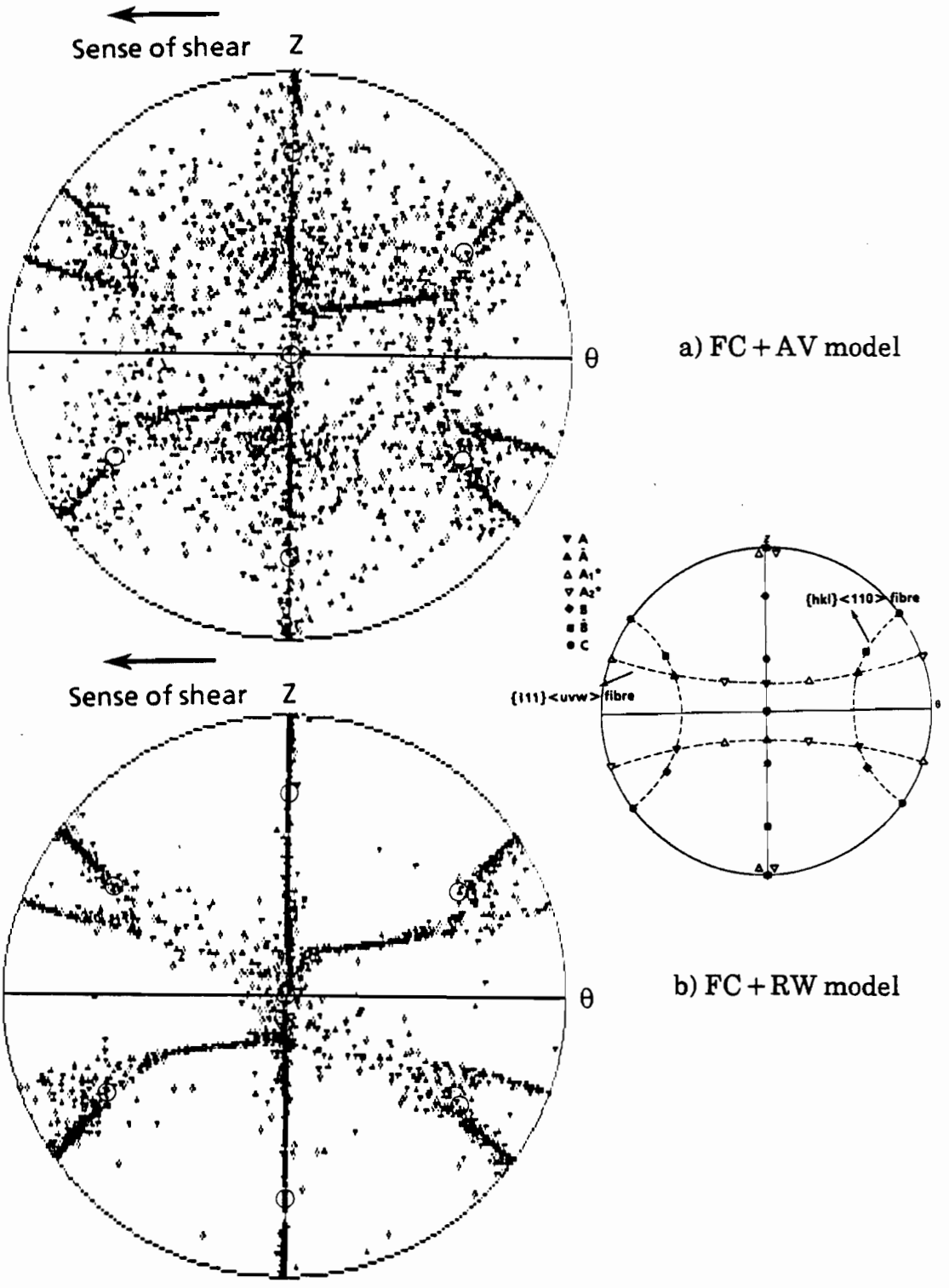

Figure 5.11. Predicted torsion textures at $\bar{\varepsilon}=2$. {111} pole figures; the open circles specify the position of the B/$\bar{B}$ component.

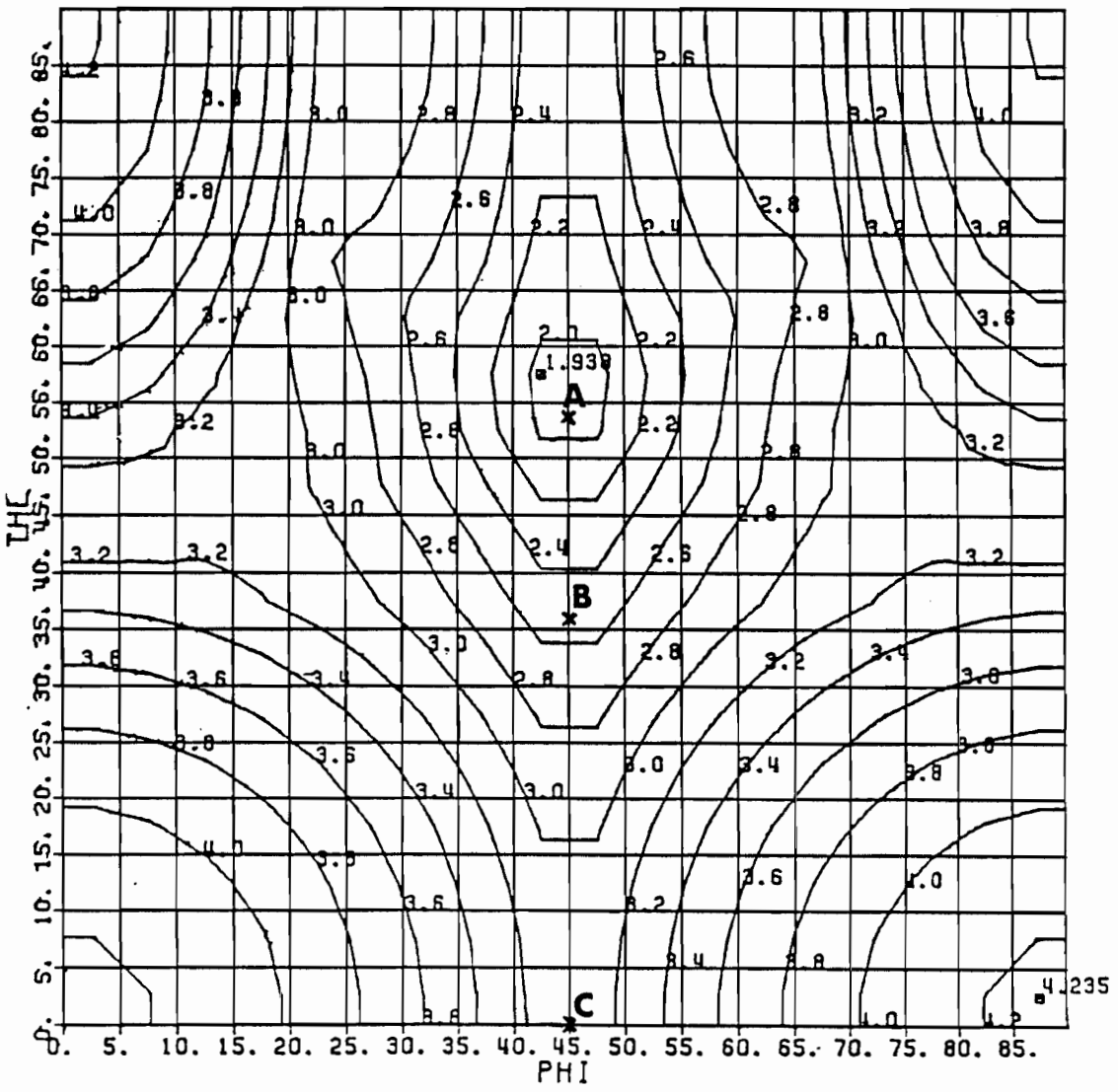

Figure 5.12. M contours in selected section of Euler space ($\omega = 90°$) obtained from computer solutions of the Taylor analysis for torsion. This section contains the A, B and C orientations.

conditions with the two different models, even though the number of ambiguities is almost reduced to zero. In Figure 5.13, the results obtained with the FC-RC + AV model are presented for strains of 4, 6, 8 and 10 and the results obtained with the FC-RC + RW model for the same strains are presented in Figure 5.14. Here again, it is evident that the texture is sharper with the RW model. Furthermore, some other differences between the two sets of figures can be noted. The FC-RC + RW theory predicts a partial {hkl}<110> fibre (approximately between {100}<110> (C) and {112}<110> (B)), whereas the

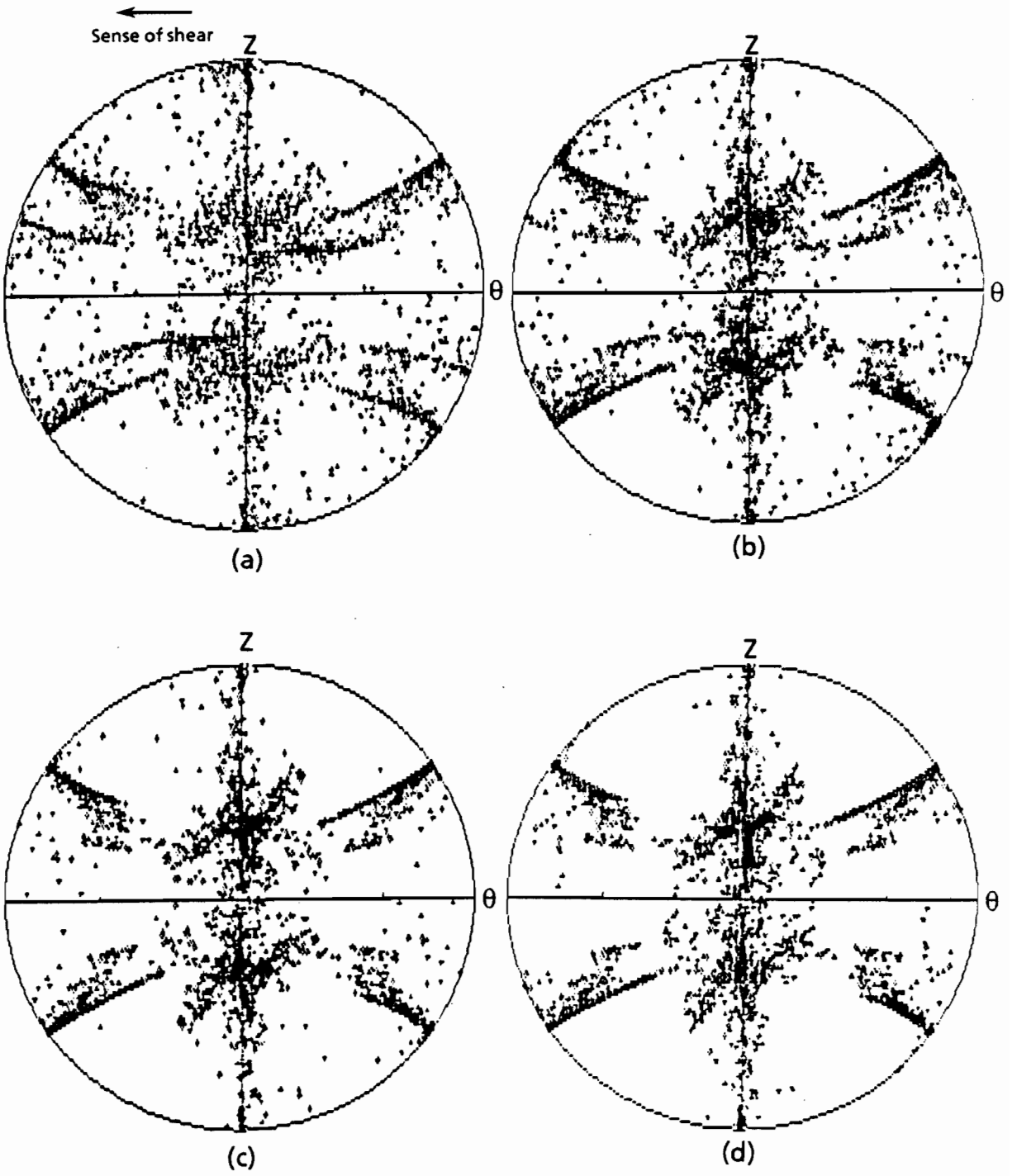

Figure 5.13. Torsion textures predicted using the FC-RC+AV model, {111} pole figures. a) $\bar{\varepsilon}=4$, b) $\bar{\varepsilon}=6$, c) $\bar{\varepsilon}=8$, and d) $\bar{\varepsilon}=10$.

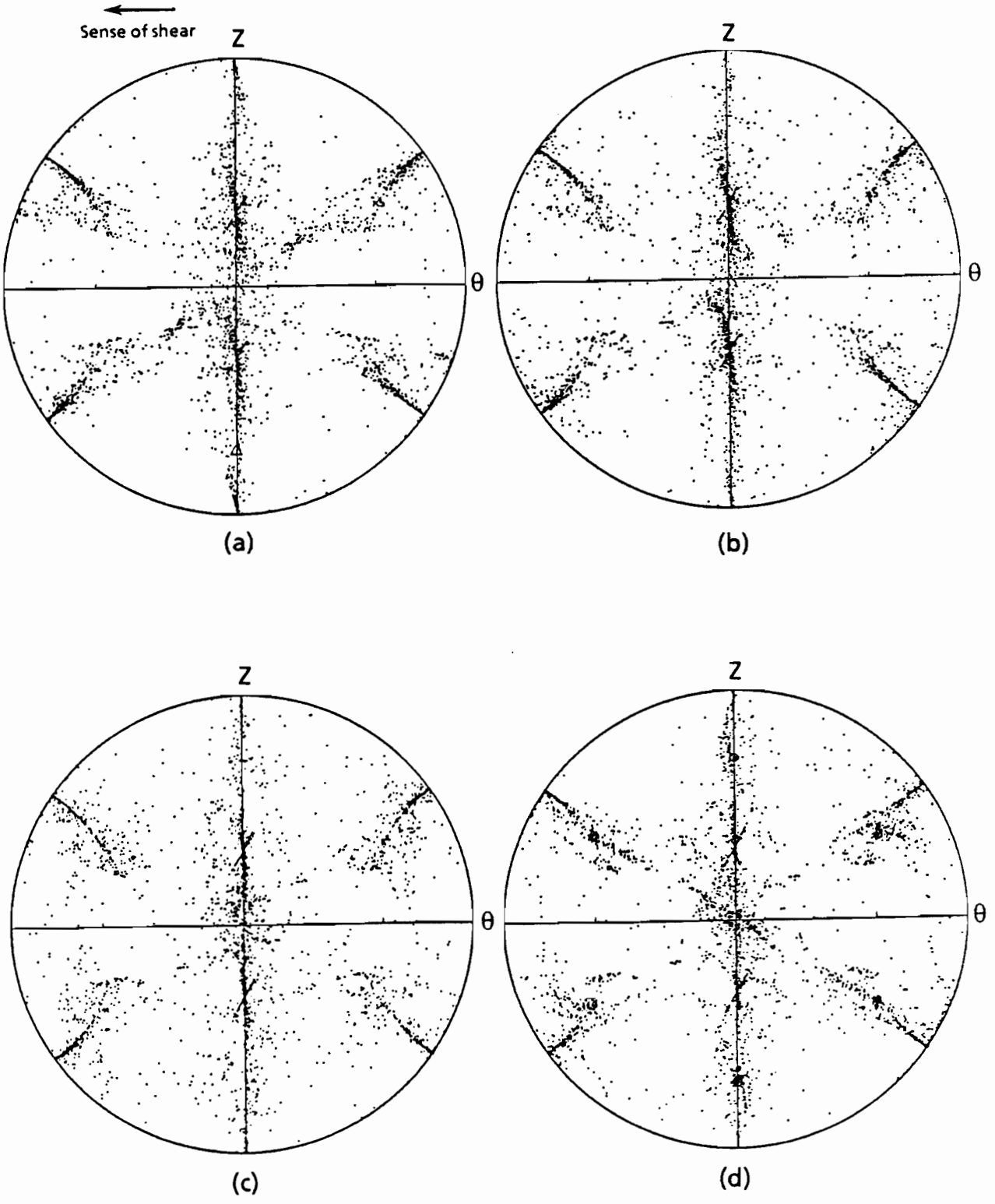

Figure 5.14. Torsion textures predicted using the FC-RC + RW model, {111} pole figures. a) $\bar{\varepsilon} = 4$, b) $\bar{\varepsilon} = 6$, c) $\bar{\varepsilon} = 8$, and d) $\bar{\varepsilon} = 10$.

FC-RC+AV model predicts instead a partial {100}<uvw> fibre, including a strong C component. Comparing these two sets of diagrams with Figures 2.26a and 2.26b, it appears that the FC-RC+AV predictions (see especially Figure 5.13a) are in good agreement with the experimental texture of copper deformed at room temperature (Figure 2.26a), whereas the FC-RC+RW predictions (Figure 5.14a) seem to be in better agreement with the experimental texture of copper deformed at 100°C (Figure 2.26b). Nevertheless, the percentage of the B component is too low in both cases.

V.5. CONCLUSIONS

In this chapter, the RW criterion was added to some of the classical texture prediction theories: i.e. the FC, RC and FC-RC models. These new approaches were used to simulate the reorientation of both single crystals and polycrystals and the results were compared with experimental observations as well as with the predictions obtained from the classical models. The following conclusions can be drawn from this work:

i) The use of the RW criterion influences texture development under full constraint conditions, but not appreciably under relaxed constraint conditions. This is because, in the RC model, the extent of the ambiguities is rather small.

ii) As a consequence, texture development in an FC-RC+RW calculation also differs from the one predicted by the FC-RC+AV model.

iii) The FC+RW model applied to tension predicts some texture components which are not observed experimentally.

iv) The FC-RC+RW approach produces a sharper texture than the FC-RC+AV model. This is due to the faster rate of development of the texture when the RW criterion is used, when the reorientation towards stable positions is accelerated. This can be explained schematically with the aid of Figure 5.15. In this two dimensional example, positions 1 and 3 are stable positions; they correspond to crystallographically equivalent or symmetrical orientations and activate only one slip system. This is the case for the A component in torsion,

for example, which corresponds to a minimum in the Taylor factor. By contrast, the position labelled 2 is a metastable one which activates two slip systems equally and corresponds to a maximum (or local maximum) in the Taylor factor. The latter description applies to the C component in torsion. With the RW criterion, the rotation rate between 1 and 2 (during which the Taylor factor is constantly increasing) tends to be as slow as possible, whereas between 2 and 3 (when M is decreasing) the rotation rate tends to be as rapid as possible.

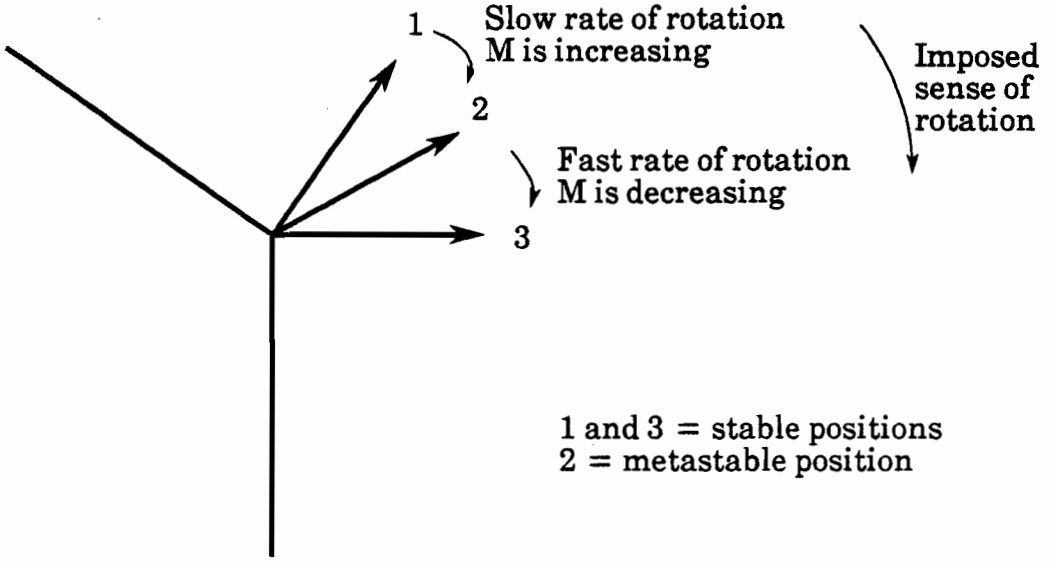

Figure 5.15. Two dimensional illustration of the RW criterion. Between positions 1 and 2, the Taylor factor is increasing and the RW criterion selects the solution which reduces the rate of rotation. By contrast, between positions 2 and 3, M is decreasing and the use of the RW criterion results in a fast rotation rate.

v) The texture obtained in torsion with the FC-RC + AV model is in rather good agreement with the one obtained experimentally for copper deformed at room temperature. The texture obtained in torsion with the FC-RC + RW model, on the other hand, agrees better with the results obtained with copper deformed at 100°C although it is still sharper than the experimental result. This is partly due to the small number of grains chosen for the calculation, but the effect could have been lessened by the superposition of gaussian orientation distributions on the theoretical results.

vi) At very large strains (i.e. after $\bar{\varepsilon}=8$), the two models are very close and both sets of textures are very sharp. No increase in the B component is observed in torsion. This increase should have evolved from the FC-RC + RW model if the latter were truly adequate for the simulation of high temperature deformation. However, at such large strains, the exact deformation mode of each grain is unknown, as is the extent to which grain shape arguments, on which the RC theory is based, are still valid. This is a topic to which we return in Chapter VIII.

CHAPTER VI

THE INFLUENCE OF CROSS-SLIP

Two different procedures were used to simulate the relative ease of cross-slip in high stacking fault energy metals. The first is based on the method initially proposed by Chin [6], in which the activity of colinear systems is maximized (or alternatively minimized) in the presence of ambiguities in the choice of slip systems. The second procedure consists of incorporating a suitable hardening law into a classical FC or RC model. These two procedures are described below.

VI.1. THE CHIN THEORY

VI.1.1. REVIEW OF THE THEORY AND ORIGINAL RESULTS

Chin incorporated into a classical FC model (using the minimum work rate criterion) some selection criteria in the presence of ambiguities to account for different mechanisms such as increased or decreased ease of cross-slip or various degrees of latent hardening. In the case of cross-slip, he maximized the activity of colinear systems, i.e. those which have the same slip direction but different slip planes. He applied this selection criterion to the case of axisymmetric tension and found that, when cross-slip is favoured, an increase in the fraction of the <111> component is produced at the expense of the <100> component (after 5% of deformation). He concluded that these results are in good agreement with experimental results for high SFE materials deformed at room temperature (see Figure 2.2). The incorporation of this criterion was done with the aid of linear programming: once the activated slip systems are selected, the quantity to maximize is the sum of the shears on the colinear systems only (out of the 6 or 8 possible systems).

VI.1.2. REFORMULATION OF THE CHIN THEORY

It was decided to use the same selection criterion here but in a Bishop and Hill type of calculation instead of the Taylor type performed by Chin. The reason for doing so is that the solution is not necessarily unique (even with the additional criterion) and the linear programming algorithm selects a random solution in such a case [26]. This can be avoided by employing the procedure described below so that the average rotation can be calculated in the presence of ambiguities. Another problem encountered in the Taylor approach is that the colinear systems selected are not always independent. For example, systems 1, 10, 16 and 19 associated with vertex 23 (see Table 5.1) constitute two pairs of colinear systems which are *not* independent. If the total activity on these systems is maximized with the aid of linear programming, since they cannot, even with a supplementary system, accommodate the deformation, the actual solution will in most cases predict a large amount of shear on only one of the 4 systems and some shears on other independent and non-colinear systems. In order to avoid these problems, the colinear slip selection criterion was added to the basic FC or RC program described in Appendix 5 as follows:

i) The number of slip directions associated with each combination of 5, 4 or 3 independent systems was added to the data file. The problem of the dependence of the systems can thus be solved since the actual combination is always selected from the combinations of 5, 4 or 3 *independent* systems.

ii) The active vertex is then selected using the principal of maximum work and all possible combinations of independent systems are listed.

iii) The combinations associated with the minimum possible number of slip directions are retained and the amount of shear on each system is calculated.

iv) After having eliminated the ones for which some of the $\dot{\gamma}^s$ are negative, the sum of the shears on the colinear systems is calculated. In each combination, the number of colinear systems can be equal to 0, 2 or 4.

v) Finally, only the combination which gives the maximum value of the sum of the shears on the colinear systems is retained. In the case where several solutions lead to the same result, the average rotation is calculated.

This procedure clearly respects the idea proposed by Chin [6], but eliminates two of the problems inherent in the use of linear programming.

The modified model was first applied to the case of tension because the extent of the ambiguities is the highest in this case. It has the further advantage that the present results can be compared to those reported by Chin. These observations are presented below.

VI.1.3. APPLICATION TO AXISYMMETRIC TENSION

First, some specific orientations associated with the greatest extent of the ambiguities were selected. It is known from the work of Taylor [4], for example, that for any orientation near <110>, there is an ambiguity of 360° in the rotation. These orientations activate a C-type vertex (see Figure 5.12), each of which is associated with 4 pairs of colinear systems. For these orientations, the rotations were calculated with four different models: i) the classical FC+AV model; ii) the Chin model of cross-slip (i.e. using linear programming); iii) our modified version of the Chin model (i.e. as described above) where the sum of the shears on colinear systems is maximized (FC+CS); and iv) the modified Chin model, but where the sum of the shears on colinear systems is *minimized* to simulate the situation where cross-slip is difficult.

One example of such a calculation is presented in Figure 6.1 for a strain of 4. The paths labelled 2 and 3, which are supposed to represent the same mechanism (ease of cross-slip) and same selection criterion, do not in fact lead to the same results. The small waves which can be seen on path 2 (Chin procedure) are typical of random choices made by the computer. Moreover, it is evident that our procedure leads to results which are in complete contradiction with the conclusions drawn by Chin. To determine whether the trends illustrated in Figure 6.1 apply to polycrystals, our cross-slip model was applied to the axisymmetric extension of a polycrystal (represented by 900 orientations distributed randomly in Euler space) and compared with the predictions of an

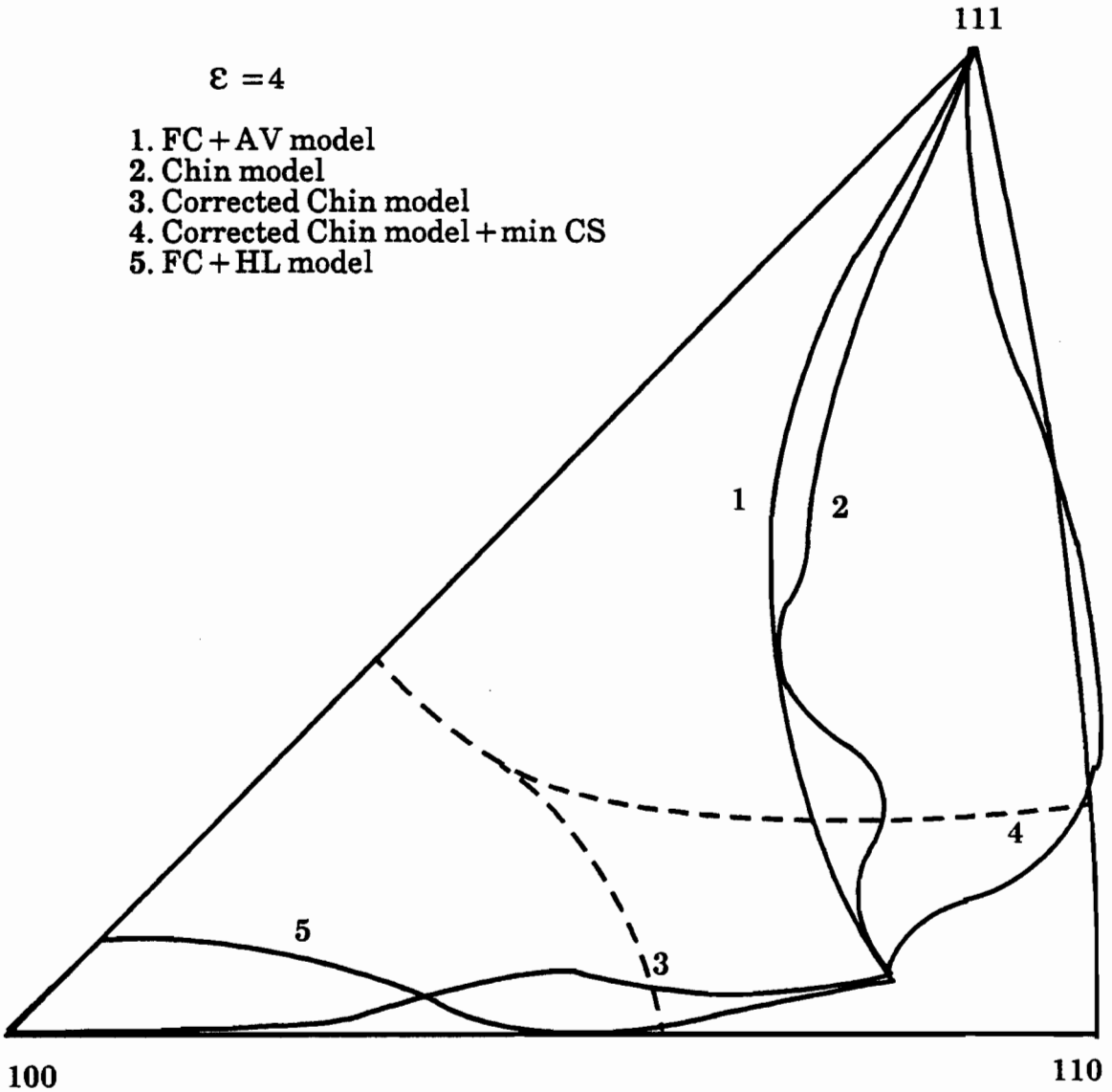

Figure 6.1. Predicted rotations for a grain deformed in axisymmetric extension. Five different models were used: 1) FC + AV; 2) the Chin model (using linear programming); 3) the present version of the Chin model (FC + CS); 4) the FC + CS model modified to *minimize* the activity of colinear systems; and 5) the FC + HL model developed in section VI.2.

FC-AV model. In Figure 6.2, the inverse pole figures obtained with the FC + AV (a and b) and FC + CS (c and d) models are presented for strains of 1 and 2. The calculated densities along a radius of the pole figure are shown in Figure 6.3. Although a strain of 2 is greater than can normally be attained in tension, it allows us to determine the trends for each model. Instead of the increase in the <111> component found by Chin, our model predicts an increase in the

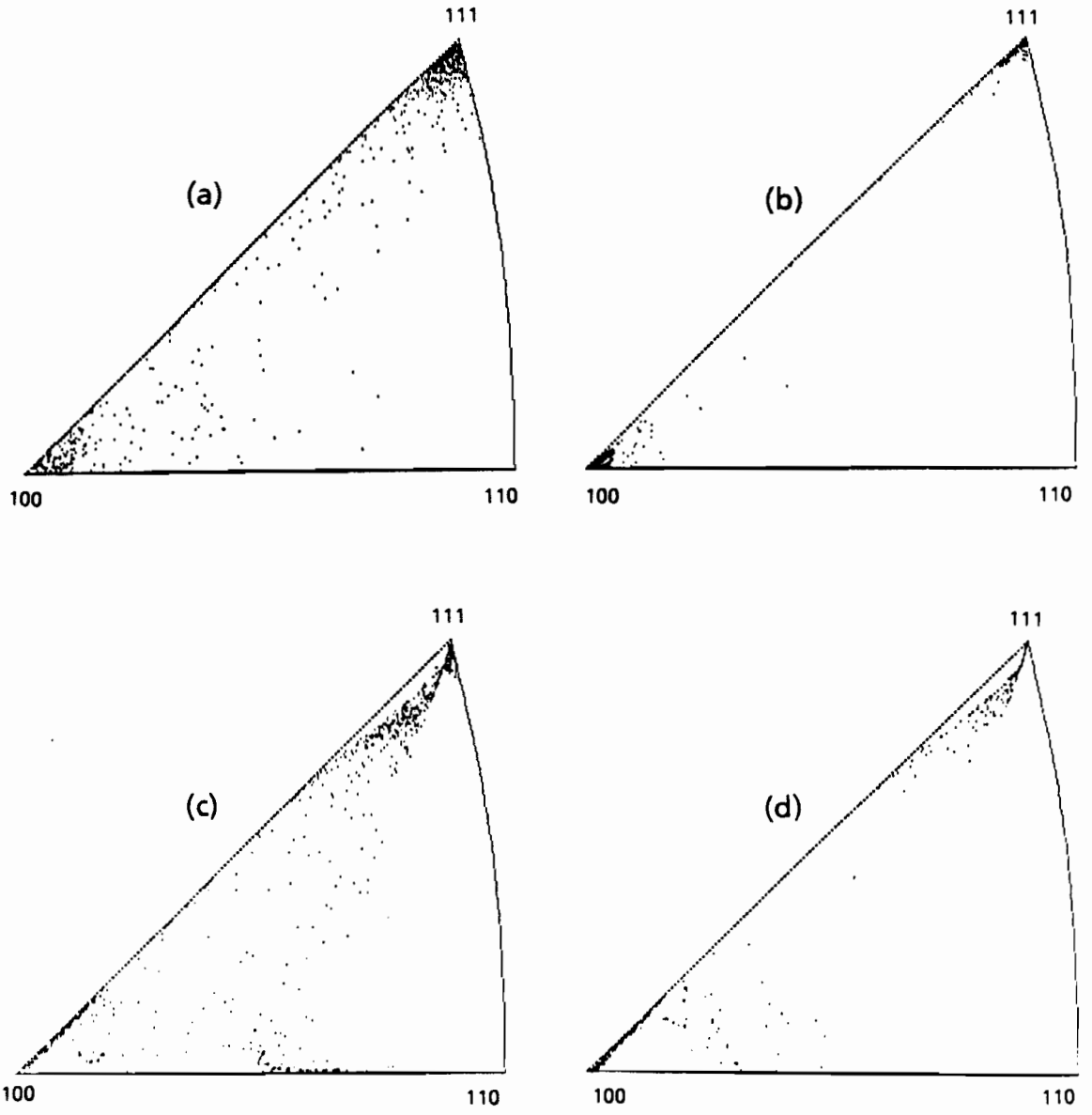

Figure 6.2. Predicted inverse pole figures for a polycrystal deformed in axisymmetric extension: a) FC+AV, $\bar{\varepsilon}=1$; b) FC+AV, $\bar{\varepsilon}=2$; c) FC+CS, $\bar{\varepsilon}=1$; and d) FC+CS, $\bar{\varepsilon}=2$.

<100> component, which is in better agreement with the results obtained at elevated temperatures (see Chapters II and IV). Apart from the two problems already mentioned, another possible explanation for this apparent contradiction is that Chin performed his calculations up to the relatively small strain of 5% and the trend observed after such a limited deformation can be reversed at larger strains. (This was in fact observed for some orientations near <110>.)

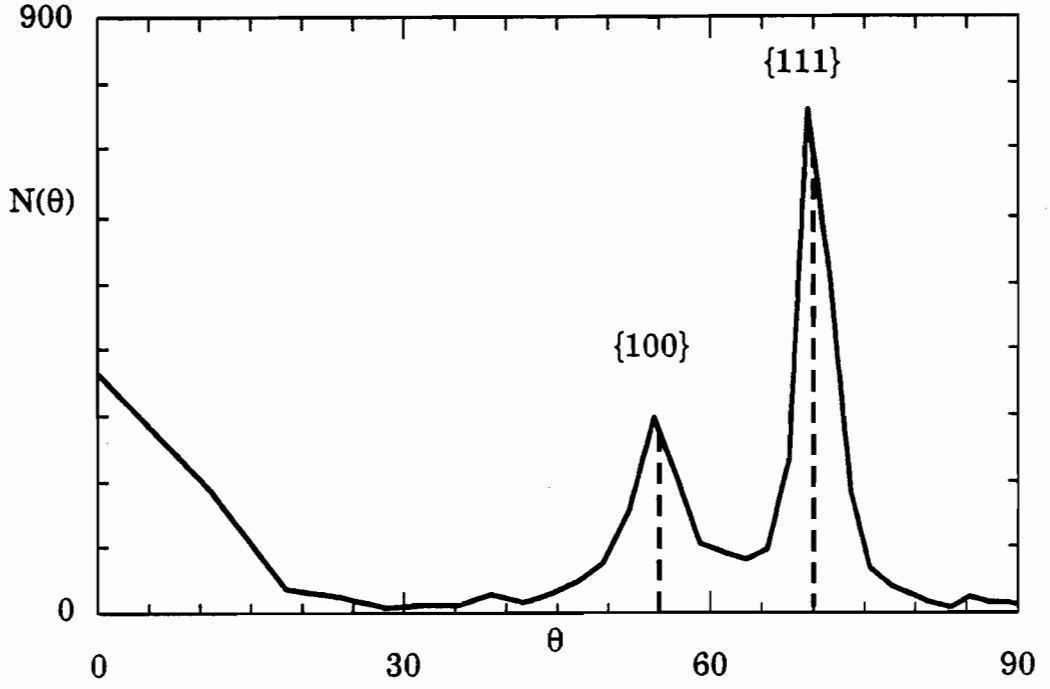

Figure 6.3a. Number of {111} poles as a function of θ at ε=1 in an FC+AV calculation.

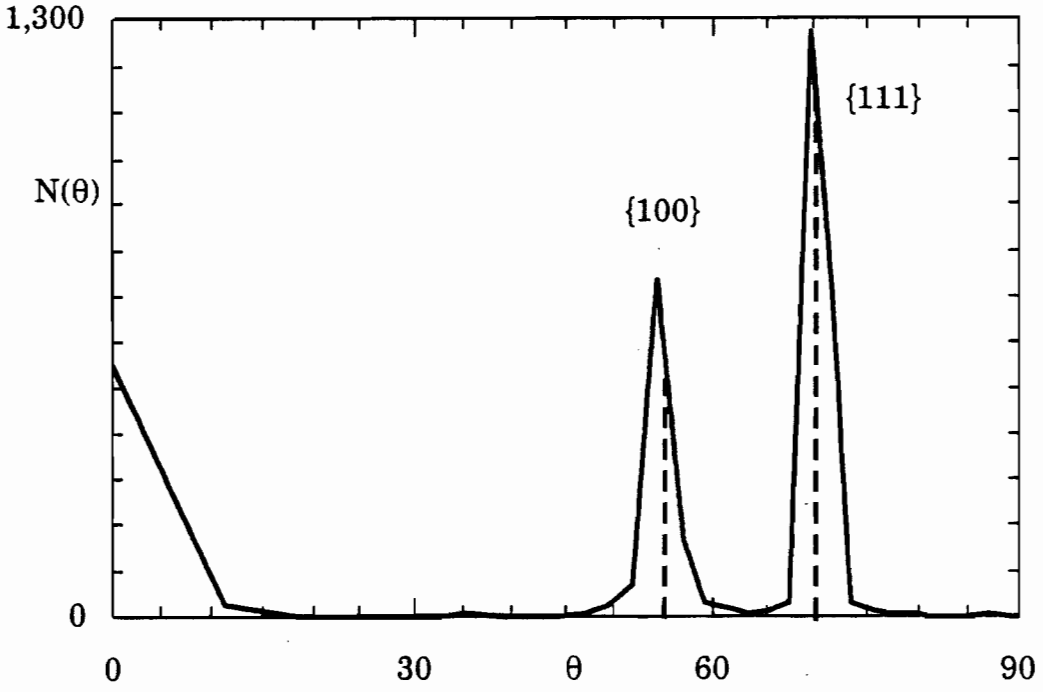

Figure 6.3b. Number of {111} poles as a function of θ at ε=2 in an FC+AV calculation.

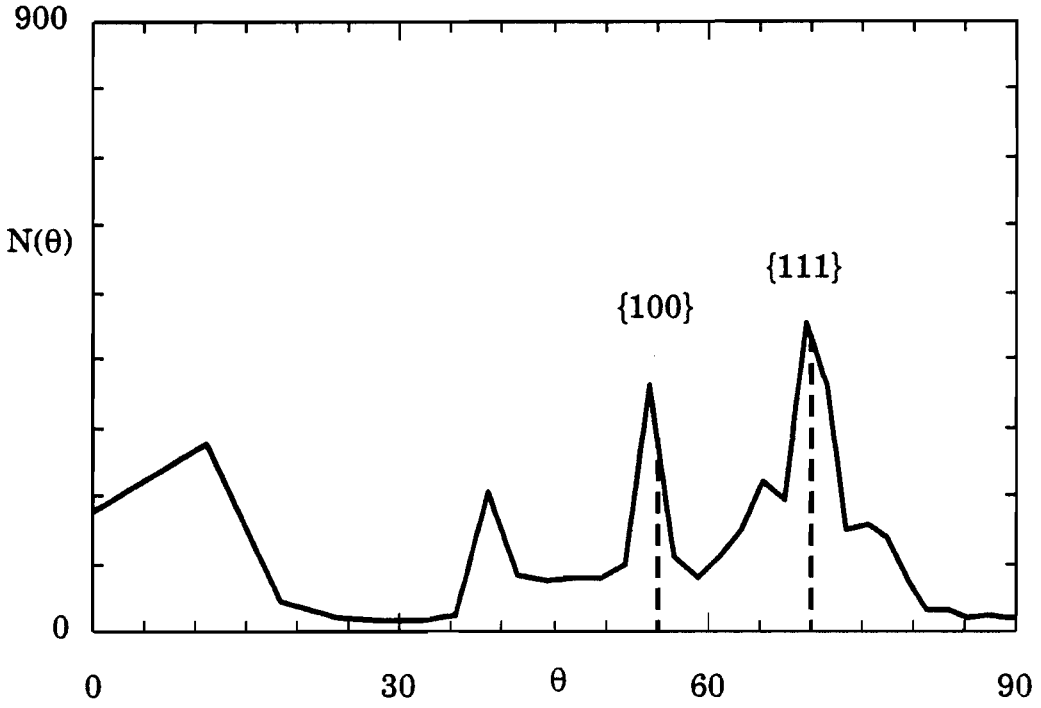

Figure 6.3c. Number of {111} poles as a function of θ at ε = 1 in an FC + CS calculation.

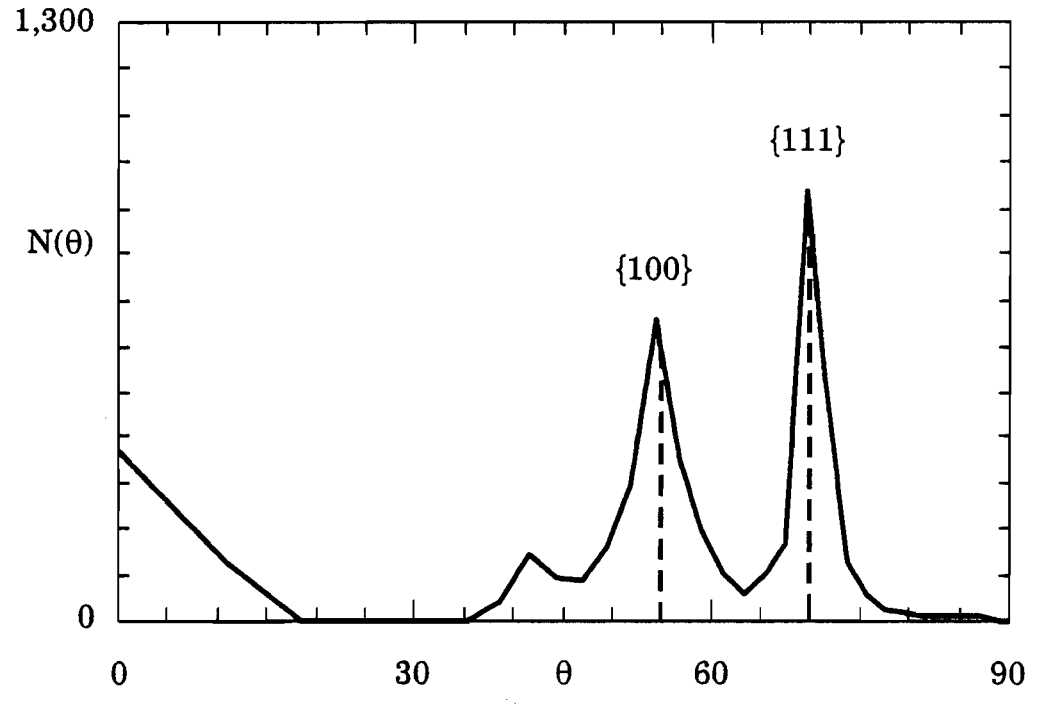

Figure 6.3d. Number of {111} poles as a function of θ at ε = 2 in an FC + CS calculation.

It is apparent from these results that our simulation of cross-slip reproduces the experimental results associated with high temperature deformation quite well in the case of extension. We now apply this model to the other deformation paths of interest here, namely rolling and torsion.

VI.1.4. APPLICATION TO TORSION AND ROLLING

For the cases of torsion and rolling, both the FC and FC-RC models were employed. The present selection criterion was introduced into these two models and the results of such simulations were compared with the FC+AV and FC-RC+AV predictions. It appeared that the FC-CS simulations were similar to the FC-AV ones for torsion and rolling and so are not reproduced here. Similar remarks apply to the FC-RC model. Nevertheless, the FC-RC results for torsion to an equivalent strain of 5 are illustrated in Figure 6.4, in which the predictions of the FC-RC+CS (cross-slip) and FC-RC+AV models are compared. Although the results are again similar, a slight increase in the B/$\bar{B}$ component is produced by the CS model. It was shown by Tomé and co-workers [125] that the average number of active slip systems in torsion is always less than the number of imposed strain rate components. This has the effect of reducing the extent of the ambiguities considerably, even in an FC model. Furthermore, when ambiguities are present, the cross-slip selection criterion does not always give a unique solution; as the average is taken in these cases, the two models considered here lead to similar results. The same remark applies to the case of rolling, and an example of the FC-RC+CS simulation applied to this strain path is presented in Figure 6.5. At a strain of 1, a good proportion of the grains still deform according to $p=5$ and the result is again similar to the classical FC-RC+AV calculation.

These observations lead us to the following conclusions:

i) For the case of rolling and torsion, any model based on a selection criterion in the presence of ambiguities (i.e. RW or CS) leads to results close to those of the classical calculations.

ii) Some differences can be observed in tension (and compression, which has not been presented here). This is because the region of the inverse pole

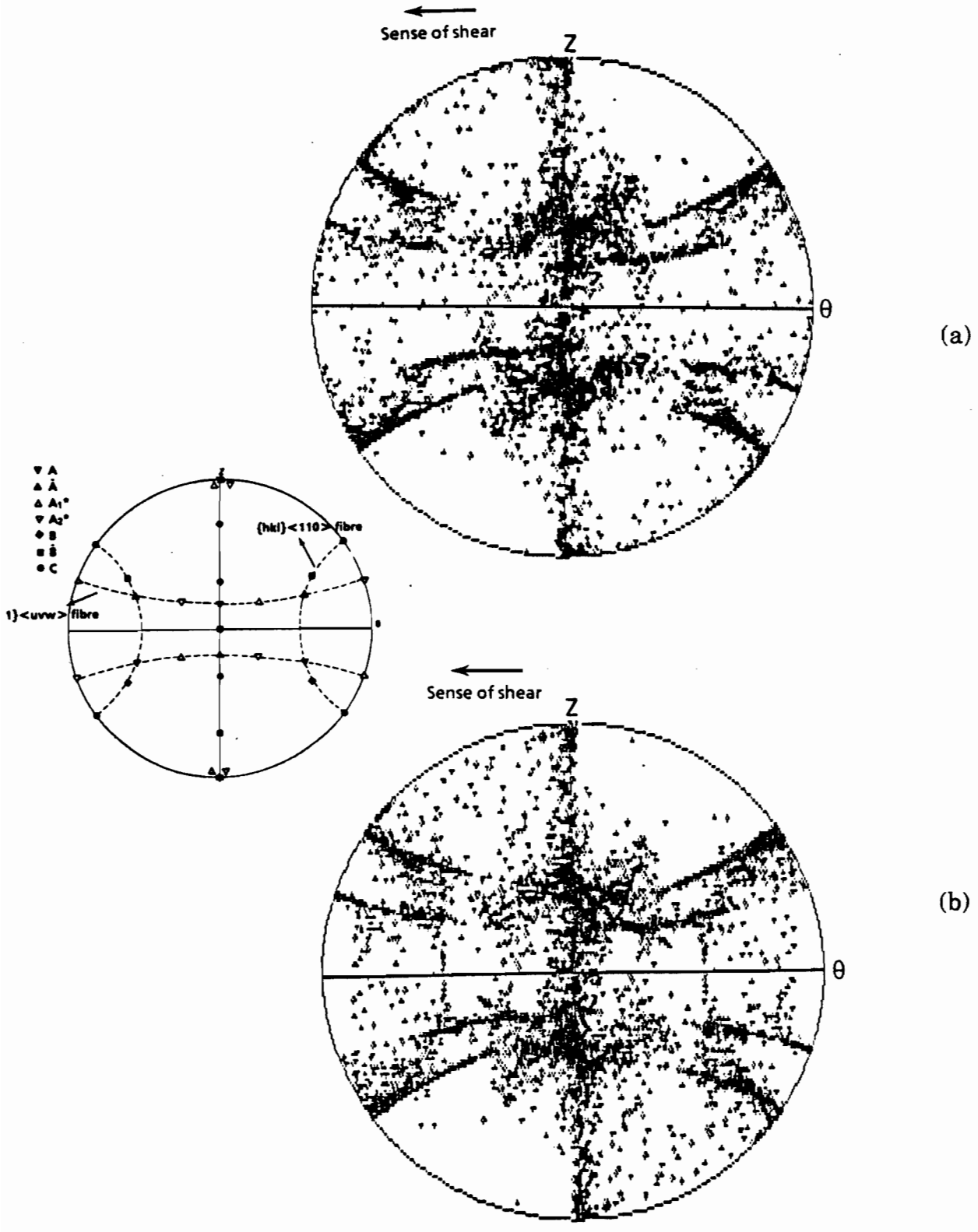

Figure 6.4. Torsion textures predicted at a strain of $\bar{\varepsilon} = 2$ using two different models a) FC-RC + AV and b) FC-RC + CS.

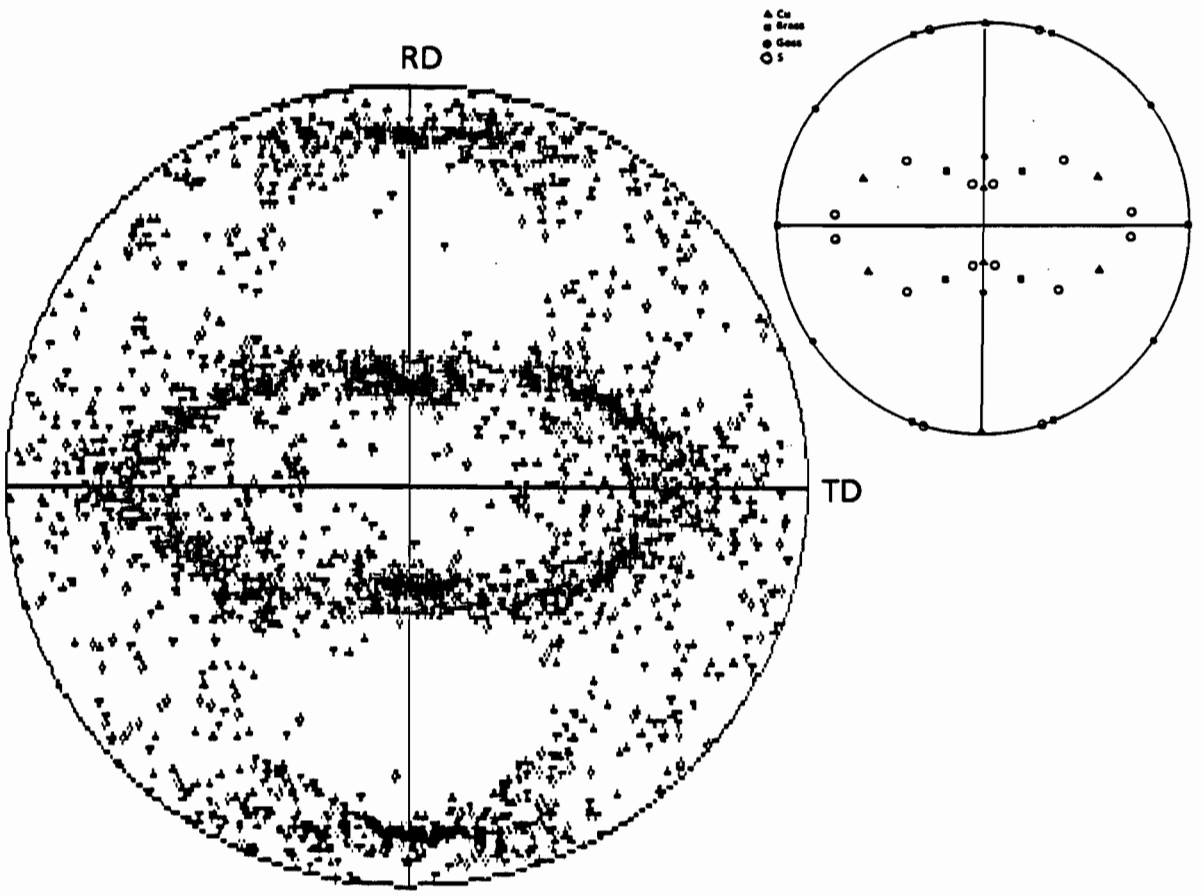

Figure 6.5. Rolling texture predicted for an equivalent strain of 1 with the FC-RC + CS model.

figure located around <110> involves many ambiguities and grains of such orientations comprise an important proportion of a random texture.

iii) In the case of tension, the CS model gives results which are in good agreement with experimental observations at elevated temperatures. But, as such a model cannot account for the differences observed between low and high temperatures for *all* the deformation paths, it does not seem suitable for adoption as a general model to represent the ease of cross-slip.

For this reason, it was decided to simulate cross-slip by incorporating a suitable hardening law into the classical models. The results obtained in this way will now be reviewed.

VI.2. INCORPORATION OF HARDENING LAWS

VI.2.1. THEORETICAL BASIS

The basic idea here is that the rate of change of the critical resolved shear stress τ_c is not the same for all slip systems. In latent hardening theories and experiments, for example, it has been determined that, when a given system is active, all the other slip systems harden more quickly than the active one (except for a coplanar one which has approximately the same CRSS as the active system). This is because a dislocation which wants to move on a previously inactive system will necessarily meet one from active systems on which the dislocation density is higher; it will thus be harder to cross an active slip system than an inactive one [139,140].

In order to simulate the ease of cross-slip and to favor the activity of the colinear slip systems, as in the Chin model, it can be assumed that the CRSS is different for the active, colinear and "unrelated" (i.e. other than active or colinear) systems in the following way: all the inactive systems are considered to harden more than the active ones, except for the colinear ones, which have a hardening rate less than or equal to that of the active systems. This can be simulated by the incorporation of a hardening matrix H_{ij} which relates the CRSS and the shear rates on the active slip systems as follows:

$$\tau_c^i(t+dt) = \tau_c^i(t) + \sum_j H_{ij}\,\dot{\gamma}^j\,dt \tag{6.1}$$

Here $\tau^i_c(t+dt)$ represents the CRSS of system i after a time increment dt, $\tau^i_c(t)$ is the CRSS of system i at instant t and H_{ij} takes the following values:

$$\begin{aligned} &H_{ii}=1 \\ &H_{ij}=1\text{-}\alpha \qquad \text{if } i \text{ and } j \text{ are colinear systems} \\ &H_{ij}=1+\beta \qquad \text{if } i \text{ and } j \text{ are not colinear systems} \end{aligned} \tag{6.2}$$

where α and β are either positive or zero (isotropic hardening). In the case of interest here, the condition $\alpha=0$ and $\beta\neq 0$ means that slip on the active and colinear systems is equally easy (and easier than on the other systems), whereas the condition $\alpha\neq 0$ means that slip on the colinear systems is even

easier than on the active ones, which may be less realistic than the previous cases. Both conditions were nevertheless investigated for different values of the α and β parameters. These hardening laws were incorporated into the FC and FC-RC models. The active slip systems were determined with the aid of the principle of minimum internal work rate (through the linear programming technique), since the shape of the SCYS constantly changes because of the variations in τ_c. The CRSS's of the 24 slip systems were held constant during each time increment and were updated at the end of each increment. In the FC-RC model, the transition from the FC to the RC mode was performed as in the previous calculation, i.e. on the basis of grain proportions. Calculations with the two models were carried out in tension, torsion and rolling and the results are presented below.

VI.2.2. THEORETICAL RESULTS OBTAINED WITH THE FC MODEL

First, the range of variation of the parameters α and β must be determined. In order to do so, we first estimate the variation in τ_c required by equation 6.1 by rewriting it as follows:

$$\tau_c^i(t+dt) = \tau_c^i(t) + \sum_j \dot{\gamma}^j\, dt + \sum_j (0, -\alpha, \beta)\, \dot{\gamma}^j\, dt \qquad (6.3)$$

In the FC model, $\Sigma\dot{\gamma}^j$ is equal to the Taylor factor M and varies between 1.732 ($\sqrt{3}$) and 4.85 ($2\sqrt{6}$). For an increment of time dt equal to 0.025, the second term involves an increase of 7.5% (for an average value of 3 for $\Sigma\dot{\gamma}^j$) which is the same for all slip systems. This is not a real increase but only arises from the use of the coefficients H_{ij} as expressed by equation 6.2. This term does not produce any texture variation compared to the classical model when τ_c is kept uniform (this corresponds to isotropic hardening). The third term, however, is different for every slip system because of the introduction of the coefficients α and β, and this term characterizes the differences between slip systems. If $\Sigma\dot{\gamma}^j$ is equal to 3 and dt to 0.025, α (or β) equal to -0.13 (or 0.13) produces a relative decrease (or increase) of about 1%, which seems a reasonable value for the first steps of deformation. At large strains, the CRSS is assumed to remain constant.

α and β were varied in this way between 0 and -0.5 or +0.5 in the first 20 steps of deformation and were set equal to zero in the steps that follow.

A first result of such a simulation is that somewhat different values of the parameters give approximately the same results. Although specific orientations can be found which produce changed behaviors for different values of α and β, for a polycrystal composed of 800 orientations (initially distributed randomly in Euler space), the deformation texture is about the same (on a statistical basis) for different values of the two parameters. This is true for all three deformation modes investigated. The results presented below are typical and correspond to the case where α is equal to zero and β to -0.1.

It was also checked that, after the first deformation step, the number of activated slip systems is nearly always 5, i.e. the ambiguities disappear almost completely and the use of linear programming is thus justified. Except for the first increment, the algorithm never chooses a random solution. In other words, the extent of the ambiguities is less with this model than with the CS model presented in section VI.1.

For the case of tension, the results obtained with this model are similar to the predictions of the modified Chin model (section VI.1.3) and consequently are not reproduced here. An increase in the {100} fibre (compared to the FC + AV model) is also predicted. We have simply added to Figure 6.1 the path corresponding to the present model for the orientation treated in that figure.

The predicted torsion textures are presented in Figure 6.6 for equivalent strains of 1, 3 and 5. In Figure 6.7, the FC + AV and FC + HL (hardening law) models are compared for a strain of 3. In the last figure, two different representations of {111} pole figures are shown. In the first, the individual {111} poles associated with each grain are plotted, whereas in the second, density lines are drawn. To calculate the density at every point of the pole figure, the latter is divided into surface elements of equal area (in Euler space) and the density is taken as the number of {111} poles located in one element divided by the number found in a random texture (i.e. the total number of poles divided by the total number of surface elements). Such a representation enables the proportions of the texture components to be determined (especially when the texture is very sharp and several poles are superimposed at the same place), and also leads to plots which are suitable for comparison with experimental pole figures.

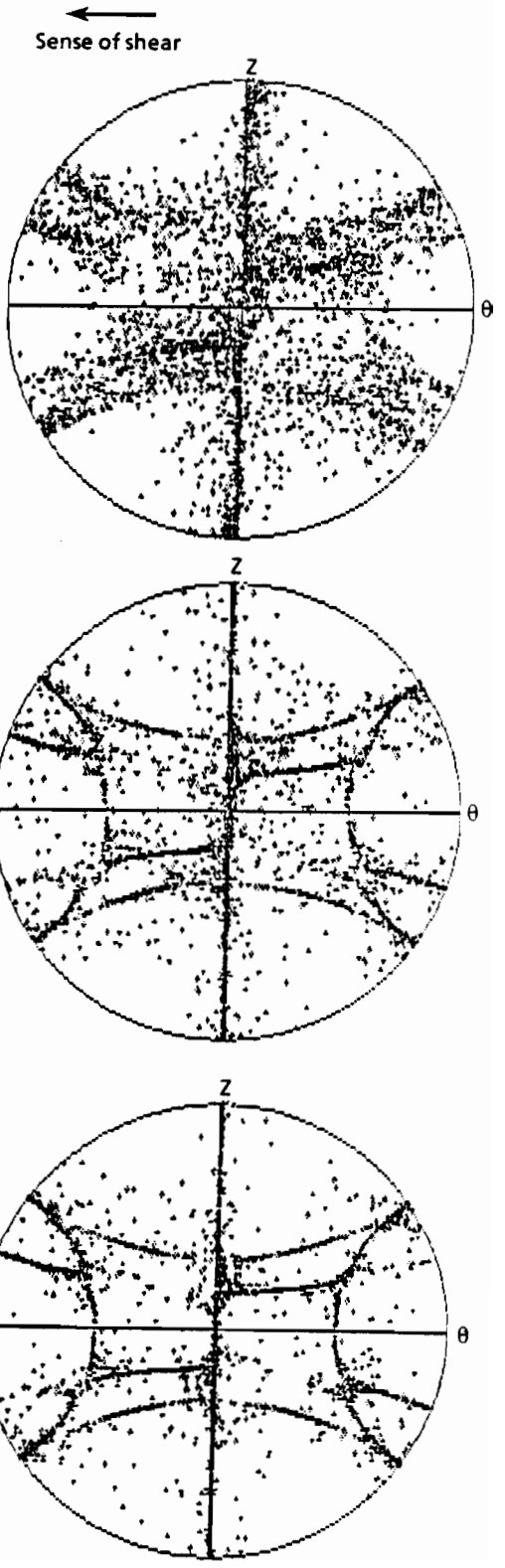

(a) $\bar{\varepsilon}=1$

(b) $\bar{\varepsilon}=3$

(c) $\bar{\varepsilon}=5$

Figure 6.6.
Torsion textures predicted with the FC-HL model.

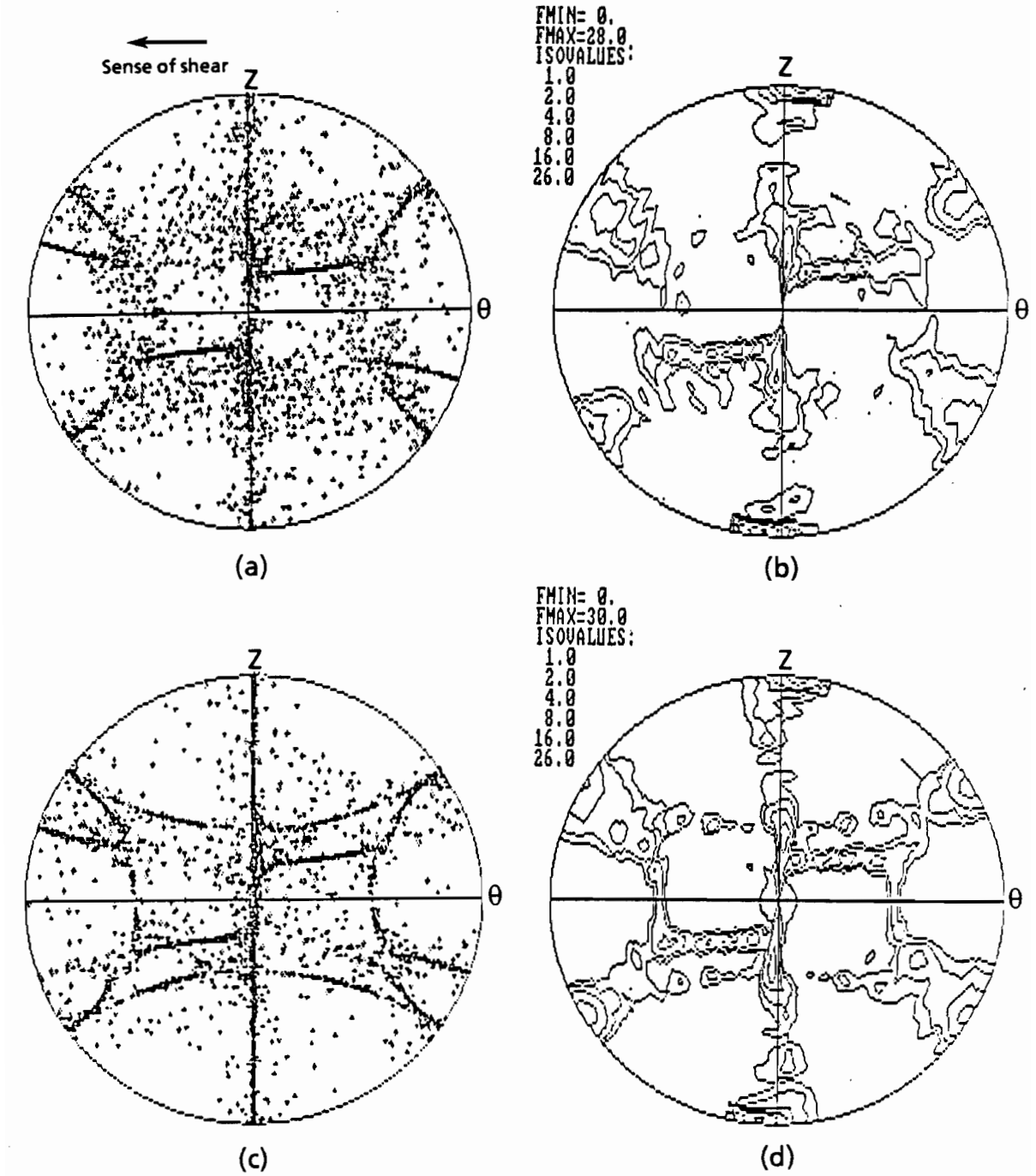

Figure 6.7. Comparison of the torsion textures predicted by the FC-AV and FC-HL models for a strain of $\bar{\varepsilon}=3$, a) and b) FC-AV model, c) and d) FC-HL model.

Whereas the FC+AV model predicts a strong A*/A partial fibre and a partial {hkl}<110> (with a strong A and a strong C component but no B), the FC+HL model predicts a strong A*/A partial fibre, and a complete {100}<uvw> fibre as well as a complete {hkl}<110> fibre (including A/$\bar{A}$, B/$\bar{B}$ and C components) (see Figures 6.7a and c). The FC+HL prediction (Figure 6.7d) would be comparable to the experimental texture of copper deformed at 100°C (Figure 2.26b) if the A/A* present in the simulation were not so strong. This component is usually the major FC component and is not found at high strain levels. Thus the present result contradicts the theory advanced by Leffers [102] which states that when cross-slip takes place in a given material, the deformation is fairly homogeneous within each grain, and every grain deforms according to the FC mode. However, the results obtained with the FC+HL model are interesting because of the increase in the B component, which is characteristic of high temperature deformation.

We turn now to the case of rolling. Again the FC+HL model was used and some simulated textures are presented in Figure 6.8 for an equivalent strain of 3. Unlike the cases of tension and torsion, the results obtained with the FC+AV and FC+HL models are similar. In particular, it is impossible to determine whether the brass component is stronger in the FC+HL calculation or not. Looking carefully at Figures 6.8a and 6.8c, it can be seen that a small number of grains is located around the brass position with the FC+AV model. However, it is difficult to determine whether these grains are approaching or leaving the brass position. With the FC+HL model on the other hand, a very small number of grains is located exactly at the brass position. This proportion is too small to be seen on the iso-density lines of Figure 6.8d. It can be added, however, that the near brass oriented grains in the FC-AV simulation are typical of the spread due to the averaging technique. In the FC-HL simulation, some grains do rotate towards the brass position. So, the small proportion of the brass component observed in the two calculations is not thought to be due to the same mechanism.

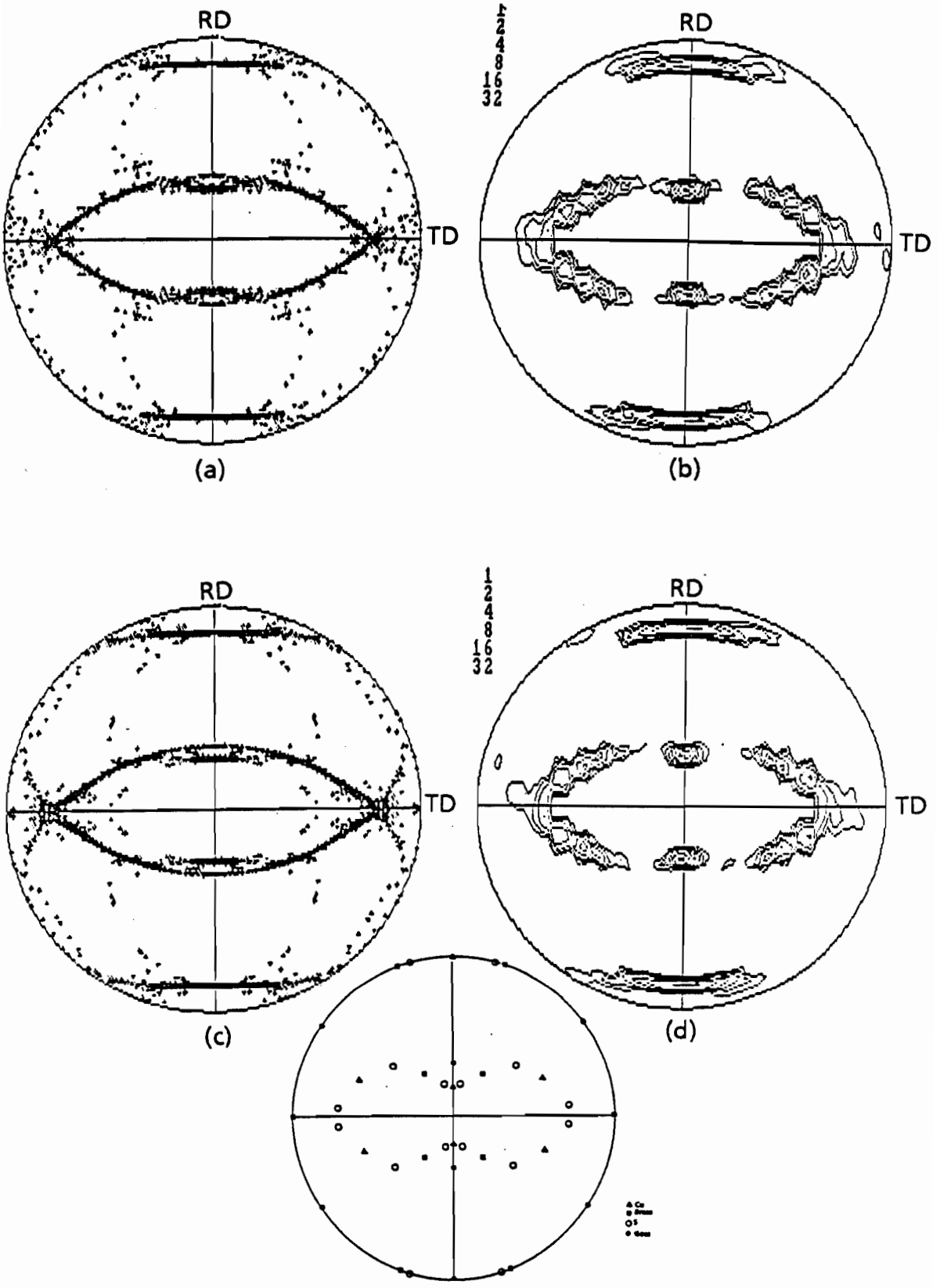

Figure 6.8. Rolling textures predicted for a strain of $\bar{\varepsilon}=3$, a) and b) FC-AV model, c) and d) FC-HL model.

VI.2.3. THEORETICAL RESULTS OBTAINED WITH THE FC-RC MODEL

The FC-RC + AV and FC-RC + HL models are compared in Figures 6.9 and 6.10 for the case of torsion for strains of $\bar{\varepsilon} = 3$ and 6. In Figure 6.10, the values of the densities are plotted for the same strains. At the final strain of 6, the FC + RC + AV texture is composed of a strong C component and a minor A/$\bar{A}$ component. A* has disappeared almost completely and B is nearly absent. The FC-RC + HL texture on the other hand, is still composed of a strong C component, but the A/$\bar{A}$, A* and B/$\bar{B}$ components are more visible than in the other model. The FC texture seems to be retained to a larger deformation than with the FC-RC + AV model. The increase in the B/$\bar{B}$ component, although rather small, is again in good agreement with experimental observations. Looking at Figure 2.26, where the final torsion textures for copper deformed at different temperatures are displayed, it is apparent that the FC + HL texture represented with density lines (Figure 6.10) is not very far from the observations for a temperature around 100°C. The C component, however, is still too strong.

Figure 6.11 illustrates the case of rolling for a strain of 3. The FC-RC + AV and FC-RC + HL results are compared and, somewhat surprisingly, a significant difference can be observed in this case (unlike with the FC model): the brass component develops with the FC-RC + HL model, whereas it is completely absent from the FC-RC + AV prediction. Again here it remains very weak. This could be due to the parameters selected or to the fact that the hardening law used remains very simple and approximate. Nevertheless, the FC-RC + HL model seems to be in better agreement with high temperature results than the FC-RC model.

VI.3. DISCUSSION AND CONCLUSIONS

Two different models have been used in this chapter to simulate the ease of cross-slip. In comparison with the results obtained from the classical FC and FC-RC theories, these models lead to little or no difference in the predicted textures. However, whenever a difference is observed, the predicted texture is

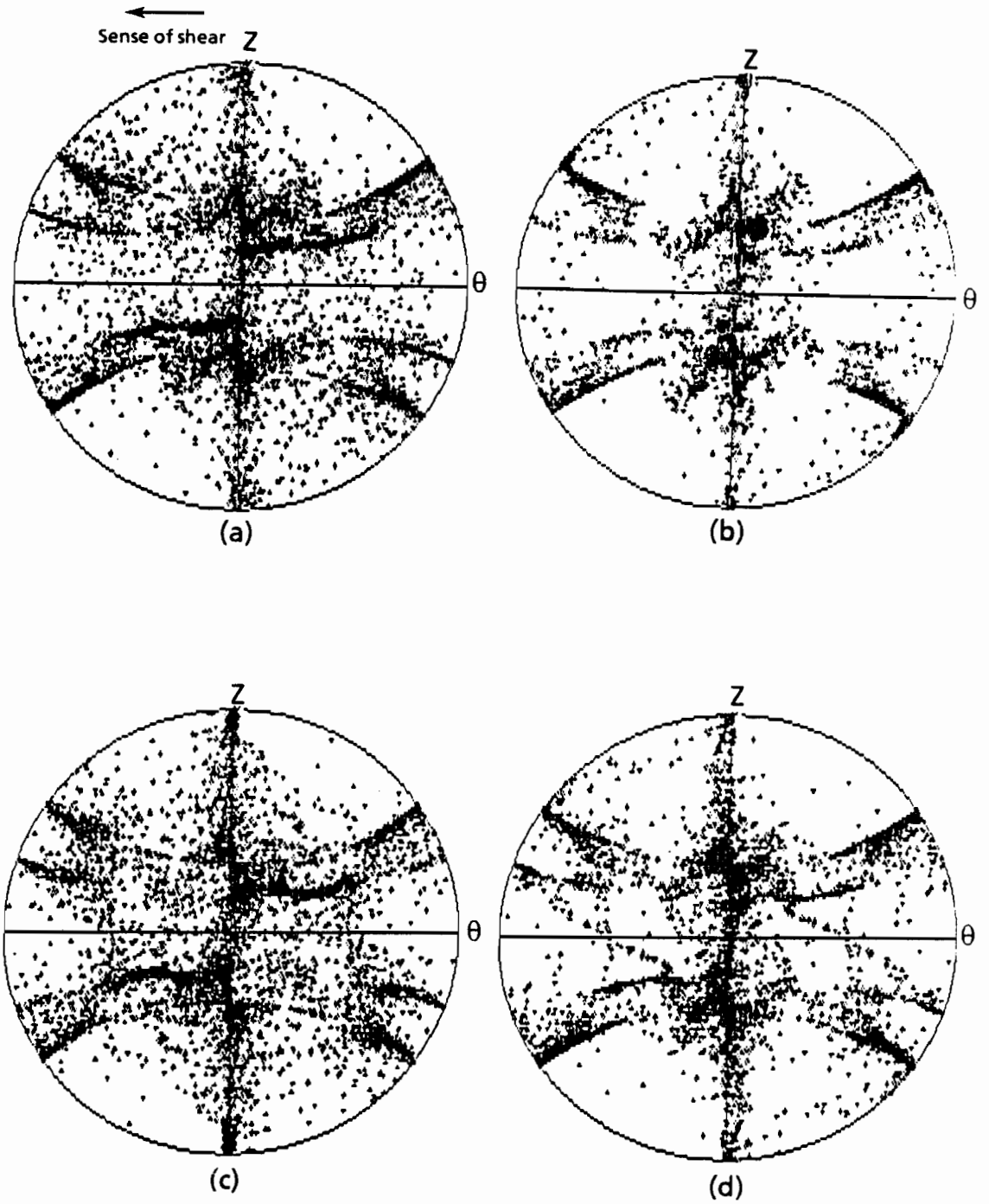

Figure 6.9. Torsion textures predicted at different strains, a) FC-RC+AV, $\bar{\varepsilon}=3$, b) FC-RC+AV, $\bar{\varepsilon}=6$, c) FC-RC+HL, $\bar{\varepsilon}=3$ and d) FC-RC+HL, $\bar{\varepsilon}=6$.

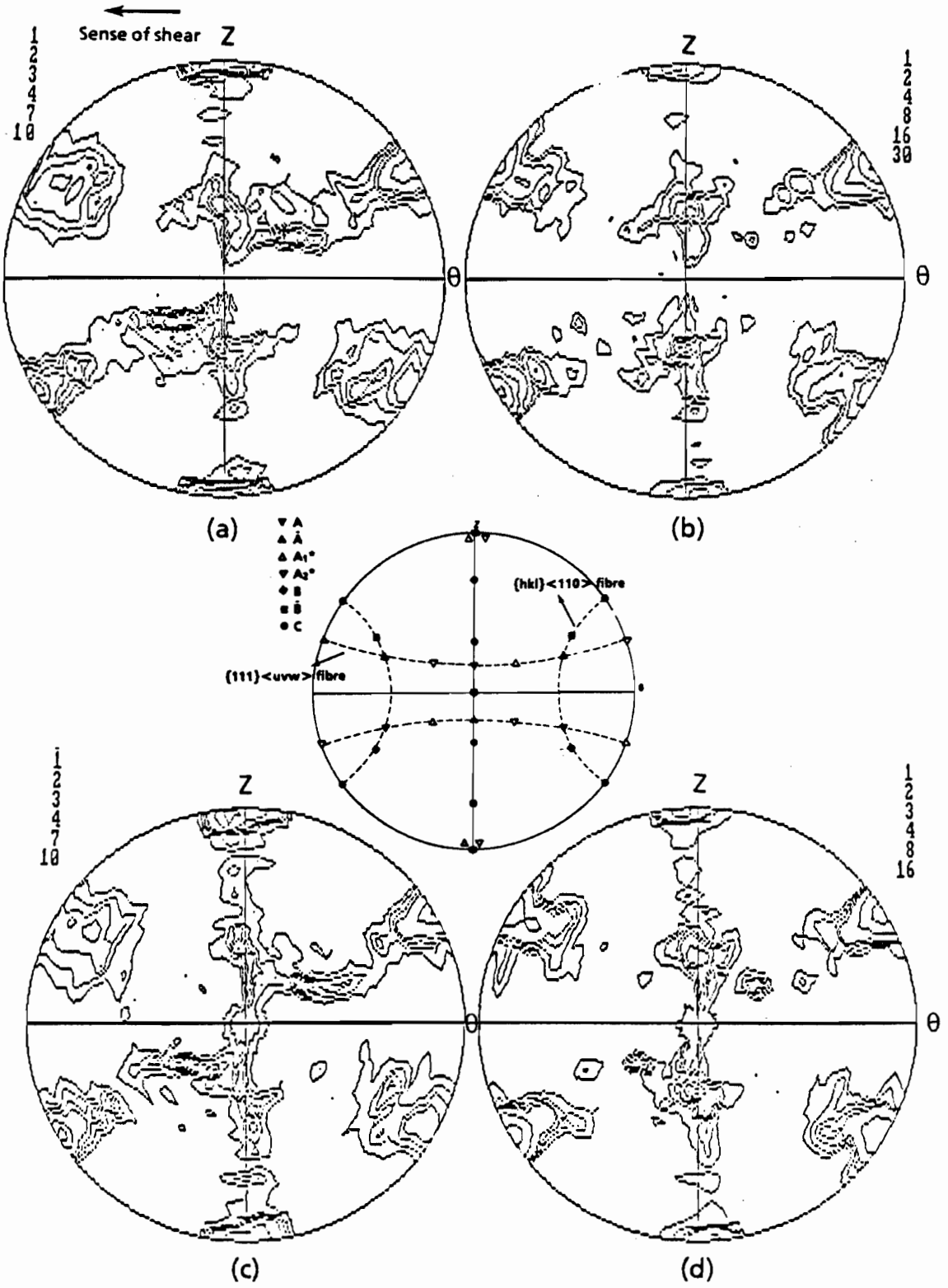

Figure 6.10. The torsion textures of Figure 6.9 represented with density lines. a) FC-RC + AV, $\bar{\varepsilon} = 3$, b) FC-RC + AV, $\bar{\varepsilon} = 6$, c) FC-RC + HL, $\bar{\varepsilon} = 3$, and d) FC-RC + HL, $\bar{\varepsilon} = 6$. Note the development of the B component with the FC-RC + HL model.

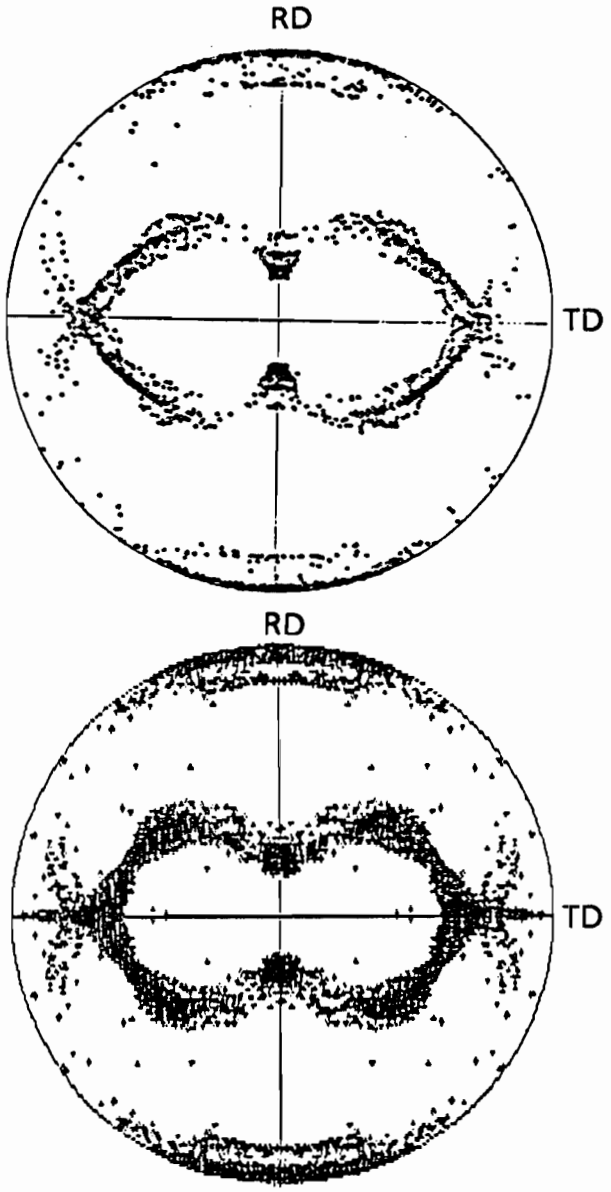

Figure 6.11.
Rolling textures predicted for a strain of 3 with:

(a) the FC-RC + AV model

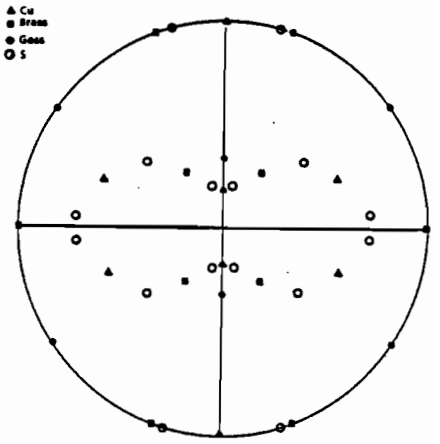

(b) the FC-RC + HL model.

in better agreement with the experimental observations associated with high temperature deformation.

The first model (CS) leads to smaller differences than the second (HL). This is due to the larger number of ambiguities present and the effect of the averaging technique in such cases. However, the two models lead to the same predicted texture in the case of tension.

The two models are both related to the presence of ambiguities. This is clear for the first approach, in which a selection criterion operates. In the second, the allowance for differences in τ_c has the effect of changing the shape of the SCYS in the following way: the 6 or 8-fold vertices are split into vertices associated with only 5 slip systems. This can be interpreted as an indirect way of selecting a single combination among the available ones. The edges are less affected by this procedure, because of the smaller number of planes intersecting an edge. Only the stress states are changed appreciably.

Ambiguities are present in a large proportion of the grains in the case of tension. The region around <110> represented by dashed lines on Figure 6.1 involves ambiguities. Thus, by introducing selection criteria, the texture can be modified. This is as true for the cross-slip criterion as for the RW procedure examined in Chapter V. However, in torsion and rolling, the extent of the ambiguities is reduced even in the FC model. This is why the two cross-slip models do not change the textures predicted in torsion and rolling by a significant amount.

Although the number of ambiguities is reduced in the RC model, the remaining ones affect a small proportion of the grains in torsion and rolling and, consequently, some differences are observed between the predictions of the FC-RC + AV and FC-RC + HL models. The extent of the ambiguities is not only determined by the number of combinations displayed in Tables 5.1-5.4 and the orientations of the grains, but is also affected by the deformation path (i.e. whether this is tension, rolling or torsion).

The main conclusion of this chapter is that the observed differences, though small, are in good agreement with experimental results in tension, torsion and rolling. This is also what was expected from the introduction of the hardening parameters. It has already been pointed out by others that latent hardening also has only a secondary effect on texture prediction [139] and that different hardening laws lead in general to similar predictions [156].

Moreover, cross-slip is not expected to be the only reason for the differences observed between experimental observations at low and high temperatures.

The limited influence on the deformation textures predicted by our two models therefore seems reasonable.

We turn now to another possible cause of difference: the activation of different slip systems.

CHAPTER VII

THE ACTIVATION OF OTHER THAN {111}<110> SLIP SYSTEMS

When the temperature is increased, the critical resolved shear stress of the {111}<110> systems decreases. It is also possible that the CRSS of other slip systems decreases sufficiently over the same interval that these become activated. The most probable ones in fcc materials are the {100}<110>, because the {100} planes are the most densely packed after the {111}. The activation of these systems has in fact been observed at elevated temperatures [152]. For this reason, it was decided to perform simulations using the classical FC and FC-RC models by adding the {100}<110> systems to the 24 {111}<110>. For this purpose, a new SCYS was first derived. In this way, the extent of the ambiguities present in such a case was determined, and the average rotation calculated. It should be noted that, although linear programming could have been used to avoid having to construct the new polyhedron, nothing would then have been known about the ambiguities (Section VII.1).

Slip on the {110} and {112} planes has also been reported in aluminium deformed above 0.35 T_m [159]. Slip on planes other than the {111} was interpreted in these cases in terms of cross-slip from a {111} to a {110} or {112} plane, especially in the instances where all the {111} planes were equally activated and where cross-slip from one {111} plane to another {111} plane was not favored (Section VII.2). This is the case for most of the stable experimental orientations in torsion and rolling, which is why the cross-slip models described previously lead to such small texture differences. {100}<110> slip can also be interpreted in terms of cross-slip, in this case from a given {111} plane to another, resulting in apparent slip on a {100} plane.

The incorporation of other slip systems than the usual ones can therefore be seen as another way of simulating differences in the ease of cross-slip in fcc materials, even if the activation of these systems seems in itself unrealistic.

Such a way of simulating cross-slip is preferable to the models developed by Wierzbanowski [129] and Gangli and Arato [160], for example, in which only the {111}<110> systems were considered, but in which a certain amount of shear was added somewhat arbitrarily on a colinear system which was not otherwise activated (in other words, the Schmid law was not respected for these systems).

VII.1. THE ACTIVATION OF {100}<110> SYSTEMS

VII.1.1. CONSTRUCTION OF THE COMPOSITE {111}+{100} YIELD SURFACE

The 6 {100}<110> systems are listed in Table 7.1, together with the 24 {111}<110>. This table includes the coordinates of all the systems considered in terms of the notation described in Appendix 2. It should first be noted that the {100}<110> systems are not independent 5 by 5 (i.e. their first two components are all equal to zero), which means that they cannot by themselves accommodate any imposed strain rate vector. In order to be able to perform a Bishop and Hill type of calculation (i.e using the principle of maximum work), the possible stress states (the coordinates of the vertices of the yield surface) have to be known. The method used to calculate these will now be described.

The characterization of the vertices of the 5 dimensional yield surface can be done numerically by considering all the combinations of 5 out of 36 slip systems (defined by N^i) and determining if there exists a solution to the following linear problem:

$$\sigma.N^i = \tau_c^i \quad \textit{for } i = 1,5 \tag{7.1}$$

$$\sigma.N^i \leq \tau_c^i \quad \textit{for the others}$$

Here σ is normalized by the CRSS of the {111}<110> systems such that $\tau_{c1}=1$ for the {111}<110> and $\tau_{c2}=\alpha$ for the {100}<110>. If the determinant of this set of equations differs from zero, then the systems under consideration are independent and it is possible to define a stress state that activates them. This

System no. i.	Slip plane n	Slip dir. b	Coordinates of N^i				
			m_1	m_2	m_3	m_4	m_5
1-13	$11\bar{1}$	011	$1/2\sqrt{3}$	-1/2	0	$1/2\sqrt{3}$	$1/2\sqrt{3}$
2-14	$11\bar{1}$	101	$-1/2\sqrt{3}$	-1/2	$1/2\sqrt{3}$	0	$1/2\sqrt{3}$
3-15	$11\bar{1}$	$1\bar{1}0$	$-1/\sqrt{3}$	0	$1/2\sqrt{3}$	$-1/2\sqrt{3}$	0
4-16	$1\bar{1}\bar{1}$	$01\bar{1}$	$-1/2\sqrt{3}$	1/2	0	$-1/2\sqrt{3}$	$1/2\sqrt{3}$
5-17	$1\bar{1}\bar{1}$	101	$-1/2\sqrt{3}$	-1/2	$-1/2\sqrt{3}$	0	$-1/2\sqrt{3}$
6-18	$1\bar{1}\bar{1}$	110	$-1/\sqrt{3}$	0	$-1/2\sqrt{3}$	$-1/2\sqrt{3}$	0
7-19	$1\bar{1}1$	011	$-1/2\sqrt{3}$	1/2	0	$1/2\sqrt{3}$	$1/2\sqrt{3}$
8-20	$1\bar{1}1$	$10\bar{1}$	$-1/2\sqrt{3}$	1/2	$1/2\sqrt{3}$	0	$-1/2\sqrt{3}$
9-21	$1\bar{1}1$	110	$-1/\sqrt{3}$	0	$1/2\sqrt{3}$	$1/2\sqrt{3}$	0
10-22	111	$01\bar{1}$	$1/2\sqrt{3}$	-1/2	0	$-1/2\sqrt{3}$	$1/2\sqrt{3}$
11-23	111	$10\bar{1}$	$-1/2\sqrt{3}$	-1/2	$-1/2\sqrt{3}$	0	$1/2\sqrt{3}$
12-24	111	$1\bar{1}0$	$-1/\sqrt{3}$	0	$-1/2\sqrt{3}$	$1/2\sqrt{3}$	0
25-31	100	011	0	0	0	1/2	1/2
26-32	100	$01\bar{1}$	0	0	0	-1/2	1/2
27-33	010	101	0	0	1/2	0	1/2
28-34	010	$10\bar{1}$	0	0	-1/2	0	1/2
29-35	001	110	0	0	1/2	1/2	0
30-36	001	$1\bar{1}0$	0	0	-1/2	1/2	0

Table 7.1. Coordinates of the 36 slip systems associated with the composite yield surface (notation described in Appendix 2).

implies a considerable amount of computing time and selection afterwards to determine all the *different* stress states.

The computing time can be reduced if the method developed by Tomé and Kocks [106] is used. They established a general procedure which takes into consideration the symmetries of the single crystal. They then derived the minimum number of slip systems and vertices required for a complete description of the yield surface. Once a vertex is found by the computer, it is automatically compared to the previously calculated vertices and, if it coincides

with one of these (case in which more than 5 hyperplanes intersect at the same point), the new slip systems associated with the vertex are added to the previous ones. Once this numerical determination has been carried out, it is possible to calculate analytically the coordinates of one of the vertices in each symmetry group. This method is completely general, can be used for any structure, and is very efficient when nothing is known a priori about the yield surface.

In the present case, we decided to use another method (based on that of Tomé and Kocks) which takes advantage of the detailed knowledge available of the classical Bishop and Hill yield surface. This method is more elegant and still reduces the computing time. All the vertices, 4th, 3rd and 2nd order edges of the conventional BH yield surface were tabulated by Kocks et al. [105]. The notation they used is specified in Tables 5.1 to 5.4 but they also listed the activated systems and surrounding vertices associated with each edge.

With all this information available, we are now ready to derive analytically the vertices of the new SCYS by determining where the planes associated with the new systems, i.e. the {100}<110> ones, intersect the BH polyhedron. But first, let us define the range of variation of α. The latter coefficient represents $1/\sqrt{2}$ times the distance of a given {100}<110> plane from the origin of the yield surface (when the stress states are normalized by τ_{c1}, the CRSS of the {111}<110> systems). If α is such that none of the vertices of the BH yield surface is eliminated by the addition of the new systems, the yield surface remains unchanged and the new slip systems are never activated. Thus, every stress state of the BH polyhedron which satisfies the relation:

$$\sigma_{BH} \cdot N^j > \alpha \tag{7.2}$$

for at least one of the 12 {100}<110> systems (indexed j), lies outside the new yield surface. The points of intersection can be located on the facets of this YS (where only one {111}<110> system is activated), or on the edges (where 2 to 6 are activated) or even at the vertices. They constitute new vertices if they activate at least 5 independent systems. The case of the facets is eliminated since it implies the activation of 4 {100}<110> systems, which are not independent 4 by 4.

Let us now consider the vertices of the BH polyhedron. To determine whether or not these are retained by the cutting procedure, we calculated the product $\sigma^i.N^j$ for each of the 28 stress states σ^i of the BHYS and every N^j vector associated with each of the 6 (plus opposite) {100}<110> systems. The results of this calculation are listed in Table 7.2. It can readily be seen that if α is greater than $\sqrt{3}$, the new systems never intersect the BHYS. For α ranging from $\sqrt{3}$ to $\sqrt{3/2}$, some vertices are retained and others are eliminated by at least one new system. For α less than $\sqrt{3/2}$, a completely new configuration exists. However, we are not interested in this case because it would signify that the {100}<110> systems are more easily activated than the {111}<110>, which is unrealistic. We will therefore examine only the case where

$$\sqrt{3/2} < \alpha < \sqrt{3} \tag{7.3}$$

Looking at Table 7.2, it is evident that for this specific range of α, the type A and E vertices still lie on the "dual" yield surface, whereas those of types B, C and D are eliminated. Turning now to the edges, it can readily be determined whether a particular edge is retained completely, only partly, or eliminated entirely when the surface is cut by new planes. In this procedure, it is sufficient to consider only one edge of each type because of the cubic symmetry. All the other edges of the same type (i.e. 4A to 4H, 3A to 3G and 2A to 2E) can be deduced from the first by applying symmetry operations. Furthermore, if a new vertex is found on a particular edge, the vertices associated with the other edges of the same group can also be found by applying the symmetry operations to the first vertex.

Let us consider, as an example, a 4th order edge of type 4C, number 19. This edge is defined by vertex numbers 4 and 8 (in the Kocks et al. notation). The points along this edge can be expressed as

$$\sigma = \alpha_1 \sigma^4 + \alpha_2 \sigma^8 \tag{7.4}$$

with

$$\alpha_1 + \alpha_2 = 1 \qquad and \qquad \alpha_1, \alpha_2 \geq 0$$

Such points lie on the new YS if they satisfy the condition:

$$\sigma . N^j \leq \alpha \tag{7.5}$$

for each of the 12 {100}<110> systems N^j. Furthermore, if $\sigma.N^j = \alpha$ for at least one new system, this point constitutes a vertex of the new YS, since 4 systems

Group	Vertex no. i.	$\sigma i.Nj$ for the 28 vertices and the 6 new systems (normalized by $\sqrt{3}$)					
		$\sigma i.N25$	$\sigma i.N26$	$\sigma i.N27$	$\sigma i.N28$	$\sigma i.N29$	$\sigma i.N30$
A	1	0	0	0	0	0	0
	2	0	0	0	0	0	0
	3	0	0	0	0	0	0
B	4	1	0	1	0	1	0
	5	1	0	0	1	0	1
	6	0	1	1	0	0	−1
	7	0	−1	0	−1	1	0
C	8	0	0	1	−1	1	−1
	9	1	−1	0	0	1	1
	10	1	1	1	1	0	0
D	11	1	0	1/2	1/2	1/2	1/2
	12	−1	0	−1/2	−1/2	−1/2	−1/2
	13	0	−1	−1/2	−1/2	1/2	1/2
	14	0	1	1/2	1/2	−1/2	−1/2
	15	1/2	1/2	1	0	1/2	−1/2
	16	−1/2	−1/2	−1	0	−1/2	1/2
	17	1/2	1/2	0	1	−1/2	1/2
	18	−1/2	−1/2	0	−1	1/2	−1/2
	19	1/2	−1/2	1/2	−1/2	1	0
	20	−1/2	1/2	−1/2	1/2	−1	0
	21	−1/2	1/2	1/2	−1/2	0	−1
	22	1/2	−1/2	−1/2	1/2	0	1
E	23	0	0	1/2	−1/2	1/2	−1/2
	24	0	0	−1/2	1/2	−1/2	1/2
	25	1/2	−1/2	0	0	1/2	1/2
	26	−1/2	1/2	0	0	−1/2	−1/2
	27	1/2	1/2	1/2	1/2	0	0
	28	−1/2	−1/2	−1/2	−1/2	0	0

Table 7.2. Value of the product $\sigma i.Nj$ for the 28 vertices of the BH polyhedron and the 6 {100}<110> systems.

are already activated at this particular point (provided also that the 5 systems are independent). On the other hand, if $\sigma.N^j > a$ for at least one system, this stress state is eliminated from the yield surface. From Table 7.2, it is readily seen that the four scalar products $\sigma^4.N^{27}$, $\sigma^4.N^{29}$, $\sigma^8.N^{27}$ and $\sigma^8.N^{29}$ are greater than a, which means that the present two vertices are eliminated in the "cutting" procedure by the two new systems, numbers 27 and 29. For each state of stress lying on this edge, we can evaluate

$$\sigma.N^{27} = a_1 \sigma^4.N^{27} + a_2 \sigma^8.N^{27} > a \tag{7.6}$$

which means that the entire edge, as well as all of the other edges of group 4C, are eliminated in the new YS.

Repeating this procedure for all the different types of edges, we can say without any further calculation and simply by looking at Table 7.2 as well as the tables in reference [105], that the 4C, 4D, 4E, 4F, 3D, 3E and 2B edges do not belong to the new yield surface and only the remaining edges need be considered further. In this way, it can be shown that all of the type 4B and 3B edges are retained. The other ones are only partly retained. We will thus look at a representative example of each of the following groups: 4A, 4G, 4H, 3A, 3C, 3F, 3G, 2A, 2C, 2D and 2E, and determine the new vertices which lie on these edges.

To do so, we take advantage of another property of the BH yield surface, i.e. that each n^{th} order edge is delimited by edges of higher order. For example, a 4^{th} order edge constitutes a one dimensional space and is delimited by 2 vertices. (These are points in 5 dimensional space and thus have no dimension.) This is represented schematically in Figure 7.1a. A 3^{rd} order edge constitutes a two dimensional surface and is delimited by 3 or 4 vertices defining 3 or 4 4^{th} order edges (see Figure 7.1b). Similarly, a 2^{nd} order edge, surrounded by 5, 6 or 8 vertices, constitutes a 3 dimensional volume, whose faces are 3^{rd} order edges and whose edges are 4^{th} order edges (see Figure 7.1c). It is therefore possible to consider only the 2^{nd} order edges (more specifically one of each type), since they include all the possible types of 3^{rd} and 4^{th} order edges, and determine on these where the planes associated with the new systems intersect to create vertices.

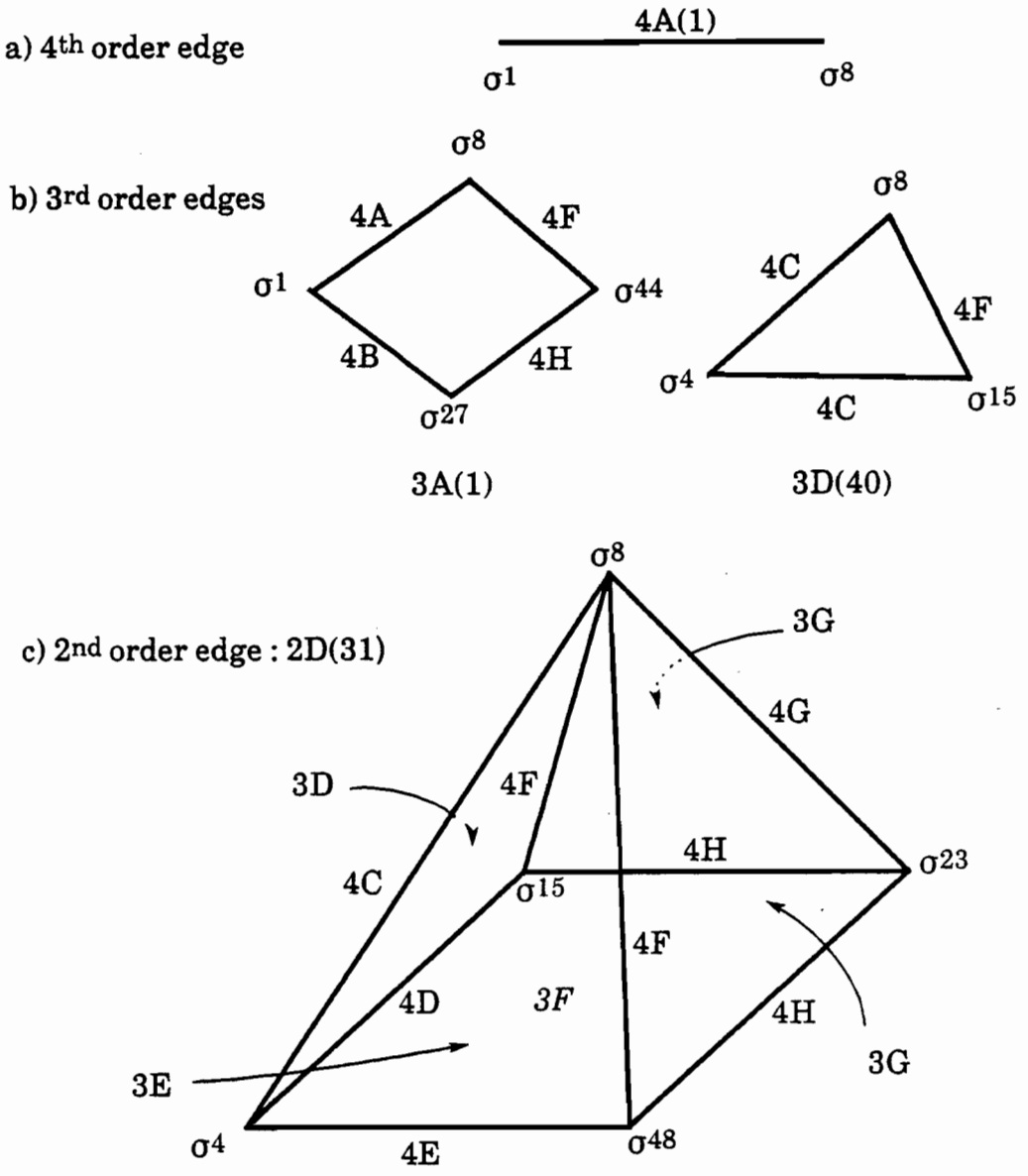

Figure 7.1. Examples of edges of different types (notation of Kocks et al. [105]).

The problem can in this way be reduced to the following. We consider a particular 2nd order edge of the BHYS, defined by its connecting vertices and edges, as well as its activated slip systems. We need to know which stress states included in the volume of this edge are part of the new YS, and which ones activate at least 5 independent slip systems so as to constitute a vertex?

If 3 planes associated with the {100}<110> systems intersect at a point within the volume defined by the edge, this point constitutes a vertex since 2 {111}<110> systems are already activated at this point; this situation nevertheless requires that:

1) the 5 systems be independent, and that
2) the stress state considered satisfies the relation $\sigma.N^j \leqq \alpha$ for all the other {100}<110> systems.

If 2 planes intersect at a point of a 3rd order edge (a facet of the 2nd order edge), this point is also a vertex, since 3 systems are already active at this point (provided that the above 2 conditions are again fulfilled). The same holds if a plane intersects a 4th order edge. The two conditions listed above have to be checked every time a new vertex is being tested.

Let us now consider a specific example to describe the complete procedure. Second order edge number 31 of type 2D is delimited by vertices 4, 8, 15, 23 and 48 in the notation of Kocks et al. [105] and is represented schematically in Figure 7.1c, together with the associated edges of 3rd and 4th order. It is already known that, among these different edges, only the 4G, 4H, 3F, 3G and 2D are partly retained, the others being completely eliminated. We can thus examine these edges one by one and establish the actual intersection points.

i) *Edge 4G*: This edge is delimited by vertices 8 and 23 and activates systems 2, 8, 18 and 24. Every stress state lying on this edge is covered by:

$$\sigma = a_1 \sigma^8 + a_2 \sigma^{23} \tag{7.7}$$

with

$$a_1 + a_2 = 1 \qquad \textit{and} \qquad a_1, a_2 \geq 0$$

Looking at Table 7.2, we can see that systems 27, 29, 34 and 36 intersect this edge. Calculating the product $\sigma.N^j$ for these 4 systems gives us:

$$\begin{aligned} \sigma.N^{27} &= \sqrt{3}(a_1 + a_2/2) \\ \sigma.N^{29} &= \sqrt{3}(a_1 + a_2/2) \\ \sigma.N^{34} &= \sqrt{3}(a_1 + a_2/2) \\ \sigma.N^{36} &= \sqrt{3}(a_1 + a_2/2) \end{aligned} \tag{7.8}$$

If one of these products is equal to α, the corresponding stress state constitutes a vertex of the new yield surface (provided that the independence of the systems is satisfied). It is readily seen that for:

$$\sigma = \sigma^8 + \beta(\sigma^{23} - \sigma^8) \quad with \quad \beta = 2(1 - \alpha/\sqrt{3}) \tag{7.9}$$

the 4 systems are critical and this point constitutes a vertex of the yield surface associated with the 8 systems: 2, 18, 8, 24, 27, 29, 34 and 36 (4 {111}<110> and 4 {100}<110> systems). This of course requires that a combination of 5 independent systems can be found among the 8, a matter which will be checked later.

ii) *Edge 4H*: This edge is defined by vertices 48 and 23 and is associated with the 5 slip systems 1, 2, 8, 16, and 18. Repeating the above procedure, we find that the stress state:

$$\sigma = \sigma^{48} + \beta(\sigma^{23} - \sigma^{48}) \quad with \quad \beta = 2(1 - \alpha/\sqrt{3}) \tag{7.10}$$

activates the following 6 systems: 1, 2, 8, 16, 18 and 35 (i.e. 5 {111}<110> +1 {100}<110> systems).

iii) *Edge 3G*: Edge number 113 is delimited by vertices 8, 15 and 23 and systems 2, 18 and 24. Every stress state lying on this edge can be represented by:

$$\sigma = a_1\sigma^8 + a_2\sigma^{15} + a_3\sigma^{23} \tag{7.11}$$

with

$$a_1 + a_2 + a_3 = 1 \quad and \quad a_1, a_2, a_3 \geq 0$$

We now calculate the product $\sigma.N^j$ for systems 27, 29, 34 and 36, since only these new systems intersect with edge 3G. The stress state σ constitutes a vertex if at least 2 of the 4 products are equal to α. The 4 inequalities involved (expressing the fact that σ lies on the yield surface) are

$$\begin{aligned}
\sigma.N^{27} &= \sqrt{3}(a_1 + a_2 + a_3/2) \leq \alpha \\
\sigma.N^{29} &= \sqrt{3}(a_1 + a_3/2) \leq \alpha \\
\sigma.N^{34} &= \sqrt{3}(a_1 + a_2/2 + a_3/2) \leq \alpha \\
\sigma.N^{36} &= \sqrt{3}(a_1 + a_2/2 + a_3/2) \leq \alpha
\end{aligned} \tag{7.12}$$

The only possible solution is $\alpha_2 = 0$, which means that the point lies on edge 4G and has already been found. Thus there is no new vertex within (and strictly within) the triangle defined by vertices 8, 15 and 23.

iv) *Edge 3F*: This edge is defined by vertices 4, 15, 23 and 48 and associated with systems 1, 2 and 18. We now repeat the procedure employed above for edge 3G but carry it out twice for the two groups of vertices 4, 15, 48 and 4, 23, 48. In this case, we find a vertex fulfilling the condition:

$$\sigma = \sigma^4 + \beta(\sigma^{23} - \sigma^4) \quad with \quad \beta = 2/\sqrt{3}(\sqrt{3} - a) \tag{7.13}$$

It activates 3 {111}<110> systems (1, 2 and 18) and two {100}<110> systems (27 and 29).

v) *Edge 2D*: To find the vertices located within edge 2D, we decompose this edge into 2 separate volumes: one is delimited by vertices 4, 8, 15 and 48 and the other by vertices 8, 15, 23 and 48. Any stress state lying within the first volume is described by:

$$\sigma = \alpha_1\sigma^4 + \alpha_2\sigma^8 + \alpha_3\sigma^{15} + \alpha_3\sigma^{48} \tag{7.14}$$

with

$$\alpha_1 + \alpha_2 + \alpha_3 + \alpha_4 = 1 \quad and \quad \alpha_1, \alpha_2, \alpha_3, \alpha_4 \geq 0$$

Systems 25, 27, 34, 29 and 36 intersect with this volume. Three of these have to intersect at the same point to create a new vertex (since two systems are already active on edge 2D). The set of inequalities to be satisfied is:

$$\begin{aligned}
\alpha_1 + \alpha_3/2 + \alpha_4/2 &\leq a/\sqrt{3} \\
\alpha_1 + \alpha_2 + \alpha_3 + \alpha_4/2 &\leq a/\sqrt{3} \\
\alpha_2 + \alpha_4/2 &\leq a/\sqrt{3} \\
\alpha_1 + \alpha_2 + \alpha_3/2 + \alpha_4 &\leq a/\sqrt{3} \\
\alpha_2 + \alpha_3/2 &\leq a/\sqrt{3}
\end{aligned} \tag{7.15}$$

With the extra condition that $\Sigma\alpha_i = 1$, this can be rewritten as:

$$\begin{aligned}
&(1) \quad 2\alpha_2 + \alpha_3 + \alpha_4 \geq 2(1 - a/\sqrt{3}) \\
&(2) \quad \alpha_4 \geq 2(1 - a/\sqrt{3}) \\
&(3) \quad 2\alpha_2 + \alpha_4 \leq 2a/\sqrt{3}
\end{aligned} \tag{7.16}$$

$$(4) \qquad \alpha_3 \geq 2\,(1 - \alpha/\sqrt{3})$$

$$(5) \qquad 2\,\alpha_2 + \alpha_3 \leq 2\alpha/\sqrt{3}$$

and can be solved geometrically, as shown in Figure 7.2. Only equations (7.16) have been represented on this figure and it is evident that a point can be found which satisfies at least 3 of these relations. This point does not, however, fulfill the condition $\Sigma\alpha_i = 1$ and therefore cannot be retained. As it was the only possible point, there is no solution to the problem expressed by equation 7.16 and there is no new vertex in this volume.

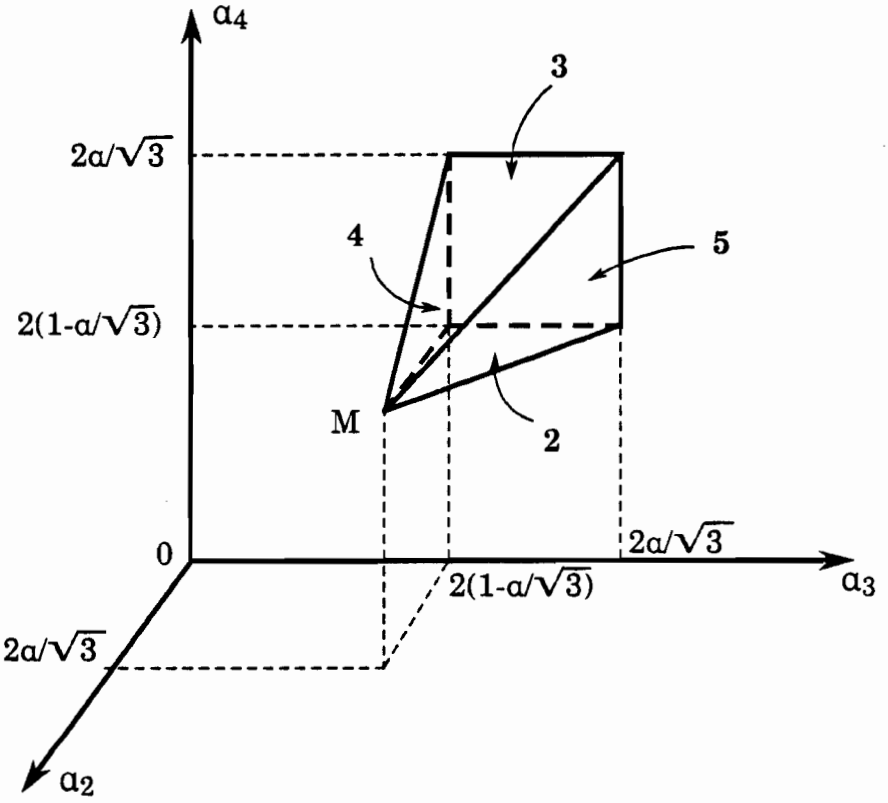

Figure 7.2. Geometrical solution of the set of equations 7.16. The point M is the only one where at least 3 planes intersect. The bold numbers refer to the equation numbers. At point M, equations 2, 3, 4 and 5 are satisfied.

The above procedure can be repeated for one of each second order edge of types 2A, 2C and 2E to enable all the vertices of the yield surface to be determined analytically.

VII.1.2. DESCRIPTION OF THE COMPOSITE {111}+{100} YIELD SURFACE

The procedure described above leads to the determination of the stress states which activate at least 5 systems among the 36 available. It remains to check if, among the 5, 6 or 8 found, it is possible to find 5 which are independent. This has been done with the aid of a computer and it was thus found that the new yield surface is composed of 93 vertices divided into 8 groups. These are defined in Table 7.3, which gives the vertices or edges of the BH yield surface on which these new vertices are located, the number of vertices in each group, as well as the number of combinations of 5 independent systems associated with each vertex. Also included are the coordinates of one representative of each group. The coordinates of the 93 vertices and the associated systems are listed completely in Appendix 7.

It should be noted that for 21 vertices out of 93, the extent of the ambiguities is expected to be large (32, 36 or 40 combinations are possible), whereas for the 72 others, there is only one possible combination of 5 independent slip systems.

We can now derive the 4^{th} order edges, so as to have an idea of the ambiguities present in an RC calculation. These edges were determined by the method of Kocks et al. [105], i.e. by examining the connections between vertices and testing whether these pairs activate at least four common slip systems. The independence of the systems also has to be verified. A similar procedure was used to determine the 3^{rd} order edges and the results are presented in Tables 7.4 and 7.5. It can be seen that the composite YS comprises 288 4^{th} order edges associated with 672 combinations of 4 independent systems and 310 3^{rd} order edges associated with 364 combinations of 3 independent systems. The complete list of the edges (the connecting vertices and the associated systems) is also given in Appendix 7. The procedure described in this paragraph has also been applied with success to the construction of a mixed yield surface for bcc materials [127].

Type	BH edge or vertex	Types of slip planes	No. of vertices	Vertex index, i	No. of comb. of 5 indep. systems	Coordinates of vertex σ^i as a function of α					Norm of σ^i
						σ_1	σ_2	σ_3	σ_4	σ_5	
I	5A	8 {111}	3	1	32x3[b]	$-\sqrt{3}$	-1	0	0	0	2
II	5E	8 {111}	6	4	36x6[b]	$\sqrt{3/2}$	$-3/2$	$\sqrt{3}$	0	0	$\sqrt{6}$
III	4A	4{111}+4 {100}	6	10	40x6[b]	$\alpha-\sqrt{3}$	$\alpha/\sqrt{3}-1$	2α	0	0	2.17
IV	4G	4{111}+4 {100}	6	16	40x6[b]	$\sqrt{3}-\alpha$	$\alpha\sqrt{3}-3$	2α	0	0	2.48
V	4H	5{111}+1 {100}	24	22	4x24[b]	$\alpha-1.5\sqrt{3}$	$0.5-\alpha/\sqrt{3}$	0	$2\alpha-\sqrt{3}$	$\sqrt{3}$	2.37
VI	3F	3{111}+2 {100}	24	46	1x24	$2(\alpha-\sqrt{3})$	0	$2\alpha-\sqrt{3}$	$2\alpha-\sqrt{3}$	$\sqrt{3}$	2.30
VII	2A	2{111}+3 {100}	12	70	1x12	$\alpha-\sqrt{3}$	$\alpha/\sqrt{3}-1$	α	$-\alpha$	α	1.93
VIII	2C	2{111}+3 {100}	12	82	1x12	$\alpha-\sqrt{3}$	$\alpha/\sqrt{3}-1$	α	α	α	1.93
			93[a]		936[a]						

[a]Plus their opposites
[b]Ambiguities present

Table 7.3. Types of vertices making up the composite yield surface.

Type of edge and no. of associated slip systems (n)	Types of slip planes	Types of connecting vertices	Number of edges of given type	Total number of comb. of 4 systems per edge	Number of comb. of 4 independent systems
4A(6)	6{111}	I-II	12	15	12x12[b]
4B(4)	4{111}	I-III	6	1	1x6
4C(4)	4{111}	II-IV	6	1	1x6
4D(5)	5{111}	II-V	24	5	4x24[b]
4E(6)	2{111}+4{100}	III-IV	12	15	13x12[b]
4F(4)	3{111}+1{100}	III-V	24	1	1x24
4G(4)	2{111}+2{100}	III-VII	12	1	1x12
4H(4)	2{111}+2{100}	III-VIII	12	1	1x12
4I(4)	3{111}+1{100}	IV-V	24	1	1x24
4J(4)	2{111}+2{100}	IV-VI	24	1	1x24
4K(5)	4{111}+1{100}	V-V	12	5	4x12[b]
4L(4)	3{111}+1{100}	V-VI	48	1	1x48
4M(4)	2{111}+2{100}	VI-VII	24	1	1x24
4N(4)	2{111}+2{100}	VI-VIII	24	1	1x24
4O(4)	1{111}+3{100}	VII-VIII	24	1	1x24
Totals			288[a]		672[a]

[a]Plus their opposites.
[b]Ambiguities present.

Table7.4. Number of combinations of four independent slip systems under tetraslip (p=4) conditions in the composite yield surface.

VII.1.3. FC-RC PREDICTIONS FOR THE CASE OF DUPLEX SLIP

It was first checked that the extent of the ambiguities in terms of rotations was very small in the case of torsion and rolling for both the FC and FC-RC models. Whenever there were several solutions, however, the average rotation was calculated. The influence of the parameter α was also investigated in the

Type of edge and no. of associated slip systems (n)	Types of slip planes	Types of connecting vertices	Number of edges of given type	Number of comb. of 3 independent systems
3A(3)	3{111}	I-II-III-V	24	1x24
3B(4)	4{111}	I-II-I-II	3	4x3[b]
3C(4)	4{111}	II-I-II-V-V	12	4x12[b]
3D(3)	3{111}	II-V-V-VI	24	1x24
3E(3)	3{111}	II-IV-V	24	1x24
3F(4)	4{100}	III-III-IV-IV	3	4x3[b]
3G(3)	2{111}+1{100}	III-IV-V-V	24	1x24
3H(3)	1{111}+2{100}	III-IV-VI-VII-VIII	48	1x48
3I(3)	2{111}+1{100}	III-V-VI-VII	48	1x48
3J(3)	3{100}	VII-VIII-VII-VIII-VII-VIII	4	1x4
3K(3)	2{111}+1{100}	V-V-VI-VI-VII	24	1x24
3L(3)	1{111}+2{100}	VI-VII-VIII	24	1x24
3M(3)	2{111}+1{100}	IV-V-VI	48	1x48
Totals			310[a]	364[a]

aPlus their opposites.
bAmbiguities present.

Table7.5. Number of combinations of three independent slip systems under trislip (p=3) conditions in the composite yield surface.

FC-RC calculations. It is worth noting that the value of α has no influence on the FC predictions as long as α remains in the range defined above. Although it affects the stress state, the activated slip systems remain the same. This is illustrated in Figure 7.3, where a 2 dimensional section of a composite yield surface is shown. For two different values of α, the stress vector is different, but the active slip systems for a given strain rate vector $\dot{\varepsilon}_{FC}$ remain the same; consequently, the amount of shear on these systems (and in turn the rotation) is the same. In an RC calculation, even if the vertices are associated with the

same systems for different values of α, a plane $\sigma_4 = 0$ can cut the yield surface in different places for different values of α, as also illustrated in Figure 7.3. So the value of α does have an influence on FC-RC predictions.

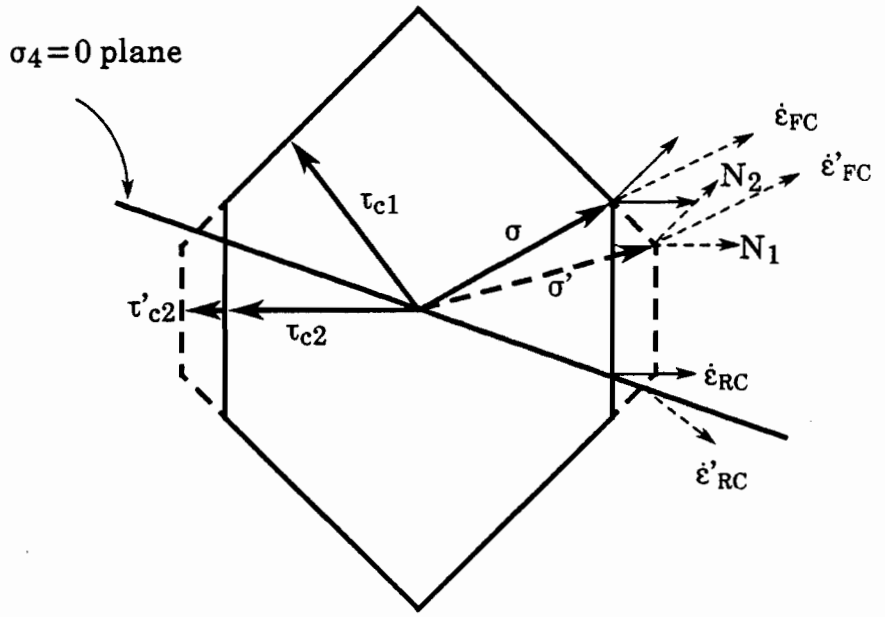

Figure 7.3. A two dimensional section of a composite yield surface. Variation of $\alpha = \tau_{c2}/\tau_{c1}$ does not affect the selection of the active slip systems in the FC mode ($\sigma \neq \sigma'$ but $\dot{\varepsilon}_{FC} = \dot{\varepsilon}'_{FC}$) but can affect selection in the RC mode ($\dot{\varepsilon}_{RC} \neq \dot{\varepsilon}'_{RC}$).

The FC-RC predictions obtained in torsion are presented in Figure 7.4 for $\alpha = 1.5$ and in Figure 7.5 for $\alpha = 0.89$. These two values are located at the two extremes of the allowable range. For $\alpha = 1.5$, the {100}<110> systems cut the BHYS only slightly, so that the predictions are close to the classical FC-FC ones. The A/$\bar{A}$, B/$\bar{B}$ and C components are present in the same proportions: C is the strongest at large strains, followed by A/$\bar{A}$, whereas B/$\bar{B}$ is almost absent. For $\alpha = 0.89$, on the other hand, the {100}<110> systems have more influence in the calculations and a new texture component appears: the {100}<010> component, which activates equally two of the new systems. This component is the equivalent of the C orientation for the {111}<110> systems. Unfortunately, it is not observed at high temperatures. Moreover, introduction of the {100}<110> systems does not lead to an increase in the B/$\bar{B}$ component, as can be seen from Figure 7.5.

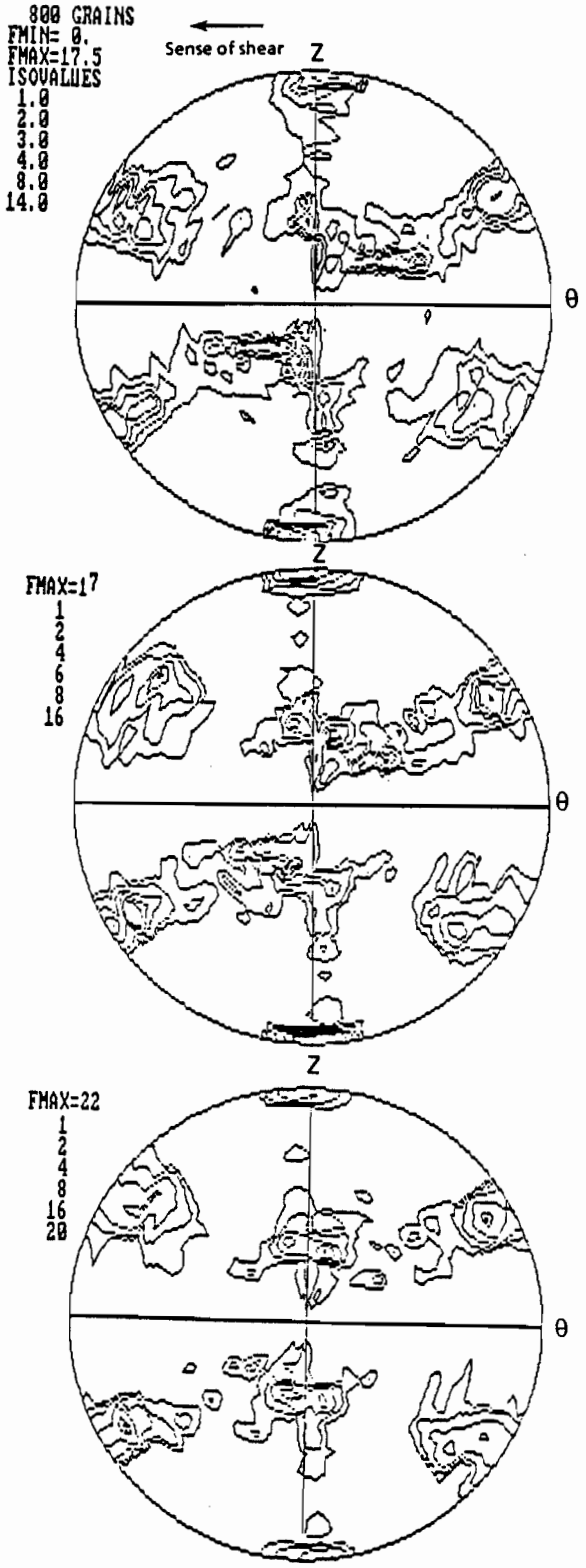

Figure 7.4. Torsion textures predicted using the FC-RC model with $\{111\}+\{100\}<110>$ slip. $\tau_{c(100)}/\tau_{c(111)}=1.5$.

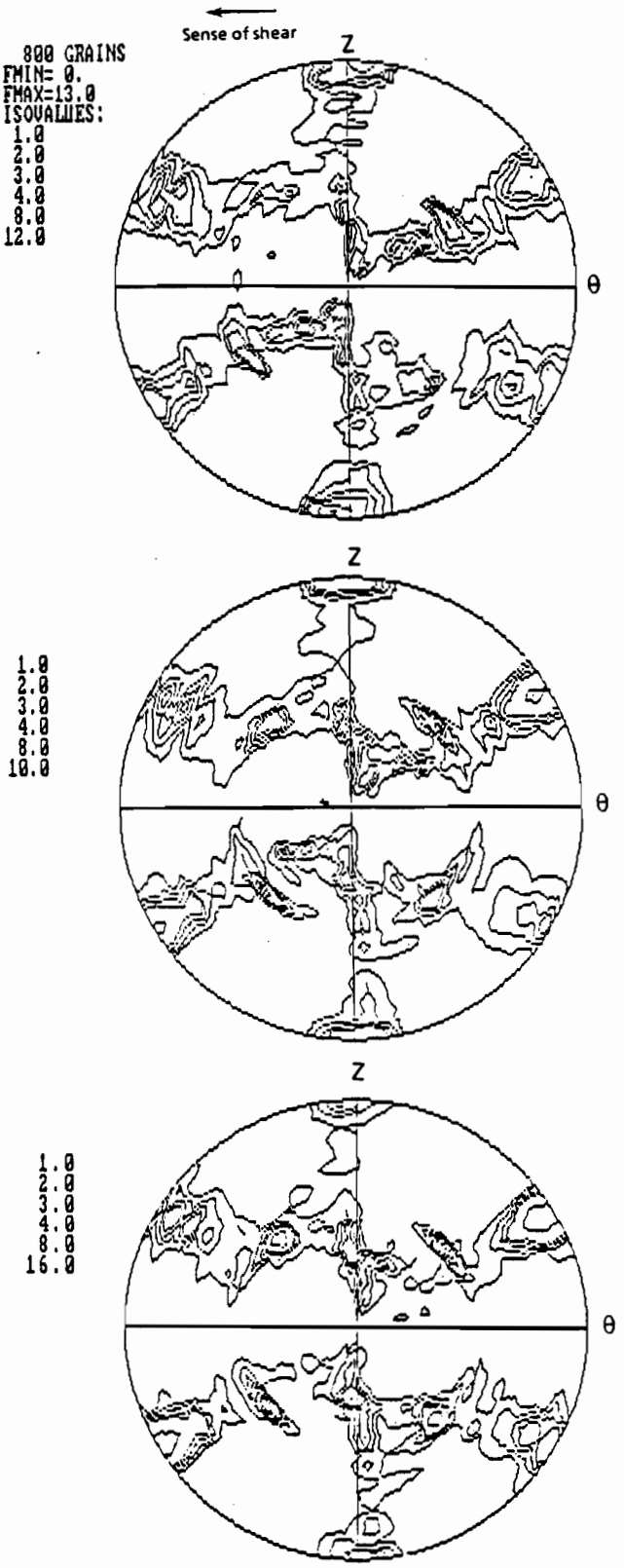

Figure 7.5. Torsion textures predicted using the FC-RC model with {111}+{100}<110> slip. $\tau_{c(100)}/\tau_{c(111)}=0.89$.

Figure 7.6 illustrates the FC-RC predictions obtained for the case of rolling with $\alpha=1$ for strains of 1 and 3. Here again the {100}<010> component is present, together with the copper component. The results are very close to the usual FC-RC predictions, the difference being the addition of the {100}<010>, which is not observed experimentally at high temperatures. The brass component is no stronger than before.

From these figures, it can be seen that the introduction of {100}<110> slip does not lead to the observed high temperature deformation textures. It was thus decided to simulate the addition of the {110}<110> and {112}<110> systems as well, since cross-slip has also been observed on these planes.

VII.2. ACTIVATION OF THE {110}+{112}<110> SYSTEMS

The incorporation of these systems is based on the experimental observations of Le Hazif et al. [161]. These authors reported that slip on the {110} and {112} planes is possible in fcc materials under some conditions. They compressed single crystals of Ag, Al, Au, Cu and Ni with a {100} axis parallel to the compression axis in each case. They then determined the temperatures T_1 under which only the {111} planes were active and the temperatures T_2 above which only the {110} planes were active. They also found that there was a nearly linear relationship between T_1 (or T_2) and $1/\gamma$ (the SFE). They interpreted their observations in terms of cross-slip from {111} to {110} planes and defined a critical resolved shear stress for cross-slip which is strongly dependent on the temperature, especially for the two types of slip plane quoted above.

They proposed the following mechanism to account for their observations: for the particular orientation studied, deformation takes place, in the early stages, by an equal amount of slip on the 4 {111} planes. Since all the {111} are primary planes and dislocations are equally hindered on all of them, nothing would be gained by cross-slipping from one to another. The deformation can only be continued if the dislocations are able to escape onto {110} planes. Then, the glide may be stabilized on the latter by the creation of stable stacking faults on these planes. Their T_1 and T_2 temperatures for aluminum were 77 and

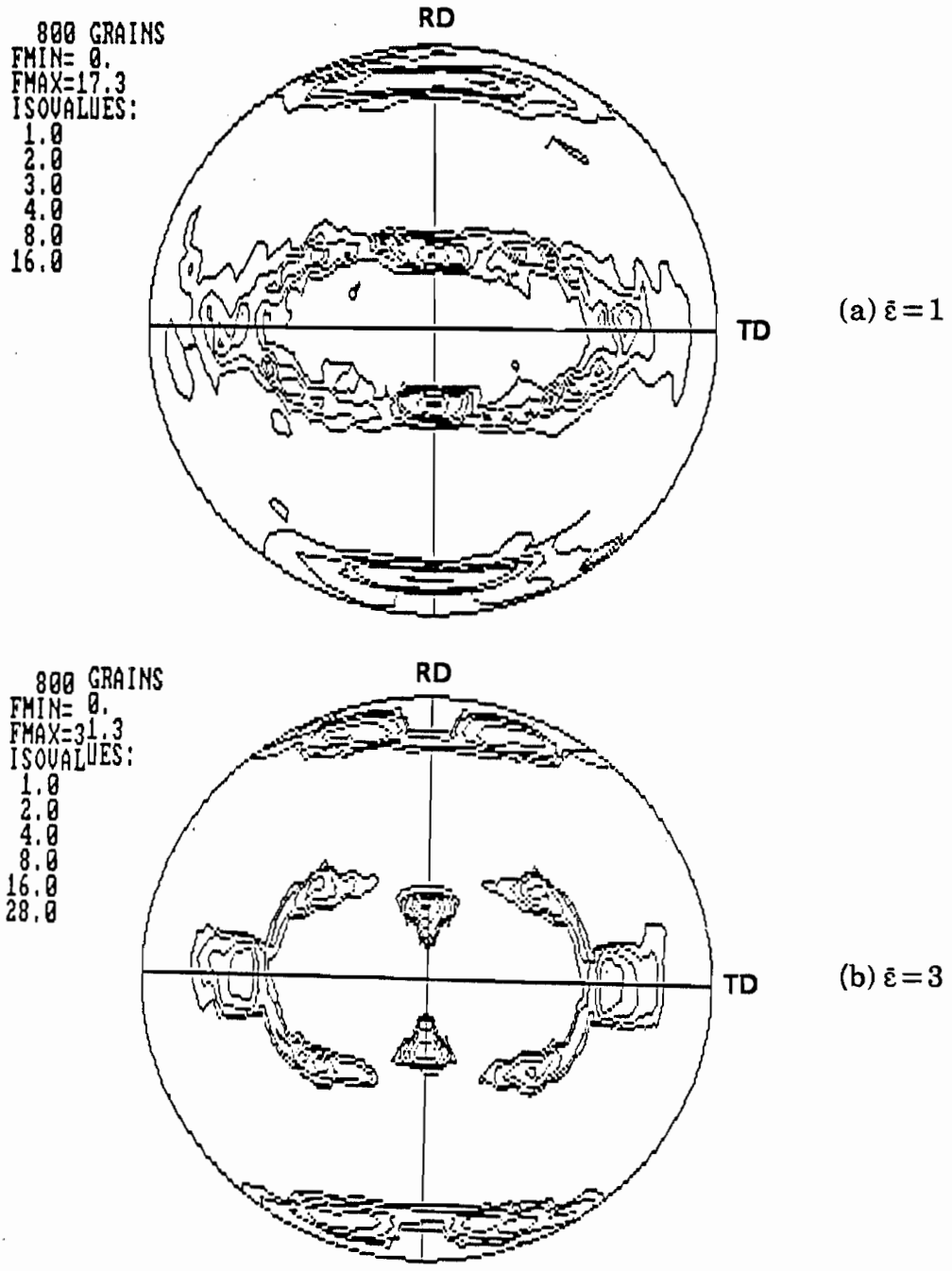

Figure 7.6. Rolling textures predicted using the FC-RC model with $\{111\}+\{100\}<110>$ slip. $\tau_{c(100)}/\tau_{c(111)}=1$.

267°C, respectively. It can be argued that these are unreasonably low, but it must be borne in mind that they were determined for very specific orientations. For an untextured material, the equivalent average temperatures for all possible orientations can be assumed to be higher. Cross-slip from the {111} to the {112} planes was also given the same interpretation [159].

It was thus decided to simulate such a cross-slip situation by simply adding the {110}<110> and {112}<110> systems to the classical {111}<110> ones. In terms of the model proposed above, this neglects the first stages of deformation, when slip only occurs on the {111} planes. There are 6 {110}<110> systems (plus their opposites), but these systems have to be grouped into 3 pairs. For example, systems (110)[1$\bar{1}$0] and (1$\bar{1}$0)[110] constitute one pair, since any strain rate vector which can be accommodated by a given shear rate on one of them can also be accommodated by the same shear rate on the other. In other words, when the components of the vectors N^s associated with each of the systems are written in the 5 dimensional notation described in Appendix 2, it is readily seen that the two vectors coincide, just as the {111}<110> systems in fcc materials and the {110}<111> systems in bcc materials correspond to the same yield surface. Consequently, it is sufficient to consider only 3 {110}<110> systems plus their opposites. However, the activation of one or the other of the two {110}<110> systems of a given pair will not lead to the same lattice rotation [162]; it was therefore assumed as a first approximation that the shear rate on each member of the pair is half the total shear rate on the pair. The other systems which were considered are the {112}<110> and there are 12 of these (plus their opposites).

The new yield surface considered here corresponds to 3 families of slip systems, which have 3 different values of τ_c, τ_{c1} for the {111}, τ_{c2} for the {110}, and τ_{c3} for the {112}. As the experimental observations described above do not allow us to differentiate between τ_{c2} and τ_{c3}, we first assume that these two quantities are equal but different from τ_{c1}. Three extreme cases can be considered:

i) $\tau_{c1} = 1$ and $\tau_{c2} = \tau_{c3} = 10$, which is the case when only {111}<110> slip is possible (below T_1). This case has already been treated above.

ii) $\tau_{c1} = \tau_{c2} = \tau_{c3} = 1$, where the three types of systems are equally favored ($T_1 < T < T_2$), and

iii) $\tau_{c1} = 10$, $\tau_{c2} = \tau_{c3} = 1$, where the cross-slip systems are favored over the conventional slip systems. This corresponds to the temperature range above T_2.

Cases (ii) and (iii) were tested in torsion and rolling with the FC-RC model using the linear programming technique. Figure 7.7 illustrates the extreme case where $\tau_{c1} = 10$ and $\tau_{c2} = \tau_{c3} = 1$ for torsion up to strains of 4 and 6 (case iii); Figure 7.8 illustrates the same conditions for rolling (for strains of 1 and 3). It can be seen from Figure 7.7 that the torsion textures at $\bar{\varepsilon} = 4$ and 6 are similar and that 2 main texture components can be identified: a strong C and a strong near B/$\bar{\text{B}}$. The fact that the latter orientation is not exactly B/$\bar{\text{B}}$ may be due to the assumption made concerning the distribution of the shears on the {110}<110> systems. However, the textures obtained are in reasonably good agreement with high temperature results.

Looking now at Figure 7.8, it can be seen that the main texture component at large strains is the brass orientation and there is also some spread around the Goss position. We obtain in this case something which is similar to the brass texture, which corresponds to the trends observed at high temperatures. Figures 7.9 and 7.10 illustrate the condition $\tau_{c1} = \tau_{c2} = \tau_{c3} = 1$, which corresponds to the temperature range between T_1 and T_2 (case ii). The textures obtained for torsion in this case are similar to the ones predicted by the classical model when only the {111}<110> systems are operating (i.e. there is no B/$\bar{\text{B}}$ component). By contrast, in the rolling predictions, the brass component is still present, particularly at the larger strain.

VII.3. CONCLUSIONS

In this chapter, the possibility of having more slip systems than the usual {111}<110> systems was investigated. This was motivated by two different lines of reasoning:

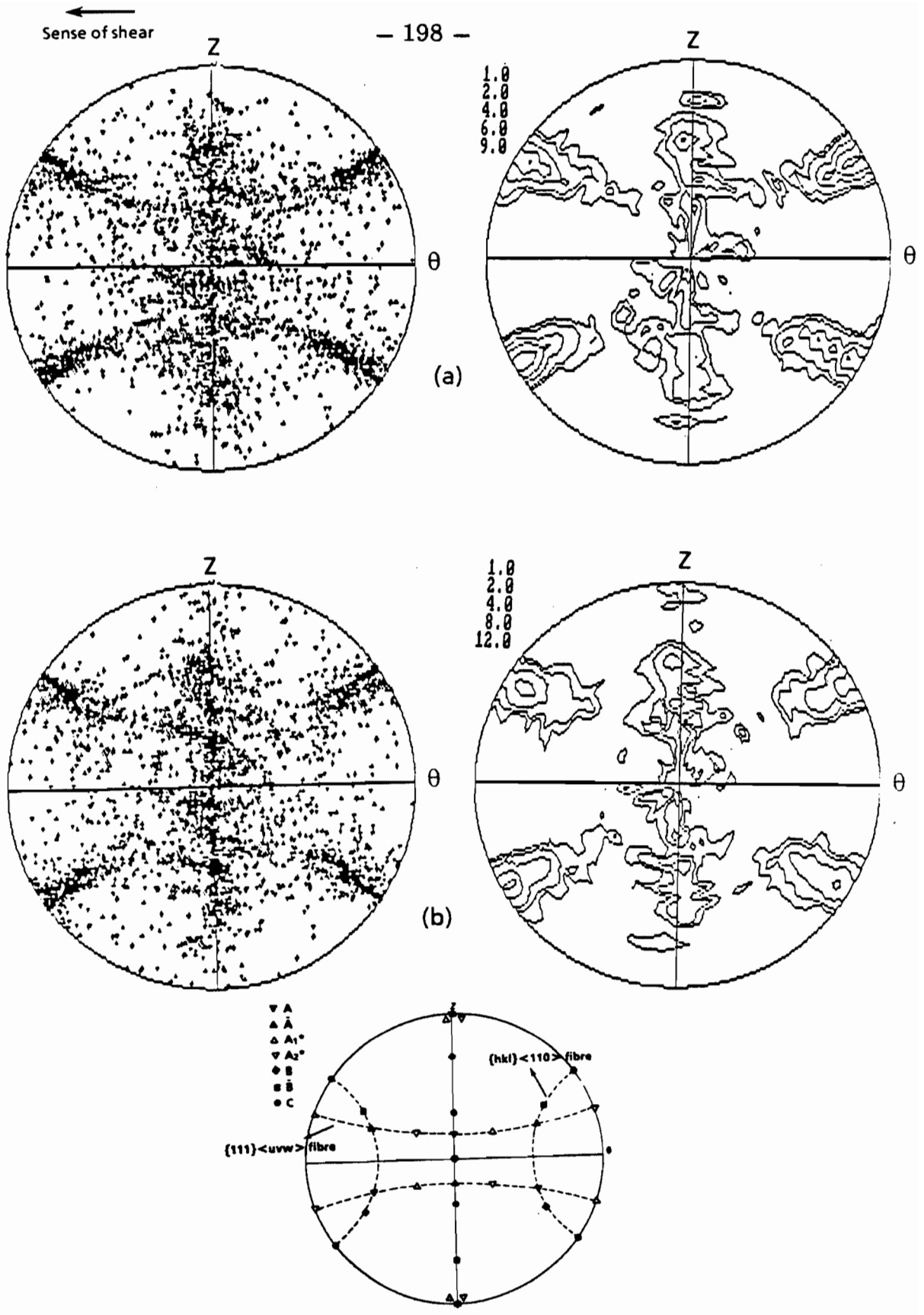

Figure 7.7. Torsion textures predicted using the FC-RC model with slip on the {111}+{110}+{112} planes. $\tau_{c(111)}=10$, $\tau_{c(110)}=\tau_{c(112)}=1$; a) $\bar{\varepsilon}=4$ and b) $\bar{\varepsilon}=6$.

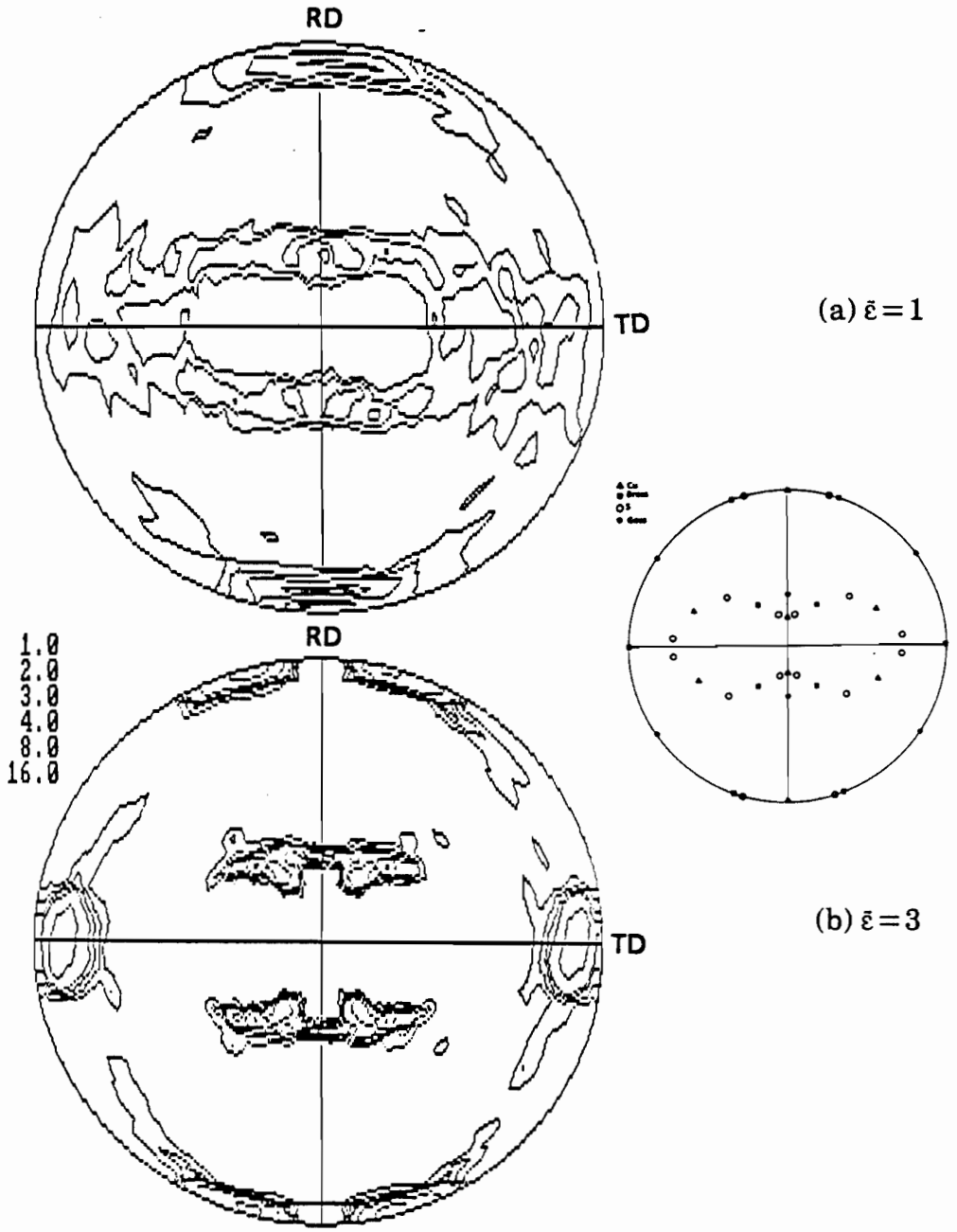

Figure 7.8. Rolling textures predicted using the FC-RC model with slip on the {111}+{110}+{112} planes. $\tau_{c(111)} = 10$, $\tau_{c(110)} = \tau_{c(112)} = 1$.

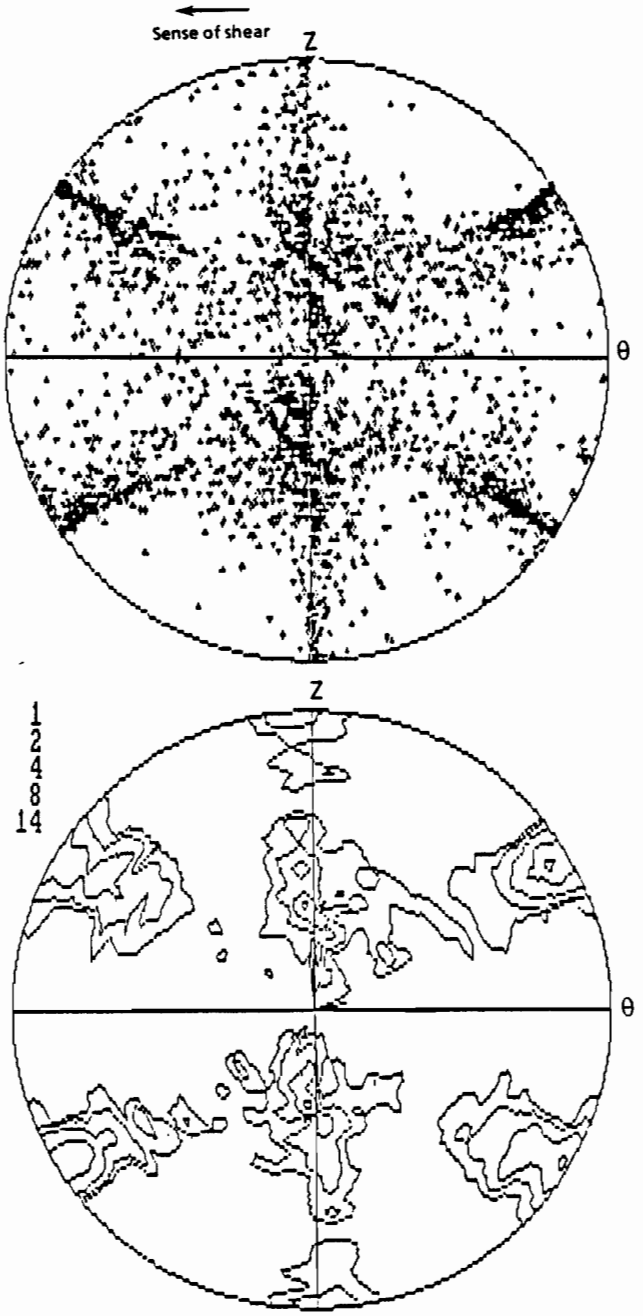

Figure 7.9. Torsion textures predicted using the FC-RC model with slip on the $\{111\}+\{110\}+\{112\}$ planes. $\tau_{c(111)}=\tau_{c(110)}=\tau_{c(112)}=1;\ \bar{\varepsilon}=4$.

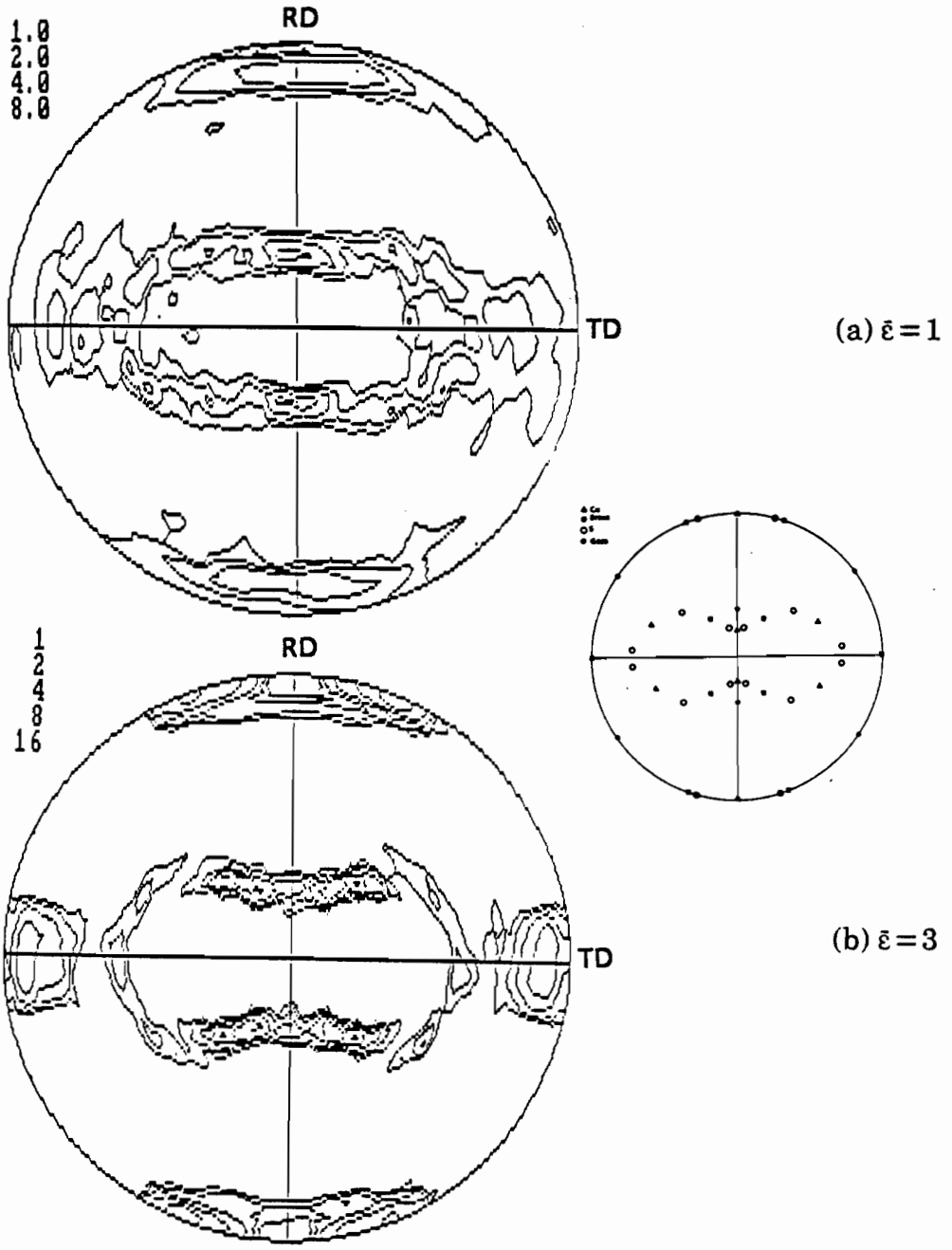

Figure 7.10. Rolling textures predicted using the FC-RC model with slip on the $\{111\}+\{110\}+\{112\}$ planes. $\tau_{c(111)}=\tau_{c(110)}=\tau_{c(112)}=1$.

i) The first is that new systems can become active when the temperature is increased; the most probable ones are the {100}<110> systems.

ii) The second is that extensive cross-slip on {110}<110> and {112}<110> systems can take place in fcc metals at high temperatures.

These two approaches, although motivated by different reasons, have been treated in the same way, i.e. by adding the new systems to the usual ones. The simulations were restricted to rolling and torsion. From these results the following conclusions can be drawn:

i) The addition of {100}<110> systems does not reproduce the trends observed at high temperatures. This part of the work has allowed us, however, to develop a new method (based on the one proposed by Tomé and Kocks [106]) to derive a composite YS from one which is already known.

ii) The addition of the cross-slip systems, on the other hand, produces the trends observed for high temperature deformation. It should be noted, however, that the cross-slip systems were considered as ordinary slip systems in this chapter, which is only an approximation. A more suitable way of simulating such mechanisms would be to consider a hardening law which takes into account the cross-slip capabilities of these systems. Such an approach would, of course, require more experimental data than were available, which is why it was not investigated here. We turn now to the last parameter which can influence texture formation at high temperatures: the grain boundary energy.

CHAPTER VIII

THE INFLUENCE OF DYNAMIC RECOVERY

In order to account for the influence of the temperature of deformation, we have so far added the following "mechanisms" to the classical prediction models: (i) the RW criterion of minimization of work hardening rate; (ii) the simulation of cross-slip; and (iii) the activation of additional slip systems. All these expanded models were based on the same idea, i.e. that an increase in the temperature modifies the microscopic hardening law of the material either by modifying the value of the critical resolved shear stress on different families of slip systems or by affecting the evolution of the CRSS with strain. But in all the previous chapters, the deformation mode (i.e. FC or RC) was the same as for low temperature deformation and the transition from the FC to the RC mode was only based on grain shape arguments. We must now ask a further question: is the evolution of grain shape similar at low and high temperatures? If the answer is no, we must then modify the "deformation mode" for the polycrystal deformed at high temperature. It is well known that the elevated temperature form of dynamic recovery produces an essentially equiaxed substructure; before describing the model conceived to account for this effect, we will first describe the main features of the dynamic recovery process.

VIII.1. THE BASIC MECHANISMS INVOLVED IN DYNAMIC RECOVERY

VIII.1.1. DESCRIPTION OF RECOVERY

Recovery is usually described as a process in which the density of atomic defects such as dislocations is gradually reduced. This reduction occurs locally by the annihilation of pairs of dislocations and not on a massive scale, as during recrystallization. Such annihilation is rendered possible by the fact that dislocations can glide *and* climb to rearrange themselves into more stable

configurations. Climb is a thermally activated process and thus takes place during or after hot deformation.

The process of rearrangement into stable configurations is often called polygonization and is generally observed in high SFE materials such as aluminum. To illustrate this mechanism, a single crystal is deformed by bending (the orientation is such that only one slip system is active), as shown in Figure 8.1a [163]. The first stage of recovery (Figure 8.1b) consists of the elimination of dislocations of opposite signs. After this stage, only dislocations of the same sign remain and are homogeneously distributed. In the second stage of recovery (e.g. at higher temperatures), these dislocations rearrange themselves into walls normal to the slip direction and slip plane (Figure 8.1c); here the driving force is the minimization of the boundary energy. Finally, a third stage can also occur, in which the subgrain size increases by wall coalescence to further minimize the boundary energy (Figure 8.1d).

When the deformation is accommodated by slip on several systems (which is usually the case), the situation is more complex, but similar mechanisms are involved, i.e. the climb of dislocations, rearrangement into walls and formation of an equiaxed substructure. During this process of polygonization, no high angle boundary migration is observed [163], whereas the migration of low angle boundaries can take place, although this possibility is not universally recognized. For example, Exell and Warrington [164] claim that the migration of low angle boundaries contributes significantly to the total strain, whereas McQueen and Jonas [165] attribute as little as 6% of the total strain to this phenomenon.

An important consequence of the recovery process is the presence of an equiaxed *substructure*, even at very large deformations. For example, Wong et al. [166] observed such structures at extrusion strains of up to 2000% in aluminum. (Their material was the same as the one tested in the present work and described in Chapter IV.) Because of the simultaneous occurrence of polygonization and low angle boundary migration (or polygonization and boundary coalescence), the deformation substructure remains stable in size and shape, although the grains themselves follow the shape change of the sample as a whole.

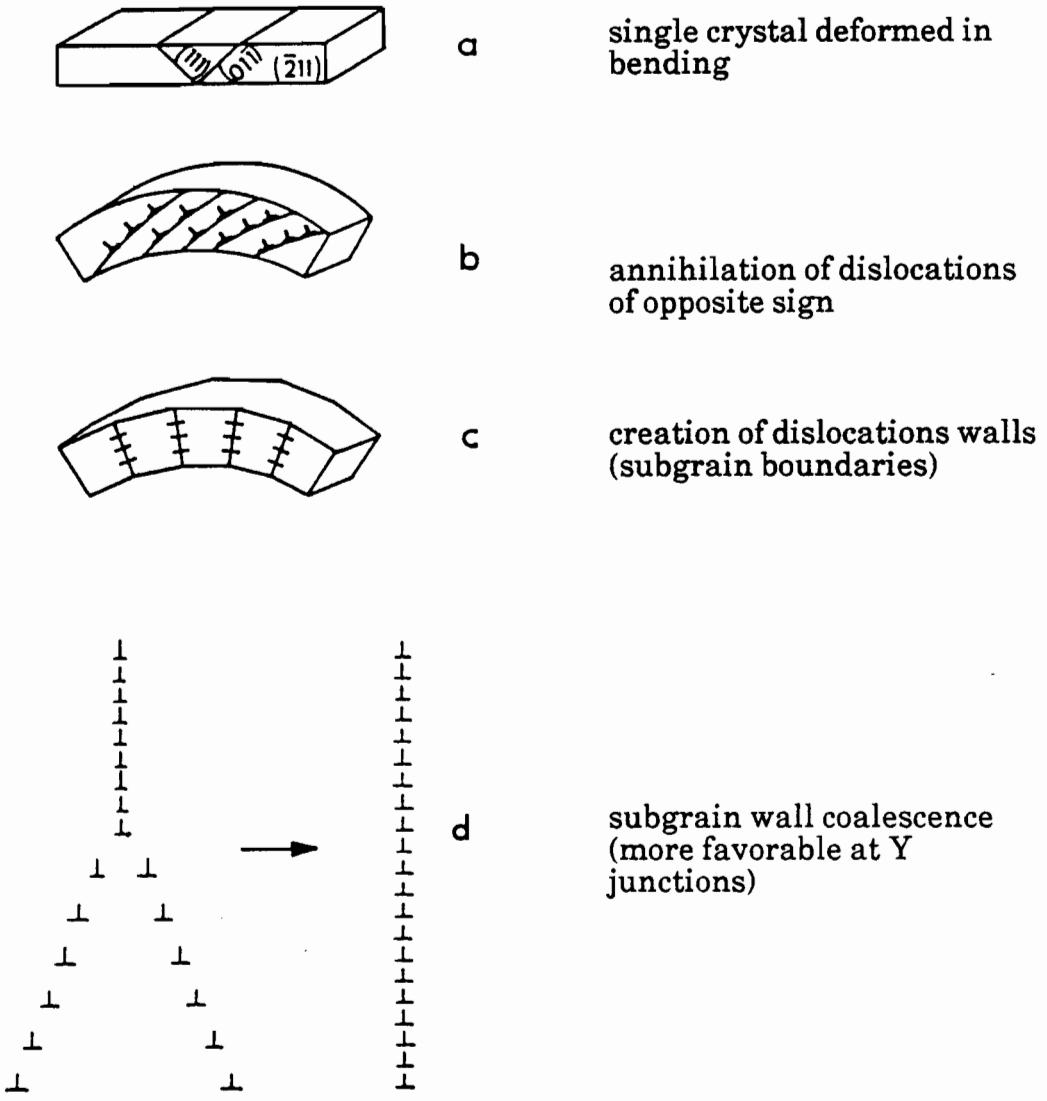

Figure 8.1. Illustration of steps in the polygonization process [163].

Another important aspect of recovery is that the rearrangement of dislocations takes place in order to minimize the sub-boundary energy. To better interpret this last observation, we now have to introduce the concept of coincidence sites.

VIII.1.2. THE COINCIDENCE SITE MODEL

The free energy of a given boundary is generally assumed to depend on the misorientation across the boundary (i.e. on the orientation difference between the adjacent grains or subgrains) and on the orientation of the plane in which the boundary lies. This leads to a total of 5 orientation parameters which can affect the energy: 2 angles to specify the position of the rotation axis, one rotation angle (these 3 describe the rotation to go from the orientation of the first grain to that of the second), and two further angles which describe the orientation of the boundary plane itself. Generally, not all of these parameters are used to describe the free energy of the boundary. It is common, for example, to specify the rotation axis, to ignore the orientation of the boundary plane, and to represent the energy as a function of the rotation (or misorientation) angle only.

Extensive experimental work on small and large angle boundaries has been carried out and the results of this research can be represented on the schematic diagram shown in Figure 8.2. The first part of the curve corresponds to low angle boundaries and extensive work in this area has been published by Read and Shockley [167]. The second part of the diagram is associated with high angle boundaries. For these boundaries, the energy is usually measured as being almost constant, except for special values of the angle of rotation where a cusp is seen on the curve. These special boundaries not only exhibit a lower energy but are often associated with high mobility and play an important role in the growth theory of annealing textures (see Chapter II).

The presence of special orientation relationships can be interpreted in terms of the coincidence site lattice (CSL) model due to Bollmann [168]. This model is based on the observation that, for specific axes and angles of misorientation, two grains separated by a boundary possess a number of lattice sites in common. The energy of such a boundary will depend on the reciprocal density of common lattice points in the two grains (denoted Σ) as well as on the reciprocal density of common lattice points in the boundary itself (denoted σ). The simplest coincidence boundary is the twin boundary, for which Σ is equal to 3; but coincidence boundaries exist for all odd values of Σ. Any coincidence relationship can also be expressed by an axis-angle pair; in the cubic system,

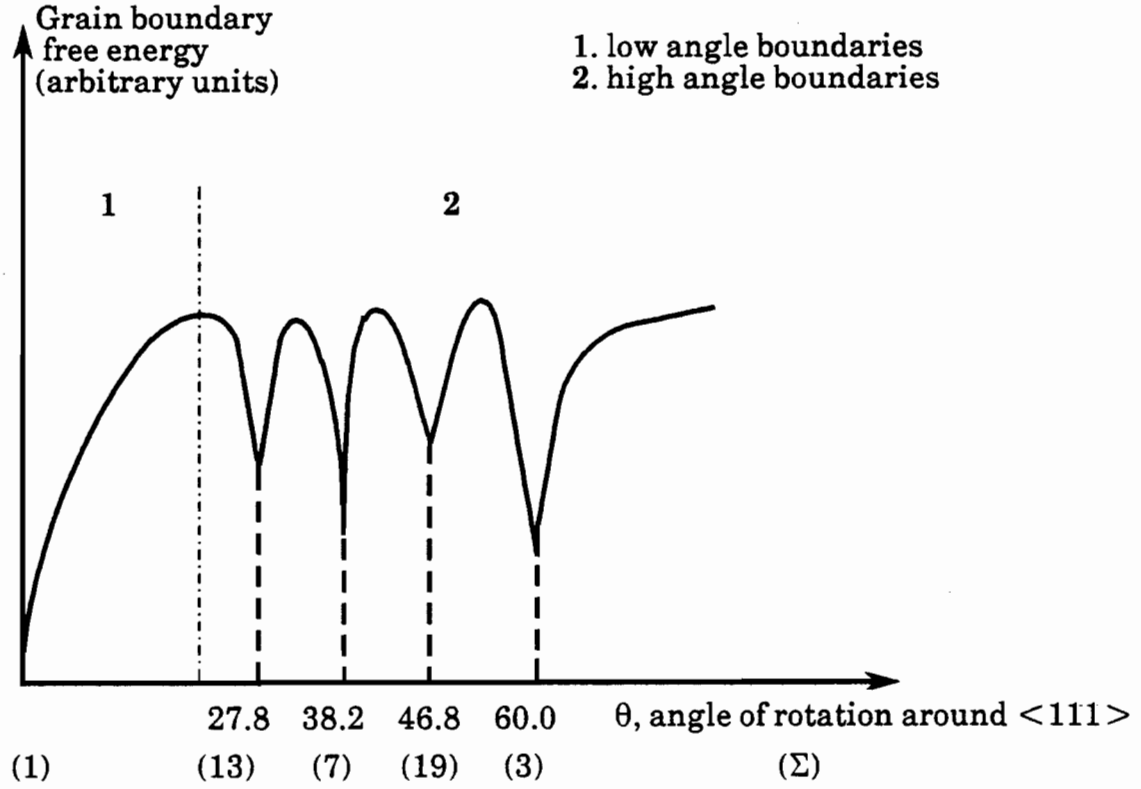

Figure 8.2. Schematic illustration of the dependence of grain boundary energy on angle of rotation around any <111> axis in cubic metals.

there are 24 different axis-angle pairs, corresponding to the 24 symmetry elements of the cubic system [169,170].

Brandon et al. [169] listed all the coincidence sites found in cubic crystals (for Σ less than 19). Their results are reproduced in Table 8.1. The properties of such boundaries can be described as follows:

i) the lower the Σ, the lower the energy;
ii) if the boundary lies in the most densely packed planes of the coincidence lattice (i.e. the lattice formed by the common sites only), the mobility of the boundary is the lowest. This applies, for example, to the coherent twin boundary [171]. At orientation differences slightly removed from coincidence, the mobility of the boundary can be very high, a property which is of importance in the growth theory of annealing texture formation, as already indicated above.

Axis of rotation	Coincidence Site		Axis of rotation	Coincidence Site	
	Σ	ω(°)		Σ	ω(°)
100	5	36.9	*311*	*3*	*146.4*
	13a	22.6		5	154.2
	17a	28.1		9	67.1
110	*3*	*70.5*		11	180
	9	38.9		15	50.7
	11	50.5		15	117.9
	17b	86.6	320	7	149
	19a	26.5		11	100.5
111	*3*	*60*		13a	180
	7	38.2		17b	121.9
	13b	27.8		19b	71.6
	19b	46.8	321	7	180
210	*3*	*131.8*		9	123.7
	5	180		15	150.1
	7	73.4	322	9	152.7
	9	96.4		13a	107.9
	15	48.2		17b	180
211	*3*	*180*	331	5	95.7
	5	101.6		7	110.9
	7	135.6		11	82.1
	11	63		17b	63.8
	15	78.5		19a	180
221	5	143.2	410	9	152.7
	9	90		13b	107.9
	9	180		17a	180
	13b	112.6	411	9	180
	17b	61.9		11	129.6
310	5	180		17a	93.4
	7	115.4		19b	153.5
	11	141.9			
	13b	76.7			
	19a	93			

Table 8.1. Coincidence site relationships for the cubic lattice and for Σ less than 20, where Σ is the reciprocal density of common points and ω is the least angle of rotation. The indices a and b correspond to the same value of Σ but to different most densely packed planes for the coincidence lattice. The italic numbers are the ones taken into account in our simulations [169].

VIII.1.3. EXPERIMENTAL OBSERVATIONS

It was mentioned above that polygonization occurs during annealing or deformation (at high temperatures). During annealing, the average misorientation between subgrains is generally low (1 or 2°) and remain approximately constant with annealing time. This results from the superimposition of two processes: (i) an increase due to glide and climb; and (ii) a decrease due to energy minimization [172,173]. However, during deformation, some relatively large polygonization angles (greater than 15°) have been observed, especially in pure metals [174-176]. It is even possible that, once a given grain has been split into subgrains, the initially close orientations transform into distinctly different ones because of the imposed deformation (see Section VIII.4.3 below). The low angle boundaries are gradually transformed into high angle boundaries and the energy minimization process then tends to produce coincidence sites.

Of the coincidence site relationships listed in Table 8.1, not all are in fact observed in cubic materials. Some have been reported in annealed, as well as cold and hot worked metals. For example, Schnell and Grüwe [177] identified $\Sigma=3$ boundaries in cold worked and annealed copper. Lim and Raj [178] deduced the presence of $\Sigma=3$ and $\Sigma=11$ boundaries in annealed and deformed aluminum and $\Sigma=3$, 9 and 27 boundaries in nickel (these specific values are considered to be due to twinning). Finally, Dahms et al. [179] observed a high proportion of $\Sigma=3$ boundaries in annealed AlMn alloys, which also had high mobility. In most cases though, no mention of the boundary orientation was given.

The experimental observations reported here show that dynamic recovery not only leads to an equiaxed substructure, but also produces a large number of special boundaries. These can be of the low (due to recovery only) or high (due to recovery and deformation) angle types. We are now ready to describe in detail how these features of recovery can be modelled: i.e. the climb of dislocations, which produces an equiaxed substructure in order to minimize the sub-boundary or grain boundary energy.

VIII.2. DESCRIPTION OF THE MODEL

VIII.2.1. INTERPRETATION OF DYNAMIC RECOVERY

The following steps will be considered in the present model:

i) The smallest entity to be associated with a particular orientation is not the grain but the subgrain. These subgrains can be separated by low angle boundaries as well as by high angle boundaries (coincidence sites). In both cases, the misorientation can lead to very large stress discontinuities; these are inadmissible even in the framework of the FC model, where stress discontinuities are assumed to be accommodated by elastic stresses.

ii) The stress discontinuities are assumed to be due to one of two different causes:

– For a stable orientation, the strain rate vector generally lies at the edge of the cone of normals of several vertices. In this case, a small deviation from the stable position can produce two slightly different orientations, which will eventually activate two neighboring vertices and in this way give rise to high stress discontinuities.

– For a stable high angle boundary (i.e. a coincidence site), some of the stress components are continuous across the boundary and some are not. This is the case for the B/$\bar{B}$ pair of orientations in torsion, which are separated by a $\Sigma = 3$ boundary. For this orientation, the only one found in aluminum at high temperatures, the stress components† calculated with the FC model are:

$$\sigma_B = (0, 0, -2, 0, \sqrt{2}) \qquad (8.1)$$

$$\sigma_{\bar{B}} = (0, 0, -2, 0, -\sqrt{2})$$

† The components are expressed in terms of the notation described in Appendix 2. The last 3 terms represent the shear stresses: $\sigma_3 = \sqrt{2}\sigma_{\theta Z} = -2$, $\sigma_4 = \sqrt{2}\sigma_{RZ} = 0$ and $\sigma_5 = \sqrt{2}\sigma_{R\theta} = \pm\sqrt{2}$ (in units of τ_c). In the B and $\bar{B}$ cases, 6 vertices are activated simultaneously; accordingly, the stress state is ambiguous, and the vectors listed in relation 8.1 represent the average values.

In the classical RC model for torsion, according to which $\sigma_4 = \sigma_{13} = 0$, the stress vectors have exactly the same components. However, it can be seen that there is a very high σ_{12} shear stress, almost as large as the torsion shear stress σ_{23}. It seems unrealistic then to assume that this pair of grains or subgrains deforms according to the FC or RC model used at low temperatures. It is more likely, instead, that the two orientations deform according to another RC model, i.e. one in which σ_{12} is set equal to zero. In such a case, even with a large orientation difference between the two grains, the continuity of stress is respected.

A consequence of assuming this special deformation mode is that it leads to a strain ε_{12} which could produce large displacements and thus create voids in the material. We prefer to think here in terms of the cooperative deformation described by Van Houtte [128], in which neighboring grains are submitted to opposite shear strain rates, but in which the overall shear rate for the pair has a zero average value. Moreover, if such cooperative deformation takes place in an equiaxed substructure, it leads to smaller displacements than in an elongated structure.

iii) In the first stages of deformation, a given grain corresponds to a single orientation. But very soon (i.e. once several slip systems become active, which corresponds to the end of the first increment in a purely plastic model), the climb of dislocations takes place, resulting in small misorientations in every grain. As a first approximation, each grain is simply divided into two subgrains, the rotation axis being taken as parallel to $\mathbf{n} \times \mathbf{b}$, where n and b are the slip plane normal and slip direction of the most active slip system (see Figures 8.1 and 8.3). In the case where two systems are equally active, the rotation axis is the arithmetic average of the two $\mathbf{n} \times \mathbf{b}$ vectors. For most stable orientations (i.e. at large strains), this results in the formation of sub-boundaries perpendicular to the largest boundary of the initial grain. Consequently, compatibility is still satisfied accross this boundary on an average basis. This approximation (i.e. the fact that each grain is split into just two orientations) is only employed for convenience here, but several other subgrains can be added, if necessary. This would, however, increase the computing time. The angle of misorientation α_0 is taken as a variable in the model and its magnitude is linked to the ease of climb in a given material.

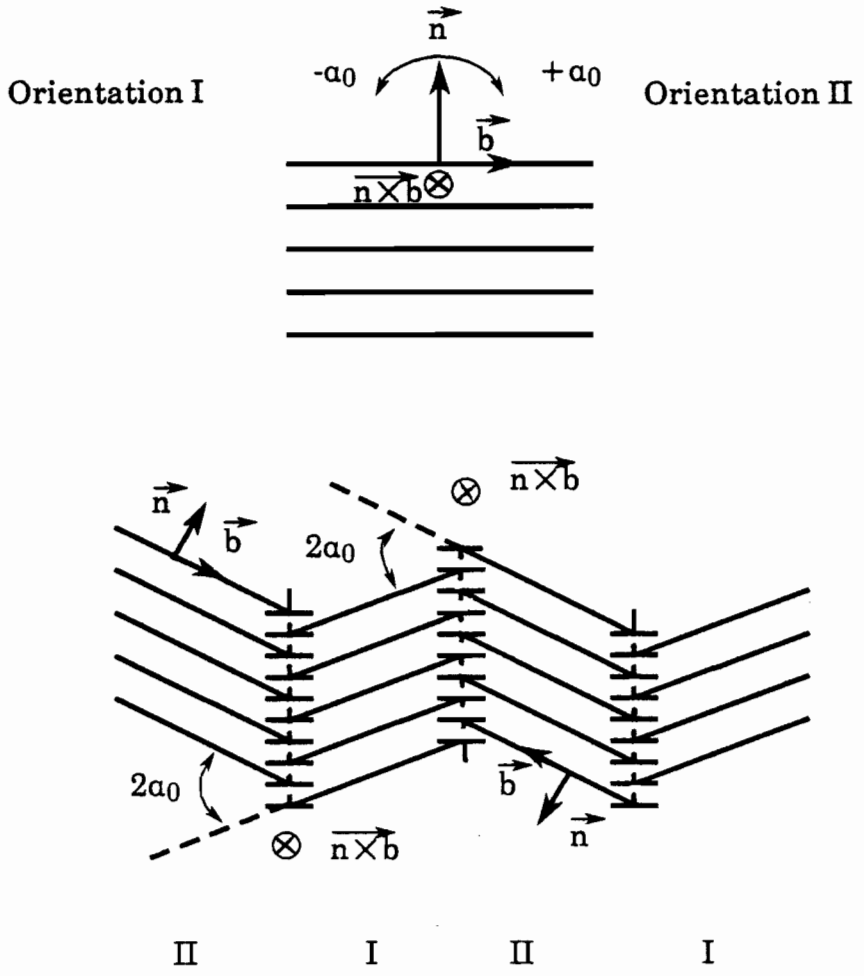

Figure 8.3. The effect of polygonization. Under the action of climb, a grain is split into two subgrains by a rotation around the axis n×b of the most active slip system.

iv) Such pairs of orientations, although very close at the beginning of deformation, can rotate towards different orientations under the sole action of slip. This can, in turn, lead to high stress discontinuities, which is why it is necessary to treat the two subgrains simultaneously. For this purpose, two parameters have to be minimized:

– some stress component differences;
– the sub-boundary energy (in order to introduce the effect of climb).

Minimizing a stress difference means that, whenever this difference becomes higher than an acceptable limit, the corresponding strain rate component is relaxed in each of the two subgrains. Then, once the deformation mode is set up, the shear rates are calculated in such a way that the grain boundary energy is minimized. It will be seen below that the change in grain boundary energy depends only on the shear rates. However, this energy can only be minimized in the presence of ambiguities. It is thus a second order effect, but it will be seen that its influence on texture development is not negligible.

A choice now has to be made which concerns the stress components for which the differences are minimized. These depend on the deformation mode, just as the choice of the non-imposed strain rate components depends on the grain shape in the RC model. Some grain shape arguments have been used here, but in the present case, the subgrain is assumed to remain equiaxed. From the work of Tiem et al. [157], it can be seen that, for an equiaxed grain deformed in rolling, the lowest interaction coefficients are associated with the components ε_{13}, ε_{23} and ε_{12}. This means that, if these components are relaxed (i.e. non-zero), the corresponding reaction stresses will not be too high. Moreover, whereas the three components do not have the same interaction coefficients in an elongated grain, they become equivalent in an equiaxed subgrain. By contrast, the normal components are not relaxed, but are constrained to remain equal to the macroscopic quantities. Similarly, in torsion, in order to assure partial stress continuity, two shear components are permitted to differ from the macroscopic ones. These strain rate components are the $\dot{\varepsilon}_{12}$ and $\dot{\varepsilon}_{13}$ shear rates. Note that in the RC model adapted for torsion, only $\dot{\varepsilon}_{13}$ is allowed to differ from its macroscopic equivalent. Again here, in an equiaxed substructure, the two shear rates have equal interaction coefficients.

The last thing to consider before describing the simulation concerns the grain boundary energy. It was seen in the previous paragraph that not all the coincidence sites typical of cubic structures are observed in the cubic metals. We therefore decided to take into account only the ones found in pure aluminum and copper, i.e. the $\Sigma = 1$ (low angle) and $\Sigma = 3$ boundaries. The $\Sigma = 11$ boundaries sometimes detected in aluminum, as well as other boundaries with higher values of Σ, could be added to the model, if desired, at a later stage.

VIII.2.2. METHOD OF SIMULATION

The different steps of the program that was devised are the following:

i) Every grain (only one orientation at this stage) is given an FC deformation step. Once the active slip systems are selected, the $n \times b$ vector associated with the most active system is determined and each grain is split into two orientations ($\alpha_0 = 1°$ for example), as illustrated in Figure 8.3.

ii) For each further step of deformation, the stress vectors $\sigma(1)$ and $\sigma(2)$ associated with the two subgrains are calculated according to the FC model. For the case of rolling, the following stress differences are evaluated

$$\begin{aligned} \Delta\sigma_3 &= |\sigma_3(1) - \sigma_3(2)| \\ \Delta\sigma_4 &= |\sigma_4(1) - \sigma_4(2)| \\ \Delta\sigma_5 &= |\sigma_5(1) - \sigma_5(2)| \end{aligned} \tag{8.2}$$

and compared with 3 "tolerance" values, T_3,T_4 and T_5 (Only T_4 and T_5, calculated in the grain axes, are considered in the case of torsion). Whenever one of these stress differences is higher than the corresponding admissible value, the associated strain rate component is relaxed in the two subgrains and the new stress states and activated slip systems are determined.

iii) In the presence of ambiguities, the shear rates are calculated from the minimization of the grain boundary energy, as described in Appendix 8.

iv) At every step, the misorientation between adjacent subgrains is calculated; whenever it decreases below a given value, α_{min}, (which means that the sub-boundary is disappearing), the grain is again split into two different subgrains, according to the rule employed in step i).

In this model, different pairs of subgrains deform according to different modes (FC or various types of RC). For example, a B/$\bar{\text{B}}$ pair of orientations in torsion deforms according to a $p = 4$ mode (only the $\dot{\varepsilon}_{12}$ component is relaxed in the two subgrains), whereas an A/$\bar{\text{A}}$ pair of orientations deforms according to the FC mode, since the stresses σ_{12} and σ_{13} are zero in this case. When a given

stress difference exceeds the set limit, the associated strain rate component is relaxed. In most cases (especially for stable orientations), the average strain rate component in the grain (i.e. the average for the two subgrains) is small (zero in the case of $B/\bar{B}$), and thus large discontinuities of displacement are avoided between grains.

It should be noted that when grain boundary energy minimization is neglected, this model approaches the cluster model [156], i.e. the stress differences between neighboring grains are minimized. In the latter, however, instead of using only two orientations, twelve are considered (which can be very different, even at the beginning of deformation); also, whenever a stress component departs appreciably from the corresponding average pertaining to the twelve neighbors, the component is adjusted instead of being set equal to zero. This procedure avoids the appearance of large discontinuities in stress from one increment to the next, but leads to the same selection of systems, given the assumption that, the average stress state of the 12 grains is in most cases close to the macroscopic one (i.e. the one for which the shear stress component of interest is zero).

The parameters associated with this model will now be described.

VIII.2.3. PARAMETERS EMPLOYED IN THE MODEL

1) $\underline{\alpha_0}$: This is the angle of splitting after the first step of deformation; its magnitude indicates the ease of climb in the material tested. Values higher than 3 degrees seem unrealistic. To account for differences in SFE and ease of climb, it is also possible to introduce the splitting of the grains at a later stage of deformation. We have treated here only the extreme case where climb plays a significant role at the beginning of deformation (i.e. for very high SFE metals). For low SFE materials, the calculation could begin according to the classical FC-RC model; then, after a suitable amount of strain, the grains can be split and the stress continuity and GBE minimization criteria superimposed on the classical grain shape arguments.

2) $\underline{T_3}$,$\underline{T_4}$,$\underline{T_5}$: These are the tolerance values for the stress differences. In order to remain as faithful as possible to the room temperature RC model, these

limits are given the following values: in rolling, $T_3 = T_4 = 0.2$ ($\dot{\varepsilon}_3$ and $\dot{\varepsilon}_4$ are the two relaxed components in the RC model for room temperature), and $T_5 \simeq 0.4 > T_3$ and T_4 ($\dot{\varepsilon}_5$ is not relaxed at room temperature). In torsion, T_4 is again assumed to be less than T_5, and values similar to those listed above for rolling are assigned.

3) $\underline{\alpha_{min}}$: This is the limiting angle for the misorientation α between subgrains. Whenever α is smaller than α_{min}, an increment of "climb" is performed. The introduction of this parameter permits the simulation of a continuous climb process without having to introduce new subgrains at each step. α_{min} is usually taken as equal to α_0 (i.e. between 1 and 3°).

4) $\underline{\Sigma}$: This refers to the type of coincidence site, which varies somewhat with the material. The choice involves two different considerations:

- First, we have to decide if we will take into account both low and high angle boundaries, for example $\Sigma = 1$ and 3, or just the high angle boundaries, $\Sigma = 3$. In the work described below, we have included both the low and the high angle boundaries.

- Then, the selection (among the possible high angle coincidence sites) depends on the material; for aluminum and copper, we have only employed the $\Sigma = 3$ boundaries, which are found more frequently.

5) Another latitude inherent in the model is the option to consider only stress differences or whether the grain boundary energy is also minimized. Both options were studied, and will be presented below.

Before examining the results of these simulations, a word of warning must be added: grain boundary energy minimization is only a first order calculation and is consequently very approximate. It nevertheless has the advantage of being readily solvable with the aid of linear programming, whereas a more exact calculation would involve the minimization of a complex quadratic function.

VIII.3. SIMULATED ROLLING AND TORSION TEXTURES

The parameters α_0, T_3, T_4 and T_5 were varied systematically and found to have little influence on the results. This generalization does not apply to α_{min}, the angle below which "resplitting" of the grains is performed. An interesting value for α_{min} is 0, which means that climb takes place only at the very beginning of the calculation. We will therefore consider the cases $\alpha_{min}=0$ and $\alpha_{min}\neq 0$ separately.

VIII.3.1. CLIMB OF DISLOCATIONS AT THE BEGINNING OF DEFORMATION ONLY

In this case, the interaction between grains is modelled in terms of the Taylor assumption, whereas the interaction between subgrains is always related to stress discontinuities and the grain boundary energy. The latter signifies that, if the misorientation remains small, the subgrains, and consequently the grains, deform according to the FC mode. At the beginning of deformation, as the grains are randomly oriented, and in general not near stable orientations, the small deviations due to climb rarely create strong stress discontinuities, and most of the grains simply deform according to the FC mode. This is illustrated in Figure 8.4 for rolling ($\bar{\varepsilon}=2$), where two different cases are considered:

a) only stress continuity is taken into account (referred to as the SC model);

b) both stress continuity and GBE are taken into account (referred to as SC + GBE).

The two textures illustrated are close to the FC prediction, as expected; however, some odd components appear due to the GBE minimization. Moreover, the pole figures obtained do not fully respect the symmetry of the process (see Figure 8.4b). This is due to the small number of subgrains considered, and suggests that the misorientation produced by climb does not only depend on the active slip systems, but also on the imposed deformation mode. Although the textures predicted are not in particularly good agreement with experimental observations, they are different enough to indicate that the

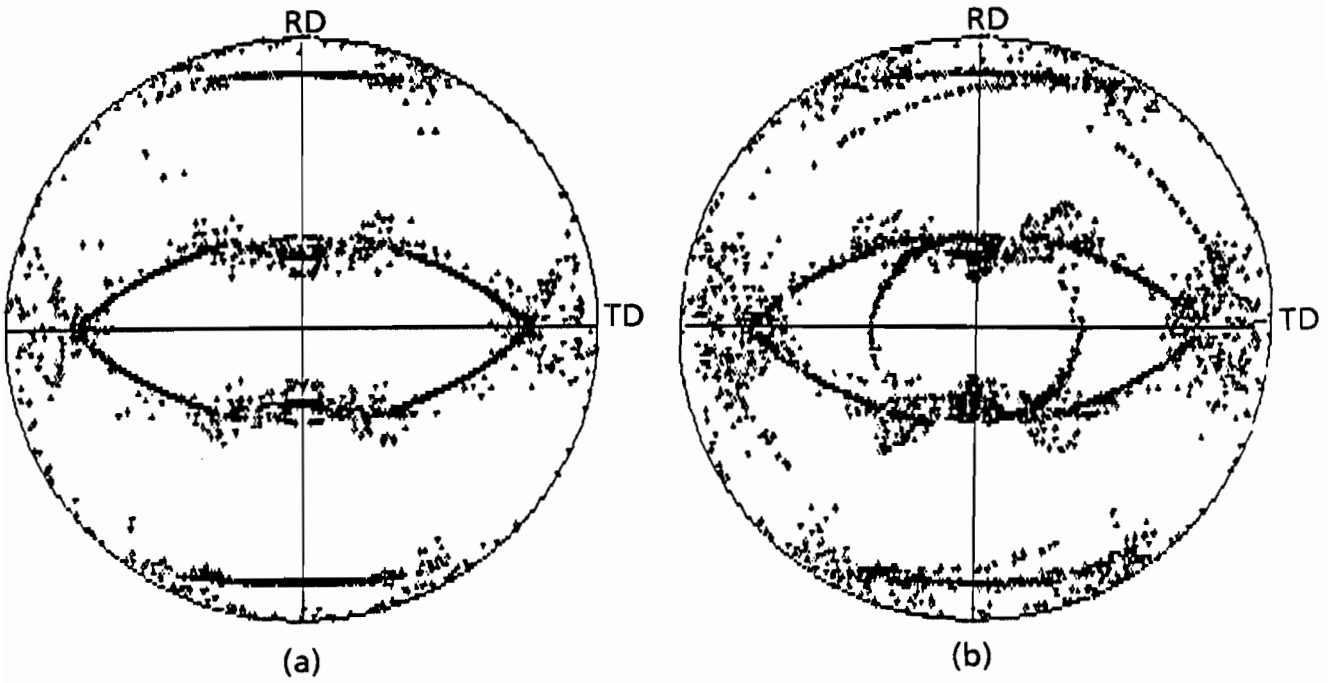

Figure 8.4. Rolling textures at a strain of 2 simulated with:
a) the SC model ($\alpha_0 = 3$);
b) the SC + GBE model ($\alpha_0 = 3$ and $\Sigma = 1$ and 3).
In both cases, splitting of the grains because of climb only takes place at the beginning of the deformation.

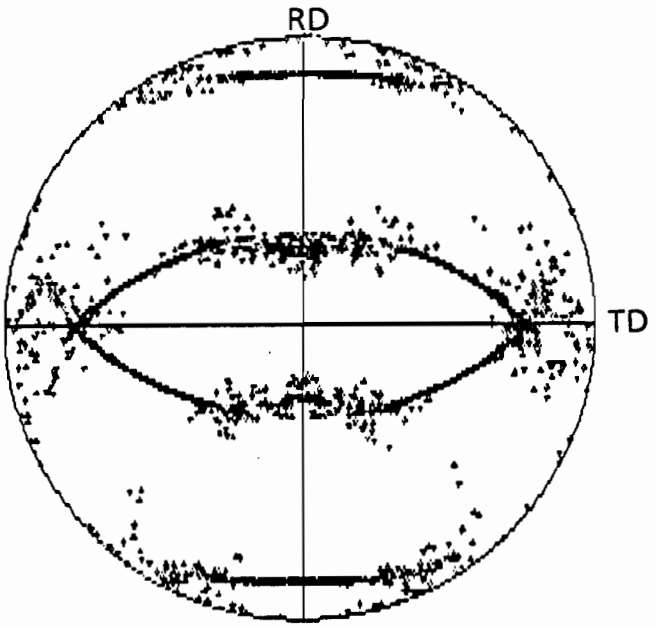

Figure 8.5.
Rolling texture simulated with the SC model to a strain of 2. Splitting of the grains only takes place at the beginning of deformation ($\alpha_0 = 1$).

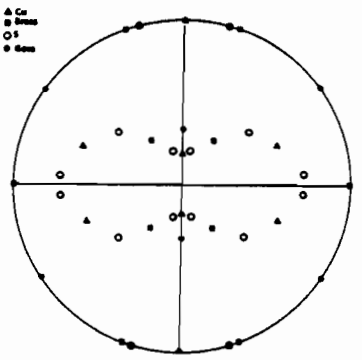

effect of GBE minimization is not negligible. In particular, the proportion of the brass component is slightly higher than when only stress continuity is taken into consideration. The results presented in Figure 8.4 were obtained for $\alpha_0 = 3$. In Figure 8.5, the case where only the stress continuity is taken into account is presented for $\alpha_0 = 1$. The results are similar to those of the previous case, so, it was decided to use $\alpha_0 = 1$ in the subsequent calculations. This choice also leads to better agreement with experimental observations.

VIII.3.2. CONTINUOUS CLIMB

The parameters used in this case were the following: $\alpha_0 = \alpha_{min} = 1$, $\Sigma = 1$ and 3, $T_3 = T_4 = 0.2$ and $T_5 = 0.4$ in the case of rolling and $T_4 = 0.2$ and $T_5 = 0.4$ in the case of torsion. The results obtained for rolling to a strain of 2 are presented in Figure 8.6 for: (i) the condition where only the stress continuity is considered (8.6a); and (ii) where both the stress continuity and GBE minimization are taken into account (8.6b). The brass component is present in both cases, whereas it is absent from the classical FC-RC calculation; note also that the brass orientation is more intense in the second case. These results are in good agreement with experimental observations (see Figure 2.18). The reason for the difference between the two calculations remains to be seen, however, and will be investigated in the next section. Before taking up this topic, we will look at the torsion textures predicted by these two models. These are presented in Figure 8.7 for an equivalent strain of 4, and in Figure 8.8 for an equivalent strain of 8. The results can be analyzed as follows:

i) Figure 8.7a: At $\bar{\varepsilon} = 4$, the first model (stress continuity only) produces a texture which is close to the FC-RC result. This indicates that the proportion of grains deforming according to the RC mode (because of stress differences) is approximately the same as that produced by the grain shape criterion. The small divergence between the present calculation and the usual FC-RC pole figure is due to the relaxation of the second strain rate component in the current case.

ii) Figure 8.7b: When the GBE is taken into consideration with $\Sigma = 1$ and 3, the texture contains most of the FC features seen in the previous case. In the early stages of the deformation, small angles boundaries ($\Sigma = 1$) are more

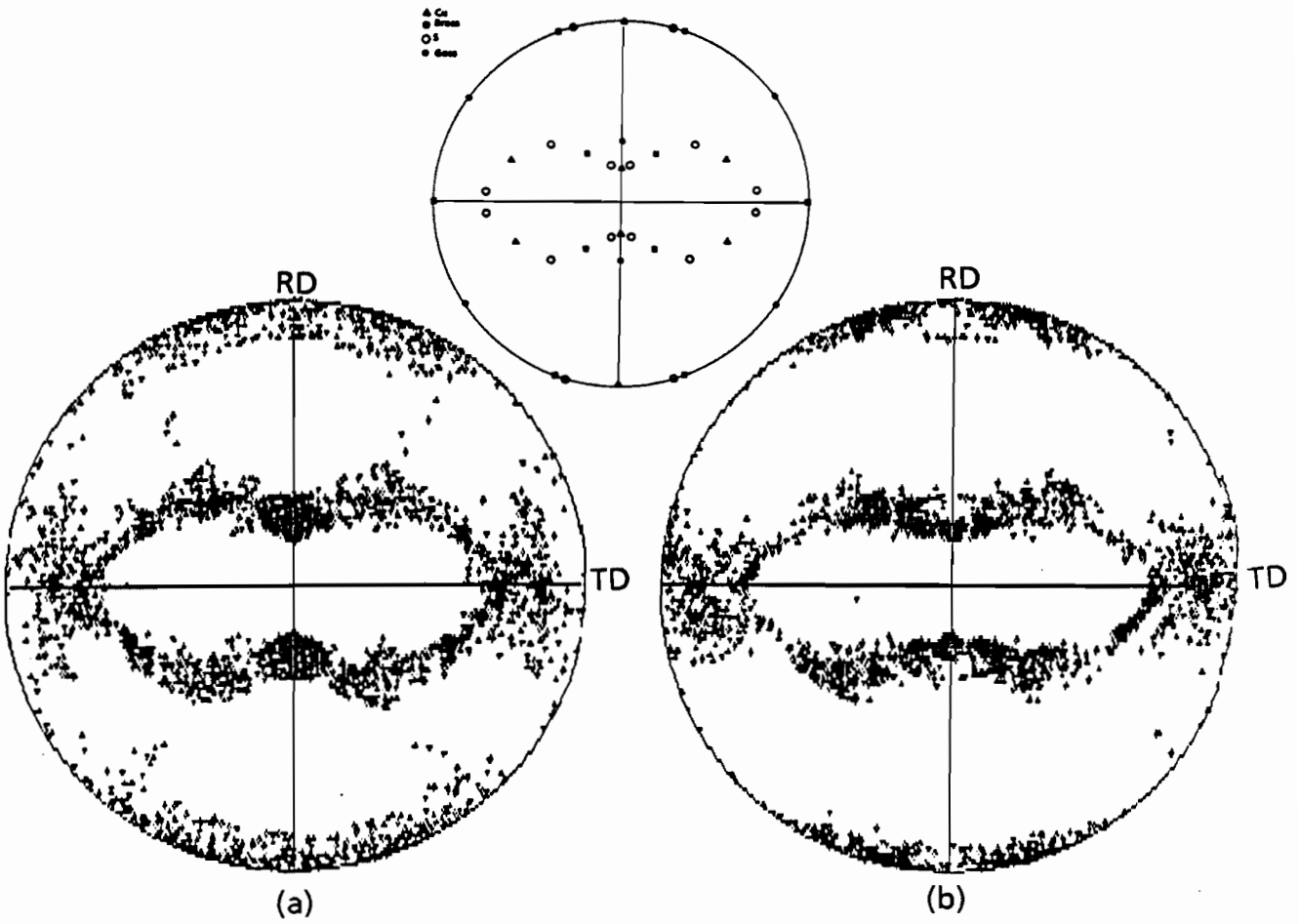

Figure 8.6. Rolling textures ($\bar{\varepsilon}=2$) simulated with : a) the SC + continuous climb model; b) the SC + GBE + continuous climb model. In both cases, $\alpha_0 = \alpha_{min} = 1$.

numerous than large angle boundaries ($\Sigma=3$) and GBE minimization tends to keep the misorientations as close as possible to the $\Sigma=1$ values (i.e. close to 0 degrees). Furthermore, as the grains have not yet reached stable positions (which are critical for stress continuity), the grains remain longer in the FC mode. It can also be seen that the B/$\bar{\text{B}}$ orientation begins to appear, although its proportion is very small.

iii) Figure 8.8a: When stress continuity is employed to higher strains, the texture adopts a strong {100} fibre, and includes some components which are not usually observed. This may be due to the linear programming technique, which performs a random choice in the presence of ambiguities, although the extent of the ambiguities is known to be rather limited in this case.

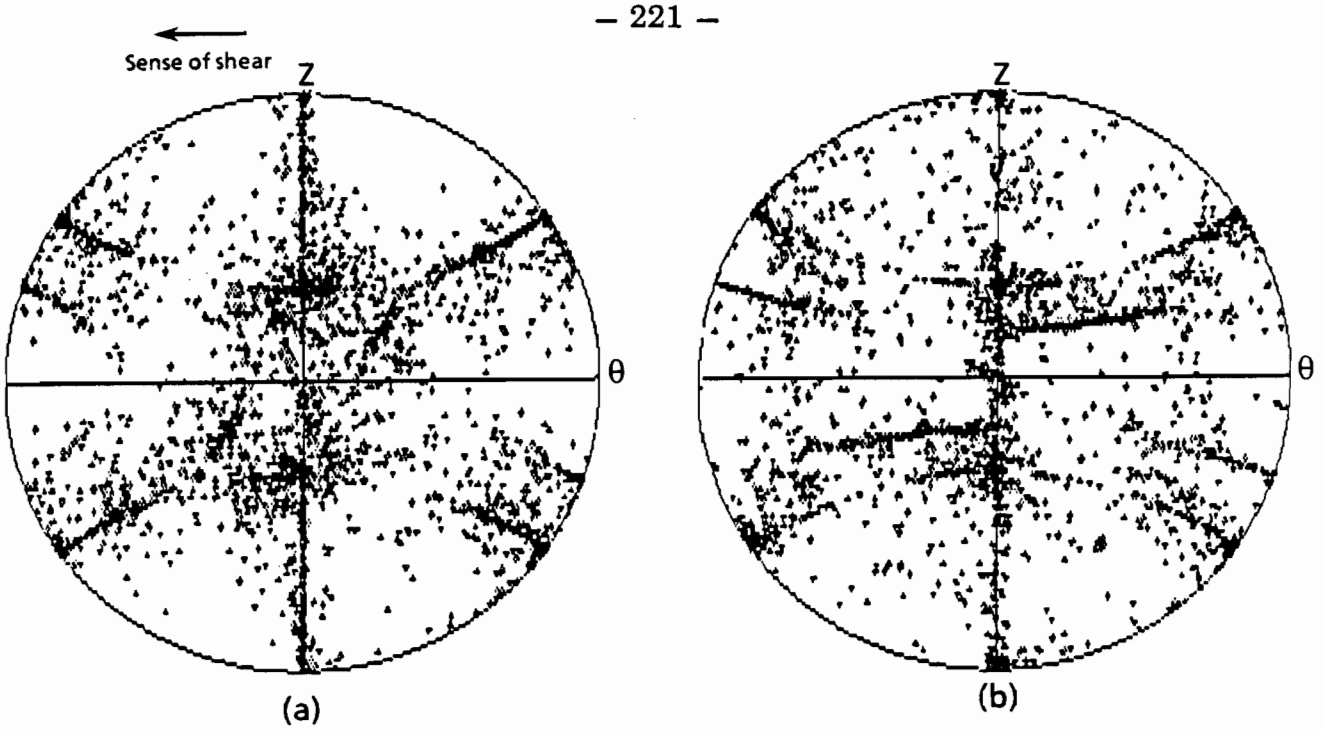

Figure 8.7. Torsion textures ($\bar{\varepsilon}=4$) simulated with: a) the SC + continuous climb model; b) the SC + GBE + continuous climb model. In both cases, $\alpha_0=\alpha_{min}=1$.

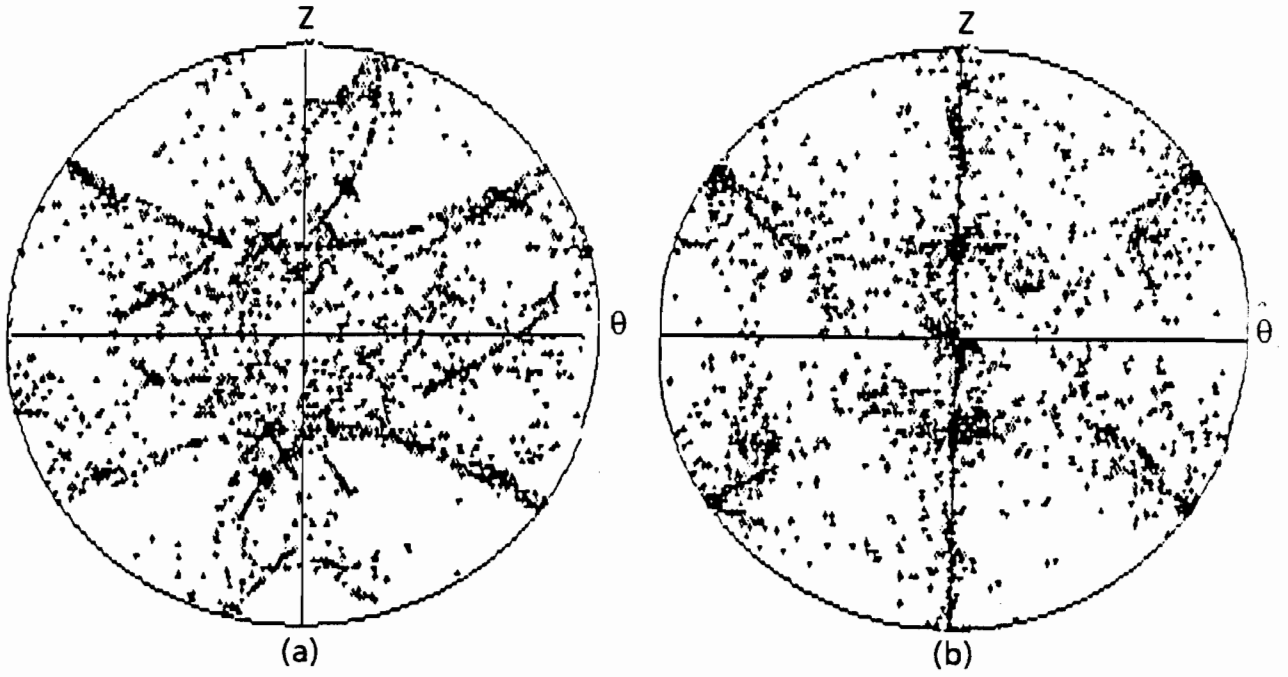

Figure 8.8. Torsion textures ($\bar{\varepsilon}=8$) simulated with: a) the SC + continuous climb model; b) the SC + GBE + continuous climb model. In both cases, $\alpha_0=\alpha_{min}=1$.

iv) Figure 8.8b: When GBE minimization is taken into account, it produces a strengthening of the B/$\bar{B}$ component at large strains. The C component also remains very strong, an orientation which is in good agreement with experimental results.

VIII.4. VALIDITY OF THE MODEL

VIII.4.1. SOURCES OF ERROR

From the above results, it is evident that the new model described here (stress continuity + grain boundary energy minimization, SC + GBE) predicts textures which are in good agreement with experimental observations at high temperatures. However, the present model may seem somewhat arbitrary in the way α_0, α_{min}, T_3, T_4 and T_5 are selected. The angles characterizing the ease of climb seem to have realistic values, but are known to vary with composition and the SFE of the material. Selection of a very small value for α_0 and 0 for α_{min} is certainly an unreasonable choice, as it would lead to the formation of no subgrains at all, and the resulting elongated grains would be expected to deform mostly according to the RC mode. The "tolerance" values for the stress difference can also be modified, the problem here being to decide on an acceptable level for the stress discontinuity.

We have also limited the possible low energy boundaries to the $\Sigma = 1$ and $\Sigma = 3$ types. This is again an arbitrary choice, although it seems to be supported by experimental observations and also by the fact that the influence of boundaries of higher Σ decreases with increasing Σ.

Another part of the simulation which can be questioned concerns the choice of the rotation axis for climb (i.e. n x b of the most active slip system). In real grains, certainly more than one rotation axis is present and in any event this particular choice only corresponds to tilt boundaries. Finally, it should be noted that the first order calculation for GBE minimization prevents the stabilization of the orientations at an exact coincidence site; instead oscillations occur around it.

All these details can certainly be improved in the future, but at this stage of knowledge, it seems better to check first if the deformation conditions imposed on the grains and the predicted types of the coincidence sites are in good agreement with experimental observations.

VIII.4.2. ADVANTAGES OF THE PRESENT MODEL

The deformation conditions imposed on the different grains of the material permit the development of a cooperative mode of deformation, a phenomenon which has been reported several times in the past. The influence of the GBE has been shown to be non-negligible, although it appears to be a second order effect at the beginning of each simulation. Polygonization has also been observed by other workers [172,180,181] and certainly plays a role in high temperature recovery processes. The present model emphasizes the influence of the sub-structure, and underlines the fact that a given grain is no longer described by a single orientation once deformation begins. This is again in good agreement with the work of Schmitt [182].

Two supplementary results will now be given to further support the validity of the present model: i.e. the number of $\Sigma=1$ and $\Sigma=3$ boundaries and the predicted axial stresses in torsion.

VIII.4.3. CALCULATED NUMBER OF STABLE BOUNDARIES

The number of sub-boundaries† close to $\Sigma=1$ and $\Sigma=3$ positions were calculated for torsion and rolling and are presented in Figure 8.9. The deviation from a $\Sigma=3$ boundary was taken as 10° because rearrangement into a stable position takes time, and the numbers obtained are still small after a deformation of 2 in rolling, for example. For both models, the number of $\Sigma=1$ positions decreases slightly with strain, whereas the number of $\Sigma=3$ positions increases. The trends obtained, particularly with the SC + GBE simulation, are

† Note that, whereas the $\Sigma=1$ boundaries between subgrains are low angle interfaces of the conventional type, the $\Sigma=3$ boundaries referred to here were developed *purely by deformation*. Thus they refer to misorientations between subgrains of the original grains and *not* to misorientations between the grains themselves.

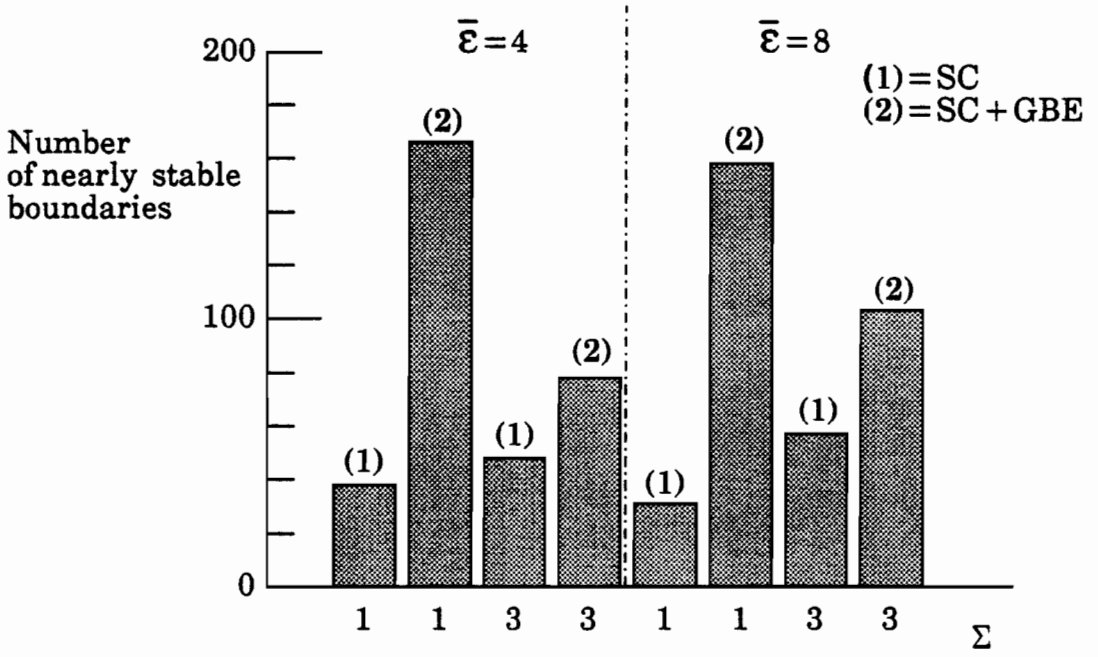

Figure 8.9a. Number of nearly stable boundaries in torsion at $\bar{\varepsilon}=4$ and $\bar{\varepsilon}=8$ for the SC and SC+GBE models. The deviation from the coincidence site is equal to 5° for $\Sigma=1$ and to 10° for $\Sigma=3$.

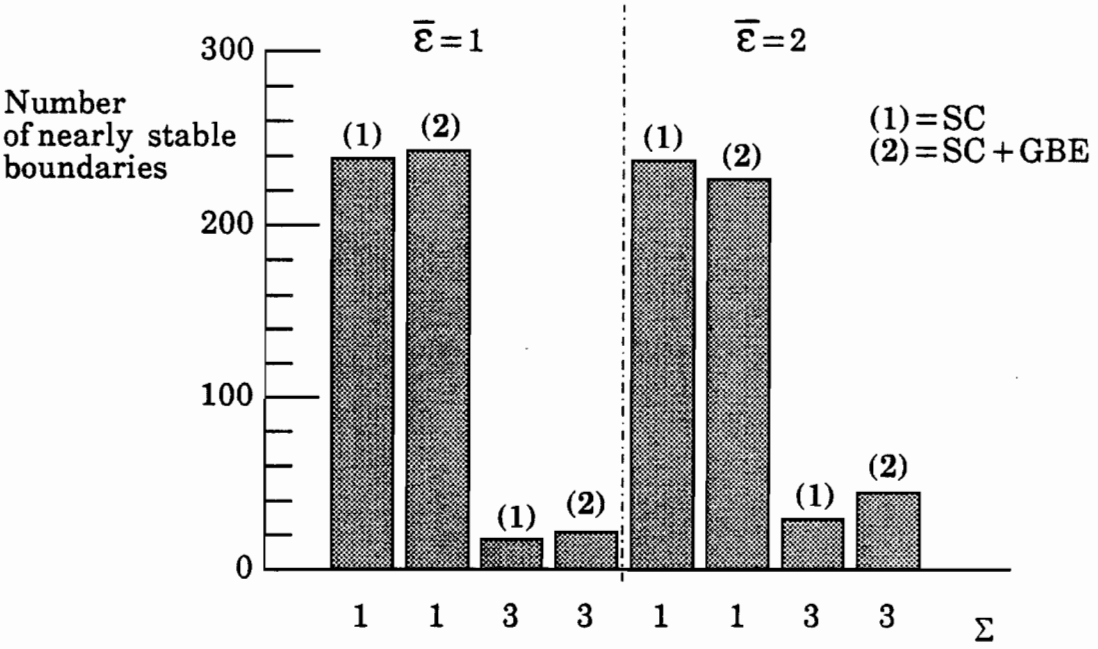

Figure 8.9b. Number of nearly stable boundaries in rolling at $\bar{\varepsilon}=1$ and $\bar{\varepsilon}=2$ for the SC and SC+GBE models. The deviation from the coincidence site relationship is equal to 5° for $\Sigma=1$ and to 10° for $\Sigma=3$.

in good agreement with the basic philosophy of the model and the differences between the mechanisms are more pronounced in torsion, where the strain is considerably higher. The small differences obtained in rolling are consistent with the small differences in the textures apparent from the pole figures.

Although the intensities vary as expected with the two models, the $\Sigma=3$ numbers seem rather small. This can be due to the choice of the rotation axis for splitting and the fact that only two subgrains are considered. Such an approach is certainly not very realistic for highly symmetric orientations. In this case, the crystallographic rotations as well as the rotations due to climb must respect the symmetry of the process [5]. However, the numbers of $\Sigma=3$ sub-boundaries are in good agreement with experimental measurements, both in rolling [174] and torsion [176]. For the latter case, it was clearly demonstrated that some of the *high angle* boundaries found in Al were "*sub-boundaries formed by polygonization*". As mentioned by Perdrix [176], it is often difficult to distinguish between the original grain boundaries and the "sub-boundaries" formed by enhanced recovery during continuous recrystallization. The latter mechanism has also been reported to occur in steel [183,184]. It is possible to interpret the resulting equiaxed substructure with high misorientations as being due solely to dynamic recovery, as in the present model.

VIII.4.4. AXIAL STRESSES IN TORSION

It is known from the work of Cohen [72] and of Montheillet and co-workers [76,82] that the axial stress in fixed end torsion varies with the strain. This is mainly due to the development of texture. In copper, for example, the axial stress is first compressive; then it changes into tension as the deformation proceeds. The change from compression to tension takes place earlier (at lower strains) when the temperature is increased. The calculated axial stress is displayed in Figure 8.10 for the following two models: FC-RC and SC+GBE. The first reproduces the trend observed at room temperature prior to fracture, whereas the second predicts the decrease in the compressive stress followed by the development of tensile stresses, as observed experimentally at high temperatures. The calculated values are also lower at high (SC+GBE) than at room (FC-RC) temperature. At strains above about 6, the SC+GBE model predicts the return of the compressive force. Although present in Al at large

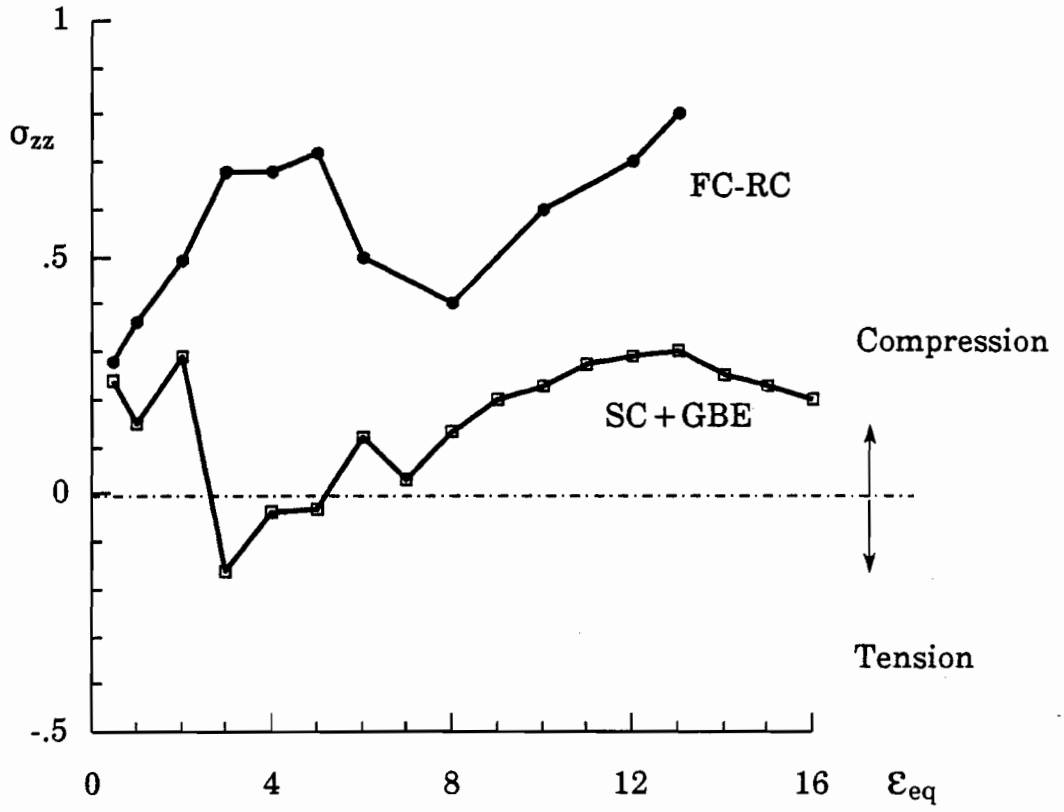

Figure 8.10. Dependence of the axial stress σ_{zz} in torsion on the equivalent strain ε_{eq} for the FC-RC and for the new model based on stress continuity and minimization of grain boundary energy.

strains, the axial stress in Cu remains tensile. The values of the parameters that are required to produce such a result have not yet been determined, but are under continuing investigation.

It can be concluded that the number of stable boundaries, the predicted axial stresses as well as the actual textures all favor the SC+GBE simulation. It could even be argued that this calculation works so well, because of the way it relaxes certain stress components. Nevertheless the SC and SC+GBE models do not predict the same textures. Moreover, the two sets of textures are not really typical of a strict RC calculation. In Figure 8.11, the rolling texture predicted for a strain of 2 according to a strict RC mode (p=2) is presented. It can be seen that the relaxation of all 3 shear stresses leads effectively to the prediction of a strong brass component; thus the results produced by the SC and SC+GBE theories can be considered as due in part to the relaxation of these stresses. This is not, however, true in torsion. The predicted RC (p=3) texture

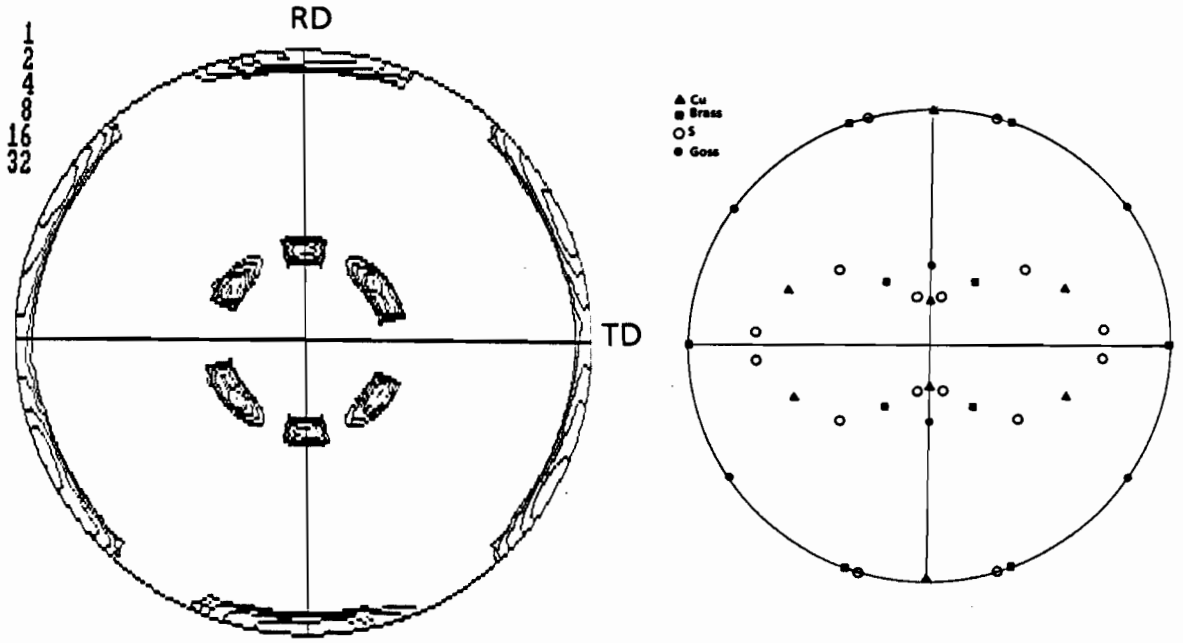

Figure 8.11. Rolling texture ($\bar{\varepsilon}=2$) simulated with a strict RC calculation. All 3 shear rates, $\dot{\varepsilon}_{12}$, $\dot{\varepsilon}_{23}$ and $\dot{\varepsilon}_{13}$ are relaxed in every grain.

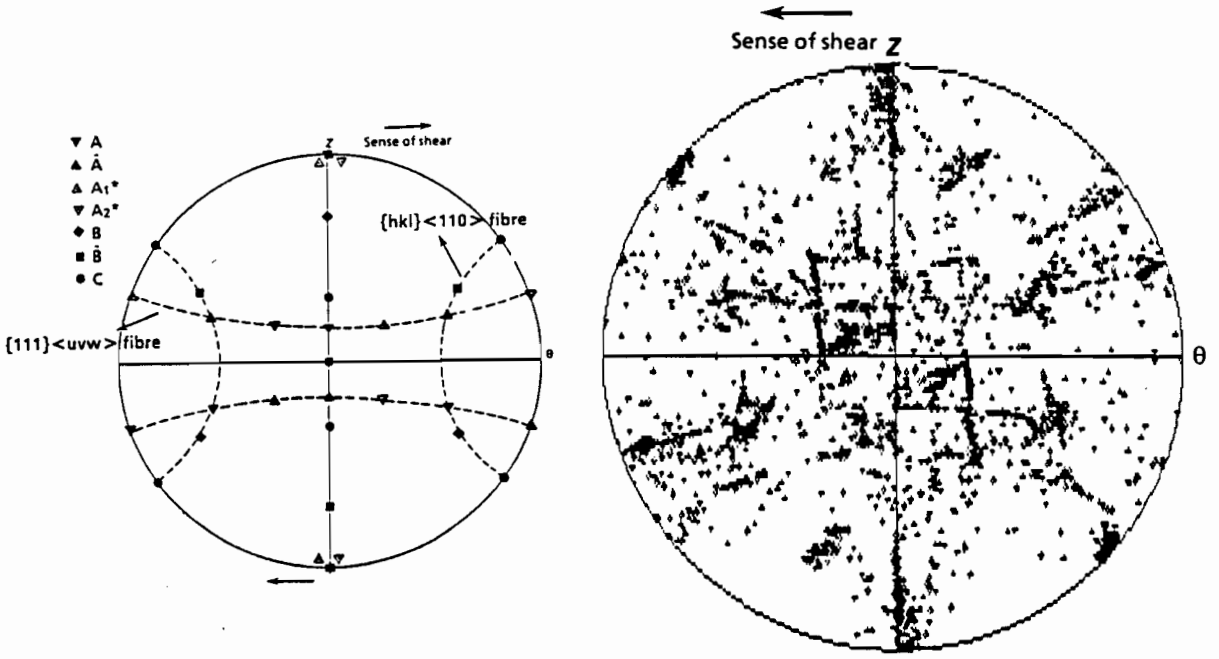

Figure 8.12. Torsion texture ($\bar{\varepsilon}=4$) simulated with a strict RC calculation. $\dot{\varepsilon}_{R\theta}$ and $\dot{\varepsilon}_{RZ}$ are allowed to differ in each grain from the macroscopic quantities.

pertaining to a strain of 4 is illustrated in Figure 8.12 and no B/$\bar{B}$ component is evident in this case, whereas only the SC + GBE model predicts it.

Before concluding this chapter, it is now time to compare all the theories investigated in this work and to decide (if possible) which one best reproduces experimental observations at high temperature.

VIII.5. COMPARISON OF THE DIFFERENT MODELS INVESTIGATED

Four possible mechanisms for the formation of high temperature textures were investigated in this work. These were:

1) the RW criterion of minimum work hardening rate;
2) the increased ease of cross-slip;
3) the activation of new slip (or cross-slip) systems;
4) the increased ease of climb and grain boundary energy minimization.

The first does not reproduce experimental observations, and is seen to be more suitable for room temperature deformation [5]. At high temperatures, other mechanisms take place which become more important. The last three, on the other hand, all predict the right trends, although in different proportions. This can be attributed to the limitations of the different models, as well as to the real effects of the different mechanisms. We will now review briefly the limitations of each model.

Cross-slip is certainly one of the mechanisms of high temperature deformation. The HL model developed here, however, suffers from two approximations:

– the hardening laws are very simple;

– the change in τ_c during an increment of deformation is neglected. In particular, the possibility that some systems may become "over-active" (τ greater than τ_c) was not checked, as in the work of Havner and Chidambarrao [185] and of Berveiller and co-workers [135,149]. The absence of "over-activity" is nevertheless probable for most of the grains.

The elimination of these two problems would, however, increase the computing time considerably and render the models much more complex.

The activation of new slip systems has been observed experimentally in a few cases. The model developed here is as rigorous as the classical FC-RC theory. The only arbitrary assumption made was that the rotation rate on the {110}<110> systems is calculated on the basis that both systems of a given pair are equally active.

The approximations which are part of the *recovery* model have been discussed above.

It now remains to carry out experimental work to test the validity of the different theories and to decide the extent to which cross-slip, the activation of new systems, and recovery and climb are active in different fcc materials. This experimental work could include the following points:

-Characterization of the active slip planes and directions for different temperatures and materials. This would help to determine the importance of cross-slip and of glide on new systems.

-Determination of the structures and substructures developed during high temperature deformation so as to verify the validity of the recovery model.

-Measurement of the misorientations between subgrains and determination of the rotation axes.

-Measurement of the shears undergone by different grains of a material to verify the assumption of cooperative deformation. In particular, it would be of interest to study aluminum deformed in torsion at 400°C, which is characterized by the development of a strong B/$\bar{B}$ texture.

VIII.6. CONCLUSIONS

In this chapter, a model was proposed to account for the occurrence of climb, the formation of an equiaxed substructure and the influence of grain boundary energy. It was shown that this model correctly predicts the trends observed at

high temperatures in terms of the textures (see Figures 8.13 and 8.14) as well as the axial stresses developed in torsion.

This model was compared to those developed in the earlier chapters and the limitations and possible sources of error of the different theories have been listed. Finally, more detailed experimental investigations are now seen to be necessary in order to decide about the validity and relative influence of the different mechanisms simulated here. The fact that the predicted textures are in good agreement with experimental ones is not enough; the mechanisms on which the different models are based must also be observed experimentally.

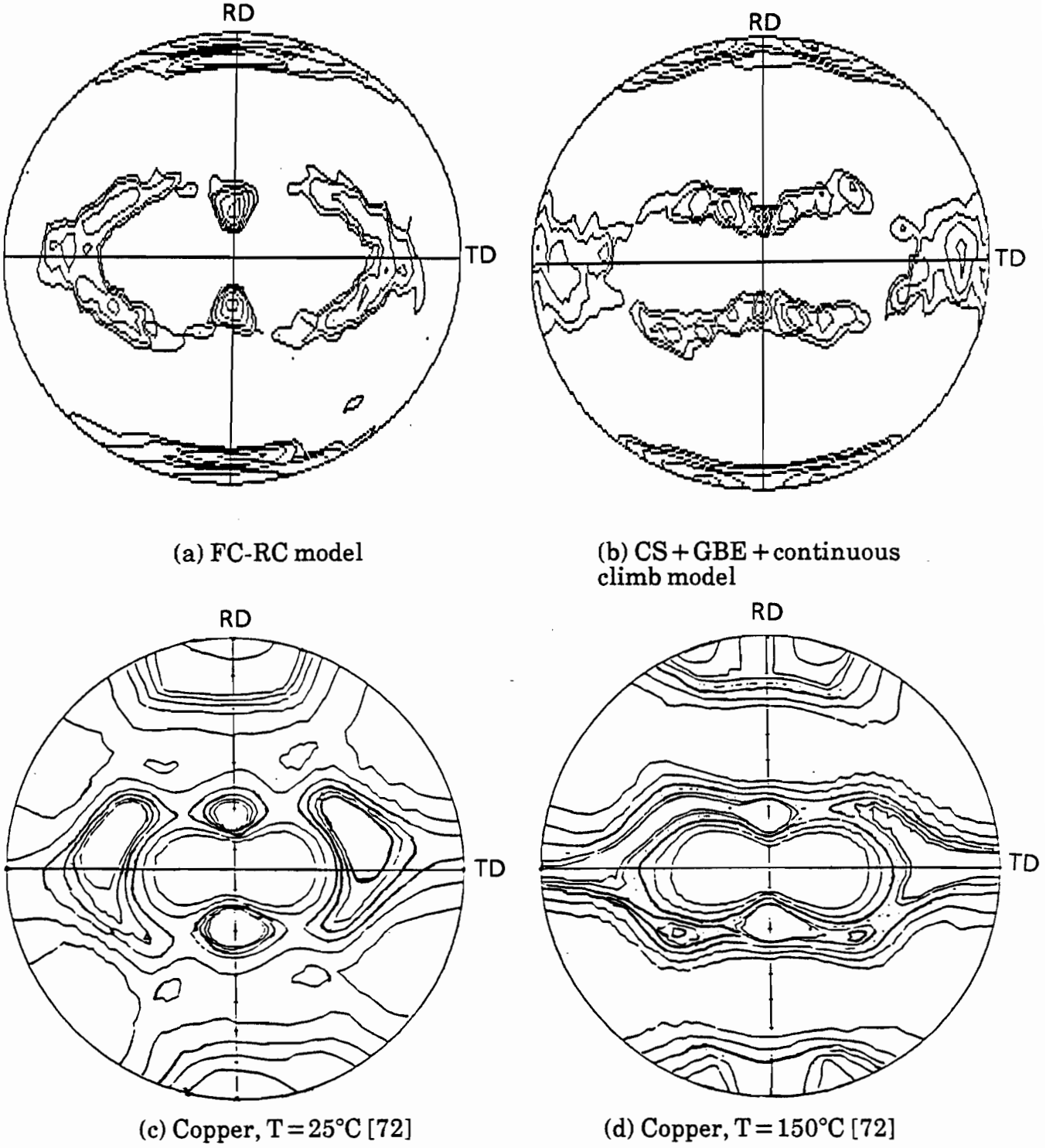

(a) FC-RC model

(b) CS + GBE + continuous climb model

(c) Copper, T = 25°C [72]

(d) Copper, T = 150°C [72]

Figure 8.13. Comparison of some experimental and predicted rolling textures.

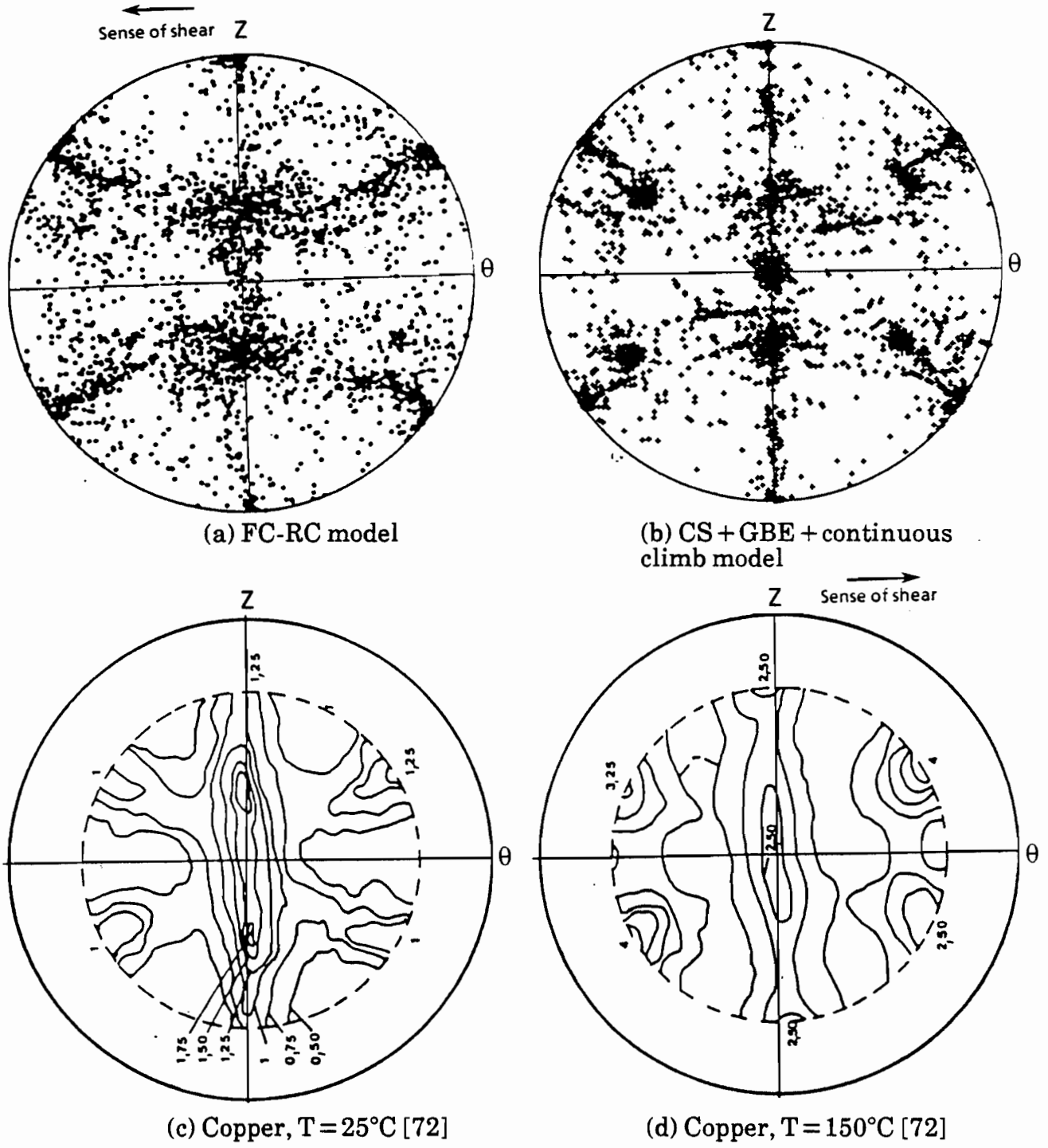

(a) FC-RC model

(b) CS + GBE + continuous climb model

(c) Copper, T = 25°C [72]

(d) Copper, T = 150°C [72]

Figure 8.13. Comparison of some experimental and predicted torsion textures.

CHAPTER IX

CONCLUSIONS

The aim of this work was the development of methods for the prediction of high temperature deformation textures. The various steps that were investigated during the progress of this research were the following:

i) Experimental textures in which the high temperature components were clearly identified were reviewed and the possible mechanisms responsible for their development were listed.

ii) The theoretical models for texture evolution were described and evaluated. An outcome of this analysis was the finding that there was no systematic investigation in the literature of the theories for texture development at high temperature. The models which could serve as the starting point for the present work were selected on the basis of the following two criteria: the model first had to be relatively simple; furthermore, it had to have the potential for adaptation to the conditions of high temperature deformation. The FC-RC model was selected for this purpose, to be used in conjunction with either the principle of maximum external work rate (yield surface examination) or the principle of minimum internal work rate (linear programming). The main assumptions in all the models developed later were that slip occurs on $\{111\}<110>$ systems and that the Schmid law is obeyed.

iii) The extension textures developed in aluminum at high temperatures were determined experimentally; this was done in order to supply data which were missing from the literature review.

iv) The mechanisms proposed in step one were incorporated into the models identified in step two. These were: (i) thermal activation, through minimization of the work hardening rate; (ii) the increased ease of cross-slip; (iii) the activation of new systems; and (iv) the effect of recovery through enhanced climb and polygonization. In the modelling of the first three

mechanisms, the grain shape arguments employed for large strains at room temperature were retained unchanged; in the last model, by contrast, the grain shape arguments were modified.

v) The predicted textures were compared with the experimental ones and the validity of the various models was discussed. The theoretical results obtained with the different models developed in this thesis are summarized in Tables 9.1 to 9.3. The quality of the agreement with the experimental textures is also given, as well as the assumptions and mathematical simplifications inherent in each model.

From this work, the following conclusions can be drawn:

1) In the experimental review, it was clearly shown that, the percentage of the so-called "brass" component increases, in both torsion and rolling, when the deformation temperature is increased. This component is usually found at room temperature in low SFE metals. It was thus proposed that the intensity of the brass component first decreases and then increases as the temperature is raised, and that this is a generalization which can be extended to any deformation mode, e.g. to tension, where the brass component is identified as the <100> fibre (found at room T in low SFE metals).

2) The experimental determination of the texture of aluminum deformed by swaging at room temperature and at 250°C confirmed the above hypothesis: the percentages of the <100> and <111> fibres were 13.3 and 2.7, respectively, in the hot deformed samples, compared to 11.3 and 3.5 in those that were cold deformed. Moreover, the larger spread around the room temperature fibres suggests that grain rotation toward stable positions takes place more quickly at higher temperatures.

3) The RW theory of minimum work hardening rate can be modified so as to simplify its application and extended to cover polycrystal deformation. It was also shown that the rotation rate of individual orientations towards stable positions is faster with the RW criterion than with the AV technique. This observation correlates well with experimental data.

4) The Chin model simulation of the ease of cross-slip was modified in the framework of the maximum external work rate instead of the minimum internal work rate principle. This modification has the advantage of suppressing two problems inherent in the Chin theory: (i) random choice in the case of remaining ambiguities and (ii) uncertainty about the independence of slip systems.

5) The RW and modified Chin models use selection criteria in the presence of ambiguities. A careful examination of the extent of these ambiguities confirms that they are more numerous in tension than in rolling and torsion and in the FC compared to the RC model. As a result, for the case of tension, which is usually treated according to the FC model, the textures predicted using the RW or modified Chin criteria differ appreciably from the ones obtained with the averaging technique. By contrast, in torsion and rolling, which are treated according to the FC-RC mode, the results are similar. This implies that any model based simply on a selection criterion is not really adequate for general purposes since it cannot account for the observed differences pertaining to *all* deformation modes.

6) The two other models developed for cross-slip, HL (hardening law) and cross-slip on {110} and {112}<110>systems, predict the right trends, i.e. an increase in the brass component in tension, torsion and rolling. The influence of cross-slip is small with the first model and depends on the value of the CRSS of the cross-slip systems in the second case; nevertheless, they have two advantages compared to the previous ones: they are first simple, and second the Schmid law is respected for every active slip system.

7) In the treatment of new active slip (or cross-slip) systems, it was demonstrated that different values of the CRSS for the various families of systems affect texture evolution in an RC model, even in the range where the number of vertices remains constant.

8) The various models can be classified in order of agreement with experiment as follows: the simulation of recovery gives the best results for the three deformation modes investigated, followed by the activation of cross-slip systems, the HL model, the modified Chin theory, the RW model and the

activation of new slip systems. Nevertheless, the recovery model suffers from a number of approximations, which are listed in Tables 9.1 to 9.3. These can be defended in terms of the following considerations:

- The climb of dislocations observed at elevated temperature can be modelled by splitting the grains into subgrains.
- The occurrence of cooperative deformation at high temperatures can be taken to justify the assumption that less constraints need to be applied to each grain or subgrain under these conditions and that stress continuity becomes more important.
- Polygonization, which also occurs at elevated temperatures and is described as the rearrangement of dislocations into more stable configurations, justifies the use of GBE minimization.

Finally, it should be mentioned that all the mechanisms proposed in Chapter II were investigated in the framework of the assumptions listed in Chapter III. This does not imply that the present study of high temperature deformation textures has been exhaustive with respect to the number of possible mechanisms or treatments of these mechanisms. In particular, rate sensitive effects were purposely neglected since they were thought to have only a small influence on texture development. Moreover, the models developed here do not have always the beauty of mechanical approaches such as the self-consistent models [135,149] or the Havner theory [185]. This work must therefore be seen as only a first approach to the simulation of high temperature textures.

Model	Predicted texture	Agreement with exper. (high T)	Simulated mechanism	Assumptions and mathematical simplifications
FC-RW	10% near <100> fibre	Not good	Min. WH rate. Thermal activation	FC mode based on GS considerations. $\tau_c(t) = C$ First order calculation
FC + modified Chin	30% <100> fibre	Very good	Cross-slip	FC mode based on GS considerations. $\tau_c(t) = C$ Special selection of ss
FC + HL	30% <100> fibre	Very good	Cross-slip	Room T GS (FC mode) Simplified hardening laws $\dot{\tau}_c$ not considered
FC + {100} slip planes	27% <100> fibre	Good	$\tau_c(T)$	FC mode based on GS considerations. $\tau_c(t) = C$

Table 9.1. Summary of the results obtained with the different models for tension.

Model	Predicted texture	Agreement with exper. (high T)	Simulated mechanism	Assumptions and mathematical simplifications
FC-RC + RW	{hkl}<110> fibre between B and C	Good at interm.T Too sharp B too weak	Min. WH rate. Thermal activation	Room T grain shape $\tau_c(t) = C$ First order calculation
FC-RC + modified Chin	Same as FC-RC model	Not very good	Cross-slip	Room T grain shape $\tau_c(t) = C$ Special selection of ss
FC-RC + HL	Strong C + A, A* and B	Good at interm. T	Cross-slip	Room T grain shape Simplified hardening laws $\dot{\tau}_c$ not considered
FC-RC + {100} slip planes	same as FC-RC	Not good	$\tau_c(T)$, $a = 1.5$	Room T grain shape $\tau_c(t) = C$
	strong cube + A, A*		$\tau_c(T)$, $a = 0.89$	
FC-RC + {110} + {112} cross-slip planes	same as FC-RC	Not good	Cross-slip & $\tau_c(T)$ with $\tau_{c1} = \tau_{c2} = \tau_{c3}$	Room T grain shape $\tau_c(t) = C$ same $\dot{\gamma}^s$ on 2{110} planes
	strong C + near B	Good	$\tau_{c1} = 10$, $\tau_{c2} = \tau_{c3} = 1$	
SC no resplitting	Close to FC	Not good	Climb (beginning) Equiaxed substr.	Partial SC between subgrains, $\tau_c(t) = C$ Arbitrary selection of variables
SC + GBE no resplitting	Close to FC	Not good	Climb (beginning) Equiaxed subst. GBE minimization	Partial SC between subgrains, $\tau_c(t) = C$ Arbitrary selection of variables 1st order calculation of GBE
SC + cont. climb	Near FC-RC	Not good	Continuous climb Equiaxed subst.	Partial SC between subgrains, $\tau_c(t) = C$ Arbitrary selection of variables
SC + GBE + cont. climb	Strong C + B + A*	Very good	Continuous climb Equiaxed subst. GBE minimization	Partial SC between subgrains, $\tau_c(t) = C$ Arbitrary selection of variables 1st order calculation of GBE

Table 9.2. Summary of the results obtained with the different models for torsion.

Model	Predicted texture	Agreement with exper. (high T)	Simulated mechanism	Assumptions and mathematical simplifications
FC-RC + modified Chin	Same as FC-RC model	Not very good	Cross-slip	Room T grain shape $\tau_c(t) = C$ Special selection of ss
FC-RC + HL	Strong Cu + S, + weak Bs	Good at interm. T Bs too weak	Cross-slip	Room T grain shape Simplified hardening laws $\dot{\tau}_c$ not considered
FC-RC + {100} slip planes	same as FC-RC	Not good	$\tau_c(T)$, $a = 1.5$	Room T grain shape $\tau_c(t) = C$
	same as FC-FC + cube	Not good	$\tau_c(T)$, $a = 0.89$	
FC-RC + {110} + {112} cross-slip planes	FC-RC + Bs	Good	Cross-slip & $\tau_c(T)$ with $\tau_{c1} = \tau_{c2} = \tau_{c3}$	Room T grain shape $\tau_c(t) = C$ same $\dot{\gamma}^s$ on 2{110} planes
	Brass + Goss	Very good	$\tau_{c1} = 10$, $\tau_{c2} = \tau_{c3} = 1$	
SC no resplitting	Close to FC	Not good	Climb (beginning) Equiaxed substr.	Partial SC between subgrains, $\tau_c(t) = C$ Arbitrary selection of variables
SC + GBE no resplitting	Close to FC	Not good	Climb (beginning) Equiaxed subst. GBE minimization	Partial SC between subgrains, $\tau_c(t) = C$ Arbitrary selection of variables 1st order calculation of GBE
SC + cont. climb	Intermediate Bs + Cu	Very good	Continuous climb Equiaxed subst.	Partial SC between subgrains, $\tau_c(t) = C$ Arbitrary selection of variables
SC + GBE + cont. climb	Intermediate Bs + Cu	Very good	Continuous climb Equiaxed subst. GBE minimization	Partial SC between subgrains, $\tau_c(t) = C$ Arbitrary selection of variables 1st order calculation of GBE

Table 9.3. Summary of the results obtained with the different models with rolling.

SUGGESTED TOPICS FOR FURTHER INVESTIGATION

This work constitutes a first attempt at the understanding and simulation of the mechanisms responsible for the development of deformation textures at high temperatures. The continuation of this research could include the following steps:

1) The occurrence of the simulated mechanisms could be experimentally verified; i.e. the ranges of temperature and stacking fault energy in which extensive cross-slip, the activation of new systems, extensive climb, recovery, and grain boundary minimization occur could be determined, by preference on single crystals tested in *constrained* deformation.

2) One or several of the proposed models could be refined, depending on the experimental results obtained from 1) above. This would involve the introduction of more realistic hardening parameters, realistic values for the CRSS of different slip systems, statistics regarding the frequency of occurrence of various types of coincidence sites, and of misorientation angles and data regarding tolerance criteria. Some of the mathematical limitations (first order calculations) could also be eliminated in this way.

3) The possible interaction of some of the proposed mechanisms could be investigated. For example, in the T and SFE range where both cross-slip and recovery are determined to be active, a combined model could be developed.

4) The plastic properties of hot worked materials could be calculated. Once the mechanisms responsible for high temperature deformation have been identified and more or less well simulated, plastic properties can be readily deduced from these models. This would involve calculation of the strain rate ratio R in sheet and axial stresses in torsion. Because of the industrial importance of anisotropy, this must be the final aim of any texture study.

STATEMENT OF ORIGINALITY AND CONTRIBUTION TO KNOWLEDGE

1) This work, as one of the first to focus on the influence of deformation temperature on texture, provides clear and extensive evidence of the differences between low and high temperature deformation textures. This resulted from the literature review which centered on temperature effects and also from a complementary small-scale experimental investigation.

2) The mechanisms which could be responsible for the above differences were tabulated and described. This list involves the effects of: thermal activation, cross-slip, the activation of new systems and recovery. All four mechanisms were simulated in a number of ways and the results of the various predictions compared to experimental data.

3) The present treatment of the RW theory comprises as original contributions:

a) clarification of the theory itself, i.e. the use of a more convenient notation;
b) complete listing of the ambiguities present in the FC and RC models; and
c) application of the theory to polycrystal deformation.

4) The Chin theory for cross-slip was rewritten in terms of the maximum work principle; this innovation avoids two of the problems inherent in the original theory. The results of the Chin and modified Chin models are also compared.

5) The increase ease of cross-slip was simulated by two further new models: i) the incorporation of simple hardening laws (usually introduced to simulate latent hardening); and ii) the introduction of cross-slip systems.

6) Slip systems other than the $\{111\}<110>$ have been employed in the past. However, their influence has only been treated in rolling; in the present work, a

more complete investigation of the activation of other systems was carried out, both in terms of deformation modes as well as possible slip planes.

7) A new model was developed to simulate the recovery process; this was expressed in terms of climb, cooperative deformation and grain boundary energy minimization. This model constitutes the first introduction of these three elements concurrently.

8) Most of the proposed models predict experimental trends reasonably well. Nevertheless, their limitations and the disagreements with experimental observations have been clearly identified, a task which eliminates the need to carry out certain unnecessary investigations and also focuses attention on the issues that remain to be settled.

REFERENCES

1. M. Hatherly and W.B. Hutchinson, "An Introduction to Textures in Metals", The Institution of Metallurgists, Monograph no 5 (1979).
2. H. Hu, R.S. Cline and S.R. Goodman, "Recrystallization, Grain Growth and Textures", Chapter 8, ASM, Metals Park, Ohio (1966), p. 295.
3. G. Sachs, Z. Ver. dent. Ing., 72 (1928), p. 734.
4. G.I. Taylor, J. Inst. Metals, 62(1938), p. 307.
5. B. Bacroix, J.J. Jonas, F.Montheillet and A. Skalli, Acta Metall., 34(1986), p. 937.
6. G.Y. Chin in "Textures in Research and Practice", Proceedings of the Int. Symposium, Clausthal-Zellerfeld (1968), Springer-Verlag Co., Berlin (1969), p. 236.
7. H. Gleiter in "Physical Metallurgy", R.W. Cahn and P. Haasen editors, Elsevier Science Publishers, BV, 1983.
8. H. Mecking in "Preferred Orientation in Deformed Metals and Rocks: An Introduction to Modern Texture Analysis". H.R. Wenk editor, Academic Press Inc. (1985), p. 267.
9. W.R. Hibbard Jr., J. Inst. Metals, 77(1950), p. 581.
10. W.R. Hibbard Jr., Trans. AIME, 185(1949), p. 598.
11. E.A. Calnan, Acta Metall., 2(1954), p. 865.
12. E.A. Calnan and B.E. Williams, Trans. AIME, 194(1952), p. 743.
13. I.L. Dillamore and W.T.Roberts, Metallurgical Reviews, 10(1965), p. 271.
14. J. Grewen and G. Wassermann, Z. Metallkunde, 45(1954), p. 498.
15. H.J. Bunge, Mber. Dt. Akad. Wiss., 5(1963), p. 293.
16. C.S. Barrett and L.H. Levenson Jr., Trans. AIME, 135(1939), p. 327.

17. C.J. McHargue, L.K. Jetter and J.C. Ogle, Trans. Met. Soc. AIME, 215(1959), p. 831.

18. R.J. Butt, Ph. D. Thesis, University of Birmingham, 1962.

19. W.T. Roberts and R.J. Butt, unpublished work quoted in (13).

20. J. Grewen and G. Wassermann, Metall., 12(1958), p. 523.

21. A.T. English and G.Y. Chin, Acta Metall., 13(1965), p. 327.

22. C.S. Barrett and T.B. Massalski, "The Structure of Metals: Crystallographic Methods, Principles and Data", McGraw Hill Book Company, 3rd Edition (1966).

23. N. Brown, Trans. Met. Soc. AIME, 222(1961), p. 236.

24. E. Aernoudt, I. Kokubo and H.P. Stüwe, Z. Metallkunde, 57(1966), p. 216.

25. H. Ahlborn, Z. Metallkunde, 57(1966), p. 877.

26. J. Gil Sevillano, P. van Houtte and E. Aernoudt, Progress in Mat. Science, 25(1980).

27. F.R.N. Nabarro, Z.S. Basinski and D.B. Holt, Adv. Physics, 13(1964), p. 193.

28. R.E. Smallman and D. Green, Acta Metall., 12(1964), p. 145.

29. I.L. Dillamore and W.T. Roberts, Acta Metall., 12(1964), p. 281.

30. E.S. Dana, "A Text Book of Mineralogy", 3rd Edition, New York (1922).

31. E.O. Hall, "Twinning and Diffusionless Transformations in Metals", Butterworths, London (1954).

32. J. Venables, J. Phys. Chem. Solids, 25(1964), p. 685.

33. J. Venables, J. Phys. Chem. Solids, 25(1964), p. 693.

34. B. Ramaswami, U.F. Kocks and B. Chalmers, Trans. Met. Soc. AIME, 233(1965), p. 927.

35. U.F. Kocks and T.J. Brown, Acta Metall., 14(1966), p. 87.

36. P.J. Jackson and Z.S. Basinski, Can. J. Phys., 45(1966), p. 707.

37. C.S. Barrett and L.H. Levenson, Trans. AIME, 137(1940), p. 112.

38. H. Naaman, R. Talreja, D. Juul Jensen and N. Hansen, submitted to Textures and Microstructures.

39. H. Mecking, Proc. ICOTOM5, March 28-31 1978, Aachen, Germany, p. 1573.

40. H. Hu, P.R. Sperry and P.A. Beck, Trans. AIME, 194(1952), p. 76.

41. H.Hu and S.R. Goodman, Trans. AIME, 227(1963), p. 627.

42. F. Haessner, Z. Metallkunde, 53(1962), p. 403.

43. R.E. Smallman, J. Inst. Metals, 83(1954-55), p. 408.

44. R.E. Smallman, J. Inst. Metals, 84(1955-56), p. 10.

45. Y.C. Liu and R.H. Richman, Trans. Met. Soc. AIME, 218(1960), p. 668.

46. R.H. Richman and Y.C. Liu, Trans. Met. Soc. AIME, 221(1961), p. 720.

47. A. Merlini and P.A Beck, Trans. AIME, 203(1955), p. 385.

48. H. Hu and R.S. Cline, J. Appl. Phys., 32(1961), p. 760.

49. H. Hu, R.S. Cline and S.R. Goodman, J. Appl. Phys. 32(1961), p. 1302.

50. S.R. Goodman and H. Hu, Trans. Met. Soc. AIME, 227(1963), p. 627.

51. R. Maddin, C.H. Mathewson and W.R. Hibbard Jr, Trans. AIME, 185(1949), p. 527.

52. F. Haessner, Z. Metallkunde, 54(1963), p. 98.

53. C.J. Beevers and R.W.K. Honeycombe, Acta Metall., 9(1961), p. 513.

54. H. Ahlborn, J. Grewen and G. Wassermann, Z. Metallkunde, 55(1964), p. 598.

55. F. Haessner in reference 2, p. 386.

56. R.E. Bauer, Ph.D. Thesis, Aachen (1970).

57. P.J. Regenet and H.P. Stüwe, Z. Metallkunde, 54(1963), p. 273.

58. M. Hatherly, A.S. Malin, C.M. Carmichael, F.J. Humphreys and J. Hirsch, Acta Metall., 34(1986), p. 2247.

59. H.J. Bunge, "Texture Analysis in Materials Science", Butterworths, 1982.

60. R.J. Roe, J. Applied Phys., 36(1965), p. 2024.

61. P. van Houtte and E. Aernoudt, Mat. Sci. and Eng., 23(1976), p. 11.

62. J. Hirsch, Ph.D. Thesis, Aachen (1984).

63. J.S. Kallend and G.J. Davies, J. Inst. Metals, 98(1970), p. 242.

64. H.J. Bunge and F. Haessner, J. of Appl. Physics, 39(1968), p. 5503.

65. J. Hirsch, K.H. Virnich and K. Lücke in Proc. ICOTOM6 (edited by S. Nagashima), Tokyo, Japan, ISIJ (1981), p. 375.

66. M.Y. Huh, J. Hirsch and K. Lücke, Proc. ICOTOM7, Noordwijkerhaut, Holland, 1984, Eds. C.M. Brakman et al., 1985, p. 651.

67. H. Eichelkraut, J. Hirsch and K. Lücke, Z. Metallkunde, 75(1984), p. 113.

68. J. Hirsch, private communication.

69. M. Bull, private communication.

70. M.J. Bull and D.J. Lloyd, in "Al-Li Alloys III", Proc. Conf. Oxford, 1985, Eds. Baker et al., 1986.

71. J.R. Holland, Ph.D. Thesis, University of Kentucky (1962).

72. M. Cohen, Thèse de Docteur-Ingénieur, Ecole des Mines de Paris (1983).

73. W.A. Backofen, Trans. Am. Inst. Min. Met. Eng., 188(1950), p. 1454.

74. W.A. Backofen and B.B. Mundy, ibid., 197(1953), p. 61.

75. P.O. Williams, Trans. Met. Soc. AIME, 224(1962), p. 129.

76. F. Montheillet. P. Gilormini and J.J. Jonas, Acta Metall., 33(1985), p. 705.

77. G.R. Canova, U.F. Kocks and J.J. Jonas, Acta Metall., 32(1984), p. 221.

78. P. van Houtte, E. Aernoudt and K. Sekine, Proc. ICOTOM 6 (see ref. 65), p. 337.

79. J. Gil Sevillano, P. van Houtte and E. Aernoudt, Scripta Metall., 11(1977), p. 581.

80. K. Sekine, P. van Houtte, J. Gil Sevillano and E. Aernoudt, Proc. ICOTOM6 (see ref. 65), p. 396.

81. P. van Houtte, Acta Metall., 26(1978), p. 591.

82. F. Montheillet, M. Cohen and J.J. Jonas, Acta Metall., 32(1984), p. 2077.

83. H.P. Stüwe, Iron and Steel Inst. Rep. 108 (1968), p. 1.

84. R.F. Lynch, Ph. D. Thesis, Lehigh University, 1971.

85. U. Schmidt and K. Lücke, Texture of Cryst. Solids, 3(1979), p. 85.

86. K. Ito, R. Müsik and K. Lücke, Acta Metall., 31(1983), p. 2137.

87. J. Hirsch and K. Lücke, Acta Metall., 33(1985), p. 1927.

88. W. G. Burgers and P.C. Louwerse, Z. Physik, 61(1931), p. 605.

89. C. S. Barrett, Trans. AIME, 137(1940), p. 128.

90. P.R. Rowland, J. Inst. Met., 83(1954), p. 455.

91. W.G. Burgers and C.A. Verbraak, Acta Metall., 5(1957), p. 765.

92. P.A. Beck and H. Hu, reference 2, chapter 9, p. 393.

93. B. Liebmann, K. Lücke and G. Masing, Z. Metallkunde, 47(1956), p. 57.

94. M.L. Kronberg and F.H. Wilson, Trans. AIME, 185(1949), p. 501.

95. J.C.M. Li in "Recovery and Recrystallization of Metals", L. Himmel Ed., Interscience, New York, 1963, p. 160.

96. P. Gordon and R.A. Vandermeer, reference 2, chapter 6, p. 205.

97. C. Schnell and H.G. Grewe, Proc. ICOTOM5 (see ref. 39), p. 389.

98. J. Grewen and J. Huber, in "Recrystallization of Metallic Materials", F. Haessner ed., Dr. Riederer-Verlag GMBH, Stuttgart, 1978, p. 111.

99. E. Schmid, Proc. Int. Congr. Appl. Mech. Delft, 1924, p. 342.

100. U.F. Kocks, Metall. Trans. 1(1970), p. 1121.

101. J.F.W. Bishop and R. Hill, Phil. Mag., 42(1951), p. 414.

102. T. Leffers, Risø Report No.184 (1968).

103. U.F. Kocks and H. Chandra, Acta Metall., 30(1982), p. 695.

104. G.R. Canova, Ph.D. Thesis, McGill University, Montreal,1982.

105. U.F. Kocks, G.R. Canova and J.J. Jonas, Acta Metall., 31(1983), p. 1243.

106. C.N. Tomé and U.F. Kocks, Acta Metall., 33(1985), p. 603.

107. G.R. Canova, U.F. Kocks, C.N. Tomé and J.J. Jonas, J. Mech. Phys. Solids, 33(1985), p. 371.

108. Ph. Lequeu, P. Gilormini, F. Montheillet, B. Bacroix and J.J. Jonas, to be published in Acta Metall..

109. Ph. Lequeu, Ph.D. Thesis, McGill University, Montreal, Canada, 1986.

110. G.I. Taylor, in "Deformation and Flow of Solids", Proc. IUTAM Colloq. Madrid (R. Grammel ed.), Springer, Berlin, 1955, p. 3.

111. P. van Houtte and E. Aernoudt, Z. Metallkunde, 66(1975), p .4.

112. J.F.W. Bishop and R. Hill, Phil. Mag., 42(1951), p. 1298.

113. G.Y. Chin and W.L. Mammel, Trans. Met. Soc. AIME, 245(1969), p. 1211.

114. P. van Houtte, Proc. ICOTOM6 (see ref. 65), p. 428.

115. M. Renouard and M. Wintenberger, C.R. Acad. Sc. Paris, B283(1976), p. 237.

116. A. Kochendörfer, Reine und angewandte Metallkunde, Springer Berlin, 1941.

117. H. Honneff and H. Mecking, Proc. ICOTOM5 (see ref. 39), p. 265.

118. A. Skalli, Thèse d'Etat, Ecole des Mines de Saint Etienne, France, 1982.

119. U.F. Kocks and G.R. Canova, Proc. 2nd Risø Int. Symp.: "Deformation of Polycrystals: Mechanisms and Microstructures", Hansen et al. eds., 1981, p. 35.

120. P.van Houtte, Mem. Sci. Rev. Met., 82(1985), p.57.

121. M. Renouard and M. Wintenberger, C.R. Acad. Sc. Paris, B290(1980), p. 403.

122. J.H. Driver, A. Skalli and M.Wintenberger, Mem. Sci. Rev. Met., 80(1983), p. 293.

123. J.H. Driver, A. Skalli and M. Wintenberger, Phil. Mag., A49(1984), p. 505.

124. A. Skalli, R. Fortunier, R. Fillit and J.H. Driver, Acta Metall., 33(1985), p. 997.

125. C. Tomé, G.R. Canova, U.F. Kocks, N. Christodoulou and J.J. Jonas, Acta Metall., 32(1984), p. 1637.

126. P.R. Morris, TMS AIME Fall Meeting, Toronto, Oct. 1985.

127. B. Orlans-Joliet, B. Bacroix, F. Montheillet, J.H. Driver and J.J. Jonas, to be published.

128. P. van Houtte, Proc. ICSMA7, Montreal, 1985, vol.3, p. 1701.

129. K. Wierzbanowski, Proc. ICOTOM5 (see ref. 39), p. 309.

130. R. Fortunier and J.H. Driver, to be published in Acta Metall..

131. E. Kröner, Acta Metall., 9(1961), p. 155.

132. J.D. Eshelby, Proc. Roy. Soc. London, A241(1957), p. 376.

133. R. Hill, J. Mech. Phys. Solids, 13(1965), p. 89.

134. J.W. Hutchinson, Proc. Roy. Soc. London, A319(1970), p. 247.

135. M. Berveiller and A. Zaoui, J. Mech. Phys. Solids, 26(1979), p. 325.

136. A. Zaoui, Advanced School, Udine (Italy) 1985.

137. K. Wierzbanowski, A. Hihi, M. Berveiller and A. Clement, Proc. ICOTOM7 (see ref. 66), p. 179.

138. P. Franciosi, M. Berveiller and A. Zaoui, Acta Metall., 28(1980), p. 273.

139. P. Franciosi and A. Zaoui, Acta. Metall., 30(1982), p. 1627.

140. U.F. Kocks, Trans. Met. Soc. AIME, 230(1964), p. 1160.

141. K.S. Havner, Mech. Mat., 1(1982), p. 97.

142. N.T. Le and K.S. Havner, Mech. Mat., 4(1985), p. 33.

143. R.J. Asaro and A. Needleman, Acta Metall., 33(1985), p. 923.

144. G.R. Canova and U.F. Kocks, Proc. ICOTOM7 (see ref. 66), p. 573.

145. U.F. Kocks, G.R. Canova and C.N. Tomé, unpublished work.

146. R. Fortunier and J.H. Driver, unpublished work.

147. P. van Houtte, unpublished work.

148. W.F. Hosford, Trans. Met. Soc. AIME, 230(1963), p. 12.

149. M. Berveiller and A. Zaoui, Proc. ICOTOM5 (see ref. 39), p. 319.

150. M. Renouard and M. Wintenberger, C.R. Acad. Sci. Paris, B292(1981), p. 385.

151. A.V. Hershey, J. Appl. Mech., 21(1954), p. 241.

152. J.P. Hirth and J. Lothe, "Theory of Dislocations", McGraw Hill, New York (1968).

153. R. Fortunier, J.H. Driver and M. Wintenberger, C.R. Acad. Sci. Paris, Ser. II 301(1985), p. 69.

154. T.C. Lowe, unpublished work.

155. J.H. Driver and A. Skalli, Rev. Phys. Appl., 17(1982), p. 447.

156. G.C. Canova, Thèse d'Etat, Université de Metz, France, 1986.

157. S. Tiem, M. Berveiller and G.C. Canova, Acta Metall., 34(1986), p. 2139.

158. G.Y. Chin and W.L. Mammel, Trans. Met. Soc. AIME, 239(1967), p. 1400.

159. G. Vanderschaeve and B. Escaig in "Dislocations et Déformation plastique", Ecole d'été d'Yravals (1979), Les Editions de Physique, Paris.

160. P. Gangli and P. Arato, Acta Metall., 34(1976), p. 465.

161. R. Le Hazif, P. Dorizzi and J.P. Poirier, Acta Metall., 21(1973), p. 903.

162. G.Y. Chin and W.L. Mammel, Met. Trans., 4(1973), p. 335.

163. J. Benard, A. Michel, J. Philibert and J. Talbot, " Métallurgie générale"., Masson ed., 1984.

164. S.F. Exell and D.H. Warrington, Phil. Mag., 26(1972), p. 112.

165. H.J. McQueen and J.J. Jonas, Treatise on Materials and Technology, Vol. 6, Academic Press, 1975.

166. W.A. Wong, H.J. McQueen and J.J. Jonas, J. Inst. Met., 95(1967), p. 129.

167. W.T. Read and W. Shockley, Phys. Rev., 78(1950), p. 275.

168. W. Bollmann, "Crystal Defects and Crystalline Interfaces, Springer, Berlin, 1970.

169. D.G. Brandon, B. Ralph, S. Ranganathan and M.S. Wald, Acta Metall., 12 (1984), p. 813.

170. D.G. Brandon, Acta Metall., 14(1966), p. 1479.

171. H. Gleiter, Phys. Stat. Sol., 45(1971), p. 9.

172. J. Flaquer and J. Gil Sevillano, J. Mat. Sci., 19(1984), p. 423.

173. N. Hansen, Metall. Trans., 16A(1985), p. 2167.

174. J. Gil Sevillano and F.J. Torrealdea, reference 119, p. 185.

175. B. Bay and N. Hansen, ibid., p. 137.

176. Ch. Perdrix, Thèse Docteur-Ingénieur, Ecole des Mines de Paris, 1983.

177. C. Schnell and H.G. Grüwe, ICOTOM 5 (see ref. 39), p. 389.

178. L.C. Lim and R. Raj, Acta Metall., 32(1984), p. 1177.

179. M. Dahms, P.I. Welch and H.J. Bunge, Scripta Metall., 16(1982), p. 827.

180. D.C. Crites, R.K. Raghavan and B.L. Adams, submitted to Metall. Trans., February 1986.

181. J. Zhao, B.L. Adams and P.R. Morris, submitted to Textures and Microstructures, March 1986.

182. J.H. Schmitt, Thèse d'Etat, Université de Grenoble, France, 1986.

183. C. Donadille, C. Rossard and B.J. Thomas, Proc. 7th Risø Int. Symp.: "Annealing Processes - Recovery, Recrystallization and Grain Growth", Hansen et al. eds., 1986, p. 285.

184 R. Lombry, C. Rossard and B.J. Thomas, Revue de Métallurgie, CIT, 12(1981), p. 975.

185. K.S. Havner and D. Chidambarrao, submitted for Aris Phillips Memorial Issue of Acta Mechanica, September 1986.

APPENDIX 1

CALCULATION OF THE CRYSTALLOGRAPHIC ROTATION

The orientation of a given grain in a polycrystal is specified by a 3x3 rotation matrix which indicates the position of the three <100> axes of the crystal with respect to 3 external reference axes. These axes are usually defined with respect to the test geometry. In the case of rolling, the axes usually selected are the transverse, rolling, and normal directions. In torsion, the axes are generally the radial, transverse and longitudinal axes of the specimen. To remain general here, we will specify the orientation of a given grain by a matrix A expressed in terms of 3 Euler angles ϕ, θ and ω. This can be written schematically as:

$$CS \xrightarrow{A} SS \tag{A1.1}$$

Thus, a vector V_c in the crystal system CS will become V_s in the sample system SS as given by:

$$V_S = A\,V_C \tag{A1.2}$$

with A being defined by:

$$A = \begin{bmatrix} cos\omega cos\phi - sin\omega cos\theta sin\phi & cos\omega sin\phi + sin\omega cos\theta cos\phi & sin\omega sin\theta \\ -sin\omega cos\phi - cos\omega cos\theta sin\phi & -sin\omega sin\phi + cos\omega cos\theta cos\phi & sin\theta cos\omega \\ sin\theta sin\phi & -sin\theta cos\phi & cos\theta \end{bmatrix} \tag{A1.3}$$

The reference axes are called V_{s1}, V_{s2} and V_{s3} on the one hand and V_{c1}, V_{c2} and V_{c3} on the other.

When slip takes place on several slip systems during an increment of time dt, a given vector V transforms into another V' according to the relation:

$$V' = V + \sum_s \dot{\gamma}^s \, dt \, (V . n^s) \, b^s \tag{A1.4}$$

The above can be written using matrix notation as

$$V' = B V \tag{A1.5}$$

where the matrix B defines the displacement gradient tensor associated with simple shear on the s systems.

$$B = \begin{vmatrix} 1 + \sum_s \dot{\gamma}^s n_1^s b_1^s & \sum_s \dot{\gamma}^s n_2^s b_1^s & \sum_s \dot{\gamma}^s n_3^s b_1^s \\ \sum_s \dot{\gamma}^s n_1^s b_2^s & 1 + \sum_s \dot{\gamma}^s n_2^s b_2^s & \sum_s \dot{\gamma}^s n_3^s b_2^s \\ \sum_s \dot{\gamma}^s n_1^s b_3^s & \sum_s \dot{\gamma}^s n_2^s b_3^s & 1 + \sum_s \dot{\gamma}^s n_3^s b_3^s \end{vmatrix} .dt \tag{A1.6}$$

Similarly, a normal N to a given plane specified by

$$N = u_1 \times u_2 \tag{A1.7}$$

where u_1 and u_2 are two unit vectors belonging to the plane of interest tranforms into [104]:

$$N' = B u_1 \times B u_2 \tag{A1.8}$$

We now calculate the new position of the sample axes with respect to the crystal axes by stating that certain planes and directions remain fixed in space. Let us first consider the two dimensional example illustrated in Figure A1.1. Under the action of the shear $\dot{\gamma} dt$, the vectors V_{s1} and V_{s2} transform into V^*_{s1} and V^*_{s2} according to (Figure A1.1a)

$$\begin{aligned} V^*_{s1} &= B V_{s1} \\ V^*_{s2} &= B V_{s2} \end{aligned} \tag{A1.9}$$

We first note that the vectors V^*_{s1} and V^*_{s2} are not orthonormal. Now if the axis V_{s1} is required to remain fixed in space (for example, if this axis is the tensile axis of the specimen of Figure 3.1), the axes V_{c1} and V_{c2} will rotate through an angle α to transform into V'_{c1} and V'_{c2} (Figure A1.1b). The positions of these two vectors with respect to V_{s1} and V_{s2} lead to the new value of the matrix A, i.e. A'. But Figure A1.1 indicates that we can define a vector V'_{s2}, orthogonal to V^*_{s1}, which together with $V'_{s1} = V^*_{s1} / V^*_{s1}$ also defines the new matrix A' (Figure A1.1c). Calculating the positions of V_{s1} and V_{s2} with respect to V'_{c1} and V'_{c2} is thus completely equivalent to calculating the positions of V'_{s1}

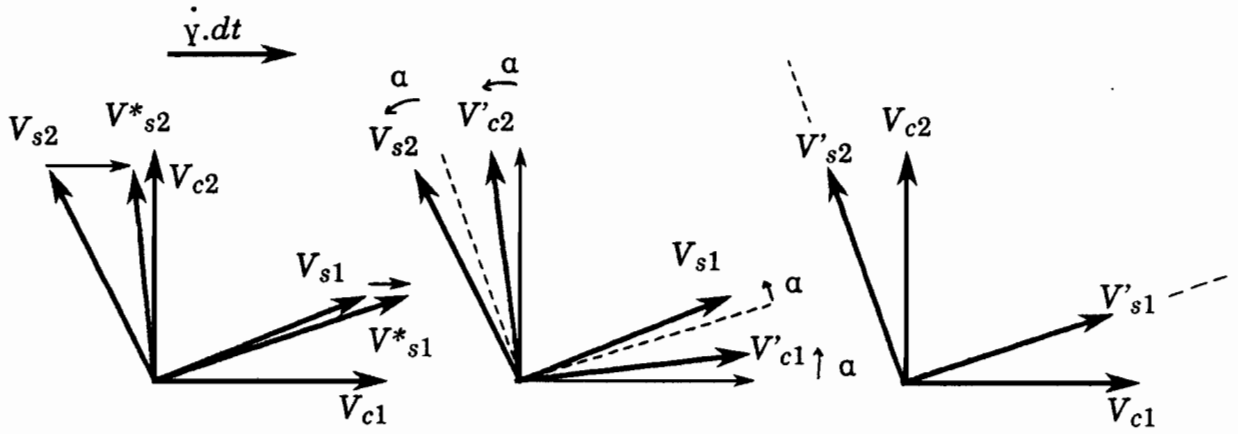

Figure A1.1. Crystallographic rotation in a two-dimensional example. The axis SS_1 is assumed to be fixed in space.

and V'_{s2} with respect to V_{c1} and V_{c2}. The coordinates of the vectors V'_{s1} and V'_{s2} are first calculated from V_{s1} and V_{s2} as:

$$V'_{s1} = B\,V_{s1} / \|B\,V_{s1}\| \tag{A1.10}$$

$$V'_{s2} = \textit{unit vector perpendicular to } V'_{s1}$$

The first condition is the transcription of the fact that V_{s1} remains fixed in space. A matrix T having the two vectors V'_{s1} and V'_{s2} as row vectors with respect to V_{s1} and V_{s2} is defined in this way so that we can write that

$$A' = T\,A \tag{A1.11}$$

Turning now to the three dimensional case, we assume, for example, that the axis labelled 2 and the normal to the plane labelled 3 in the sample system remain fixed in space. This corresponds to rolling, where the rolling plane and rolling direction are taken as fixed in each grain of the polycrystal as well as to torsion, where the shear direction and shear plane are taken as fixed in every grain. We now reconstruct the sample reference system (SS') as follows. As in the 2 dimensional case, instead of searching for the *new* position of the CS with respect to the SS, we look for the positions of the vectors V'_{s1}, V'_{s2} and V'_{s3} with respect to the old CS, from which we get the new orientation A' of the grain. The 3 base vectors of the SS transform into V^*_{s1}, V^*_{s2} and V^*_{s3} according to :

$$V^*_{s1} = B\,V_{s1}$$

$$V^*_{s2} = B\,V_{s2} \qquad \text{(A1.12)}$$

$$V^*_{s3} = B\,V_{s3}$$

Assuming that V_{ss2} remains fixed implies that:

$$V'_{s2} = V^*_{s2} / \| V^*_{s2} \| = BV_{s2} / \| BV_{s2} \| \qquad \text{(A1.13)}$$

Similarly, assuming that plane 3 remains fixed implies that:

$$V'_{s3} = V^*_{s1} \times V^*_{s2} / \| V^*_{s1} \times V^*_{s2} \| = B\,V_{s1} \times B\,V_{s2} / \| B\,V_{s1} \times B\,V_{s2} \| \qquad \text{(A1.14)}$$

Since no particular condition is imposed on the 1 axis, the vector V'_{s1} is simply taken as orthogonal to V'_{s2} and V'_{s3}, which gives:

$$V'_{s1} = V'_{s2} \times V'_{ss3} \qquad \text{(A1.15)}$$

This condition assures the orthonormality of the reference system SS'. If the matrix B is now expressed in the sample reference system, we can construct with V'_{s1}, V'_{s2} and V'_{s3} a matrix T

$$T = \begin{vmatrix} V'^{1}_{s1} & V'^{2}_{s1} & V'^{3}_{s1} \\ V'^{1}_{s2} & V'^{2}_{s2} & V'^{3}_{s2} \\ V'^{1}_{s3} & V'^{2}_{s3} & V'^{3}_{s3} \end{vmatrix} \qquad \text{(A1.16)}$$

which has the V'_s vectors as row vectors with respect to the V_s vectors, from which the new matrix A' is given by

$$A' = T\,A \qquad \text{(A1.17)}$$

We have thus defined a procedure which allows us to calculate the new orientation of a crystal step by step. This procedure is equivalent to the one used by Kocks and Chandra and can be used in any kind of calculation (FC or RC). It is equivalent to saying that certain components of the displacement gradient tensor of the grain are allowed to differ from the macroscopic ones. Returning to Figure 3.4, we have seen that the RC theory allows the two shear rates $\dot{\varepsilon}_{23}$ and $\dot{\varepsilon}_{13}$ to be different from 0 in a grain of a polycrystal being deformed in rolling. Assuming now that the rolling direction and plane remain fixed in space implies that these two shear rates correspond to the displacement rates $\dot{u}_{2,3}$ and $\dot{u}_{1,3}$. The displacement rates $\dot{u}_{3,2}$ and $\dot{u}_{3,1}$ are equal to 0.

In tension, the calculation is performed by assuming that the tensile direction remains fixed. This single condition allows us to determine only the new position of the tensile axis and to plot inverse pole figures. Also, because of the axial symmetry, the other two base vectors can be taken, arbitrarily, as being orthogonal to the first ones, thus specifying matrix A' completely. This procedure allows us to plot the results on pole figures whenever this representation is desired for comparison purposes, and from there to calculate average pole densities (see Chapters IV and V). In compression, the calculation is similar. In this case, however, the single condition is that the compression plane is assumed to remain fixed.

APPENDIX 2

DEFINITION OF A FIVE DIMENSIONAL VECTORIAL NOTATION

It was seen in Chapter III that only the deviator stress components are relevant, and because elastic dilatation is being neglected as well, it is simpler to write the deviatoric stress and strain rate tensors as five dimensional vectors of the form:

$$\sigma = (\sigma_1, \sigma_2, \sigma_3, \sigma_4, \sigma_5) \qquad \text{(A2.1)}$$

$$\dot{\varepsilon} = (\dot{\varepsilon}_1, \dot{\varepsilon}_2, \dot{\varepsilon}_3, \dot{\varepsilon}_4, \dot{\varepsilon}_5)$$

The last three components are customarily defined as proportional to the off-diagonal components [100,105-107] and any convenient convention for contracting the three diagonal tensor components into the first two vector components may be used, as long as the stress and strain rate are work conjugate, i.e. as long as

$$\sigma_{ij}\dot{\varepsilon}_{ij} = \sigma_i \dot{\varepsilon}_i \qquad \text{(A2.2)}$$

It was demonstrated by Canova et al. [107] that the normality rule holds in such a vector space if it holds in the tensor space.

One example of such a notation is the following [108,109]:

$$\sigma = \left(\frac{(\sigma_{22} - \sigma_{11})}{\sqrt{2}}, \sqrt{3/2}\,\sigma_{33}, \sqrt{2}\,\sigma_{23}, \sqrt{2}\,\sigma_{31}, \sqrt{2}\,\sigma_{12}\right) \qquad \text{(A2.3)}$$

$$\dot{\varepsilon} = \left(\frac{(\dot{\varepsilon}_{22} - \dot{\varepsilon}_{11})}{\sqrt{2}}, \sqrt{3/2}\,\dot{\varepsilon}_{33}, \sqrt{2}\,\dot{\varepsilon}_{23}, \sqrt{2}\,\dot{\varepsilon}_{31}, \sqrt{2}\,\dot{\varepsilon}_{12}\right)$$

It can readily be shown that these two vectors are work-conjugate. The interesting point about this notation is that it corresponds to a single *orthonormal* five dimensional space in which both σ and $\dot{\varepsilon}$ are defined [108]. This means that, starting from a nine dimensional space which is also taken to be orthonormal (i.e. described by 9 orthogonal unit vectors) and in which the

nine components of the stress and strain rate tensors are defined, 5 orthogonal unit vectors can be found such that the 5 components of stress and strain rate have the form given in equation A2.3. These components are functions of the 9 original ones. The same unit vectors (i.e. the same space) are used for both σ and $\dot{\varepsilon}$, and this is quite unusual. Normally these vectors are defined in two different spaces which are known to be "conjugate" or "dual"; they can coincide only if they are orthonormal. As a result of the orthonormality, the norm of any vector σ expressed in this reference system is simply:

$$\|\sigma\| = \sqrt{\sigma_i \sigma_i} \tag{A2.4}$$

In this particular space, the requirement that a given strain rate is accommodated by slip can be written as:

$$\dot{\varepsilon}_{ij} = \sum_s m_{ij}^s \dot{\gamma}^s \quad \Leftrightarrow \quad \dot{\varepsilon} = \sum_s \dot{\gamma}^s N^s \tag{A2.5}$$

where N^s has the components:

$$N^s = \left(\frac{(n_2^s b_2^s - n_1^s b_1^s)}{\sqrt{2}}, \sqrt{3/2} n_3^s b_3^s \right. \tag{A2.6}$$

$$\left. \frac{\sqrt{2}}{2}(n_2^s b_3^s + n_3^s b_2^s), \frac{\sqrt{2}}{2}(n_1^s b_3^s + n_3^s b_1^s), \frac{\sqrt{2}}{2}(n_1^s b_2^s + n_2^s b_1^s) \right)$$

The parallel between equations A2.3 and A2.6 is immediate. The vector N^s defines the normal to one facet of the single crystal yield surface proposed by Bishop and Hill. Calculating the components of N^s for each of the 12 $\{111\}<110>$ systems gives the following result:

$$\|N^s\| = 1/\sqrt{2} \qquad \forall s \tag{A2.7}$$

which means that the N^s vectors are not unit vectors.

Going further, the Schmid law can be rewritten in this notation as:

$$\tau^s = \sigma . N^s \leq \tau_c^s \tag{A2.8}$$

If we now consider a combination of five independent slip systems defined by five vectors , we can define a 5x5 matrix M from the N^i vectors (whose components are $N^i{}_j$ with $j = 1, 5$):

$$M = \begin{vmatrix} N_1^1 & N_1^2 & N_1^3 & N_1^4 & N_1^5 \\ N_2^1 & N_2^2 & N_2^3 & N_2^4 & N_2^5 \\ N_3^1 & N_3^2 & N_3^3 & N_3^4 & N_3^5 \\ N_4^1 & N_4^2 & N_4^3 & N_4^4 & N_4^5 \\ N_5^1 & N_5^2 & N_5^3 & N_5^4 & N_5^5 \end{vmatrix} \tag{A2.9}$$

such that equation A2.5 can be rewritten as:

$$\dot{\varepsilon} = M \dot{\gamma} \tag{A2.10}$$

where the vector $\dot{\gamma}$ is simply:

$$\dot{\gamma} = (\dot{\gamma}^1, \dot{\gamma}^2, \dot{\gamma}^3, \dot{\gamma}^4, \dot{\gamma}^5) \tag{A2.11}$$

Similarly, the fact that the Schmid law is satisfied on one set of 5 independent slip systems (defined by M) can be written in compact form as:

$$\tau_c = {}^tM \sigma \tag{A2.12}$$

with

$$\tau_c = (\tau_c^1, \tau_c^2, \tau_c^3, \tau_c^4, \tau_c^5) \tag{A2.13}$$

We can now examine how the transformation of a tensor from one reference system to another evolves in this 5 dimensional representation. A given tensor $\underset{\sim}{E_1}$ expressed in a reference system labelled 1 can be expressed in a reference system labelled 2 as $\underset{\sim}{E_2}$ according to the transformation rule:

$$\underset{\sim}{E_2} = A \underset{\sim}{E_1} A^t \tag{A2.14}$$

Here A is a matrix in which the rows represent the coordinates of the new base vectors expressed in the old base. With the aid of the present notation, equation A2.14 transforms into the following:

$$E_2 = C E_1 \tag{A2.15}$$

E_1 and E_2 are the two vectors associated with the tensors $\underset{\sim}{E_1}$ and $\underset{\sim}{E_2}$ and C is a 5x5 matrix whose terms depend on the terms of the matrix A as follows:

$$C_{11} = \frac{1}{2}(A_{11}^2 + A_{22}^2 - A_{12}^2 - A_{21}^2) \qquad C_{12} = \frac{\sqrt{3}}{2}(A_{23}^2 - A_{13}^2) \qquad C_{13} = A_{22}A_{23} - A_{12}A_{13}$$

$$C_{14} = A_{21}A_{23} - A_{11}A_{13} \qquad C_{15} = A_{21}A_{22} - A_{11}A_{12}$$

$$C_{21} = \frac{\sqrt{3}}{2}(A_{32}^2 - A_{31}^2) \qquad C_{22} = \frac{1}{2}(2A_{33}^2 - A_{13}^2 - A_{23}^2) \qquad C_{23} = \sqrt{3}\,A_{32}A_{33}$$

$$C_{24} = \sqrt{3}\,A_{31}A_{33} \qquad C_{25} = \sqrt{3}\,A_{31}A_{32} \qquad \text{(A2.16)}$$

$$C_{31} = A_{22}A_{23} - A_{21}A_{32} \qquad C_{32} = \sqrt{3}\,A_{23}A_{33} \qquad C_{33} = A_{22}A_{33} + A_{23}A_{32}$$

$$C_{34} = A_{21}A_{33} + A_{23}A_{31} \qquad C_{35} = A_{21}A_{32} + A_{22}A_{31}$$

$$C_{41} = A_{12}A_{32} - A_{11}A_{31} \qquad C_{42} = \sqrt{3}\,A_{13}A_{33} \qquad C_{43} = A_{12}A_{33} + A_{13}A_{32}$$

$$C_{44} = A_{11}A_{33} + A_{13}A_{31} \qquad C_{45} = A_{11}A_{32} + A_{12}A_{31}$$

$$C_{51} = A_{12}A_{22} - A_{11}A_{21} \qquad C_{52} = \sqrt{3}\,A_{13}A_{23} \qquad C_{53} = A_{12}A_{23} + A_{13}A_{22}$$

$$C_{54} = A_{11}A_{23} + A_{13}A_{21} \qquad C_{55} = A_{11}A_{22} + A_{12}A_{21}$$

The complete derivation of this matrix can be found in reference 109. It should be noted, however, that any other notation respecting equation A2.2 also leads to a matrix C. But the expression of C is not the same for the tensors σ and $\dot{\varepsilon}$ defined in two non-orthonormal spaces [77].

So in all cases, the introduction of a vector notation leads to the reduction of computation time by replacing tensor transformations by vector ones. In the special case treated here, this reduction is still greater since only one matrix C has to be calculated. Before terminating this Appendix, it should be noted that the present notation differs from the one used by Canova and co-workers [104,105] in that it is defined in an orthonormal space which also simplifies the graphical representation of cross-sections of yield surfaces. On the other hand, Canova et al [105] selected a notation such that the norm of the strain rate vector defined by $\sqrt{\dot{\varepsilon}_i \dot{\varepsilon}_i}$ is equal to the von Mises equivalent strain rate defined by:

$$\dot{\varepsilon}_{eq} = \sqrt{2/3\,\dot{\varepsilon}_{ij}\,\dot{\varepsilon}_{ij}} \qquad \text{(A2.17)}$$

In the case of the present notation, it is readily seen that there is a factor of $\sqrt{2/3}$ between the two, since $\dot{\varepsilon}_{ij}\,\dot{\varepsilon}_{ij} = \dot{\varepsilon}_i\,\dot{\varepsilon}_i$.

APPENDIX 3

DERIVATION OF THE LOWER AND UPPER BOUNDS OF THE MACROSCOPIC STRESS VECTOR

This derivation issues from the work of Bishop and Hill [101] but is reformulated in the notation used in the present treatment. Also, unlike the original text of Bishop and Hill, the parallel between the *lower bound* and Sachs theories on the one hand and between the *upper bound* and Taylor theories on the other is made explicit.

Bishop and Hill [101] have shown that, if slip is the only deformation mechanism, the principles of maximum external and minimum internal work rate hold for the macroscopic yield surface. (As a consequence, the normality principle also holds for this macroscopic yield function.) Consider now a polycrystalline aggregate in which the macroscopic quantities are described by S for the stress state and $\dot{E}$ for the strain rate state. The macroscopic yield function is then expressed by

$$f(S_{ij}) \leq C \tag{A3.1}$$

The corresponding microscopic quantities are σ and $\dot{\varepsilon}$. These quantities are unknown, and generally only the macroscopic stress direction or strain rate vector is known. The difficulty then is to calculate the unknown macroscopic quantities from the unknown microscopic ones. It will be demonstrated in this Appendix that it is possible to determine two scalars λ^* and μ^*, which satisfy the relation:

$$\lambda^* \leq \| S \| \leq \mu^* \tag{A3.2}$$

The *maximum external work rate principle* for an aggregate has been expressed by Bishop and Hill [101] as follows: for any macroscopic stress S^* corresponding to an *equilibrium* microscopic distribution σ^* not violating the Schmid law, we always have:

$$(S - S^*) . \dot{E} \geq 0 \tag{A3.3}$$

Similarly, the *minimum internal work rate principle* for an aggregate says that for any microscopic shear rate distribution $\dot{\gamma}^*$ associated with the actual microscopic stress distribution σ, we have

$$\sum \tau_c \dot{\gamma} \leq \sum \tau_c \dot{\gamma}^* \tag{A3.4}$$

where the signs Σ denote the average taken over the whole aggregate. $\dot{\gamma}$ designates the actual shear rates associated with σ and $\dot{\varepsilon}$, and $\dot{\gamma}^*$ designates the shear rates associated with a *continuous* displacement distribution, with zero divergence, and with the same values on the surface as the actual displacement distribution.

1) EXISTENCE OF A LOWER BOUND

Suppose that each grain of the polycrystal is subjected to the following *uniform* stress distribution:

$$\sigma^* = \lambda^* r \tag{A3.5}$$

with r being a unit vector in the macroscopic stress direction:

$$r = S / \| S \| \tag{A3.6}$$

λ^* is defined such that the critical resolved shear stress corresponding to σ^* is attained in only one grain (the "weakest point") of the aggregate. It is thus certain that σ^* does not violate the Schmid law anywhere and that the polycrystal is in equilibrium, since it is constant everywhere through the aggregate. Also, the macroscopic quantity S^* associated with σ^* is equal to σ^*.

$$S^* = \sigma^* \tag{A3.7}$$

As S^* satisfies the conditions pertaining to equation A3.3, it follows that:

$$(S - S^*) . \dot{E} \geq 0 \tag{A3.8}$$

which can be rewritten as:

$$(1 - \lambda^* / \| S \|) . S \dot{E} \geq 0 \tag{A3.9}$$

in which $S.\dot{E}$ is the macroscopic work rate, which is positive; consequently

$$\| S \| \geq \lambda^* \tag{A3.10}$$

Hence, for each direction r in stress hyperspace, equation A3.9 supplies the lower limit to the actual "length" of the stress vector S. Such a limit is obtained by imposing the same stress direction on each grain of the polycrystal (this

direction is that of the macroscopic one) in such a way that only one grain is plastified. This is exactly what is described in Chapter III as the lower bound model derived from the Sachs theory, which is sometimes called the static model. It is worth noting here that, for a given stress direction, we have found only one possible lower limit for $\|S\|$. This is because it is difficult to find a stress distribution other than the one defined above which is in equilibrium, and which does not violate the Schmid law at any point of the aggregate.

2) EXISTENCE OF AN UPPER BOUND

Now we subject each grain of the polycrystal to a *uniform* strain rate distribution

$$\dot{\varepsilon}^* = \dot{E}^* \tag{A3.11}$$

such that

$$r.\,\dot{\varepsilon}^* \geq 0 \tag{A3.12}$$

where r is the unit vector defining the macroscopic stress direction. This condition can also represent a uniform strain rate distribution $\dot{\varepsilon}^*$ which is not "too far" from the actual macroscopic strain rate $\dot{E}$ on the macroscopic yield surface. In this way, an outward pointing normal can be taken so that the work rate is positive. To this microscopic strain rate distribution corresponds a microscopic stress distribution σ^* which can readily be calculated by applying the principal of maximum external work to the single crystal yield function. Since both microscopic stress states σ^* and σ lie on the SCYS, the principle of maximum work rate implies that:

$$(\sigma^* - \sigma).\,\dot{\varepsilon}^* \geq 0 \tag{A3.13}$$

and, by taking the average over all the grains in which $\dot{\varepsilon}^*$ is constant, that:

$$(S^* - S).\,\dot{E}^* \geq 0 \tag{A3.14}$$

Here, S^* is the average macroscopic stress corresponding to σ^*. We can now rewrite the norm of the stress vector S as:

$$\|S\| = \|S\|.\frac{S.\dot{E}^*}{S.\dot{E}^*} = \frac{S.\dot{E}^*}{r.\dot{E}^*} \tag{A3.15}$$

and, from equation A3.14, deduce that

$$\|S\| \leq \frac{S^*.\dot{E}^*}{r.\dot{E}^*} = \mu^* \qquad \text{(A3.16)}$$

All the terms on the right hand side of inequality A3.16 being known, we have thus found an upper limit μ^* to the value of $\|S\|$. Unlike the case of the lower bound, in this case any uniform strain rate distribution which satisfies equation A3.12 provides an upper limit to $\|S\|$. It is probable that all the upper values found in this way will be different. However, there is no means at this point to classify them in order to find the lowest upper limit possible. Let us now consider two particular cases.

i) Take first the case where $\dot{E}^*$ is equal to the actual macroscopic strain rate $\dot{E}$. This particular strain rate distribution constitutes the Taylor assumption of uniform strain rate and obviously satisfies condition A3.12. Moreover, it is the strain rate distribution most often used to determine an upper bound (if not the only one). The value of μ^* associated with this value of $\dot{E}^*$ thus constitutes an upper limit to $\|S\|$. It has been demonstrated in this way that the Taylor assumption leads to an upper limit to the norm of the stress vector, but it must be kept in mind that this is not the only one.

ii) Consider now another possible strain rate distribution which also forms an upper limit:

$$\dot{E}^* = r \qquad \text{(A3.17)}$$

Since r is a unit vector, μ^* is simply equal to :

$$\mu^* = S^* \dot{E}^* = S^* r \qquad \text{(A3.18)}$$

where S^* designates the average macroscopic stress vector associated with $\dot{E}^*$. In this case, the value of μ^* is equal to the work rate which would be done in the aggregate in which all the grains are separately subjected to the strain rate r.

It is worth noting that, because of equation A3.14, any uniform strain rate distribution satisfying equation A3.12 also provides an upper limit to the macroscopic work rate, $\dot{W} = S.\dot{E}$. This is in particular true for the Taylor assumption and it is often with respect to $\dot{W}$ that the Taylor assumption is said to be an upper limit. However, we prefer here to refer to the norm of the macroscopic stress vector to remain consistent with the lower bound treatment.

In this way, the quantities μ^* and λ^* define two extreme values for the same physical parameter, i.e. the norm of the macroscopic stress vector. This can also be interpreted as signifying that there are two limiting yield surfaces for the polycrystal, the real one falling between these two surfaces.

APPENDIX 4

GENERALIZATION OF THE PRINCIPLES OF MAXIMUM EXTERNAL AND MINIMUM INTERNAL WORK RATE TO THE CASE OF RC DEFORMATION

Renouard and Wintenberger have demonstrated that these two principles can be generalized so as to permit the selection of the active slip systems under mixed boundary conditions [115,121]. They developed their theory for a single crystal deformed in such a way that the components of the strain rate tensor are not entirely known and prescribed. In what follows, we extend their generalization to the case of a polycrystal for which the strain rate tensor is not fully prescribed due to grain shape considerations [119].

Let us first define the notation to be used. We first distinguish between the free and prescribed stress and strain rate components as follows:

i) $\dot{\varepsilon}'_{ij}$ are the *prescribed* strain rate components, so that the associated stress components σ_{ij} are *free* (i.e. they are not prescribed in the case of the single crystal and are free to differ from the corresponding specimen components in the case of a grain in the polycrystal). Accordingly, the number $p<5$ of σ'_{ij} components is equal by definition to the number of $\dot{\varepsilon}'_{ij}$ components.

ii) $\dot{\varepsilon}''_{ij}$ are the remaining (5-p) components of the strain rate tensor. These are not prescribed in the case of the single crystal, and are free to differ from the corresponding specimen components in the case of a grain in the polycrystal). Associated with each $\dot{\varepsilon}''_{ij}$ is the corresponding stress component σ''_{ij}, which is prescribed, i.e. imposed on the single crystal, or prescribed to equal the corresponding specimen component in the polycrystal.

In Figure A4.1, the stress and strain rate tensors for a single crystal deformed in plane strain compression are shown, as well as those pertaining to a polycrystal deformed in rolling.

Boundary Conditions for single crystal

$\dot{\varepsilon}_{13}=0$

$\dot{\varepsilon}_{12}, \dot{\varepsilon}_{23}$ free $\qquad\qquad$ $\sigma_{12}=\sigma_{23}=0$ (no friction)

$$\begin{bmatrix} \dot{\varepsilon}'_{11} & \dot{\varepsilon}''_{12} & \dot{\varepsilon}'_{13} \\ \dot{\varepsilon}''_{21} & \dot{\varepsilon}'_{22} & \dot{\varepsilon}''_{23} \\ \dot{\varepsilon}'_{31} & \dot{\varepsilon}''_{32} & \dot{\varepsilon}'_{33} \end{bmatrix} \qquad \begin{bmatrix} \sigma'_{11} & \sigma''_{12} & \sigma'_{13} \\ \sigma''_{21} & \sigma'_{22} & \sigma''_{23} \\ \sigma'_{31} & \sigma''_{32} & \sigma'_{33} \end{bmatrix}$$

$\dot{\varepsilon}'_{ij}, \sigma''_{ij}$ = imposed

$\sigma'_{ij}, \dot{\varepsilon}''_{ij}$ = free

(a)

Grain Shape Considerations for polycrystal

$\dot{\varepsilon}_{12}=0$

$\dot{\varepsilon}_{13}, \dot{\varepsilon}_{23}$ free $\qquad\qquad$ $\sigma_{13}=\sigma_{23}=0$ usually

$$\begin{bmatrix} \dot{\varepsilon}'_{11} & \dot{\varepsilon}'_{12} & \dot{\varepsilon}''_{13} \\ \dot{\varepsilon}'_{21} & \dot{\varepsilon}'_{22} & \dot{\varepsilon}''_{23} \\ \dot{\varepsilon}''_{31} & \dot{\varepsilon}''_{32} & \dot{\varepsilon}'_{33} \end{bmatrix} \qquad \begin{bmatrix} \sigma'_{11} & \sigma'_{12} & \sigma''_{13} \\ \sigma'_{21} & \sigma'_{22} & \sigma''_{23} \\ \sigma''_{31} & \sigma''_{32} & \sigma'_{33} \end{bmatrix}$$

$\dot{\varepsilon}'_{ij}, \sigma''_{ij}$ = imposed to be equal to the macroscopic components

$\sigma'_{ij}, \dot{\varepsilon}''_{ij}$ = free to differ from the macroscopic components

(b)

Figure A4.1. Stress and strain rate tensors (defined in the reference frame of the sample) applicable to: a) a single crystal deforming in a channel die; and b) a polycrystal deformed by flat rolling. The compression and elongation axes are the 3 and 2 axes, respectively.

The microscopic shear rates $\dot{\gamma}^s$ on the activated slip systems are always related to the prescribed components of strain rate by

$$\dot{\varepsilon}'_{ij} = \sum_s m^s_{ij} \dot{\gamma}^s \tag{A4.1}$$

It is worth noting that once the active slip systems are known, the *unprescribed* components of the strain rate tensor can be calculated by a similar equation

$$\dot{\varepsilon}''_{ij} = \sum_s m^s_{ij} \dot{\gamma}^s \tag{A4.2}$$

The Schmid law can now be written in a slightly different form than employed above, i.e.:

$$\tau^s = \sigma_{ij} m^s_{ij} = \sigma'_{ij} m^s_{ij} + \sigma''_{ij} m^s_{ij} \tag{A4.3}$$

Note that the full tensor includes both the σ'_{ij} (free) and σ''_{ij} (prescribed) components. For convenience below, the *prescribed* component of the shear stress will be referred to as

$$\tau^s_0 = \sigma''_{ij} m^s_{ij} \tag{A4.4}$$

GENERALIZATION OF THE TAYLOR THEORY

Renouard and Wintenberger have shown that both the minimum internal work rate and the maximum external work rate analyses can be generalized to cover deformation when the number of imposed strain components $p<5$, i.e. is less than the number associated with the classical one. Under these conditions, they showed that the power of interest is the internal work increment per unit volume and per unit time $\dot{W}$ done in response to the prescribed strain rate components and carried out by the *free* stresses. This is equal to :

$$\dot{W} = \sum_s (\tau_c - \tau^s_0) . \dot{\gamma}^s \tag{A4.5}$$

Here $\Sigma\tau_c.\dot{\gamma}^s$ is the total internal work increment per unit time and $\Sigma\tau_0.\dot{\gamma}^s$ is the component of this work performed by the *prescribed* stresses (which are generally zero).

Equation A4.5 can be derived as follows. Suppose that a plastic strain rate $\dot{\varepsilon}_{ij}$ occurs under a given state of stress σ_{ij}. (Note that only the $\dot{\varepsilon}'_{ij}$ and σ''_{ij}

components of these two tensors are known at this stage.) Now consider two alternative sets of $n \geqq p$ slip systems which could be involved in producing the plastic strain: the P set, given the index s, corresponds to the real solution of the problem (which may not be unique), and the Q set, indexed k, does not. On each slip system of the P set we then have

$$\tau^s = \tau_c \tag{A4.6}$$

and on at least one of the slip systems k of the Q set we have

$$\tau^k < \tau_c \tag{A4.7}$$

The equivalent of equation A4.1 for the Q set is now written as:

$$\dot{\varepsilon}'_{ij} = \sum_k m^k_{ij} \dot{\gamma}^k \tag{A4.8}$$

Multiplying equation A4.6 by $\dot{\gamma}^s$, summing over s, and employing equation A4.3, we obtain for the P set:

$$\sum_s \tau^s \dot{\gamma}^s = \sum_s \tau_c \dot{\gamma}^s \tag{A4.9}$$

or

$$\sum_s (\sigma'_{ij} m^s_{ij} + \tau^s_0) \dot{\gamma}^s = \sum_s \tau_c \dot{\gamma}^s \tag{A4.10}$$

so that, through the use of equation (A4.1)

$$\sigma'_{ij} \dot{\varepsilon}'_{ij} = \sum_s (\tau_c - \tau^s_0) \dot{\gamma}^s \tag{A4.11}$$

In a similar manner, multiplying equation A4.7 by $\dot{\gamma}^k$ and summing over k, we obtain for the Q set:

$$\sum_k \tau^k \dot{\gamma}^k < \sum_k \tau_c \dot{\gamma}^k \tag{A4.12}$$

or

$$\sum_k (\sigma'_{ij} m^k_{ij} + \tau^k_0) \dot{\gamma}^k < \sum_k \tau_c \dot{\gamma}^k \tag{A4.13}$$

and finally, from equation A4.8,

$$\sigma'_{ij} \dot{\varepsilon}'_{ij} < \sum_k (\tau_c - \tau^k_0) \dot{\gamma}^k \tag{A4.14}$$

Note that the same stress state σ_{ij} and strain rate $\dot{\varepsilon}_{ij}$ pertain to the two possible sets of slip systems analyzed above, so that σ'_{ij} and $\dot{\varepsilon}'_{ij}$ are also identical for the two cases. Equations A4.11 and A4.14 can therefore be combined to give:

$$\sum_s (\tau_c - \tau_0^s)\dot{\gamma}^s \; < \sum_k (\tau_c - \tau_0^k)\dot{\gamma}^k \qquad \text{(A4.15)}$$

where $\dot{\gamma}^s$ and τ_c are both positive, so that $\dot{\gamma}^s.\tau_c > 0$. Equation A4.15 states that the real solution is obtained by minimizing the rate of internal (microscopic) work done *with respect to alternative sets of slip systems,* as given by $(\tau_c - \tau_0{}^s)\dot{\gamma}^s$. This corresponds to the rate of shear work done in response to the imposition of the prescribed strain rate components $\dot{\varepsilon}'_{ij}$ only, and under the sole action of the developed (free) stresses σ'_{ij}. When all the strain rate components are prescribed, as in the classical model, the term $\tau_0{}^s$ does not exist, the components σ'_{ij} and $\dot{\varepsilon}'_{ij}$ are replaced by the full tensors σ_{ij} and $\dot{\varepsilon}_{ij}$, respectively, and the RW and Taylor approaches coincide.

GENERALIZATION OF THE BISHOP AND HILL THEORY

The second method proposed by RW considers all the stress states which are compatible with the Schmid law, equation A4.1. For the real solution (the stress state P), we have $\tau^s = \tau_c$ on a certain set of slip systems. This can be written as

$$\tau^s = \sigma'_{ij} m^s_{ij} + \sigma''_{ij} m^s_{ij} = \tau_c \qquad \text{(A4.16)}$$

For the hypothetical solution (the Q stress state), we have $\bar{\tau}^s < \tau_c$ *on at least one system of the same set of slip systems* (the ones activated in the real solution), as given by:

$$\bar{\tau}^s = \bar{\sigma}'_{ij} m^s_{ij} + \sigma''_{ij} m^s_{ij} < \tau_c \qquad \text{(A4.17)}$$

Here the prescribed components σ''_{ij} are the same for both τ^s and $\bar{\tau}^s$ ($\tau_0{}^s = \bar{\tau}_0{}^s$), but the σ'_{ij} components are different. However, the strain rates $\dot{\varepsilon}_{ij}$, $\dot{\varepsilon}'_{ij}$ and $\dot{\varepsilon}''_{ij}$, as they pertain to a *single* set of systems, are identical for the two cases. We now define the individual shear rates in terms of $\dot{\varepsilon}'_{ij}$:

$$\dot{\varepsilon}'_{ij} = \sum_s m^s_{ij} \dot{\gamma}^s \qquad \text{(A4.18)}$$

Combining equations A4.4 and A4.6, we can write for the P stress state that

$$\sigma'_{ij} m^s_{ij} + \tau^s_0 = \tau_c \qquad \text{(A4.19)}$$

and then, by multiplying by $\dot{\gamma}^s$, that

$$\sum_s (\sigma'_{ij} m^s_{ij} + \tau^s_0)\, \dot{\gamma}^s = \sum_s \tau_c \dot{\gamma}^s \tag{A4.20}$$

or that

$$\sigma'_{ij} \dot{\varepsilon}'_{ij} = \sum_s (\tau_c - \tau^s_0) \dot{\gamma}^s \tag{A4.21}$$

In a parallel fashion, for the Q stress state, it is evident that:

$$\overline{\sigma}'_{ij} m^s_{ij} + \tau^s_0 < \tau_c \tag{A4.22}$$

that

$$\sum_s (\overline{\sigma}'_{ij} m^s_{ij} + \tau^s_0)\, \dot{\gamma}^s = \sum_s \tau_c \dot{\gamma}^s \tag{A4.23}$$

and finally that

$$\overline{\sigma}'_{ij} \dot{\varepsilon}'_{ij} = \sum_s (\tau_c - \tau^s_0) \dot{\gamma}^s \tag{A4.24}$$

In this case, equations A4.21 and A4.24 can be combined to give:

$$\overline{\sigma}'_{ij} \dot{\varepsilon}'_{ij}\ (\textit{hypothetical}) < \sigma'_{ij} \dot{\varepsilon}'_{ij}\ (\textit{real}) \tag{A4.25}$$

Thus the real solution is the one which maximizes the rate of external work *with respect to alternative permissible stress states*. This is again associated, as in the Taylor analysis, solely with the free components of the stress and the prescribed components of the strain rate. As before, when all the strain rate components are prescribed, equation A4.25 corresponds to the classical BH criterion.

APPENDIX 5

DESCRIPTION OF THE COMPUTER PROGRAM USED IN THE FC, RC AND FC-RC THEORIES (WITH THE AVERAGING TECHNIQUE)

This appendix describes the basic computer programs developed by Canova [104]. The same program can be used with all three models, FC, RC and FC-RC, and for the four principal deformation modes, tension, compression, rolling and torsion. The different steps to be employed are the following:

1) Read the SCYS data: the 28 vertices and the associated 6 or 8 slip systems, the 4^{th} and 3^{rd} order edges with their corresponding connecting vertices (2 in the case of the 4^{th} order edges and 3 or 4 in the case of the 3^{rd} order edges) and associated slip systems (6, 5 or 4 for the 4^{th} order edges and 3 or 4 for the 3^{rd} order edges). Then read the 480 combinations of 5 independent slip systems, the 108 combinations of 4 independent slip systems and the 135 combinations of 3 independent slip systems.

2) The test conditions are specified; these include: i) the deformation path: tension, compression, rolling or torsion; ii) for the case of torsion, whether the sample axes (in the case of FC) or the grain axes (in the case of RC) are to be employed; iii) the deformation mode: FC, RC or FC-RC; in the latter two cases, the components of strain rate which are relaxed are given.

3) With the aid of these data, the calculation is carried out grain by grain. For each step, the procedure is the following: i) read the orientation of the grain; ii) calculate the proportion of grains deforming according to $p=5$, 4 or 3 in the FC-RC model; iii) determine the stress state and all the possible combinations of independent slip systems (after having performed the appropriate transformations from the crystal system to the sample or grain system); iv) calculate the average distortion matrix and the new orientation of the grain (this depends on the deformation mode); v) go back to step (i) to update the new proportions of grains and so on.

In the case where the RW criterion is to be included or some special selection of the possible combinations of slip systems is to be made, as in the case of the cross-slip model, steps (iii) and (iv) must be modified as described in Chapters V and VI. If other slip systems are to be incorporated, step (1) must be modified to read the data corresponding to the new SCYS.

APPENDIX 6

DEPENDENCE OF THE TAYLOR FACTOR IN TORSION ON ORIENTATION OF THE CRYSTAL RELATIVE TO THE SAMPLE AXES

ϕ, θ and ω are the Euler angles defined in Appendix 1.

Present Notation		Bunge Notation (Section II.1.3)
ϕ	=	$-\phi_2$
θ	=	$-\Phi$
ω	=	$-\phi_1$

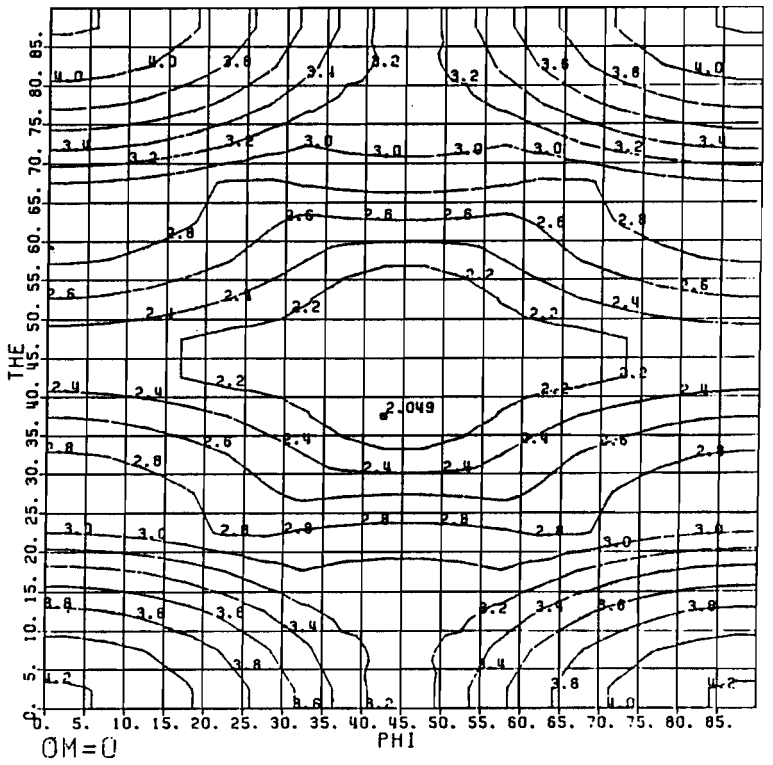
THE
PHI
0. 5. 10. 15. 20. 25. 30. 35. 40. 45. 50. 55. 60. 65. 70. 75. 80. 85.
2.049

ΘM=0

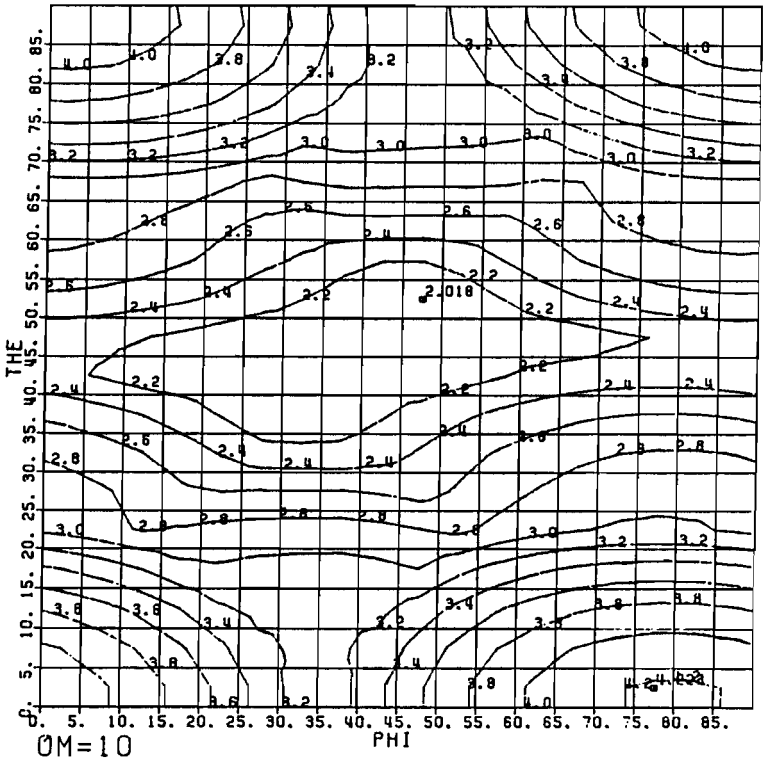
THE
PHI
0. 5. 10. 15. 20. 25. 30. 35. 40. 45. 50. 55. 60. 65. 70. 75. 80. 85.
2.018

ΘM=10

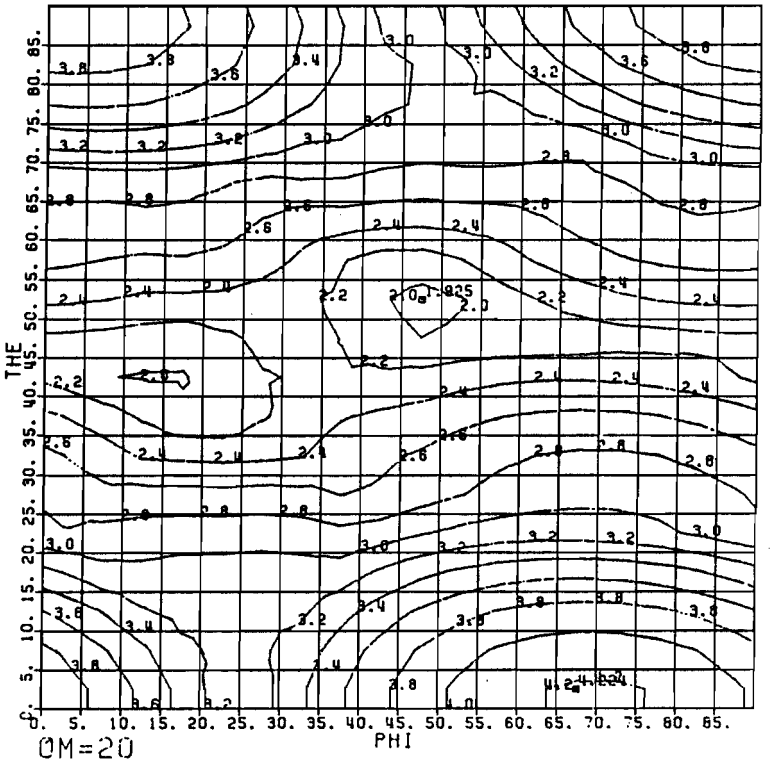
THE
PHI
0. 5. 10. 15. 20. 25. 30. 35. 40. 45. 50. 55. 60. 65. 70. 75. 80. 85.
ΘM=20

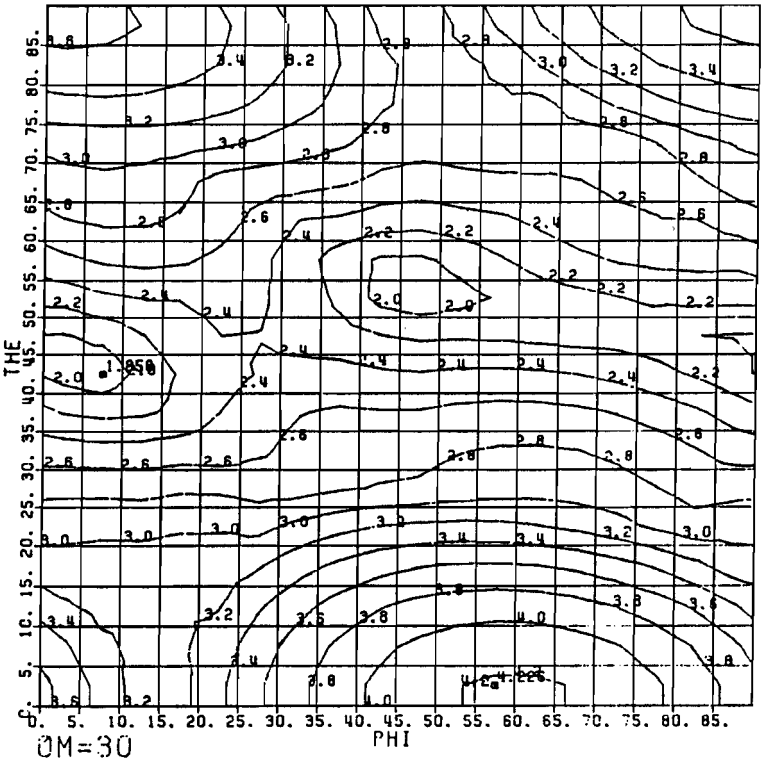
THE
PHI
0. 5. 10. 15. 20. 25. 30. 35. 40. 45. 50. 55. 60. 65. 70. 75. 80. 85.
ΘM=30

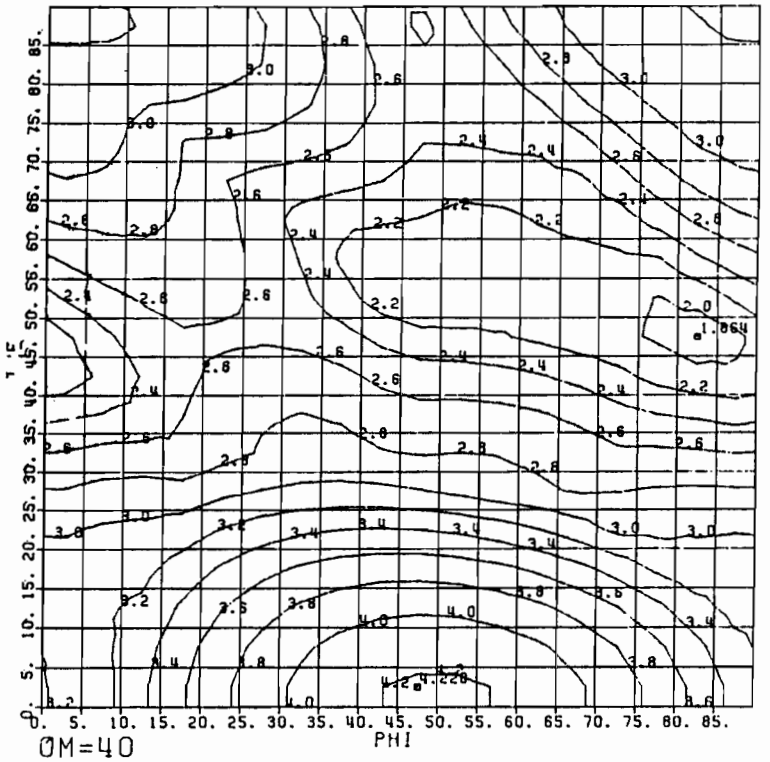
THE
0. 5. 10. 15. 20. 25. 30. 35. 40. 45. 50. 55. 60. 65. 70. 75. 80. 85.
PHI
ØM=40

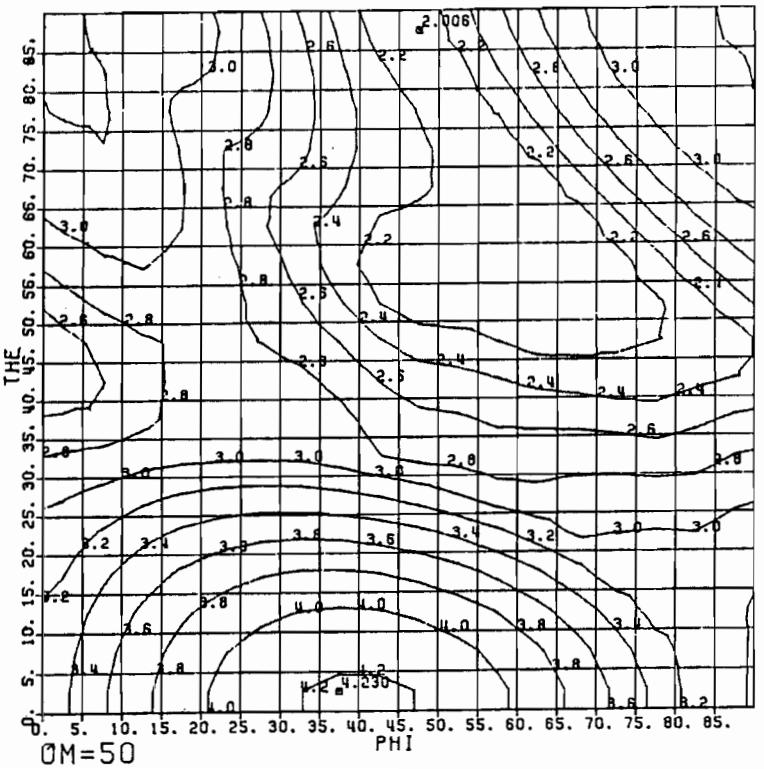
THE
0. 5. 10. 15. 20. 25. 30. 35. 40. 45. 50. 55. 60. 65. 70. 75. 80. 85.
PHI
ØM=50

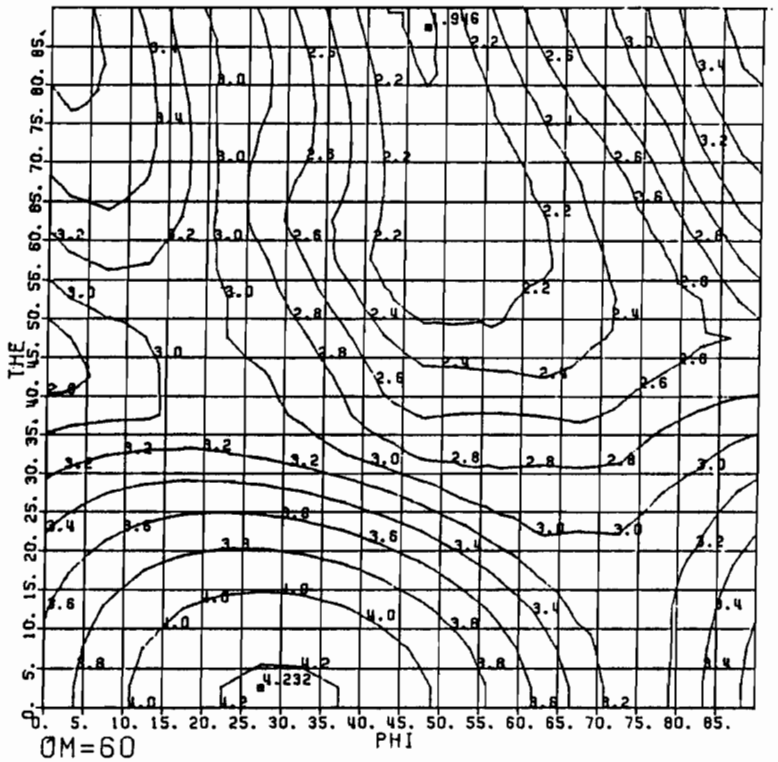
THE
PHI
0. 5. 10. 15. 20. 25. 30. 35. 40. 45. 50. 55. 60. 65. 70. 75. 80. 85.
.946
4.232

ΘM=60

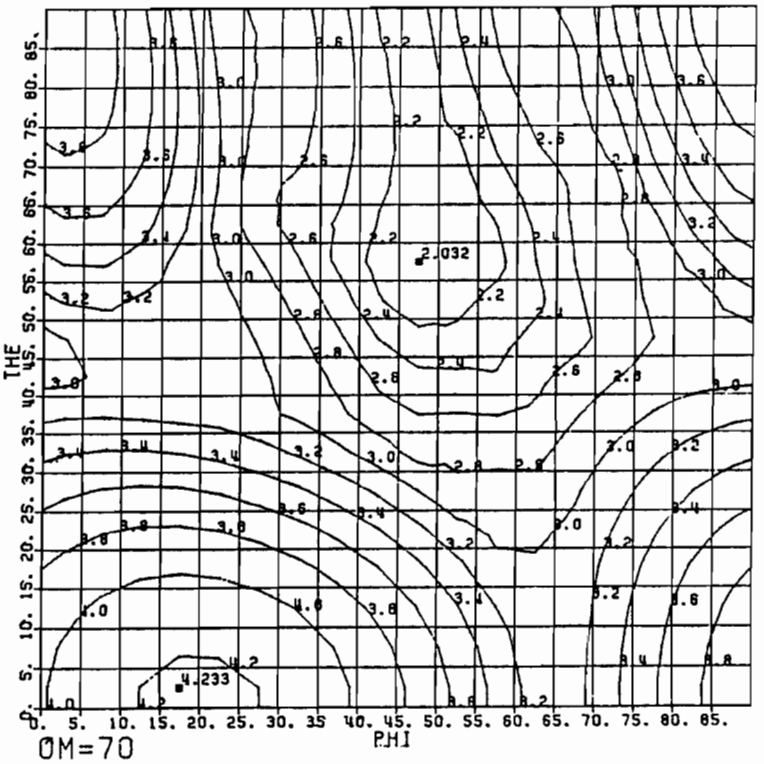
THE
PHI
0. 5. 10. 15. 20. 25. 30. 35. 40. 45. 50. 55. 60. 65. 70. 75. 80. 85.
2.032
4.233

ΘM=70

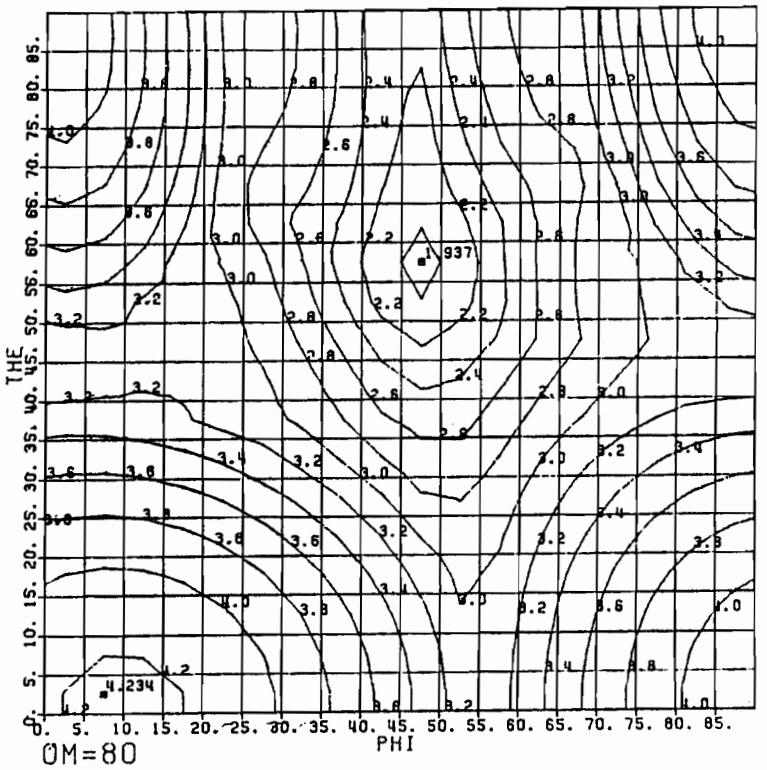
THE
PHI
ØM=80
1.937
4.234

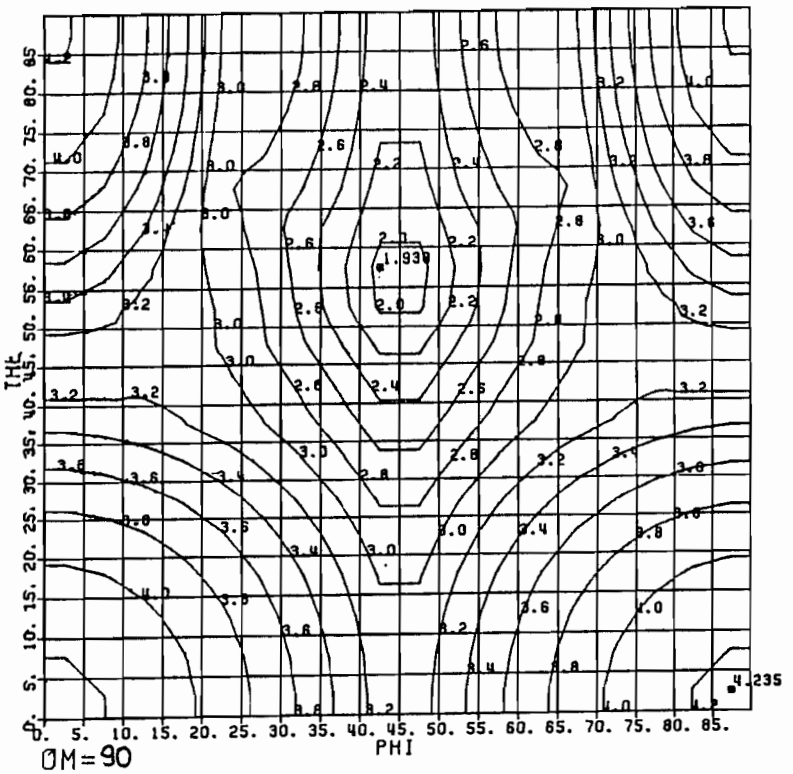
THE
PHI
ØM=90
1.930
4.235

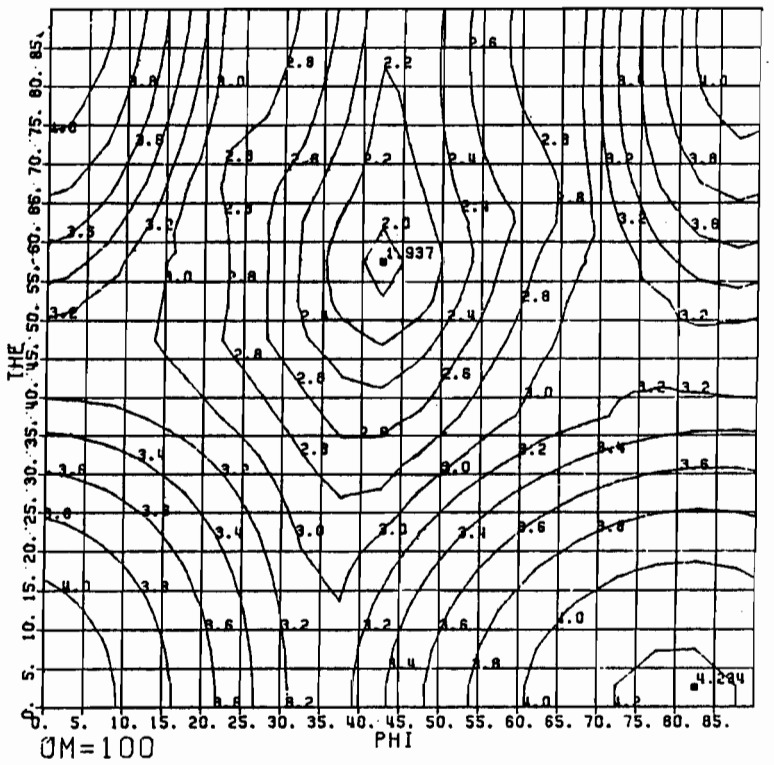
THE
PHI
ØM=100
1.937
4.294

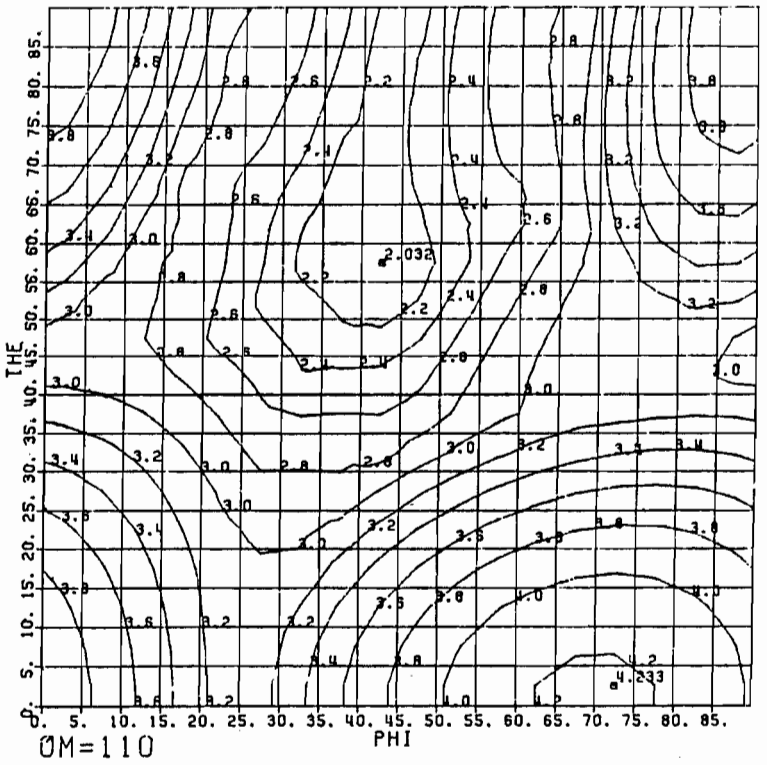
THE
PHI
ØM=110
2.032
4.233

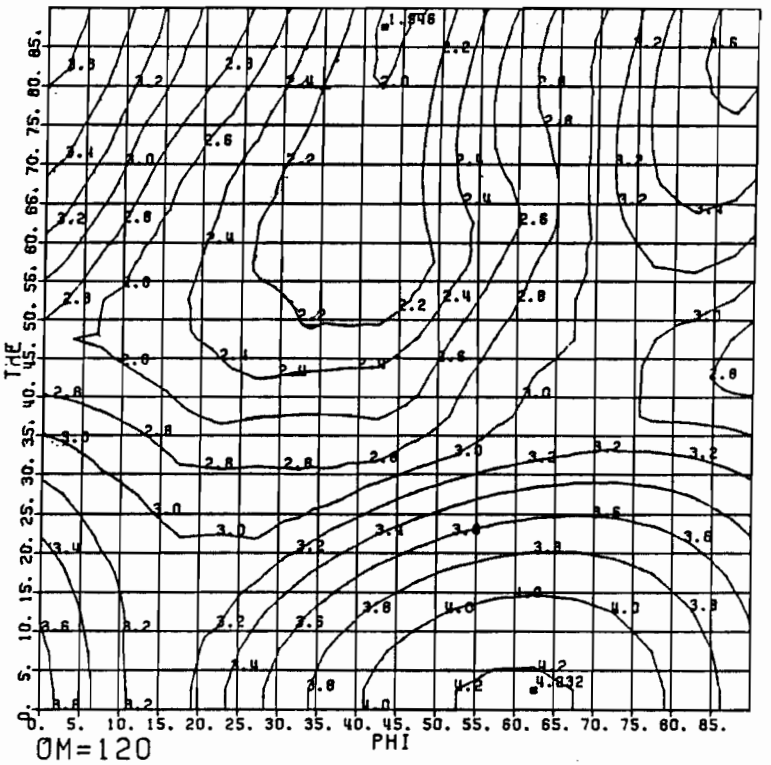
THE
PHI
0. 5. 10. 15. 20. 25. 30. 35. 40. 45. 50. 55. 60. 65. 70. 75. 80. 85.
1.946
4.832

ΘM=120

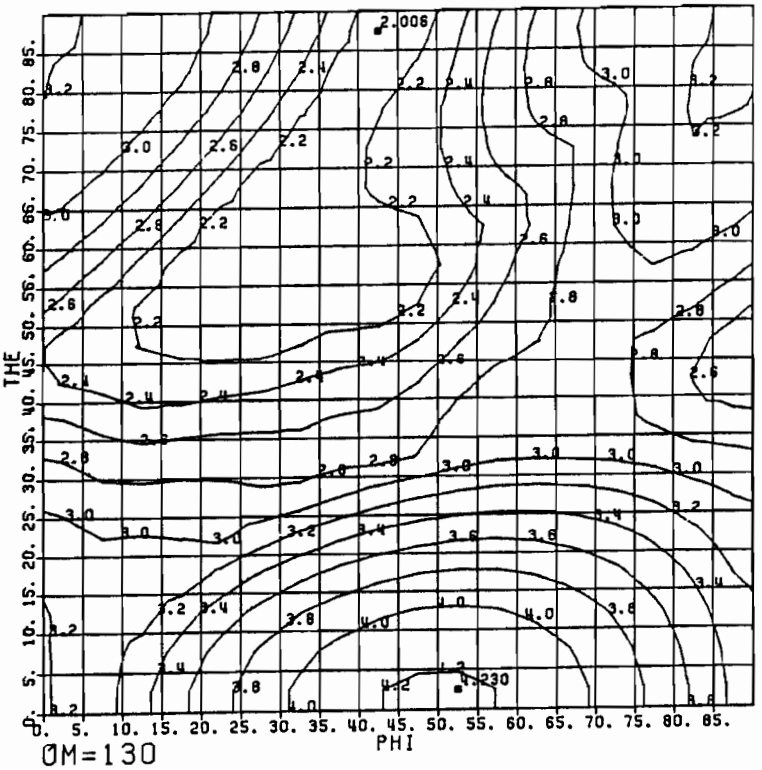
THE
PHI
0. 5. 10. 15. 20. 25. 30. 35. 40. 45. 50. 55. 60. 65. 70. 75. 80. 85.
2.006
1.230

ΘM=130

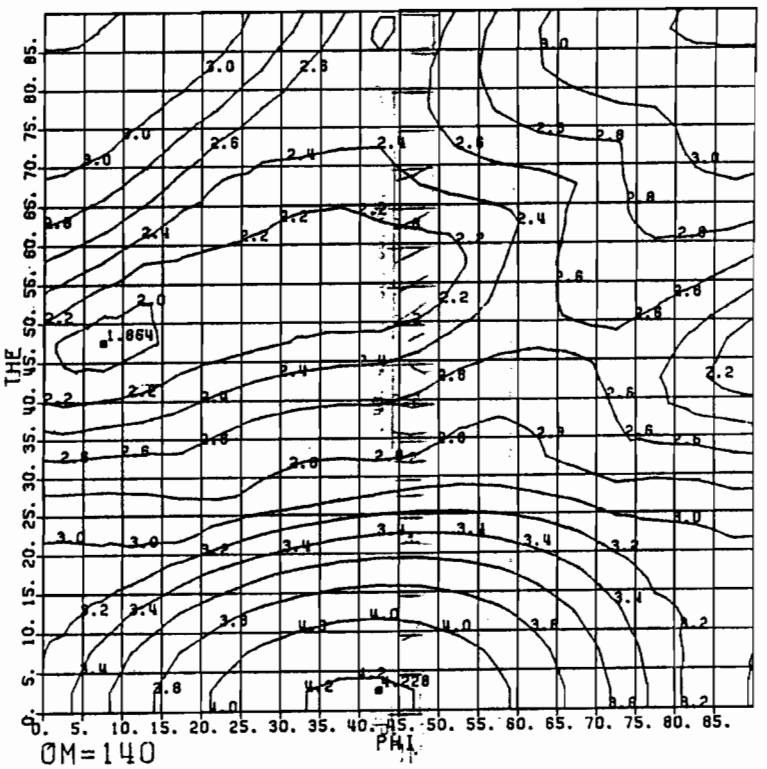
THE
PHI
0. 5. 10. 15. 20. 25. 30. 35. 40. 45. 50. 55. 60. 65. 70. 75. 80. 85.
1.864
4.228

ΘM=140

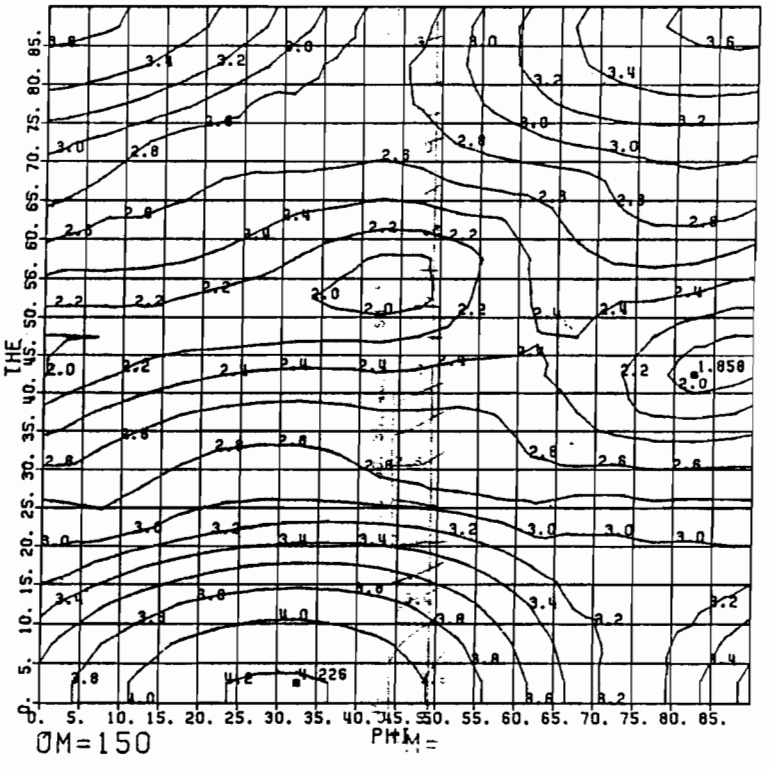
THE
PHI
0. 5. 10. 15. 20. 25. 30. 35. 40. 45. 50. 55. 60. 65. 70. 75. 80. 85.
1.858
4.226

ΘM=150

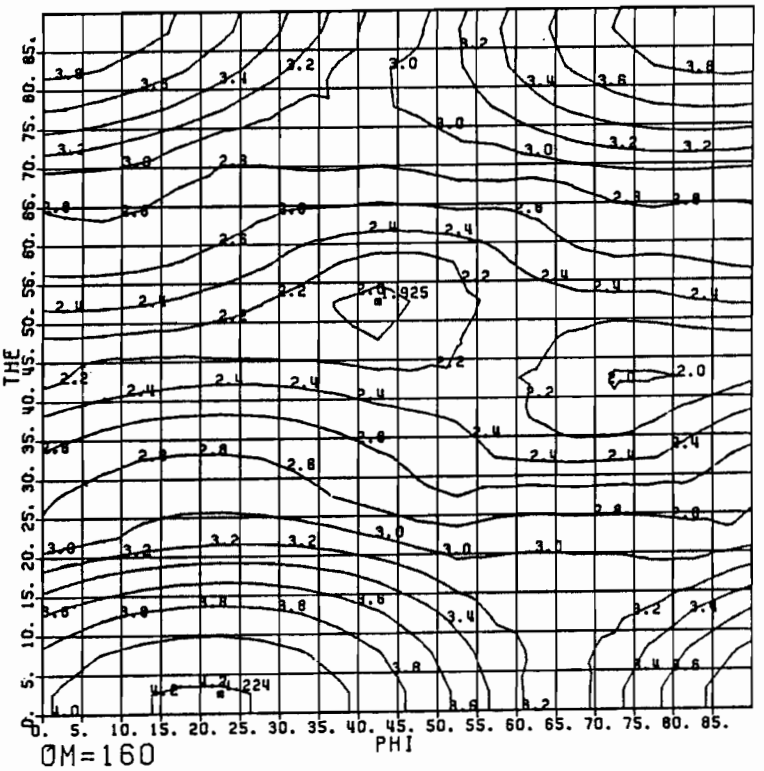
THE
PHI
0. 5. 10. 15. 20. 25. 30. 35. 40. 45. 50. 55. 60. 65. 70. 75. 80. 85.
.925
.224

ØM=160

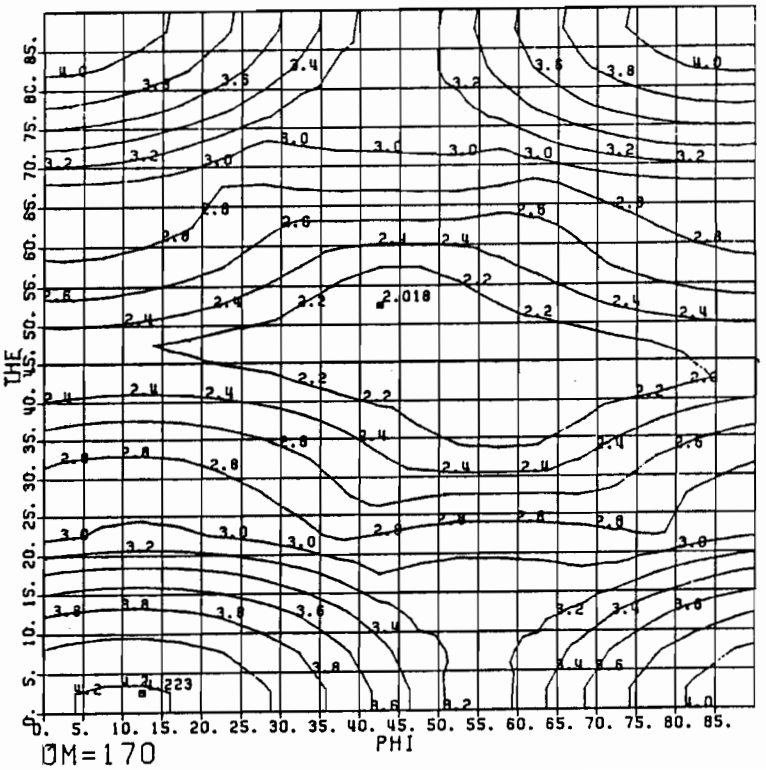
THE
PHI
0. 5. 10. 15. 20. 25. 30. 35. 40. 45. 50. 55. 60. 65. 70. 75. 80. 85.
2.018
.223

ØM=170

APPENDIX 7

VERTICES, FOURTH AND THIRD ORDER EDGES OF THE COMPOSITE YIELD SURFACE FOR SLIP ON {111} AND {100} PLANES

Notes:

1) In Table A7.1 are listed the 93 vertices and the associated systems and coordinates (referred to in terms of the notation described in Appendix 2) for $\alpha = 1$. Here the values are normalized by $\tau_{c(111)}$.

2) In Tables A7.2 and A7.3, a single representative example of each type of 4^{th} and 3^{rd} order edge is listed, with the corresponding connecting vertices and associated systems. The others can be deduced from this case by applying the 24 cubic symmetry operations.

TABLE A7.1

The 93 vertices of the composite yield surface.

Type	No.	Associated systems								Coordinates for α=1				
I	1	2	3	5	6	9	8	11	12	-1.732	-1.000	0.	0.	0.
	2	1	15	16	18	19	21	10	24	1.732	-1.000	0.	0.	0.
	3	13	14	4	17	7	20	22	23	0.	2.000	0.	0.	0.
II	4	1	2	16	18	19	8	10	24	0.866	-1.500	1.732	0.	0.
	5	1	15	16	5	19	21	10	11	0.866	-1.500	-1.732	0.	0.
	6	14	15	17	18	7	20	22	23	0.866	1.500	0.	1.732	0.
	7	13	14	4	17	21	20	23	24	0.866	1.500	0.	-1.732	0.
	8	2	3	4	6	7	9	11	12	-1.732	0.	0.	0.	1.732
	9	13	3	5	6	9	8	22	12	-1.732	0.	0.	0.	-1.732
III	10	2	3	9	8	27	29	34	36	-0.732	-0.423	2.000	0.	0.
	11	5	6	11	12	28	30	33	35	-0.732	-0.423	-2.000	0.	0.
	12	1	15	16	18	25	29	30	32	0.732	-0.423	0.	2.000	0.
	13	19	21	10	24	26	31	35	36	0.732	-0.423	0.	-2.000	0.
	14	4	17	7	20	25	26	27	28	0.	0.845	0.	0.	2.000
	15	13	14	22	23	31	32	33	34	0.	0.845	0.	0.	-2.000
IV	16	2	18	8	24	27	29	34	36	0.732	-1.268	2.000	0.	0.
	17	3	17	9	23	27	29	34	36	-0.732	1.268	2.000	0.	0.
	18	15	18	7	22	25	29	30	32	0.732	1.268	0.	2.000	0.
	19	1	16	9	12	25	29	30	32	-0.732	-1.268	0.	2.000	0.
	20	2	4	7	11	25	26	27	28	-1.464	0.	0.	0.	2.000
	21	1	17	20	10	25	26	27	28	1.464	0.	0.	0.	2.000
V	22	2	7	9	11	12	25			-1.598	-0.077	0.	0.268	1.732
	23	1	2	9	11	12	25			-0.866	-1.345	0.	1.732	0.268
	24	13	3	5	6	8	31			-1.598	-0.077	0.	-0.268	-1.732
	25	3	5	6	19	8	31			-0.866	-1.345	0.	-1.732	-0.268
	26	5	8	9	22	12	32			-1.598	-0.077	0.	0.268	-1.732
	27	16	5	8	9	12	32			-0.866	-1.345	0.	1.732	-0.268
	28	2	3	4	6	11	26			-1.598	-0.077	0.	-0.268	1.732
	29	2	3	6	10	11	26			-0.866	-1.345	0.	-1.732	0.268
	30	1	2	18	10	24	27			0.866	-1.345	1.732	0.	0.268
	31	1	17	18	10	24	27			1.598	-0.077	0.268	0.	1.732
	32	15	16	5	19	21	33			0.866	-1.345	-1.732	0.	-0.268
	33	14	15	16	19	21	33			1.598	-0.077	-0.268	0.	-1.732
	34	1	15	21	11	10	28			0.866	-1.345	-1.732	0.	0.268
	35	1	15	20	21	10	28			1.598	-0.077	-0.268	0.	1.732
	36	16	18	19	8	24	34			0.866	-1.345	1.732	0.	-0.268
	37	16	18	19	23	24	34			1.598	-0.077	0.268	0.	-1.732
	38	17	18	7	22	23	29			0.732	1.423	0.268	1.732	0.
	39	17	7	9	22	23	29			-0.732	1.423	1.732	0.268	0.
	40	13	14	4	21	20	35			0.732	1.423	-0.268	-1.732	0.
	41	13	14	4	6	20	35			-0.732	1.423	-1.732	-0.268	0.
	42	13	4	17	24	23	36			0.732	1.423	0.268	-1.732	0.
	43	13	3	4	17	23	36			-0.732	1.423	1.732	-0.268	0.
	44	14	15	7	20	22	30			0.732	1.423	-0.268	1.732	0.
	45	14	7	20	12	22	30			-0.732	1.423	-1.732	0.268	0.

Type	No.	Associated systems					Coordinates for α=1				
VI	46	2	7	9	25	27	-1.464	0.	0.268	0.268	1.732
	47	1	2	9	25	29	-0.732	-1.268	0.268	1.732	0.268
	48	1	17	18	25	27	1.464	0.	0.268	0.268	1.732
	49	1	2	18	27	29	0.732	-1.268	1.732	0.268	0.268
	50	17	18	7	25	29	0.732	1.268	0.268	1.732	0.268
	51	17	7	9	27	29	-0.732	1.268	1.732	0.268	0.268
	52	7	11	12	25	28	-1.464	0.	-0.268	0.268	1.732
	53	1	11	12	25	30	-0.732	-1.268	-0.268	1.732	0.268
	54	1	15	20	25	28	1.464	0.	-0.268	0.268	1.732
	55	1	15	11	28	30	0.732	-1.268	-1.732	0.268	0.268
	56	15	7	20	25	30	0.732	1.268	-0.268	1.732	0.268
	57	7	20	12	28	30	-0.732	1.268	-1.732	0.268	0.268
	58	2	3	4	26	27	-1.464	0.	0.268	-0.268	1.732
	59	2	3	10	26	36	-0.732	-1.268	0.268	-1.732	0.268
	60	17	10	24	26	27	1.464	0.	0.268	-0.268	1.732
	61	2	10	24	27	36	0.732	-1.268	1.732	-0.268	0.268
	62	3	4	17	27	36	-0.732	1.268	1.732	-0.268	0.268
	63	4	17	24	26	36	0.732	1.268	0.268	-1.732	0.268
	64	8	9	22	32	34	-1.464	0.	0.268	0.268	-1.732
	65	16	8	9	29	32	-0.732	-1.268	0.268	1.732	-0.268
	66	16	18	23	32	34	1.464	0.	0.268	0.268	-1.732
	67	16	18	8	29	34	0.732	-1.268	1.732	0.268	-0.268
	68	18	22	23	29	32	0.732	1.268	0.268	1.732	-0.268
	69	9	22	23	29	34	-0.732	1.268	1.732	0.268	-0.268
VII	70	2	3	26	27	36	-0.732	-0.423	1.000	-1.000	1.000
	71	9	8	29	32	34	-0.732	-0.423	1.000	1.000	-1.000
	72	11	12	25	28	30	-0.732	-0.423	-1.000	1.000	1.000
	73	5	6	31	33	35	-0.732	-0.423	-1.000	-1.000	-1.000
	74	16	18	29	32	34	0.732	-0.423	1.000	1.000	-1.000
	75	1	15	25	28	30	0.732	-0.423	-1.000	1.000	1.000
	76	10	24	26	27	36	0.732	-0.423	1.000	-1.000	1.000
	77	19	21	31	33	35	0.732	-0.423	-1.000	-1.000	-1.000
	78	7	20	25	28	30	0.	0.845	-1.000	1.000	1.000
	79	4	17	26	27	36	0.	0.845	1.000	-1.000	1.000
	80	22	23	29	32	34	0.	0.845	1.000	1.000	-1.000
	81	13	14	31	33	35	0.	0.845	-1.000	-1.000	-1.000
VIII	82	2	9	25	27	29	-0.732	-0.423	1.000	1.000	1.000
	83	3	8	31	34	36	-0.732	-0.423	1.000	-1.000	-1.000
	84	6	11	26	28	35	-0.732	-0.423	-1.000	-1.000	1.000
	85	5	12	30	32	33	-0.732	-0.423	-1.000	1.000	-1.000
	86	1	18	25	27	29	0.732	-0.423	1.000	1.000	1.000
	87	15	16	30	32	33	0.732	-0.423	-1.000	1.000	-1.000
	88	19	24	31	34	36	0.732	-0.423	1.000	-1.000	-1.000
	89	21	10	26	28	35	0.732	-0.423	-1.000	-1.000	1.000
	90	17	7	25	27	29	0.	0.845	1.000	1.000	1.000
	91	4	20	26	28	35	0.	0.845	-1.000	-1.000	1.000
	92	14	22	30	32	33	0.	0.845	-1.000	1.000	-1.000
	93	13	23	31	34	36	0.	0.845	1.000	-1.000	-1.000

TABLE A7.2

Combinations of 4 independent slip systems.

Type	No.	Connecting vertices		Associated systems					
4A	1	1	8	2	3	6	9	11	12
4B	13	1	10	2	3	9	8		
4C	19	4	16	2	8	18	24		
4D	25	8	22	2	7	9	11	12	
4E	49	10	16	2	8	27	29	34	36
4F	61	10	126	2	3	9	27		
4G	85	10	70	2	3	27	36		
4H	97	13	76	10	24	26	36		
4I	109	16	30	2	18	24	27		
4J	133	16	49	2	18	27	29		
4K	157	22	23	2	9	11	12	25	
4L	169	22	46	2	7	9	25		
4M	217	58	70	2	3	26	27		
4N	241	46	82	2	9	25	27		
4O	265	70	180	3	26	27	36		

TABLE A7.3

Combinations of 3 independent systems.

Type	No.	Connecting vertices						Associated systems			
3A	1	1	8	10	126			2	3	9	
3B	25	1	8	9	95			3	6	9	12
3C	28	1	8	28	29	99		2	3	6	11
3D	40	8	22	46	126			2	7	9	
3E	64	4	16	30				2	18	24	
3F	88	10	16	17	104			27	29	34	36
3G	91	10	17	125	126			3	9	27	
3H	115	10	16	61	70	185		2	27	36	
3I	163	10	58	70	126			2	3	27	
3J	211	70	76	79	178	180	185	26	27	36	
3K	215	28	29	58	59	70		2	3	26	
3L	239	58	70	180				3	26	27	
3M	263	16	30	49				2	18	27	

APPENDIX 8

MINIMIZATION OF THE GRAIN BOUNDARY ENERGY

It must be recognized that, as a first approximation, the GBE only depends on the misorientation between two adjacent grains. If A_1 and A_2 are the matrices associated with the two orientations, the misorientation α between the two can be calculated from:

$$trace({}^{t}A_2.A_1) = 1 + 2\cos\alpha \qquad \text{(A8.1)}$$

However, if A_1 is kept constant and A_2 is replaced by the 24 equivalent matrices, equation A8.1 leads to 24 different values of α. To find the real misorientation, the 24 equivalent products all have to be calculated so that the *minimum* value of α can be found.

In order to establish now the "closest" stable boundary (i.e. one corresponding to a coincidence site or to a low angle boundary with α equal to zero), the same procedure must be used. The trace of $C=({}^{t}A_2^*.A_1)$ must be calculated, where A_2^* is the transform of A_2 pertaining to all the coincidence rotations and all the symmetry transformations (see Figure A8.1 for the definition of the different matrices). The closest stable boundary corresponds to the minimum value of α found in this procedure.

The $\Sigma=3$ coincidence rotations can all be defined by the four matrices listed in Table A8.1; the $\Sigma=1$ coincidence rotation matrix, by contrast, is simply the identity matrix. Now, minimizing the GBE is equivalent to minimizing the angle α associated with the nearest stable boundary, or conversely, to maximizing the trace of the product $({}^{t}A_2^*.A_1)$. It will now be shown that the trace of this matrix can be expressed to a first order as a linear function of the shear rates on the active slip systems in the two subgrains.

At a given instant t, before the increment of deformation, we have:

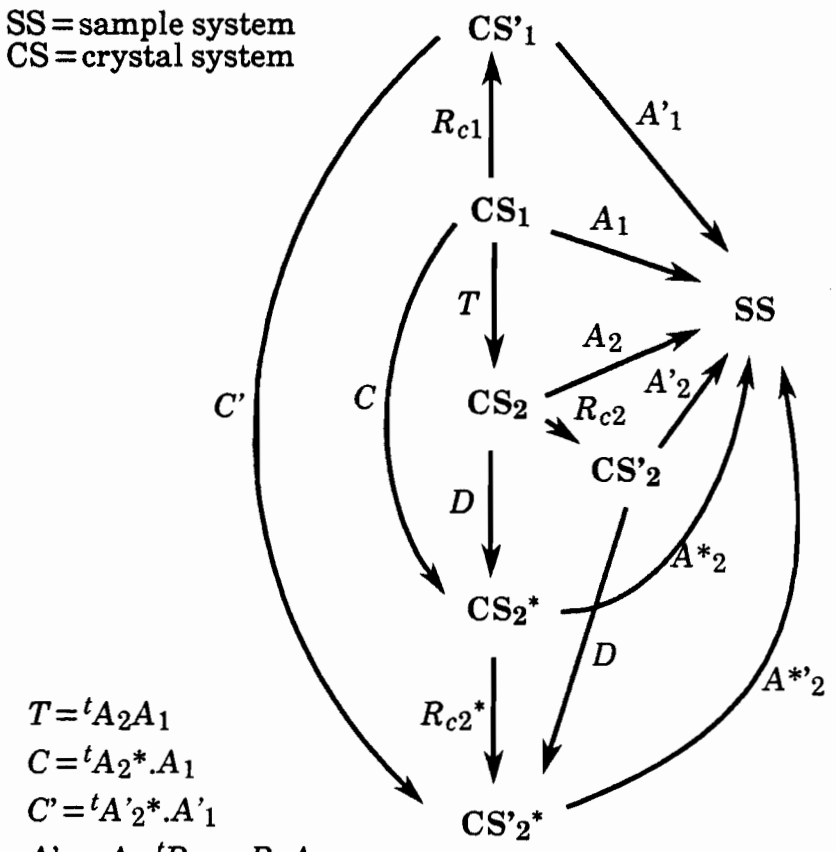

Figure A8.1. Significance of the different rotation matrices:
A_1, A_2 original orientation matrices;
A_1', A_2' orientation matrices after rotation;
R_{c1}, R_{c2} rotation matrices defined from R_1 and R_2 (Appendix 2);
D coincidence rotation (also takes into account the cubic symmetry);
A_2^* transform of A_2 by this coincidence rotation;
$A_2^{*\prime}$ transform of A_2^* by the R_{c2}^* rotation matrix.

$$trace({}^tA^*_2 . A_1) = trace\, C = 1 + 2cos\alpha = trace(A_1 . {}^tA^*_2) \qquad (A8.2)$$

During the increment of deformation, the shear rates on the active slip systems are $\dot{\gamma}^s$ in grain 1 and $\dot{\gamma}'^s$ in grain 2. This results in a reorientation of each subgrain, the new matrices being A_1' and A_2', as calculated in Appendix 2. In

$$D_1 = 1/3 \begin{bmatrix} 2 & -1 & 2 \\ 2 & 2 & -1 \\ -1 & 2 & 2 \end{bmatrix} \qquad D_3 = 1/3 \begin{bmatrix} 2 & -2 & -1 \\ 1 & 2 & -2 \\ 2 & 1 & 2 \end{bmatrix}$$

$$D_2 = 1/3 \begin{bmatrix} 2 & 2 & 1 \\ -1 & 2 & -2 \\ -2 & 1 & 2 \end{bmatrix} \qquad D_4 = 1/3 \begin{bmatrix} 2 & 1 & -2 \\ -2 & 2 & -1 \\ 1 & 2 & 2 \end{bmatrix}$$

Table A8.1. Rotation matrices corresponding to $\Sigma = 3$ boundaries.

the present calculation, we use a *first order approximation* of the matrices R_1 and R_2 which link A_1, A_2 and A_1', A_2'. We can therefore write that:

$$\begin{aligned} A'_1 &= R_1 A_1 \\ A'_2 &= R_2 A_2 \\ A'^*_2 &= R^*_2 A^*_2 \end{aligned} \tag{A8.3}$$

where R_1 and R_2 are calculated from:

$$R_1 = D_1 - G_1 + I \tag{A8.4}$$

$$R_2 = D_2 - G_2 + I$$

Here D_1 and D_2 are the displacement gradients acting on the two grains as seen from the sample system and G_1 and G_2 are the displacement gradients as seen from the crystal system. In D_1 and D_2, some terms are zero, depending on which planes and lines remain fixed in space. In the case of rolling, where 3 shear strains are relaxed, $D_{rolling}$ is equal to :

$$D_{rolling} = \begin{vmatrix} d_{11} & 0 & d_{13} \\ d_{21} & d_{22} & d_{23} \\ 0 & 0 & d_{33} \end{vmatrix} \tag{A8.5}$$

whereas in fixed end torsion, where 2 shear rates are relaxed in the grain axes, $D_{torsion}$ is equal to

$$D_{torsion} = \begin{vmatrix} 0 & 0 & d_{13} \\ d_{21} & 0 & d_{23} = \Upsilon \\ 0 & 0 & 0 \end{vmatrix} \tag{A8.6}$$

In both rolling and torsion, the 2 axis and 3 plane are assumed to remain fixed. We also have:

$$G_{ij} = \sum_s \dot{\Upsilon}^s \, n_i^s \, b_j^s \, dt \tag{A8.7}$$

which gives us for R:

$$R = \begin{vmatrix} 1 & R_{12} & -R_{31} \\ -R_{12} & 1 & -R_{32} \\ R_{31} & R_{32} & 1 \end{vmatrix} \tag{A8.8}$$

where R_{12}, R_{31} and R_{32} are equal to

$$\begin{aligned} R_{12} &= -\sum_s \dot{\Upsilon}^s \, b_1^s \, n_2^s \, dt \\ R_{31} &= -\sum_s \dot{\Upsilon}^s \, b_3^s \, n_1^s \, dt \\ R_{32} &= -\sum_s \dot{\Upsilon}^s \, b_3^s \, n_2^s \, dt \end{aligned} \tag{A8.9}$$

in both cases of rolling and torsion.

We can now consider the new matrix $C' = ({}^tA_2'^*.A_1')$, which is given by: $C' = R^*_{c2}.C.{}^tR_{c1}$ and calculate its trace so as to have the new value of the angle α'.

$$trace\, C' = trace({}^tA'^*_2 \, A'_1) = trace(A'_1 \, {}^tA'^*_2) = trace(R_1 A_1 \, {}^tA^*_2 \, {}^tR_2) \tag{A8.11}$$

with $$C^* = A_1.{}^tA^*_2$$

We find to a first order that:

$$trace\, C' = 1 + 2cos\alpha' = trace\, C - a(R_{12} - R'_{12}) - b(R_{31} - R'_{31}) - c(R_{32} - R'_{32}) \tag{A8.12}$$

with

$$\begin{aligned} a &= C^*_{12} - C^*_{21} \\ b &= C^*_{31} - C^*_{13} \\ c &= C^*_{32} - C^*_{23} \end{aligned} \tag{A8.13}$$

It is thus seen that the difference between trace(C') and trace(C) is a linear function of the $\dot{\Upsilon}^s$ and $\dot{\Upsilon}'^s$:

$$trace\, C' - trace\, C = f(\dot{\Upsilon}^s, \dot{\Upsilon}'^s) = (\sum_s c^s \, \dot{\Upsilon}^s - \sum_s c'^s \, \dot{\Upsilon}'^s) \, dt \tag{A8.14}$$

where the coefficients, c^s and c'^s are equal to:

$$c^s = \sum_s a \, b_1^s \, n_2^s + \sum_s b \, b_3^s \, n_1^s + \sum_s c \, b_3^s \, n_2^s \tag{A8.15}$$

$$c'^s = \sum_s a\, b'^s_1\, n'^s_2 + \sum_s b\, b'^s_3\, n'^s_1 + \sum_s c\, b'^s_3\, n'^s_2$$

In order to minimize α, it is necessary to minimize the function:

$$g(\dot{Y}^s, \dot{Y}'^s) = -f(\dot{Y}^s, \dot{Y}'^s)/dt \qquad \text{(A8.16)}$$

with respect to $\dot{y}^s$ and $\dot{y}'^s$ (this function represents the rate of change of trace of C). The problem can now be solved by means of the linear programming technique. It should be noted though that, when α is equal to 0, the function is zero for all values of $\dot{y}^s$ and $\dot{y}'^s$ and the problem is indeterminate in this case ($a=b=c=0$). However, in an actual computation, when α approaches zero, the function $g(\dot{y}^s, \dot{y}'^s)$ oscillates between two extreme solutions and α is never exactly zero. To solve the problem rigorously in this case, it would be necessary to calculate the function g to second order. This would, however, involve very lengthy calculations.